AN EXPERIMENTAL STUDY OF DEFORMATION AND FRACTURE OF A NANOSTRUCTURED METALLIC MATERIAL

A Thesis

by

NISRIN RIZEK ABDEL AL

Submitted to the Office of Graduate Studies of
Texas A&M University
in partial fulfillment of the requirements for the degree of

MASTER OF SCIENCE

December 2009

Major Subject: Aerospace Engineering

AN EXPERIMENTAL STUDY OF DEFORMATION AND FRACTURE OF A NANOSTRUCTURED METALLIC MATERIAL

A Thesis

by

NISRIN RIZEK ABDEL AL

Submitted to the Office of Graduate Studies of
Texas A&M University
in partial fulfillment of the requirements for the degree of

MASTER OF SCIENCE

Approved by:

Chair of Committee,	Amine Benzerga
Committee Members,	Ibrahim Karaman
	Vikram Kinra
Head of Department,	Dimitris Lagoudas

December 2009

Major Subject: Aerospace Engineering

ABSTRACT

An Experimental Study of Deformation and Fracture of a Nanostructured Metallic Material. (December 2009)

Nisrin Rizek Abdel Al, B.S, Jordan University of Science and Technology

Chair of Advisory Committee: Dr. Amine Benzerga

The mechanical properties of materials strongly depend on their microstructure. Therefore, engineering the material's microstructure can lead to improving its mechanical properties. One method for enhancing the strength of metallic materials consists of refining the grain size down to the nanometer scale. Such nanostructured materials possess remarkable strength without using conventional metallurgical strengthening methods. However, this strength often comes at the expense of work-hardening capacity, thus favoring flow localization and loss of ductility and toughness. The deformation behavior of nanostructured metallic materials has been extensively studied in the literature. However, little is known of their fracture behavior. In this study, the mechanical behavior of a nanostructured, nearly pure material is investigated in order to link processing conditions, microstructure, and fracture locus in stress space. With focus laid on BCC materials which can undergo a ductile-to-brittle transition, Interstitial-Free (IF) steel is chosen. The microstructure is refined using Severe Plastic Deformation (SPD) to achieve ultra-fine grain (UFG) materials with grain sizes in the range 100nm-1μm. Equal Channel Angular Extrusion (ECAE) is used to obtain three types of UFG-IF

steel microstructures by varying the extrusion rate and processing temperature. The deformation behavior is investigated for the three UFG materials using round smooth bars and is compared with the behavior of the as-received material. The damage behavior and the fracture mechanisms are studied using tensile round notched bars with varying notch radii. The findings indicate a remarkable combination of strength and notch ductility at room temperature, including for the material with the finest microstructure. They also point to the need for careful characterization of temperature effects before such materials can be considered in structural applications.

DEDICATION

To my mother who devoted herself to bring me up, to encourage me, and to support me all the time

To my husband who sacrifices a lot for me to reach this point.

To my family

To my father whom I have never seen

And to my father and mother in law

I will never forget what you did for me.

ACKNOWLEDGEMENTS

Foremost, I would like to express my sincere gratitude to my advisor, Prof. Amine Benzerga, for the continuous support of my master study and research, for his patience, motivation, enthusiasm, and immense knowledge. His guidance helped me throughout the research and writing of this thesis. I could not have imagined having a better advisor and mentor for my Master study. Beside my advisor, I would like to thank the rest of my committee members: Prof Ibrahim Karaman, who helped me during my research, provided the necessary material for the research work, and then provided me with his guidance, and advice. Also, special thanks for Dr Vikram Kinra, who consented to be one of my committee members and spent his valuable time reading my thesis and providing critical feedback.

I would like to thank the people in the laboratories who never stopped helping me during my experimental work, either machining my specimens, training on the microscope, or training on other instruments, Special thanks go to Rodney Inmon, Tom Stephen, Michel Pendelton, Tim Elliot, Robert Barber, and Dr Mohammed Haouaoui.

Finally, special thanks go to my colleagues and lab-mates who inspired me with their ideas and advices, and special thanks to the Aerospace Engineering Department and staff, especially Ms Karen Knabe.

TABLE OF CONTENTS

CHAPTER Page

Page

LIST OF FIGURES

Page

FIGURE

Page

FIGURE

FIGURE Page

FIGURE Page

FIGURE Page

FIGURE Page

FIGURE Page

FIGURE Page

FIGURE Page

FIGURE Page

FIGURE Page

FIGURE Page

LIST OF TABLES

CHAPTER I

INTRODUCTION

The mechanical properties of materials strongly depend on their microstructures. Therefore, engineering the material's microstructure can lead to improving its mechanical properties. For example, reducing the grain size of conventional metallic alloys has been shown to lead to a very significant enhancement in their mechanical properties. Refining the grain size of the material, for instance, leads to an increase in yield strength and ultimate tensile strength.

A high specific strength is a desirable property in many industrial applications. However, high strength is often realized at the expense of toughness and ductility. In certain applications, ductility is needed to ease the forming and machining of the material into different parts and shapes. In other applications, such as in materials for load-bearing structures, a minimum toughness is required along with other properties such as impact strength and ductile to brittle transition temperature.

In the past two decades, advanced fabrication methods have been developed which allow to refine the mean grain size (d) of polycrystalline materials below the micrometer [1,2]. This class of so-called nanostructured materials comprises Ultra-Fine Grain (UFG) materials (100nm < d <1μm) and nanocrystalline materials (d < 100nm).

This thesis follows the style of Acta Materialia.

Nanostructured polycrystalline materials have unprecedented strength. However, to date their fracture behavior has not been studied thoroughly.

This research focuses on UFG materials, i.e, polycrystalline materials with refined grain size in the range of 100 nm-1 μm. They present the advantage that they can be produced in bulk. For bulk UFG materials, there are additional preferred requirements such as a homogenous structure that has a reasonably equiaxed grains, with a majority of the grain boundaries showing a high angle of misorientation [2-4]. The optimum combination of high strength and acceptable ductility can be achieved in some UFG materials when fabricated using certain combination of the extrusion conditions represented by the fabrication route [5,6].

Severe Plastic Deformation (SPD) techniques are preferred techniques to produce UFG materials for many reasons. First, they impose extremely high amounts of strain at low homologous temperature. Second, they avoid defects like voids and impurities on the produced UFG. The superior technique among the SPD techniques is Equal Channel Angular Extrusion/Pressing (ECAE/ECAP). This results from its ability to produce homogenous structure and equiaxed grains.

UFG materials show promise for many industrial applications including aerospace, automotive, biomedical, chemical-sensor, construction, electronics, and metal-forming. Therefore, research regarding UFG materials is regarded as a matter of industrial and national importance [6,7].

For example, some UFG materials like ZE41A aeronautic magnesium alloy are preferred in certain applications such as aircraft engines, helicopters, airframe

components, wheels and gear boxes due to their adequate combination of their properties and cost [6]. Moreover, UFG SnO2 has been used in manufacturing gas sensors which are capable to detect carbon monoxide [8]. In addition, UFG of pure titanium has been used in dental implants [9].

Because the majority of the UFG materials are metals, they are expected to exhibit some ductility at room temperature. But to date, the ductile fracture mechanisms of the UFG materials have not been thoroughly studied. Therefore, in this study we will investigate the effect of grain size on the strength level and the ductile fracture behavior of a selected UFG material. Smooth round bars are used to characterize the deformation behavior of the UFG metallic materials, whereas round notched bars with different radii are used to characterize the damage behavior and the fracture mechanisms.

The material chosen for this study is Interstitial Free (IF) steel. IF steel is a vacuum decarburized low-carbon steel with extra-low carbon content, nominally 0.005%, in which the residual carbon is combined with niobium, titanium or some similar element with a strong affinity for carbon to make it interstitial free. IF steel is chosen since it is a good model of BCC materials which can undergo a ductile-to- brittle transition, it is cheap, available, and it is usually formed by deep drawing into different automotive shapes due to its malleability, strength, as well as resistance to stress and tension damage [10]. Moreover, choosing IF steel which is considered as nearly pure material will allow us to study the effect of using SPD/ECAE with three different processing conditions on strengthening the material apart from the effect of the alloying elements.

The present research focuses upon the following objectives:

1. First, investigate the fracture behavior of a BCC nanostructured material at room temperature (effect of stress-state and the microstructure).
2. Second, to investigate the mechanisms that governs the initiation and propagation of fracture in these materials at room temperature.

To fulfill the required objectives of the research, fabrication and mechanical testing of the chosen material have been performed.

1. First, IF steel has been fabricated by SPD/ECAE using route 8Bc and three different processing conditions in term of temperature and extrusion rate to vary the grain size between (200nm-1μm).
2. Second, smooth and notched bar samples are machined from the fabricated billets using Electrical Discharge Machining (EDM).
3. Both the smooth bar samples and the notched bar samples are tested in tensile test using MTS machine at room temperature are quasi-static loading conditions. The smooth bars are used to characterize the deformation behavior of the material. The notched bar samples are used to study the damage behavior and the fracture mechanisms.
4. Finally, micrographic and fractographic using Field Emission Scanning Electron Microscope (FE-SEM) are done to characterize the material microstructure and to investigate the damage mechanisms.

CHAPTER II

LITERATURE SURVEY

2.1 Properties and Applications of Interstitial Free (IF) Steel

Interstitial Free (IF) steel is a vacuum decarburized low-carbon steel with extra-low carbon content, nominally 0.005%. In IF steel the residual carbon is combined with niobium, titanium, or some similar element with a strong affinity for carbon to stabilize interstitial solutes carbon by forming titanium or niobium carbides or titanium or niobium oxides [11]. Carbon is small enough to fit into the interstices of a primarily iron matrix, making it an "interstitial element" in steel. If the steel alloy has an ultra-low carbon level (typically less than 50 parts per million), most of these gaps will not be occupied and, as such, can be called (IF) steel. Achieving this low carbon level does not occur using conventional steel processing. Instead, the molten steel must be put under a vacuum that decarburizes it by removing carbon monoxide, as well as other gases like hydrogen and nitrogen. This process is called vacuum degassing, and it is done in the production of vacuum degassed interstitial-free steels (VD-IF) [10].

Proper control of chemical compositions is important to achieve excellent properties, for example, the addition of titanium to vacuum decarburized low-carbon steels has been reported to result in low-carbon steel sheets with plastic-strain ratio (r_m) values exceeding other types of low-carbon steels. A higher value for the r_m means that the material will show desirable deep drawability properties. Insufficient addition of

alloying elements resulted in unstabilized C solutes and deteriorated the deep-drawability of the steel [11].

IF steel is chosen in this study since it represents a good model of the BCC materials, since BCC materials considered as good models to study the ductile to brittle transition. It is cheap, available, and it is usually formed by deep drawing into different automotive shapes due to its malleability, strength, as well as resistance to stress and tension damage [10]. Moreover, some industries like aerospace, automobile, dairy, lighting, and plastics rely on deep drawing in manufacturing some of their parts.

2.2 Equal Angular Channel Extrusion/Pressing (ECAE/ECAP)

It is well recognized that the mechanical performance of the materials is dependent upon their microstructures. By adjusting the microstructure of the materials new properties can be developed. Although the mechanical properties of the materials are influenced by several factors, the grain size is considered as one of the most important microstructural factors to determine the materials mechanical properties. This can be obviously seen through the Hall-Petch equation 2.1 which relates the strength of the polycrystalline material to their grain sizes [3].

$$\sigma_y = \sigma_o + K_y d^{-\frac{1}{2}} \qquad 2.1$$

where σ_y is the yield strength, σ_o is the friction stress, K_y is a constant of yielding which represents the strength of the grain boundaries, and it depends on the missorientation angle, and (d) is the average grain size. From equation 2.1, the strength increases with the reduction of the mean grain size of the material. Therefore, the formation of ultrafine grains (UFG) in metals and alloys underlies a very significant enhancement in their

mechanical and functional properties. Hence, developing new techniques to fabricate ultrafine- grained materials with the grain sizes of the submicron and nanometer reneges becomes a major interest of the engineers.

Severe Plastic Deformation (SPD) techniques are considered as the preferred techniques in refining the grain size of the material for many reasons. First, they impose extremely high amounts of strain on a bulk of solid material with coarse grains in order to refine the grain size at relatively low temperature. Imposing exceptionally high strain on a solid material will introduce high density of dislocations and for these dislocations to subsequently re-arrange to form an array of grain boundaries for smaller grains. Second, the cross-sectional dimensions of the bulk material do not change, and this is considered as the most important characteristic which distinguish the SPD over the conventional metal working operations.

The SPD technique known as Equal Angular Channel Extrusion/Pressing (ECAE/ECAP) technique was first developed in 1972 by Segal; a scholar of former Soviet Russia. Its goal was to develop a metal forming process where high strains may be introduced into metal billets by simple shear. Further reports between 1970s-1990s began to appear documenting the potential of the ECAE to produce UFG structures and sub-micrometer metals by introducing intense plastic strain into materials without changing the cross section area of billets. Due to that, repetitive extrusions are possible in this case to attain exceptionally high strains, so that it makes it possible to control the evolution of the resulting billet microstructure [12].

ECAE is considered as an attractive process to produce UFG materials among the SPD techniques for many reasons. First, this processing technique allows the creation of ultra-fine or nano-scale structures within a material by imposing a nearly uniform simple shear load in large billets. Second, it is a simple process that can be applied to various types of metals and alloys with different crystal structures. Third, it can be applied to fairly large billets so they can be used later in structural applications. Finally, high amounts of strain can be applied to produce UFG material with grain size in the range of (100nm-1μm) with a homogenous microstructure, equiaxed grains, and high angle grain boundaries (HAGB), see Fig. 2.1.

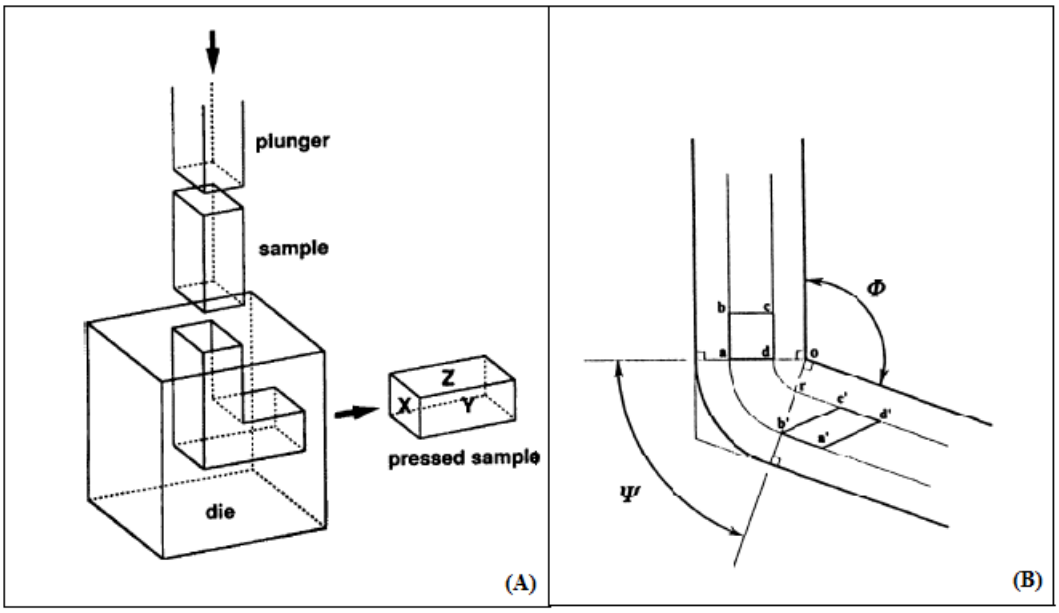

Fig. 2.1 (A) A schematic illustration of a typical ECAP facility: the X, Y, Z planes denote the transverse plane, the flow plane and the longitudinal plane respectively [13]. (B) A schematic illustration of the channel angle Φ and the curvature angle Ψ [14].

Several studies have documented significant differences in the mechanical and physical properties of the samples which had ultrafine grain sizes produced by ECAE, as

compared to the same materials in the un-pressed conditions. It is now apparent that any significant utilization of the ECAE pressing method will require a detailed understanding of the experimental parameters which determine the development of the UFG structures. The needed experimental parameters associated with the ECAE pressing fall into two distinct categories. On one hand, it has been shown that the nature of the microstructural development depends on some experimental variables based on the precise testing procedure, such as the total strain imposed on the sample during pressing [14,15], the processing route (A, B, C, Bc) which can be described as the nature of the shearing imposed in each passage through the die, which is a consequence of any rotation of the sample between consecutive pressing, and what slip systems being activated [5, 16-19], And the nature of the material including the crystal structure. On the other hand, there are also important experimental factors associated with the nature of the ECAE pressing facility including for example, the channel angle Φ and the curvature angle Ψ, Fig. 2.1 [14,15,20,21], the speed in which the pressing is conducted (pressing speed/extrusion rate)[13], and the pressing temperature [22,23].

2.2.1 Imposed Strain, Channel Angles, and The Number of Passes

In the ECAE processes the internal channel is bent into an abrupt angle Φ, and the outside curvature angle is Ψ which is called the curvature angle, Fig. 2.1. An abrupt strain is imposed on the sample in form of simple shear in every passage the sample pressed into the ECAE die. The strain is estimated by assuming a fully-lubricated specimen was pressed using the ECAE die in order to neglect any frictional effects. The

magnitude of the strain (shear strain **γ**) was estimated as in equation 2 using an analytical approach based on the die configuration [14,15].

$$\gamma = 2\cot(\frac{\Phi}{2} + \frac{\Psi}{2}) + \Psi\, cosec\,(\frac{\Phi}{2} + \frac{\Psi}{2}) \qquad 2.2$$

Equation 2.2 shows that the strain imposed on a sample during a single pass in ECAP depends primarily upon the angle between the two parts of the channel Φ, but also to a minor extent upon the angle representing the outer arc of curvature Ψ where the two parts of the channel intersect Also, the channel angle Φ has a direct influence on the nature of the pressed microstructure as we will discuss later. Equation 2.2 will be reduced to equ 2.3 if the curvature angle Ψ equals to zero.

$$\gamma = 2\cot(\frac{\Phi}{2}) \qquad 2.3$$

Finally, the equivalent strain $\boldsymbol{\varepsilon_N}$ after N number of passes maybe expressed in general form by the equation 2.4 [14].

$$\varepsilon N = \frac{N}{\sqrt{3}}\,[2\cot\left(\frac{\Phi}{2} + \frac{\Psi}{2}\right) + \Psi cosec\,(\frac{\Phi}{2} + \frac{\Psi}{2})] \qquad 2.4$$

It is obvious from equation 4 that the equivalent strain strongly depends on the angle channel Φ, and the number of passes the sample goes through during the ECAE process N, and minor dependence on the curvature angle Ψ .Some experimental evidences were supporting the result in equation 4. In those experiments the effect of the channel angle and the curvature angles were studied on the equivalent strain for different materials like colored plasticine [20], and pure aluminum [21], the results from those experiments were

matching with equation 4. Graphical representation of equation 4 is prepared [15] to give a visual understanding of the significant of the die angles Φ and Ψ on the equivalent strain.

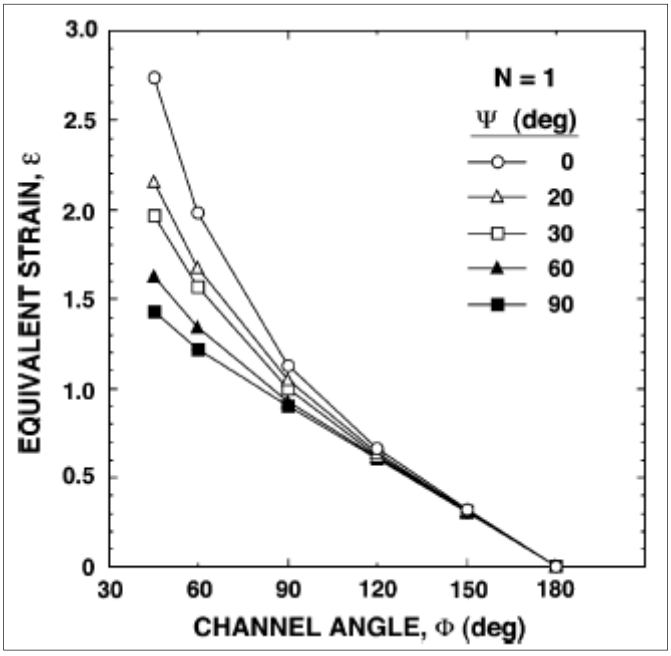

Fig. 2.2 Variation of the equivalent strain with the channel angle over an angular range of the channel angle from 45^o to 180^o for values of the angle of the arc of curvature from 0^o to 90^o: the strains are shown for a single pass where N=1 [15].

Based on Fig. 2.2 some interesting conclusions can be reached. First, the curvature angle Ψ has a relatively minor effect on the equivalent strain except for the channel angle less than 90^o. Second, High strain values can be achieved in only one pass by using a die that had very low values for both Φ and Ψ. However, despite the efficiency of the ECAE dies with channels angle less than or equal 90^o, it is easier to press billets when using dies with angles that are larger or equal 90^o. Third, for the conventional dies where the channel angle equals to 90^o, the equivalent strain around 1 and this value is independent of the curvature angle Ψ.

Moreover, some experiments were conducted using four separate dies having different channel angles (90^o, 112.5^o, 135^o, 157.5^o). The experiments were done on pure aluminum at room temperature using route Bc [24]. It was found that an array of ultrafine equiaxed grains with high angle of misorientation is achieved most easily when the sample is subjected to a very intense plastic strain using a die with a channel angle of 90^o Fig. 2.3.Further studies were done on aluminum alloys [15] showed the same results. So it is reasonable to conclude that a channel angle of 90^o represents the optimum configuration for an ECAE die, and that is why it is used in this study.

On the other hand, equ 4 shows that the equivalent strain strongly depends on the total number of passes N that the material goes through during the ECAE process. A pass is every time the material pressed through the ECAE die. Several experiments have been done to study the effect of the number of passes on the microstructure and the mechanical properties of the material [12,25-28]. The influence of the number of passes on the microstructure of the material is obvious in Fig. 2.4.

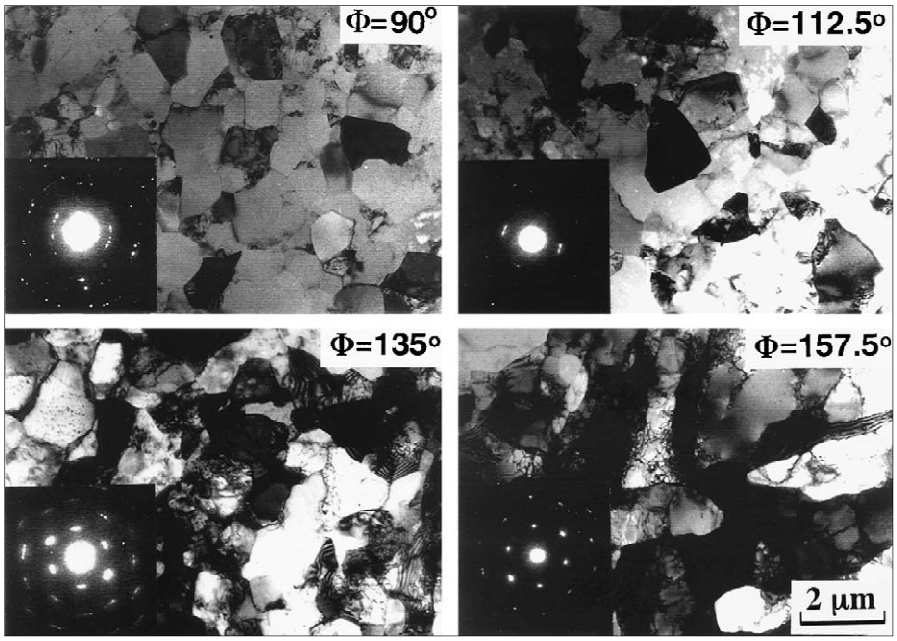

Fig. 2.3 Microstructures and SAED patterns obtained using the dies with the angles(90^o, 112.5^o, 135^o, 157.5^o) as a channel angle, and the angles (20^o, 30^o , 13^o, 10^o) as the curvature angles respectively when each sample is pressed to an imposed strain ~ 4 [24].

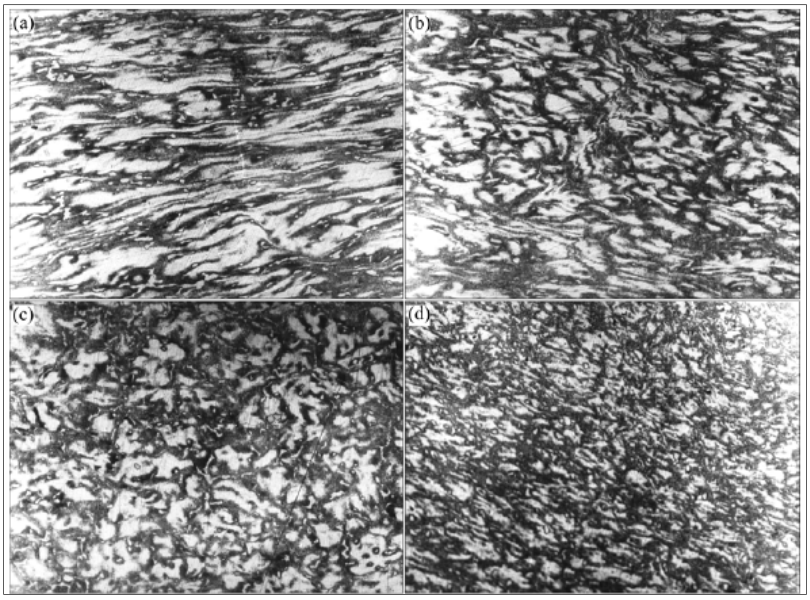

Fig. 2.4 Microstructures of AZ91D extruded for different extrusion passes by extrusion route Bc, (a) 1 Pass, (b) 2 Passes, (c) 3 Passes, (d) 4 Passes[12].

Fig. 2.4 shows the microstructures of AZ91D extruded with different number of extrusion passes using extrusion route BC. It can be seen that the crystal grains become finer and more homogeneous with the increment of extrusion passes. First, after the first pass the grains are elongated. Then they start to brake in order to form smaller grains. It is obvious from (c) and (d) that smaller grain size can be achieved with more extrusion of the material. So it can be concluded base on these images and on the results from other studies [12,25-28], that increasing the number of the extrusion passes will lead to structure has a homogenous and finer grains with a high density of high angle grain boundaries HAGB.

The reason behind the grain size refinement in the ECAE process is the imposed strain. When extremely high strains are imposed to the material it will lead to huge amounts of deformations which will introduce a high density of dislocations. The dislocations will start to rearrange in order to reach to the minimum energy configuration to be in a stable condition , and this can be achieved by forming new grain boundaries but this time they are smaller grains. This process will happen again if the material is extruded into a new pass which lead to more refinement of the grain size Fig. 2.5.

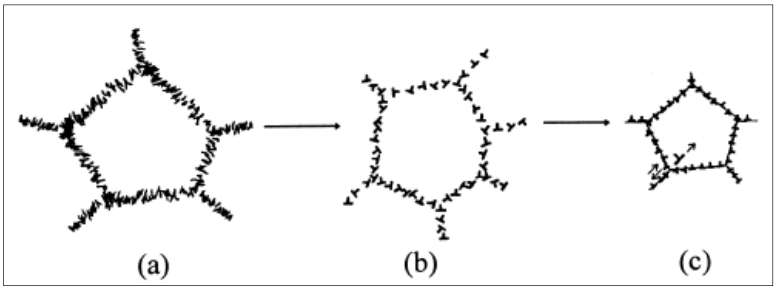

Fig. 2.5 Schematic model for the dislocation structure evolution at different stages during severe plastic deformation [28].

Grain refinement has a significant influence on the mechanical behavior of the material. For example, smaller grain size will lead to a very high hardness in various metals as well as strengthening the material, so that the ultimate tensile strength as well as the yield strength will increase. This can be interpreting as we discussed earlier by the Hall-Petch equation (1). However, strong materials usually show less ductility, because strength and ductility typically have opposing characteristics. The reason for this that the plastic deformation mechanisms associated with the generation and movement of dislocations like Frank-Read sources may not be effective in UFG materials. So that most of these materials have a relatively low ductility but they usually show higher strength than their coarse- grained counterparts.

Fig. 2.6 shows results from experiments done on Al-3004 alloy that has been processed using both ECAE and cold-rolling. Dog-bone shape flat tensile test samples were used to perform the tensile test. The ductility was measured using the percentage elongation to failure of each tensile tested sample. Based on these results it is obvious that increasing the equivalent strain by increasing the number of passes (equation 4) will lead to increase the ultimate tensile strength as well as the yield strength. On the other hand this will lead to reduction in the ductility But the overall ductility exhibit a different trend in both of the processes, when the ductility shows more reduction in the cold rolling with increasing the equivalent strain, there is no additional reduction in the ductility with additional ECAE passes after certain limit of the equivalent strain [29, 5].

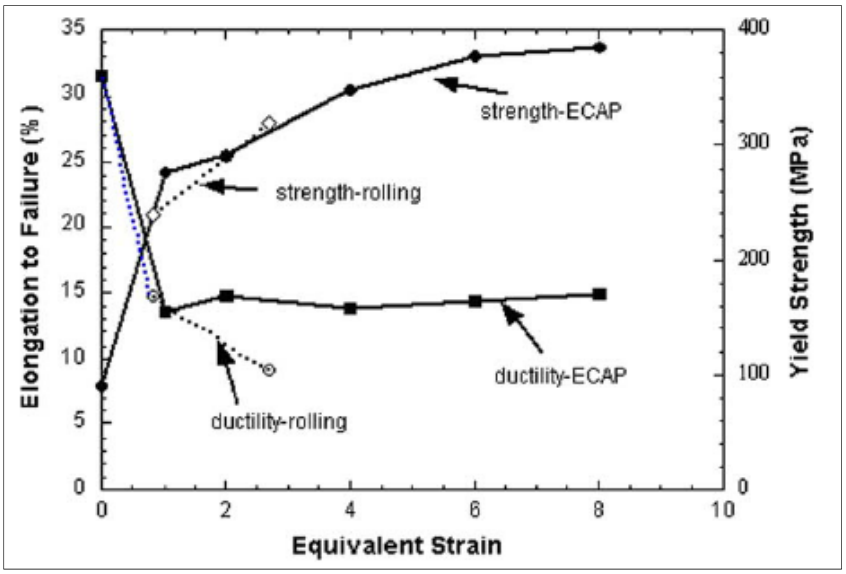

Fig. 2.6 A comparison of yield strength and ductility for an Al-3004 alloy processed by cold-rolling or ECAP [29].

2.2.2. Extrusion/Processing Routes

There are four basic processing routes in ECAE process (A, B or B_A, C, Bc or C'). These routes introduce different slip systems during the extrusion operation so that they lead to significant difference in the resulting microstructures produced by ECAE. The four different routes are shown in Fig. 2.7. In route A, the sample is pressed without rotation, in route B ($B_{A),}$ the sample is rotated by 90^o in alternate directions between consecutive passes. In route Bc (C') the sample is rotated by 90^o in the same sense (either clockwise or counter clockwise) between each pass. And in route C the sample is rotated 180^o between passes.

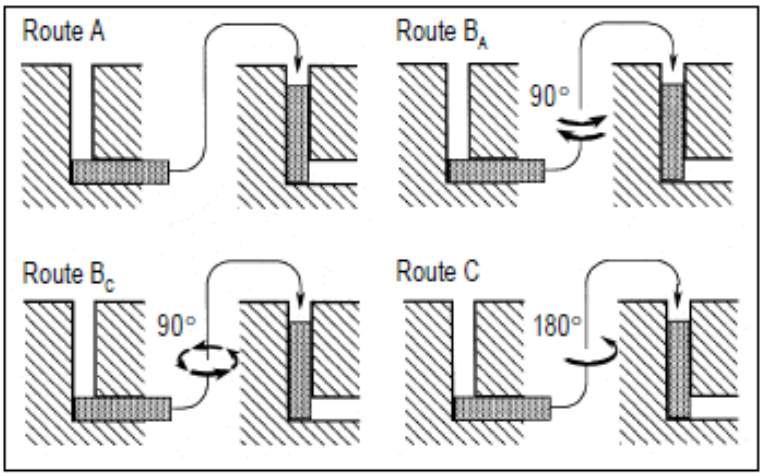

Fig. 2.7 The four fundamental processing routes in ECAE [16].

The rotation of the billet in each processing route leads to activation of different slip systems with each rotation. Some of these routes can be considered redundant since the slip in one pass will be canceled from slip in another pass such as in the case of route Bc.

Several studies have been accomplished to investigate the effect of the processing route on the resulting microstructure. One of these studies focused on polycrystalline aluminum. Polycrystalline Al was processed in ECAE using four different routes, A, B, B_A, Bc through four passes [16].It is apparent from the micrographs in Fig. 2.8 that route Bc leads to an array of reasonably equiaxed ultrafine grains, while elongated grains are obvious in the images taken for route A, B_A , and slightly in C.

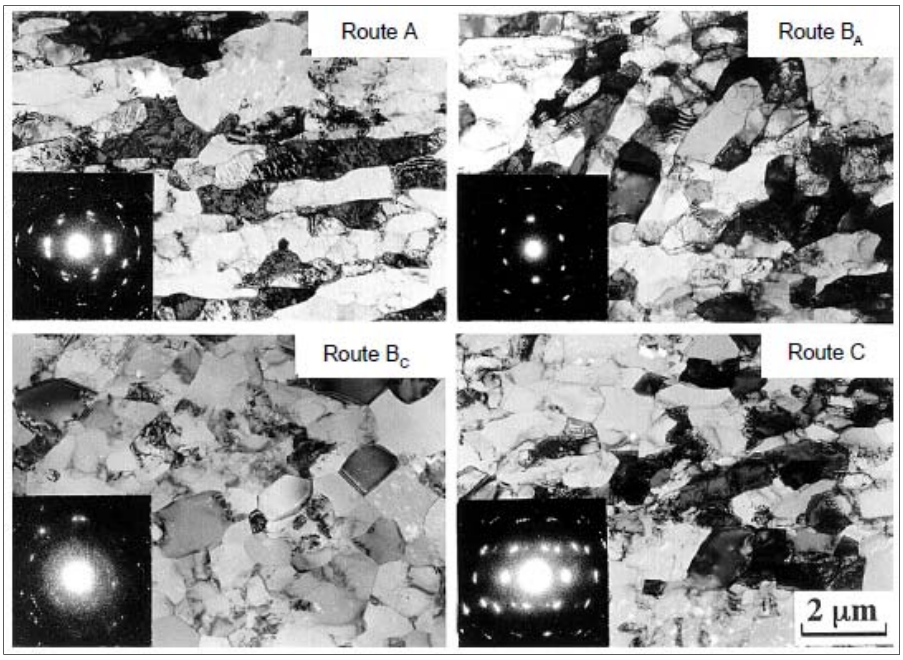

Fig. 2.8 Appearance of the microstructures on the X plane for the polycrystalline AL after ECAE through 4 passes using routes A, B, Bc, and C together with the associated SAED patterns [16].

In addition, other studies shows that when processing pure aluminum using route Bc identical equiaxed arrays of ultrafine grains were visible on each of the three orthogonal planes of sectioning [17]. Moreover, other examinations show that route Bc leads to the most rapid formation of high angle grain boundaries HAGB. Grain boundaries are considered to be high angle if they have a missorientation angle more than 15^o. Route Bc give high density of HAGB because we have 90 degree rotation so we are activating different slip systems in 2 different perpendicular systems. Using the 90 degree rotation we impose (activate different slip systems) and this will allow us to have a better chance to break the grains [18,19,25]. Route Bc will give equiaxed grain microstructure; equiaxed structure means that the grain size is the same regardless the diagonal we use. Thus it can be concluded from these studies that route Bc is considered as the optimum

ECAE processing routes to produce equiaxed grains with HAGB at least for pure aluminum.

On the other hand, other experiments have been done on IF steel using different routes and they reach to the same conclusion about route Bc with some extra valuable information [5]. In this study IF steel has been processed through ECAE process utilizing different routes (A, B, C, C', and E) and number of passes (1 to 16 passes). All the billets were extruded at room temperature at extrusion rate 0.1in/sec. Related to the microstructure analysis, it has been found that using route 8Bc to extrude IF steel will give homogenous and equiaxed structure with HAGB with grain size of 500nm. The same grain size was achieved using 4 passes, which means that the grain size does not change much between route 4Bc and 8Bc except the small amount of recovery, which is evident from the decrease in the dislocation density of grain interior when using 8 passes.

Fig. 2.9 shows the tensile deformation response (mechanical behavior) of the as-received IF steel and the ECAE processed ones in the same study [5].It worth noticing that the as-received IF steel shows lower value of the yield strength as well as the ultimate tensile strength UTS compared to the processed ones, but on the other hand it shows higher value of the ductility. By comparing the response of the fabricated billets, it can be seen that the route 8C' (8Bc) and 16E shows slightly similar response any they give very high value of the UTS and the ductility together.

This study showed that the optimum combination of high strength and ductility is exhibited by route 8Bc (8C'), and related to the microstructure analysis it has been

shows that the optimum microstructure of equiaxed structure with HAGB can be found by the same route [5].The same result has been reached using other studies like the one done by R.Z Valiev *et al.* [30] where they showed that for copper processed by ECAP using route Bc will show an enhancement of strength as well as ductility due to an increase of the number of the passes from 1 to 16, and this study was called "paradox of strength and ductility in SPD-processed metals".

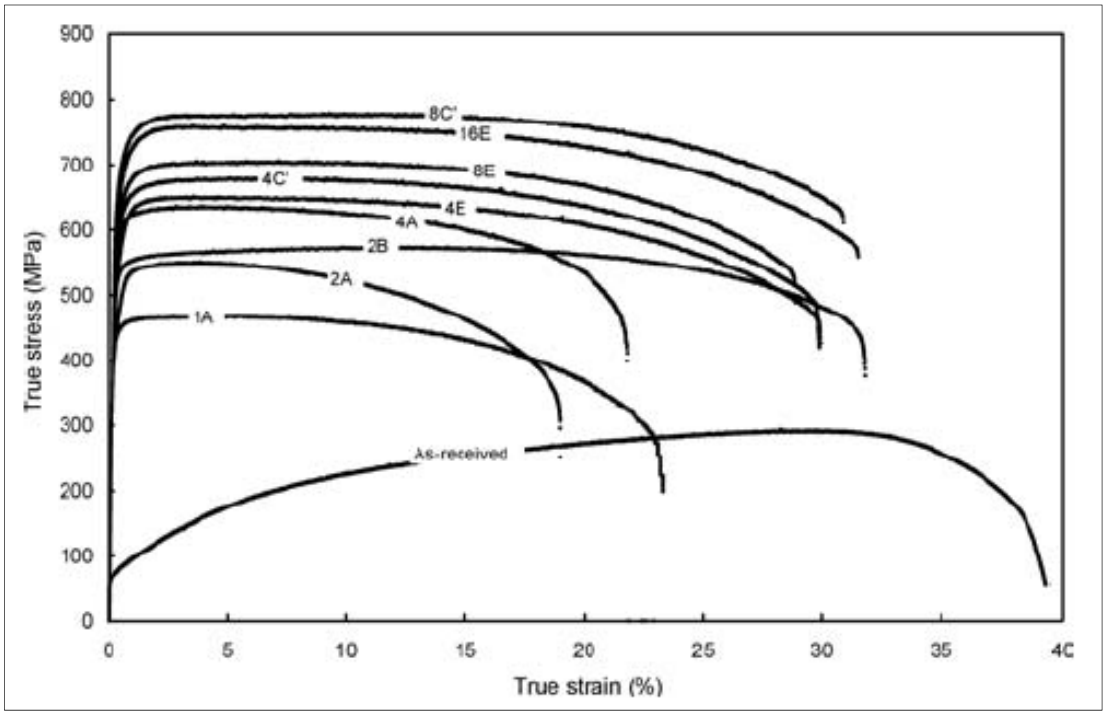

Fig. 2.9 Monotonic true stress-true strain response of different IF steel conditions, tested at room temperature with a strain rate of $5X10^{-4}S^{-1}$ [5].

Based on the results from all of these studies route 8Bc has been used in our study since it represents the optimum route for both microstructural analysis as well as the mechanical behavior of the material. In addition, one of the processing conditions in our

study was the same as the one done by Karaman *et al.* [5] when they use route 8Bc for IF steel at room temperature and strain rate of 0.1in/sec.

2.2.3 Extrusion Temperature

The pressing temperature is considered as a key factor in the ECAE processes because it can be easily controlled. Elevated temperatures were used usually in ECAE process when fabricating hard materials where the pressing load at the room temperature may exceed the capacity of the pressing machine. Then it was found that there is a significant influence of the pressing temperature on the material's microstructure and its mechanical behavior. So that the influence of the pressing temperature on the microstructural development in the ECAE pressed material started to be studied first on samples made of pure Al, Al- 3%Mg alloy, and an Al-3%Mg-0.2%Sc alloy with the pressing conducted starting from room temperature to 537K [22].The tests were performed using a solid die fabricated from tool steel, having a channel angle of 90^{o}, and a curvature angle of 45^{o}.In order to have a precise controlled on the temperature inside the die, a small hole was drilled horizontally on the die in order to insert a thermocouple in it. Some important results were concluded from these experiments. First, there was an increase in the grain size with increasing the temperature as shown in Figs. 2.10 and 2.11.

Second, it was concluded from some micrographs as well as examinations of the SAED patterns that the fraction of the low angle grain boundaries (LAGB) increased with increasing the temperature, Fig. 2.11. Therefore, the tensile strength of the material will decrease and the ductility will increase with increasing the ECAE pressing

temperature. Other experiments on other types of Al alloys supported these conclusions [23].

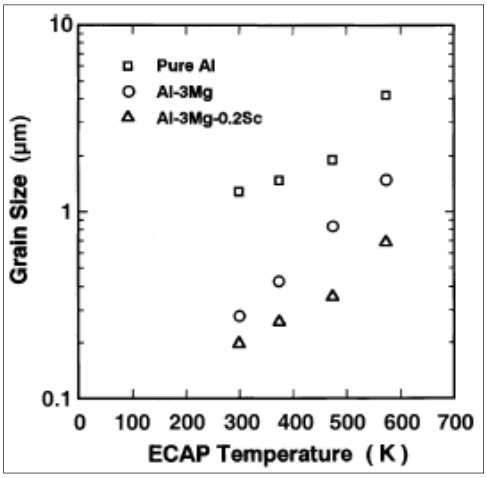

Fig. 2.10 Grain size after ECAE versus the pressing temperature for pure Al and Al-3% Mg and Al-3%Mg-0.2%Sc alloys[22].

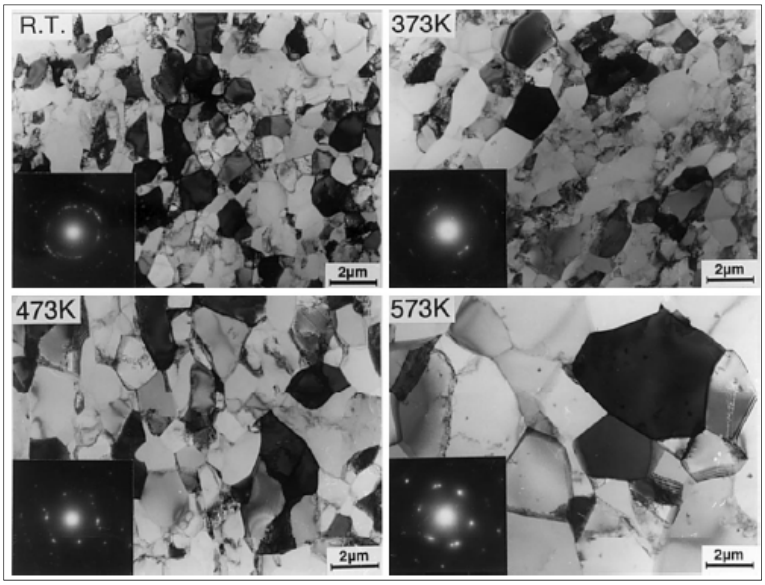

Fig.2.11 Microstructures and associated SAED patterns for pure Al after ECAE pressing at room temperature, 373K, 437K, 573K[23].

In our study we use one of our processing conditions to be at elevated temperature of 473K in order to have larger grain size compared to what we will fabricate at room temperature.

2.2.4 Extrusion/Pressing Speed (Rate)

As been discussed earlier in this chapter ECAE process is based on imposing high strains in form of simple shear on the material in order to deform it and to refine its grain size. Based on what we have seen so far the resulting microstructures and the mechanical properties strongly depend on many factors including the amount of the imposed strain. Moreover, since we know that in general the deformation of the material increase with increasing the strain rate, the same situation is expected with the ECAE process. By increasing the pressing speed/extrusion rate, the imposed strain it is expected to increase, so that the material will be subjected to more deformation, which means more activation for dislocation sources. On the other hand, these dislocations will begin to rearrange in order to form new grain boundaries, and therefore more refinements of the resulting grain size.

The first detailed examination of the influence of the pressing speed was done on pure Al and Al-1%Mg alloy at extrusion rates from 10^{-2} to 10 mm/sec, with number of passes from 1 to 4 [13]. Based on Fig. 2.12 which summarizes the results from these experiments, it can be concluded that the effect of the pressing speed on the yield strength of the material is negligible at least over the limited range of 10^{-2} to 10 mm/sec.

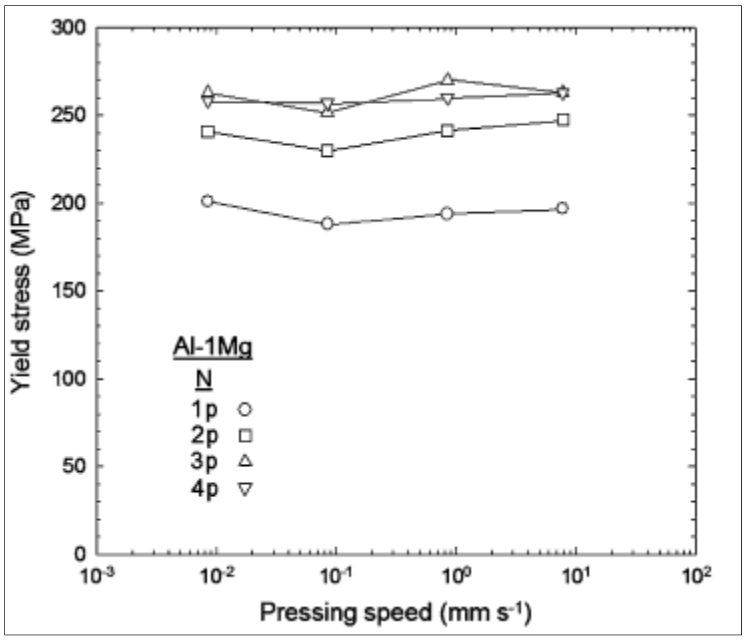

Fig. 2.12 Variation of the yield stress with the pressing speed for an Al-1%Mg alloy after ECAE through 1, 2, 3, and 4 passes. Data recorded at room temperature using a strain rate of 1.0X $10^{-1}s^{-1}$ [13].

Also, from microstructural point of view, Berborn *et al.* found that there is no effect of the pressing speed on the equilibrium grain size attained in the ECAE pressing at least for the previous range of speed. Moreover, Using slower pressing seed provides a longer time for recovery, so that a higher proportion of the extrinsic dislocations become absorbed in the grain boundaries, and this will lead to more equilibrated structure, So that at least the incidence of extrinsic dislocations is partially dependent on the pressing speed.Similar conclusions were reached also in tests done on pure Al and three Al-based alloys using pressing speeds of 18 and 0.18 mm/sec [31].

On the other hand, a study about the effect of the pressing speed on the deformation mode of Ti was conducted. This study was done on Ti which has hexagonal close-packed (hcp) structure since it is noticeable that large plastic strain can be accumulated

by using ECAP in this kind of materials in spite of their lack of plastic deformability due to their insufficient slip systems [32]. Usually a material that has a hcp crystal structure has less slip system and therefore lower ductility and deformability compared to the BCC and FCC materials. Two pressing speeds were used, 0.2mm/sec and 2.8mm/sec, and the results showed that only minor microstructural differences in these specimens after pressing through only one pass.

It is worth noticing that the previous study was done on FCC materials such as Al and its alloys [13]. However, it did not cover any BCC material like IF steel. Also, the study was done only up to 4 passes but not more than that. So we found that it worth to study the effect of the pressing speed (1 in/sec) on the development of the microstructure and the mechanical behavior of the IF steel which represent a BCC material model up to 8 passes, because as we have seen there was a minor microstructural difference in specimens made form Ti with different pressing speeds. Pressing IF steel with pressing speed higher than 0.1in/sec is considered as the third processing condition we use in our study.

2.3 Ductile Fracture Mechanisms

One of the most important and key concepts in the entire field of Materials Science and Engineering is fracture. For engineering materials there are roughly two possible modes of fracture, ductile and brittle. In general, the main difference between brittle and ductile fracture can be attributed to the amount of plastic deformation that the material undergoes before fracture occurs. Ductile fracture or what is sometimes called ductile damage or dimpled rupture can be described as the failure mechanism in most metals and their alloys at room temperatures preceded by substantial plastic deformation. In ductile fracture, extensive plastic deformation takes place before fracture, and the strain at which the fracture happens (fracture strain) is controlled by the purity of the materials.

In a uniaxial tensile bar, ductile fracture occurs in stages that initiate after necking begins. First, small microvoids start to form in the interior of the material. Next, increasing the load with the time the deformation continues and the microvoids grow, then they coalesce to form a micro-crack which will propagate through the material. The crack continues to grow and it spreads laterally towards the edges of the specimen. For purpose of discussion we will refer to these three stages as; void nucleation, void growth, and void coalescence (crack initiation and propagation) where they are considered as a sequence of overlapping processes since it is difficult to define where one stage ends and the next begins during fracture of material.

2.3.1 Void Nucleation

Void nucleation cannot be detected from the overall mechanical response of the material since it is a micro-scale phenomenon. Several studies showed that the sources of the void nucleation vary from one material to another based on the material's microstructure and its chemical composition. So that the major sources of the void nucleation can be divided into two types. The first type if the material consists of a matrix and second phase particles such as alloys and most metals, in this case the void nucleation will be associated to the presence of a second-phase particles or inclusions whether inside the grains or on the grain boundaries. Therefore, the void nucleation can be resulted from either the second-phase particle fracture, or decohesion between the matrix and the particle [33-36].

However, while the second-phase particles act as void nuclei in many systems, there are systems where voids can be nucleated by other mechanisms like in the pure metals when there is no existence of the 2^{nd} phase particles. In this case the voids can nucleate as by other mechanisms like, triple junction between the grains, initial porosity or vacancy clustering inside the material, shear band intersections, twin boundaries intersections, micro-cracks, dislocation overlap or annihilation, or any other type of defects inside the material that may cause the material to fail under the effect of the load. Sometimes both of types can be found as sources of void nucleation in one type of material based on its microstructure [37-47].

The existence of the second phase particle in the material matrix, or for example, triple junction, slip band intersections, etc will cause high stress concentrations. This

high stress concentration will lead to decohesion in the material matrix and voids will begin to nucleate.

In the case of the 2nd phase particle void nucleation is associated usually with the presence of second-phase particles or inclusions whether inside the grains or along the grain boundaries. Void nucleation can be resulted from either the second-phase particle fracture, or decohesion between the matrix and the particle [35, 48, 49]. Fig. 2.13 shows an SEM image for a second phase particle inside a 6060Al alloy. (a) Shows how the second phase particle dissociates from the matrix as a result of the applied stress in a uniaxial testing. And (b) shows how the particle breaks into pieces under the same conditions. Both mechanisms lead to creation of a void which grows driven by plastic deformation and stress [48].

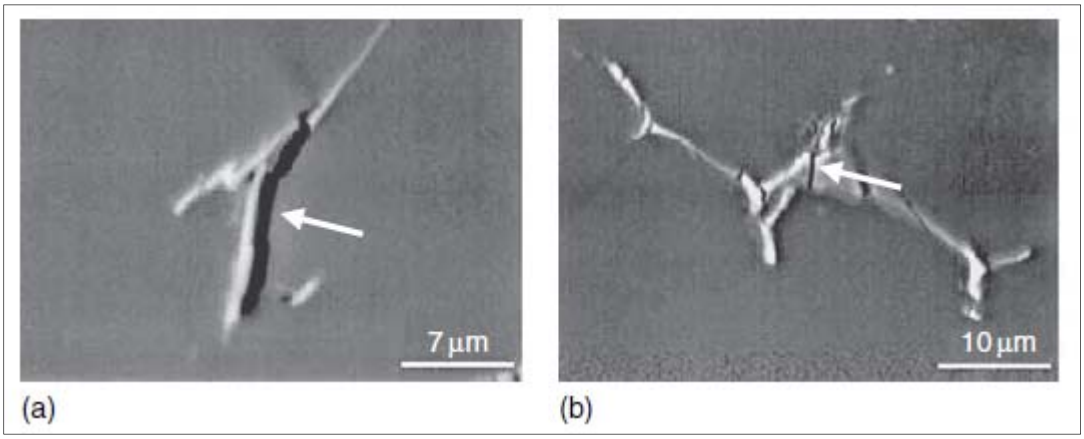

Fig. 2.13 SEM micrographs of damage nucleation in a 6060Al alloys during in situ uniaxial testing: (a) particle/matrix decohesion and (b) particle fracture, as indicated by an arrow [48].

Usually there are number of factors influencing the conditions required for the nucleation to occur such as: the particle size, the stress state (stress triaxiality), strength

of the material's matrix, interfacial cohesion (how strong is the cohesion between the matrix and the particle), and the particle volume fraction compared to the volume of the material.

Usually in the case of 2nd phase particles, the voids nucleate at the larger particles first regardless what is the mechanism, either it is particle/matrix decohesion or the particle fracture. However, usually particle fracture is favored as the particle size increases in spite of the other influencing factors such as the shape of the particle, its orientation if it is not equiaxed, and the strength of the particle-matrix bond. This result has been observed through several studies like in copper alloys contacting SiO2 [47], in aluminum alloys [48],for various types of inclusions and second phase particles in steel [50,51], thus for a given test conditions the larger particles in a given distribution inside the material matrix are expected to nucleate voids at lower strains.

On the other hand, decohesion between the particle and the matrix is favored when the weak bonds exist between the matrix and the particle, especially when the applied tensile strength exceeds the bond strength between the matrix and the particle. In addition, the decohesion does not happen simultaneously at all points along the particle/ matrix interface since there are other factors influencing it like; the shape of the particle especially if it is not equiaxed, the orientation of the particle, and the direction of the applied stress with respect to the direction of the particle. For example, in the case of the tensile stress, the voids initiate at the particle- matrix interface along the axis of the applied stress at the position of maximum tensile stress, and then they elongate/ enlarge in the same direction.

The strain at which the void nucleation occurs either by particle fracture or by particle/matrix decohesion is very dependent on the stress state. Fig. 2.14 shows the results from the study done by Cox and Low [50] where they investigate the influence of the stress state or what is sometimes called the stress triaxiality on the void nucleation of MnS particles in 4340 steel using both smooth bars and notched bars tensile samples. The stress triaxiality is defined as the hydrostatic stress (hydrostatic pressure) divided by the Misses/equivalent stress. The figure shows that when using notched bar samples where the triaxial stress is higher, the voids will nucleate at lower strain values compared to the one needed for smooth bars. Therefore, the void nucleation is dependent on the stress state and the strain at which the void nucleate. In addition, the void nucleate at lower strain values in higher strength materials [38, 39,45, 46, 51].The stress triaxiality effect on the void nucleation and fracture of the material will be discussed later in details in the void growth section.

Moreover, studies showed that the nucleation strain can be influenced by the strength of the cohesive bond between the particle and the matrix. For example, adding some alloying elements like Mo or Cr to the iron matrix improve the ductility of the material. The study done by Cane *et al.* showed that Cr increases significantly the cohesion between ferrite and MnS particles, so that more strain is needed to separate the particles from the matrix [52]. On the other hand, other types of alloying elements will play a significant role in segregation of the particles-matrix interface such as a trace of phosphorous responsible of the segregation between the ferrite-carbide interface during temper embrittlement of steels [53].

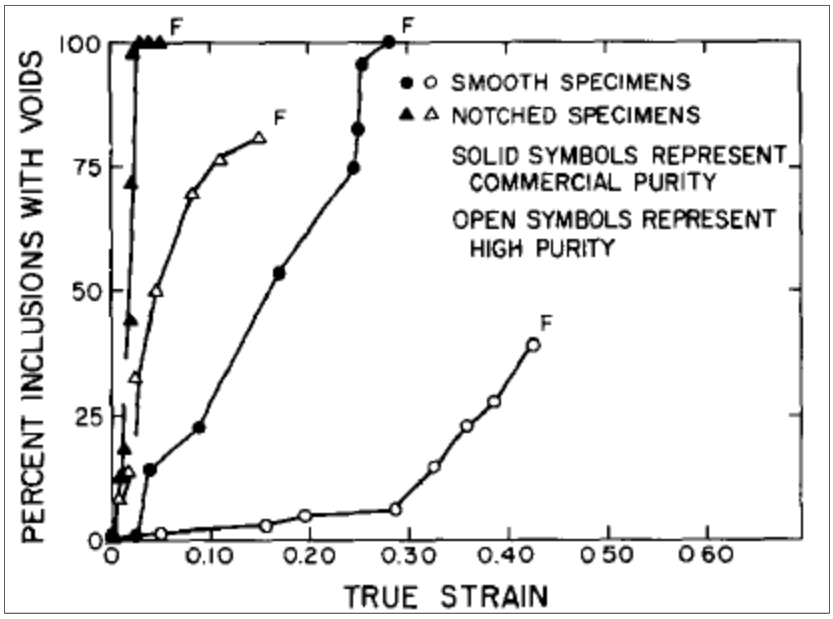

Fig. 2.14 A plot of percent inclusions with voids as a function of the true strain for commercial and high purity heats of 4340 steel. The sulfur levels and inclusion volume fractions associated with the commercial and high purity heats were 0.013wt% and 0.0014% and 0.0006 [50].

Moreover, the void nucleation depends on the orientation of the 2nd-phase particle. For example, the AlFeSi particles which are located along the grain boundaries in a platelet shape break into several fragments when aligned with respect to the main loading axis. However, decohesion between the matrix and the particles happened when they were aligned perpendicular to the loading axis [48 54]. This happens as a result of the accumulation of the plastic strain as a result of the applied stress on the interface between the particle and the matrix so that it allows the progressive opening of the submicron interface defects.

In other cases, void nucleation is observed in systems where voids nucleate from sources other than second phase particles, such as in some titanium alloys and pure

metals. For example Thompson and Williams observed some dimples formed in single-phase α Ti-Al alloys [37]. There were no void nucleating particles evident which lead the suggestion of other sources such as vacancy clustering, or slip band intersections represent the void nucleation sites. Van Stone *et al.* showed that void nucleation can occur in Ti-5Al-2.5Sn alloy tested at room temperature as a result of twin boundaries, but when tested at cryogenic temperature, the intense slip band intersection will cause the void to nucleate. Therefore he concluded that the void nucleation could be as a result of twin boundaries intersections or twin boundaries intersection with grain boundary [38]. Other studies like the done by Wu *et al*. showed that the shear bands and the step-like shear bands could cause the deformation to take place easily along the shear plane [44]. Other studies showed that triple junction between the grains, grain boundaries, dislocation overlap or annihilation, intersection between the slip band and the grain boundaries, or any other types of defects in the material are the reasons behind nucleating these voids [40-43].

In conclusion, in the case of void nucleation as a result of the 2^{nd} phase particle, voids nucleate at lower strains will be favored by large particle size, high interfacial stresses (higher stress state- triaxiality), high matrix strength, weak bonds between the matrix and the particles, and for high particle volume fraction. However, the non-particle related void nucleation is not common and important as particle related void nucleation except of titanium alloys, so that the ductile fracture could be considered mainly as a result of the initiation of voids at second-phase particles.

2.3.2 Void Growth

In the microscopic point of view, increasing the plastic deformation (the load) on the material after the void nucleation will lead to growth for the voids so that the voids will expand to a volume and shape determined by the material properties and the testing conditions. For example, voids nucleated by the particle fracture will open and become more rounded with increasing the plastic deformation, see Fig. 2.15 (a) While voids nucleated by particle/matrix decohesion tend to elongate in the direction of the applied load, but their movements maybe prohibited by the particle itself, so in some cases they tend to rotate, see Fig. 2.15 (b). In addition, the voids nucleated at the larger inclusions tended to grow faster.

From macroscopic point of view, the main aspect of ductile fracture is that the fracture strain will decrease exponentially with increasing the triaxiality, and this effect is directly related to the significant increase in the void growth rate with increasing the stress triaxiality [55-58]. The fracture strain (ε_f) can be defined from the reduction of the cross-sectional area measured from the broken sample ($\varepsilon_f = 2\ln (A_o/A_f) = 2\ln (\Phi_o/\Phi_f)$ where A_o, is the initial cross sectional area, A_f is the final cross sectional area at the fracture, Φ_o is the initial diameter, Φ_f is the final diameter at the fracture . This result matches with what we have discussed earlier in the void nucleation, the higher the stress state (stress triaxiality) the lower the strain needed to nucleate and grow the voids, and thus the lower the fracture strain. Void growth which causes the total porosity of the material to increase will proportionally increase while increasing the triaxiality. In the case of notched bar samples, the sharper the notch the more the triaxiality (especially in

the center of the sample away from the notch), and this will lead to higher void growth in the center of the sample, which will lead to decrease in the fracture strain. Moreover, the rate of void growth observed in notched tensile specimens made of 250 grade steel were much larger than those observed in the axisymmetric tensile specimens in the study done by Cox and Low [50].

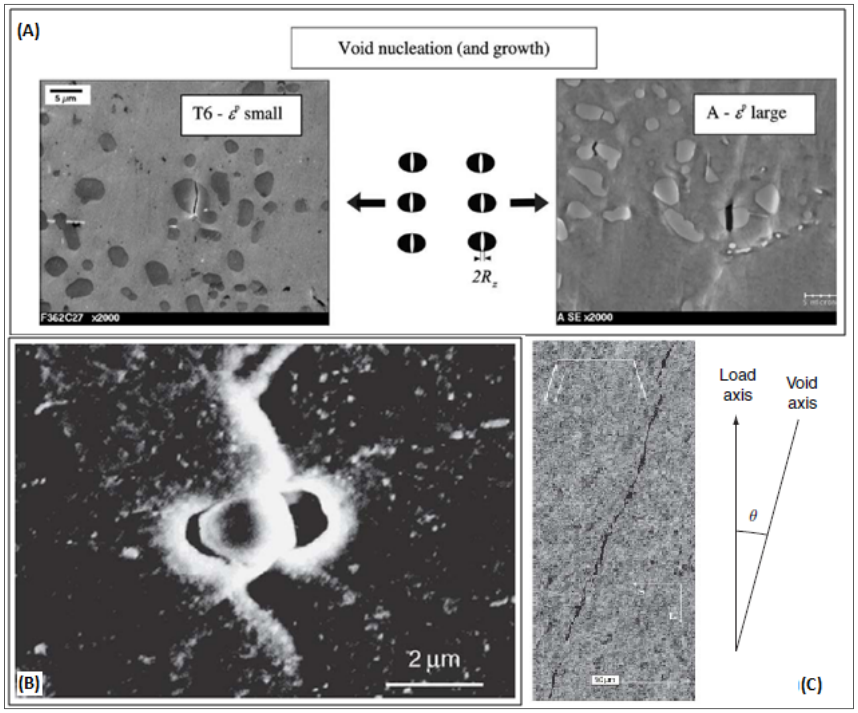

Fig. 2.15 Micrographs for voids growing by plastic yielding of the surrounding matrix (A) voids originating from particle fracture(void growth in cast Al alloys nucleated by the fracture of Fe-rich particles of Si particles)[55] (B) Voids originating from the decohesion of the particle interface (void growth around a copper oxide inclusion in copper[56] (C)3-D tomography reconstructed image where dark cavities can be seen around the large gray particles[57].

Fig. 2.16 shows the fracture strain relationship with the stress triaxiality, and it is obvious that the sharper the notch, the more the stress triaxiality and the less the fracture strain because of higher void nucleation and growth rate [34].

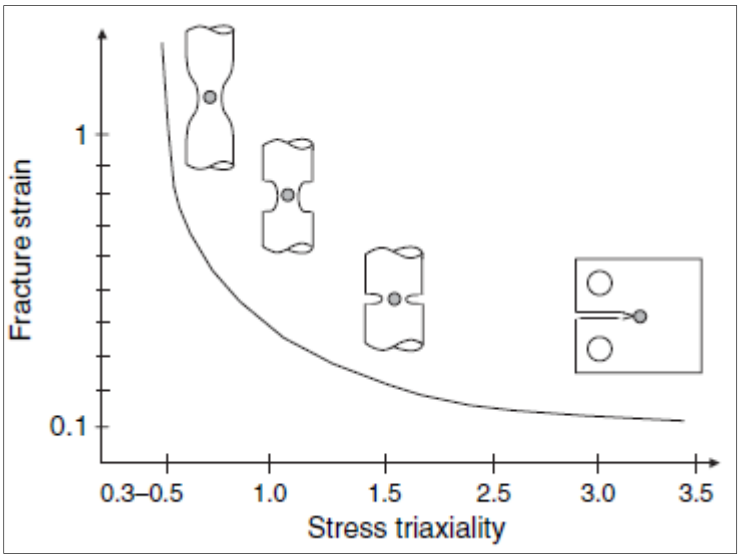

Fig. 2.16 Typical variation of the fracture strain as a function of the stress triaxiality in metallic materials [34].

The cylindrical notched round bar samples are probably considered as the best suited to study the ductile fracture of the materials for many reasons. First it allows probing a wide range of stress triaxiality by changing the radius of the of curvature of the notch, so that we can study the effect of the stress triaxiality on the void growth and fracture strain for different kinds of materials, and not to be limited on a certain range of stress triaxiality based on the axisymmetric round bars. Second, the stress triaxiality remains almost constant all over the deformation process in the center of the minimum cross section, so that when study the effect of the stress triaxiality on the void growth and fracture strain for a certain type of material the results will be precise based on an almost constant value for the stress triaxiality. However, the triaxiality in the smooth bars or what called the axisymmetric bars varies with the deformation process especially after the necking point. Third, notched samples are usually used to characterize the notch

toughness/ fracture toughness (ductility) of the material by measuring both the strain to failure and the initiation strain. And finally the notched bar samples are more sensitive to the void nucleation as a result of the associated high stress triaxiality, so that they considered as the best to be used to study the ductile fracture.

A standard procedure to test the notched bar samples and to interrupt the test has been developed by European Structural Integrity Society (ESIS P6-98, 1998) [34]. Some notched bar samples are tested up to fracture to find out the fracture strain for the material. The test of the other samples will be interrupted at different stages of the loading, and then a longitudinal median cut on the interrupted samples will be done in order to study the fracture mechanisms.

2.3.3 Void Coalescence

Void coalescence is the final stage in the failure of ductile materials. It forms in the localization of the plastic deformation in the intervoid ligament between neighboring voids. The coalescence of voids lead to a transition from a stable diffuse of plastic deformation to a localized mode of plastic deformation within the ligament between the voids located in the most critical region (like the regions that have the maximum value of stress triaxiality). In this stage the growing voids link together, and the actual fracture can proceed as seen in Fig. 2.17. Several experimental evidences obtained from fractographic analysis of broken samples or metallographic analysis of polished samples strained near fracture (interrupt the test before fracture) have investigated the phenomena of the void coalescence and study the factor influencing it.

Growing voids can coalesce by two processes, the first process would occur for materials containing only one population of void nucleating particles activated during the fracture process. In this process, there may be other type of particles in the material matrix but they have strong bonds with the material so they would not be able to nucleate voids.

In the second process, the voids nucleate first from one particle population which considered as the most distributed and the most weakly bound to the material matrix, and these voids will grow and coalesce as the plastic deformation increases. Then a second population of voids will nucleate from the second particle population, and these particles are usually much smaller than the first one, more bounded to the material matrix, and are less distributes in the material (has less volume fraction). So the coalescence will occur when the void nucleated from the first population grow until they coalesce. Then they coalesce with the second population of the growing voids, this phenomena is usually called the void sheet. Regardless the process for void coalescence void coalescence leads usually to the formation of a macroscopic crack that can then propagate through the material with small amount of additional external work; see Fig. 2.18(f) [51].

Fig. 2.18 shows a schematic representation of the void nucleation by the 2^{nd} phase particle fracture or decohesion with the matrix with the corresponding stress-strain diagram [34]. It is obvious that in the beginning when there is no force applied to the material, the second phase particles are well bounded with the material matrix, but with increasing the load the second phase particle either start to dissociate from the matrix (particle/matrix decohesion -on the left)or start to break into fragments (on the right) in

order to nucleate the voids. By increasing the load the decohesion between the particle will start to increase, and in the case of the fracture the fracture will expand until it separate the particle into two halves leading to void growth. A sharp slope change is obvious in the diagram, and it can be associated to the initiation of fracture which consists in the coalescence of two or few voids in the most damaged region of the material. Usually coalescence of void occurs after significant amount of void growth. At the end, this micro-crack will continue to propagate through the material with increasing the load.

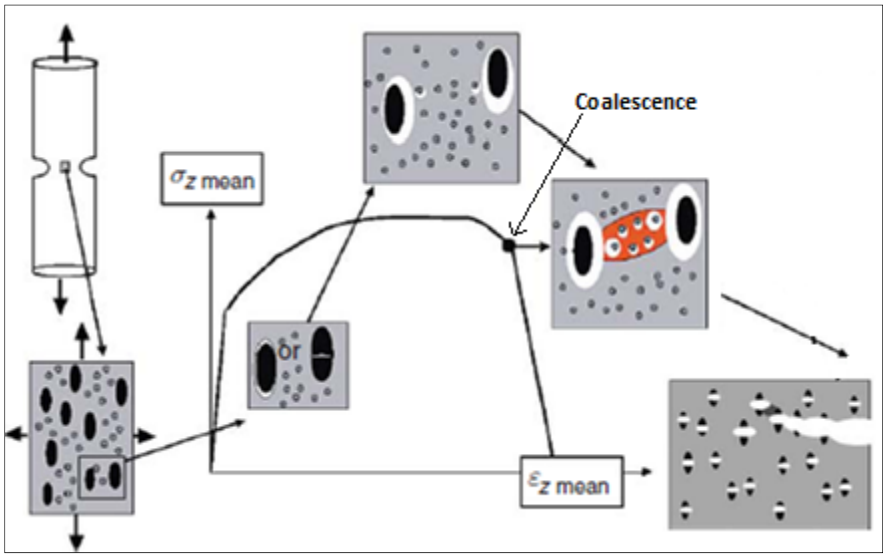

Fig. 2.17 Schematic representation of the process of nucleation, growth, and coalescence of voids nucleated on second-phase particles inside an idealized representative volume element of the microstructure, and the relationship with the macroscopic loading evolution [34].

The same procedure used in the void nucleation and growth of interrupting notched bar samples, cut them, and polish them to investigate the void nucleation and growth can be used here also to examine the void coalescence and crack initiation. But it should be

noticed that several polishing trials can be accomplished in order to reveal the region of the material involving the void coalescence and the crack initiation.

Two modes of void coalescence mechanisms have been studied, the first one is the internal necking mode, and the second is the shear localization. In the internal necking the ligament between the two voids shrinks until it reaches its minimum diameter to form a neck shape between the two voids so that the void will coalesce through this necking region, Fig. 2.18 (a, b, e).The shear localization mode which is usually observed in high strength materials with low strain-hardening capacity. In this mode, the voids will coalesce along the shear bands, Fig. 2.18(c, d). The transition between the shear localization and internal necking modes can be related to the transition between the slant fracture and the flat fracture mode, see Fig. 2.19.

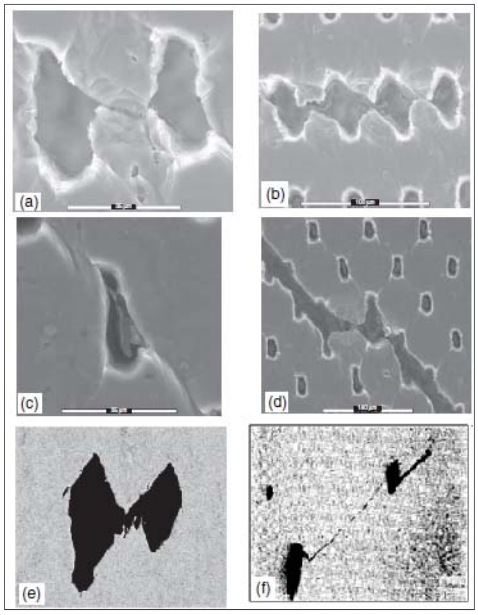

Fig. 2.18 Micrographs demonstrating the different void coalescence mechanisms in metals. The load is vertical, and the test have been made on perforated aluminum sheet with different arrangements of voids, (a, b) this arrangement lead to internal necking [59], (c, d) arrangement leads to coalescence in shear [59], (e) An internal necking process in steel showing the presence of one or two secondary voids in the ligament [60], (f) void sheet mechanism with many secondary voids along the microshear band, this is an example of void coalescence by void sheet for AISI 4340 steel [51].

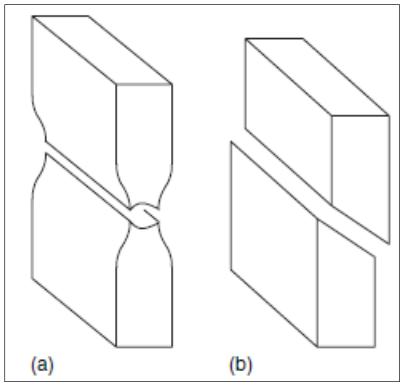

Fig. 2.19 The two usual modes of fracture observed in metallic sheet (a) is the flat mode(b) is the slant mode.

Another important mannerism of crack propagation as a result of void coalescence is the way in which the advancing crack travels through the material. A crack that passes through the grains within the material is undergoing transgranular fracture. However, a crack that propagates along the grain boundaries is termed an intergranular fracture.

On both macroscopic and microscopic levels, ductile fracture surfaces have distinct features. Macroscopically, ductile fracture surfaces have necking regions and an overall rough surface appearance. On the microscopic level, ductile fracture surfaces appear rough and irregular. The surface is covered by segments of voids which coalesced to produce the fracture path. These void segments were called dimples by Plateau *et al.* [45].The sizes of these dimples vary based on the source of the void nucleation. Usually, bigger voids or dimples results from voids nucleated from particles, where smaller ones may result from particle voids or any other sources like the one we discussed earlier, slip band intersection.

2.3.4 Fracture of UFGs

The Deformation behavior of nanostructured metallic materials has been extensively studied in the literature. However, little is known about their fracture behavior. Therefore one objective of this research is to investigate the fracture behavior of a nanostructured UFG metallic material at room temperature. Specifically, study the effect of stress state in term of stress triaxiality and microstructure in term of grain size on the fracture behavior of this UFG material. In this section a brief summary of some work that has been done in the area of fracture in UFGs will be mentioned.

Based on the extensive and careful SEM and SEM-ECC examinations done by Wu *et al*. they found that there are two kinds of shear bands responsible of fracture in cyclically deformed UFG-copper. The first one is the step-like shear bands and the second is the persistent slip bands-like shear bands [44]. In other study done by Paninn *et al*. they found that Meso- and macroscopic shear banding is the predominant mechanism of plastic deformation under quasi-static tension of armco iron with the high anisotropic banded substructure [61]. From the onset of plastic deformation the meso- and macrobands of localized plastic deformation propagate in the directions of maximum tangential stresses close to either one or both specimen-ends. The propagation of mesobands is accompanied by breaking up of elongated subgrains into approximately equiaxed micrograins. During the development of localized deformation macrobands the banded structure formed by preliminary ECAE transforms to a cellular dislocation substructure. The most anisotropic banded structure processed by ECAE in route A results in less increase in strength of UFG armco iron due to a higher propensity to shear

localization. Other studies showed that mesoscopic localized-deformation bands are responsible in fracture in UFG materials such as UFG copper and aluminum. It is along these bands that fracture takes place by the nucleation, growth, and coalescence of several microcracks. An arguments in favor of this mechanism is that in quasi-static tensile test specimens of ultrafine-grained metals undergoing even moderate plastic deformation, strain localization is observed as localized-deformation bands, and the fracture ultimately occurs along one of the bands [62].

CHAPTER III

EXPERIMENTAL PROCEEDURES

3.1 Material

This research is conducted using Interstitial Free (IF) steel. The material was obtained from Tata Steel Company Ltd in India. The chemical composition of the used IF steel is shown in Table 3.1. The existence of titanium in the material allows to capture the carbon particles in order to form titanium carbides and to make the steel interstitial free. The raw material used in this research comes in the form of Ti -stabilized IF steel transfer bar (The bar which comes out after roughing mill processing in hot strip mill). Three billets with the size of 1" x 1" x 6" are cut from the raw material to be extruded using ECAE.

Table 3.1
Chemical composition of the IF steel used in the research

Elements	Wight percent
Fe	Balance
C	0.0025
Si	0.013
Mn	0.06
P	0.013
S	0.01
Al	0.04
Ti	0.058
V	0.001
Cr	0.028
Ni	0.015
Mo	0.001
Cu	0.006
Nb	0.001

3.2 SPD – ECAE Procedures

The first step in the experimental work was fabricating the three billets made from the as-received IF steel by the SPD-EACE process using a 90^{o} inner channel angle and three different processing conditions. Three billets with the dimensions of 1” x 1” x 6” were cut from a raw bar of the material to fit within the die channel and were fabricated using the ECAE process, Fig. 3.1.

Fig. 3.1The billet used in the ECAE process.

Route 8Bc was used in the three billets. 8 refers to the number of passes the billet go through, (i.e, the billet was extruded 8 times using the 90^{o} channel angle.) And Bc refers to the angle in which the billet was rotated around its longitudinal axis before the next pass. In Bc the billet has to be rotated 90° along its longitudinal axis (extrusion axis) in the same sense either clockwise or counterclockwise between each two passes. Fig. 3.2 shows how this process was performed. This means that, after 4 passes, the billet completed a 360^{o} rotation and the original front face returned to its starting position. The die was placed in a press so that the sample could be pressed through the die using a plunger. In order to reduce the friction between the billet and the extrusion die chamber, each of the billets was wrapped with Teflon before starting each extrusion pass.

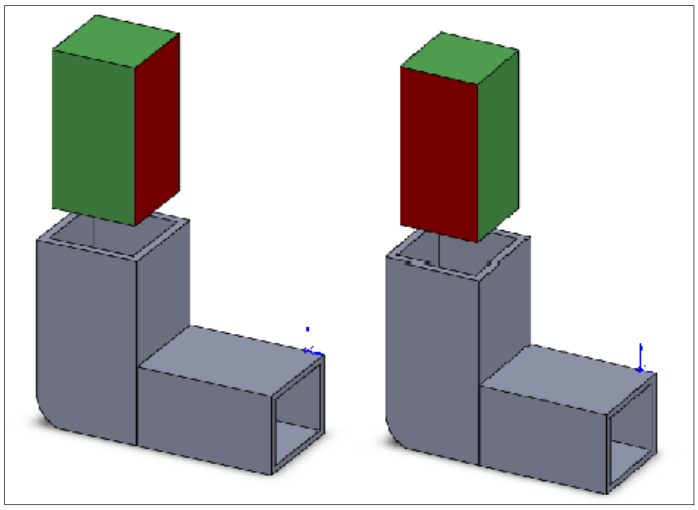

Fig. 3.2A schematic showing the 90^{o} angle die and the rotation of the billet with 90^{o} when using route 8Bc.

The size of the billet did not change before and after each pass, with the exception of some flashes which appeared along the edges of the billet that could be easily removed by a high speed rotary hand grinder after each pass.

Three different processing conditions in terms of temperature and extrusion rate were applied to the three billets to vary the grain size from 200nm-1μm. Billet 1 was extruded at room temperature and strain rate of 0.1 in/sec. Billet 2 was extruded at a temperature of 200C^{o} and strain rate of 0.1in/sec. In this case the temperature of the die was increased to 200C^{o}. Once the thermocouple read this temperature, the billet was placed inside the die and a pressure was applied to upset the billet against the die walls in order for the billet to absorb energy from the die by conduction. The pressure was released and the billet stayed inside the die for 15 minutes, then the extrusion process started. This process was repeated at each pass. Finally, billet 3 was extruded at room temperature and with an extrusion rate of 1in/sec. However, after the fourth pass, shear localization

appeared on the billet's edges. Starting fifth pass shear localization began appearing in the mid-section of the billet. Fig. 3.3 shows how shear localization occurs in billet3. Therefore, Billet 3 was extruded at room temperature and at two different strain rates. For the first four passes the extrusion rate was 1 in/sec, and for the second four passes 0.5in/sec to avoid shear localization, but shear localization occurred on one of the leading edges of the billet at the 8^{th} pass, but it did not happen on the entire of the billet.

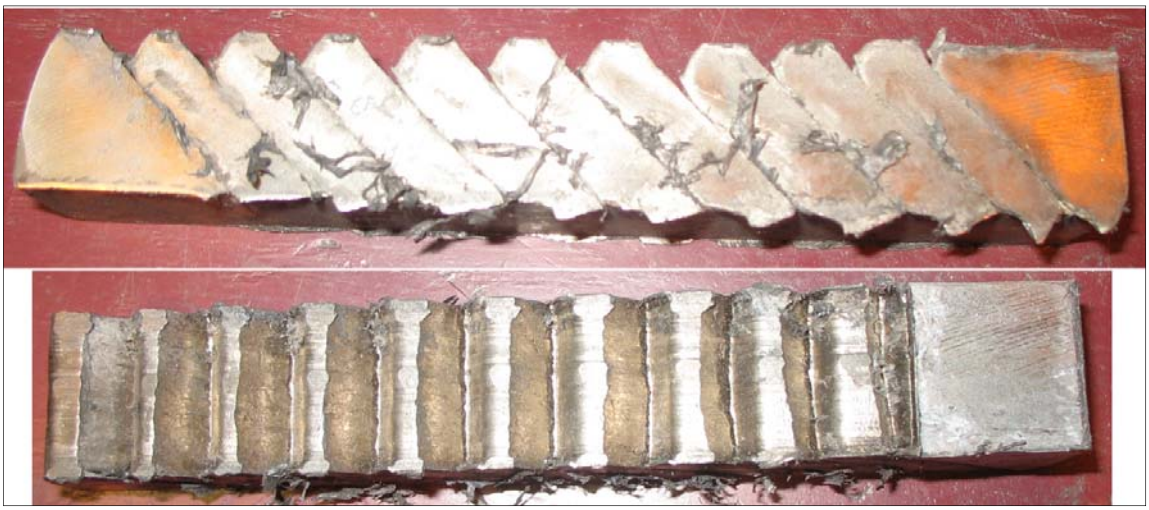

Fig. 3.3 Shear localization when using extrusion rate of 1in/sec.

It is expected that billet 2 has the biggest grain size and billet 3 has the smallest grain size. We always refer to the three billets as 1, 2, and 3 respectively, and we consider them as three different kinds of material.

3.3 Wire- Electrical Discharge Machining (EDM) Processes

EDM is a machining method typically used for hard metals, and it makes it possible to machine metals for which traditional machining techniques are ineffective. An

important point to remember with EDM machining is that it only works with materials that are electrically conductive. The word “Wire” means that it is an electro thermal production process in which thin single-strand metals wire (usually brass), in conjunction with de-ionized water (used to conduct electricity) allows the wire to cut through metal by the use of heat from electrical sparks. The used wire in this study has a diameter of 0.31 mm. The diameter of the wire was taken into account when cutting the samples in order not to have a smaller size of the machined samples. Due to the inherent properties of the process; wire EDM can easily machine complex parts and precision components out of hard conductive materials.

In this study, EDM was utilized to cut samples for a tensile test, for the microstructure analysis, and for the fractographs investigation purposes. One inch was cut from both ends of each billet to remove the non-uniform deformed region. The remaining length of each billet becomes 95mm, which was considered uniformly deformed. Each billet is cut into 3 pieces. The first piece was cut 46.5 mm from each end of the billet creating a slice with the thickness of 2mm. This slice was used for the microstructure analysis of the transverse plane and it was called M. The second two parts have the length of 46mm since the EDM wire has a 0.31mm diameter. These two parts which we will call the “Top” and the “Bottom” were used to machine the tensile test samples.

Cylinders were cut from the top and the bottom parts of each billet along its longitudinal/flow direction. 10 cylinders with a diameter of 8mm and a length of 46mm were cut from billet1 and billet 2 respectively. 5 cylinders were cut from the top part of

the billet, and 5 from the bottom. In the case of billet 3, we tried to maximize the number of the cylinders being cut in order to have more tensile test samples. Therefore, 16 cylinders with 7mm diameter, and 46mm length each were cut. 7 cylinders were cut from the top part of the billet, and 7 from the bottom, see Fig. 3.4

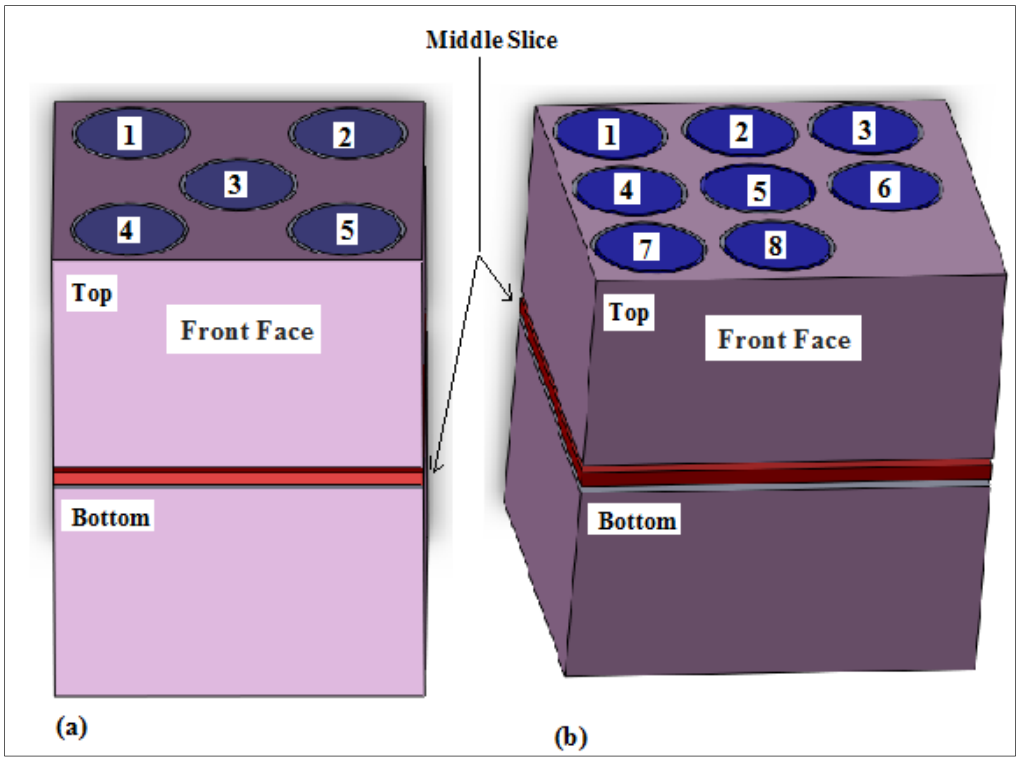

Fig. 3.4 (a) A schematic showing how the cylinders and the middle slice M are cut from both billets 1 and 2 (b) A schematic showing how the cylinders and the middle slice M are cut from billet3.

Actually, the total number of the remaining cylinders to be machined as tensile test specimens was less than the expected because some of the cylinders did not have the correct dimension because of the EDM machining. Some of the cylinders flattened on the outer surface, and the diameter at the flat region became less than 5mm which is too small for the tensile test samples.

As shown in Fig. 3.4(a) the numbering methodology of both billets 1 and 2 is the same. However, the method used in numbering billet 3 is different as illustrated in Fig. 3.4 (b). The numbering of the cylinders of the three billets is consistent in the top and the bottom parts.

When we specify the name of a cylinder or a sample, the first number (1, 2, and 3) refers to which billet it was cut from. The letter (T or B) refers to the top and the bottom parts of the billet respectively. The second number in the name refers to the position of a cylinder as illustrated in Fig. 3.4. For example, 1T3 means that this sample was cut from the top part of billet 1, and it was positioned in 3. Those cylinders were used later to machine smooth and notched bar samples.

We cut two samples from the top part of the billet by slicing out two pieces along the extrusion axis. The first piece was on top of the second piece along the extrusion axis. The first piece was named ‘A’ and the second piece was called ‘B’. The flow plane of the billet was observed under the microscope using sample A, while the longitudinal plane/ extrusion plane was observed using sample B. The flow plane was the red plane shown in the Fig. 3.5 and the longitudinal plane was shown as the blue plane in the same figure.

The names of the microstructure samples were specified by number and letter. The number refers to the billet number, and the letter refers to the face that a sample represents. For example, 1M refers to the slice sample from the middle of billet 1 which represents the transverse plane, and 3B refers to sample B which represents the longitudinal plane and taken from billet2, see Tables 3.2 and C.1.

Finally, EDM cutting was used to cut notched bar samples longitudinally after being tested by tension test in the case of interruption, and this will be discussed in the fractographs section.

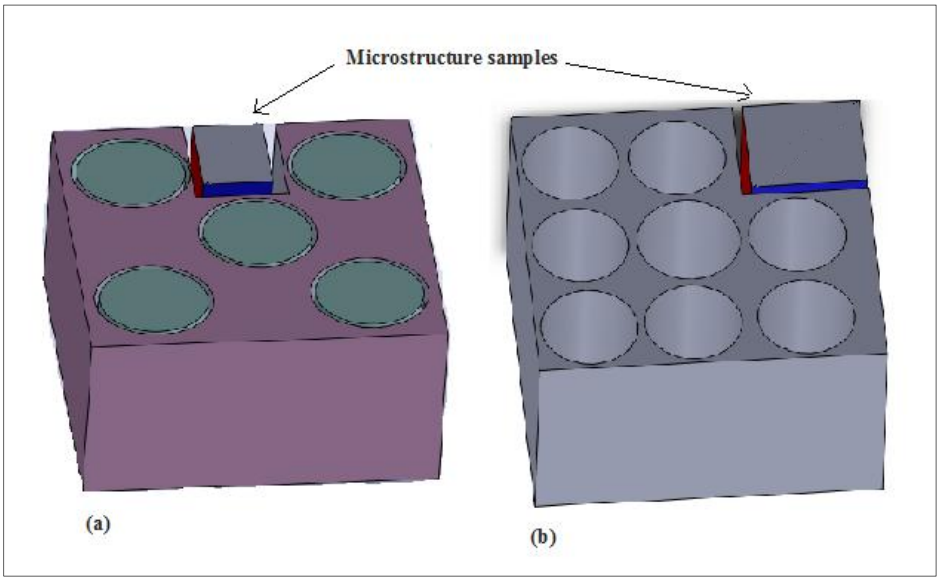

Fig. 3.5 A schematic showing how the microstructure samples A and B have been cut from the top or bottom parts of the billets.

Table 3.2

Summary of the processing conditions of the three billets with the number of the smooth and notched bar samples with the number of the smooth and notched sample being cut from each billet

Billet	Temperature	Strain rate	# of Smooth bar samples	# of Notched bar samples
Billet 1	Room temp	0.1 in/sec	3	3 – shallow 4- sharp
Billet 2	200 Celsius	0.1 in/sec	3	3 - shallow 4- sharp
Billet 3	Room temp	1 in/sec -first 4 passes 0.5 in/sec -2nd 4 passes	2	2 – shallow 3- sharp

3.4 Tensile Testing

Tensile testing is performed to study the mechanical behavior of all three materials. Smooth and notched bar specimens were machined from the cylinders using the Feeler Engine Lathe at the Texas A&M university machine shop. Smooth bars were used to characterize the deformation behavior of the material, and notched bars were used to characterize the fracture behavior and mechanisms (notch ductility). Both smooth and notched bar specimens were tested using a 100 kip hydraulic MTS machine at room temperature and quasi-static loading.

3.4.1 Smooth Bars

To study the mechanical behavior of the three materials, smooth bar specimens were machined from the 7mm and 8 mm cylinders that have been cut from the three billets. Figs. 3.6 and A.1 in the appendix show the geometries of the used smooth bars. It can be seen from the figure that the dimensions are all the same in both designs except the outer diameter.

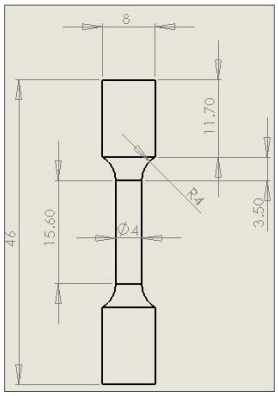

Fig. 3.6 A schematic showing the dimensions of the smooth bar samples that machined from 8 mm diameter cylinders.

Special threaded holders with 7 and 8 millimeters were machined using the Feeler Engine Lathe to mount the samples on the MTS machine. The threaded region of 11.7mm length was screwed to the threaded holders and mounts on the MTS upper and lower parts. The upper part of the MTS machine was connected to a load cell which has a maximum capacity of 100 kip to measure the load at each time step. Laser extensometer was used to measure the axial strain at each time step. As recommended two 1mm X 1mm pieces of reflector were cut and fixed on the sample with a separating distance of 14.55-15mm to reflect the laser beam in order to measure the axial strain.

This 14.55-15mm was considered as the gauge length of the sample (Lo). The distance between the laser extensometer and the sample was set to18 inch to have a precise value for the measured strain. The employed displacement rate in all of the tested smooth bar samples was the same and equal to 0.01mm/sec. The same displacement rate was used when testing all of the samples since changing the displacement rate will affect the behavior of the material. The measured values from the smooth bar tensile test were, the load in Newton, the axial strain ($\Delta L/Lo$) ,the axial displacement in millimeter, and the time.

The initial diameter Φ_o and the final diameter Φ_f (after fracture) were measured of each broken sample to calculate the fracture strain (ε_f). Therefore, the initial diameter of the sample was measured d using a digital caliper, and the final diameter was measured using a Keyence VHX-600K digital microscope. To measure the final diameter of broken samples two methods were used. The first method was to measure the diameter of the broken surface under the microscope. The second method was to connect the two

broken pieces together, then measure the diameter. More than one measurement of the diameter was taken and the average of all of them is considered as the final diameter.

3.4.2 Notched Bars

The cylindrical notched round bar geometry is probably the best suited to study the ductile fracture. It allows probing a wide range of stress triaxiality by changing the radius of the notch curvature. Moreover, the stress triaxiality remains relatively constant throughout the deformation process in the center of the minimum cross section, and this enable us to study the notch toughness or notch ductility. By way of contrast, the stress triaxiality in smooth bars is very low and varies significantly after the onset of necking. In addition, since necking is a structural instability, measures of ductility extracted from smooth bar testing are highly sensitive to the specimen geometry.

Notched bar specimens were machined from the 7 mm and 8 mm cylinders to characterize the ductile fracture of the three materials by investigating the notch ductility. Two notch geometries were used in this research to allow us to study the effect of stress triaxiality. Figs. 3.7 and 3.8 show these two geometries. The geometry in Fig. 3.7 is called shallow notched bar, and the one in Fig. 3.8 is the sharp notched bar. Each geometry was identified by a special parameter $\zeta = 10R/\Phi_o$ where R is the radius of the notch curvature and Φ_o is the initial diameter at the notch region. For the shallow geometry ζ is10, and for the sharp one it is 2. Based on the definition of ζ, it can be seen that a smaller value for ζ will correspond to a sharper notch, which will enhance the

value of the triaxiality, and this lead to less notch toughness as we will discuss in more details in the results chapter.

Moreover, two different geometries for each value of ζ were used. They were based on the 7 mm or 8 mm outer diameter of the used cylinder. For example, to machine a shallow notched bar sample from a cylinder that had a 7mm diameter, the geometry in Fig. A.2 was used. However, if the cylinder diameter is 8mm, the geometry in Fig. 3.7 was used. The same method was applied in the case of notched bar samples in both Figs. 3.8 and A.3. The same Feeler Engine Lathe was used to machine the notched bar samples.

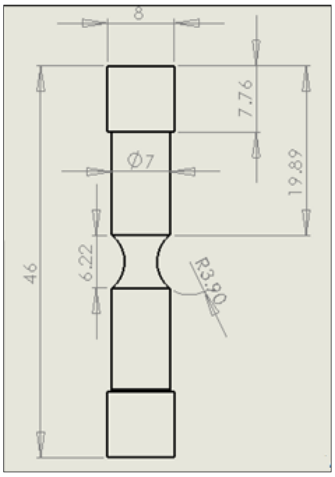

Fig. 3.7 A schematic showing the dimensions of the shallow notched bar samples that were machined from 8mm diameter cylinders.

Hydraulic MTS machine was used to perform the test on the notched bars. It was especially important to use such a machine to interrupt the test. An MTS extensometer designed for fracture mechanics tests on notched bar specimens was adapted using specially devised knives mounted on the extensometer to have a special radial

extensometer, see Fig. 3.9. This special radial extensometer was used to measure the radial strain ($\Delta\Phi/\Phi_o$), and to interrupt the test during the crack propagation to gain insight of damage micro-mechanisms in the notched specimens.

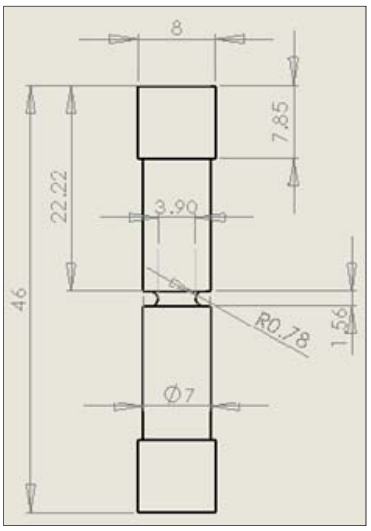

Fig.3.8 A schematic showing the dimensions of the sharp notched bar samples that were machined from 8 mm diameter cylinders.

Special concern was given to the radial extensometer calibration. The calibration process was performed using pins with diameters varying between 3.05mm and 3.97mm, considering the pin with the 3.9mm diameter as the reference diameter Φo . This diameter was chosen because the diameter of the minimum cross section of the notched samples was 3.9mm, and the measured strain was set to be zero when using this pin. The maximum strain that the extensometer was able to measure was 0.22mm. The first value of the strain was set to be zero when the pin of the diameter 3.9mm was first used. Then the strains measured by the extensometer for each used pin were compared to the calculated ones until we achieved the accurate measurements. The calibration of the

extensometer had been checked every time we tested a group of samples, since the tests were performed throughout an extended period of time (by a month or so) as a result of machining issues.

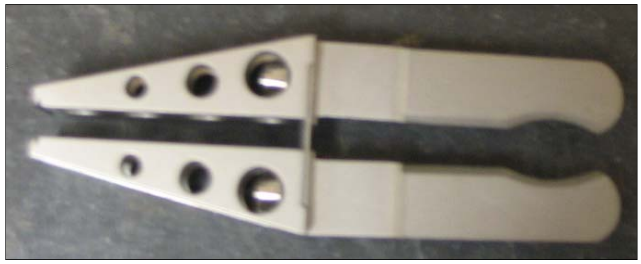

Fig. 3.9 Specially devised knives used to measure the diameter contraction in the notched samples.

The notched bars were tested using two methods. The first one was to test the notched sample up to fracture. This allowed analyzing the fracture surfaces, and to determine the fracture strain (ε_f) and the notch ductility of the material. The second method consists of interrupting the test after crack initiation; the onset of the crack initiation can be determined once the sudden change in the slope of the loading response begins. This allowed studying the fracture mechanisms for the material, especially when the sample was cut along meridian planes to investigate how the crack initiates and how it propagates. It also permitted to find the strain at the crack initiation (ε_i). Both the fracture surfaces and the crack propagation images (fractographs) permitted to understand the fracture mechanisms of the material.

All notched samples were tested at a displacement rate of 0.001 mm/sec. Also, the same displacement rate was used for both interrupted tests and fracture tests. The same displacement rate was used in all of the cases since there is an effect of the displacement rate on the behavior of the material. The measured values from the notched bar tensile

tests were the load in Newton, the radial strain ($\Delta\Phi/\Phi_o$) and the axial displacement in millimeter. The initial diameter of the notched bars Φ_o was measured using a digital caliper, and the final diameter Φ_f was measured using the Keyence VHX-600K digital microscope. All measurements were done in the same manner as for the smooth bars.

3.5 Microstructure Analysis (Micrographs)

One of the most important objectives of this study was to fabricate UFG-IF steel using the ECAE process under three different processing conditions to vary the grain size between 200nm and 1μm. Microstructure analysis was performed to measure the mean grain size of the material. For the microstructural analysis to be completed, several steps such as polishing, etching, and observations using optical and electron microscopy were accomplished.

In order to examine the microstructure of the three billets and to calculate the resulting average grain size ($\bar{d}$) from each processing condition, micrographs were taken for representative samples from each billet. This examination requires special preparation for the samples, which includes: cutting representative samples from each billet, mounting, polishing, etching, using a suitable microscope to explore the microstructures, and then analyzing the microstructures using suitable methods to find the average grain size.

As seen in Figs. 3.4 and 3.5 three samples were cut from each billet for microstructural analysis purposes. A 25mm X 25mm X 2mm slice was cut from the middle of each billet. This sample was called M and it represents the extrusion plane. Two additional samples with approximate size of 1cm X 1cm X 1.5cm were cut from the

top part of each billet. These samples were used to explore the microstructure of the longitudinal plane using sample B, and the flow plane using sample A. Finally, two additional samples were cut from the as-received IF steel for comparison purposes with the fabricated ones.

After the microstructural samples were cut, they were mounted into an epoxy to ease the polishing process because they were small. Epoxy mount resin was mixed with epoxy mount hardener in a weight percentage of 10:3. Then each sample was placed faced down in a circular shaped mount; the face nearest to the bottom was the one being investigated. Then the mix was poured onto the sample and left for 6-8 hours to solidify under room temperature.

Mechanical polishing using silicon carbide and aluminum oxide was used to polish the samples. Each sample was polished using the silicon carbide papers with grit numbers 400, 600, 800, 1200, and 2000. After that it was polished with aluminum oxide with grit numbers 0.5μm, 0.1 μm, and 0.03 μm respectively. On each stage each sample was polished for 2 minutes to end up with a mirror like shape at the end of the polishing process.

Before the etching was performed, the specimens were examined under optical microscope Lieca to observe any possible defects like surface cracks, porosity, inclusions, scratches, etc, and to ensure that the surface is a mirror-like surface. It was not possible to see any microstructure under the optical microscope before etching because the reflected light from the mirror-like polished surface was uniformly reflected.

To be able to view the microstructure and to reveal the grain boundaries, a special chemical solution called Marshall's reagent was used to etch the surface [63]. It was not possible to use the Nital to etch the surface of the IF steel to reveal the grain boundaries. The composition of the Marshall's reagent is shown in Table 3.3.

To prepare the Marshall's reagent, the water was first mixed with the sulfuric acid. Then the oxalic acid was added to the mix, and finally, equal amounts of solution A and solution B were mixed with each other.

Each sample was etched for only 5-10 seconds by Marshall's reagent, and cleaned by Alcohol, then dried by a stream of compressed air. However, the as-received ones needed around 1minute or more to react to the etching solution. In order to keep the samples dry until being examined by the SEM microscope, they were stored in a desiccant. This is because the wetness may cause oxidation for the surface of the sample, and it badly affects the SEM microscope, since the microscope works based on electron beams and in a totally vacuum environment.

Several trials were done to explore the microstructure of the three billets using the optical microscope and the JOEL-SEM, but none of them succeeded even with a magnification of 1000X. Only Field Emission-Scanning Electron Microscope (FE-SEM) was suitable to examine the microstructure.

Table 3.3

The chemical composition of the Marshall's reagent

	Composition	Wight (ml / g)
Solution A	Water	100 ml
	Sulfuric acid	5 ml
	Oxalic acid	8 grams
Solution B	Hydrogen peroxide	30% concentration is required

The FEI Quanta 600 FE-SEM was used in this study. The Quanta 600 FEI is a field emission scanning electron microscope capable of generating and collecting high-resolution and low-vacuum images. It is usually used to examine the microstructures, fracture surfaces, and chemical composition for several types of materials. The equipments associated with the Quanta 600 include: back-scattered electron detector, HKL/Oxford EBSD system, secondary electron detector, and other detectors. The main detectors used in this study are the back-scattered, and the secondary.

Cleanliness and dryness of the samples were necessary requirements before using the FE-SEM microscope. Dryness of the samples was important when using the microscope; gloves were used to hold them and put them inside the microscope. In addition, since the epoxy was not conductive, each sample was wrapped on the upper surface with a copper tape. The tape covered all of the epoxy on the upper surface except the sample surface, and the tape was long enough in order to stick it with the holder base in order to make the whole sample conductive. As shown in Fig. 3.10 black circles were drawn on the surface of the sample to keep locating the observed area under the microscope.

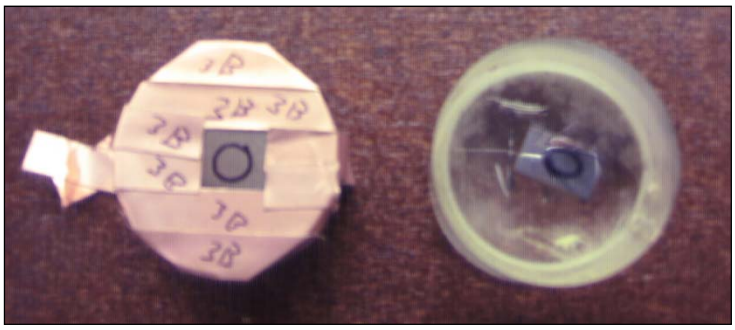

Fig. 3.10 Sample mounted in an epoxy in the right of the figure, and in the left when sample is wrapped with copper tape.

Micrographs were taken for each sample using both Backscattered (BSED) and secondary (ETD) detectors at different positions on the sample surface to investigate the variation of the microstructure and its homogeneity between the center of the sample and its edges. The lineal intercept method was used to calculate the average grain size ($\bar{d}$) of the three billets. Three micrographs representing the transverse face (Sample M) were used in the lineal intercept method to find the average grain size for each billet.

3.6 Fracture Surface Analysis (Fractography)

In its simplest form, fracture can be described as a single body being separated into pieces by an imposed stress. For engineering materials there are roughly two possible modes of fracture, ductile and brittle. In general, the main difference between brittle and ductile fracture can be attributed to the amount of plastic deformation that the material undergoes before fracture occurs. Ductile materials demonstrate large amounts of plastic deformation whereas brittle materials show little or no plastic deformation before fracture.

In this study we focused on investigating the ductile fracture of the UFG-IF steel. Ductile fracture can be described as the failure mechanism in most metals and their alloys at room temperature. In ductile fracture, extensive plastic deformation takes place before fracture, and the strain at which the fracture happens is affected by the purity of the materials.

In a uniaxial tensile bar, ductile fracture follows (in stages that initiate after) necking (begins). First, small microvoids form in the interior of the material. Next, deformation continues and the microvoids enlarge, then coalesce to form a micro-crack which will propagate through the material. The crack continues to grow and spreads laterally towards the edges of the specimen.

Fractographs were taken to examine ductile fracture materials, since they give a good idea about the damage mechanisms of the material. Two types of fractographs were used in this study; the first one was used to examine the fracture surfaces of the broken notched bar samples, and the second one was used to figure out the crack propagation inside the interrupted notched samples.

Examining the fracture surfaces of the broken samples requires certain steps to be taken; first the samples were cut using precision diamond cut-off saw to a smaller length, since long samples may cause charging problems inside the SEM microscope. Then the samples were cleaned with isopropyl alcohol and dried with compressed air. Finally the samples were placed inside the microscope and use the secondary detector to take images of the fractured surface. Images were taken of both parts of the broken sample at different levels of magnifications.

In order to examine the void nucleation and crack propagation mechanisms inside the interrupted samples, the following procedure was followed. First, the samples were cut along longitudinal plane has an offset of 0.3mm from the meridian plane of the sample using EDM. This offset was used because cutting the sample at their middle plane could lead to the loss of some fracture mechanisms features, such as the cracks and voids, during polishing.

Second, since the samples were small, and it was difficult to polish them by hand, they had to be mounted inside an epoxy. The same mix (hardener and resin) which was used in mounting the microstructural samples was used to mount the fractographic samples, see Fig. 3.11. Unfortunately, the epoxy got trapped inside some cracks, and there was no suitable way to remove completely the epoxy. Therefore, the epoxy appears in some of the crack propagation fractographs, see Fig. A.4.

After the epoxy solidified, each sample was polished using silicon carbide papers with grits 600, 1200, 2000, and 4000, then colloidal silicon oxide was used to polish the samples at the final stage in order to smear-out the inclusions inside the cracks. Ultrasonic cleaner filled with isopropyl alcohol was used to clean the samples. Cleanliness and dryness were important to avoid oxidation on the crack surface, so that after cleaning by water, isopropyl alcohol was used to clean the surface of the sample and to dry it completely from water, then a steam of compressed air was used to completely dry the samples. Finally, the samples were stored in a desiccant to protect them from oxidation and from moistures until being tested by the FE-SEM.

Finally, the samples were wrapped again on the upper surface by copper tape in order to make them conductive to be seen by FE-SEM. Three samples at a time were placed inside the microscope to be examined, and the secondary detector was used to take images of the crack propagation and void nucleation using different levels of magnifications. By following this procedure fractographs were taken of the samples without etching.

The same process of sample preparation was used again but with the additional step of using the etching solution. Fractographs were taken using the microscope but this time after etching the sample so that some fracture mechanism features like determining if the crack is intergranular or transgranular can be investigated.

Fig. 3.11 The crack propagation investigation sample mounted inside the epoxy.

CHAPTER IV

EXPERIMENTAL RESULTS

4.1 Microstructures

Microstructure is defined as the structure of a prepared surface of material as revealed by a microscope above 25X magnification. The microstructure of a material can strongly influence physical properties such as strength, toughness, ductility, hardness, corrosion resistance, wear resistance, and so on, which in turn governs the application of these materials for industrial practice. As we mentioned earlier, that the Hall Petch equation describes the relationship between the grain size and the strength of the material; the smaller the grain size the stronger the material. Micrographs were taken using Keyence VHX-600K digital microscope of the as-received IF steel. Both Back-scattered (BSED) and Secondary electron imaging (ETD) were used to take micrographs of the three fabricated materials. The micrographs of both the as-received IF steel are shown in Figs. 4.1 and 4.2.

Figs. 4.1 and 4.2 show the microstructure of the as-received IF steel. Keyence VHX-600K digital microscope is used to take these images for two reasons: First, they are taken only for comparison purposes with the UFG ones in order to explore up to what level the grain size can be refined using ECAE process. Second, the grains could not be observed using the SEM microscope. Third, the grains are large enough to be viewed by the digital microscope.

The figures show that the grain size of the as-received IF steel is large and it is between 205μm - 250μm which is consistent with previous studies [63]. The dark spots on the pictures may be artifacts or etching spots from the sample preparation.

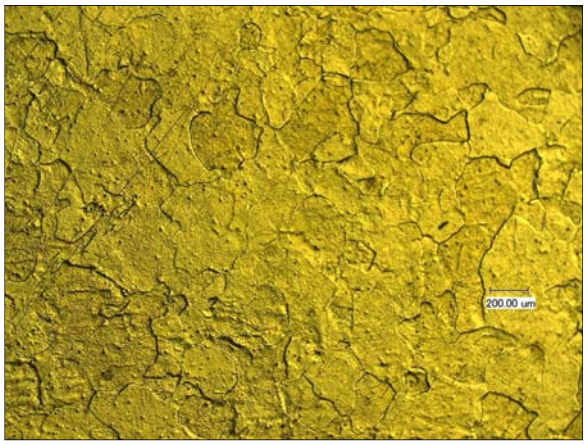

Fig. 4.1 Microstructure image for as-received IF steel taken by Keyence VHX-600K digital microscope using 100X magnification.

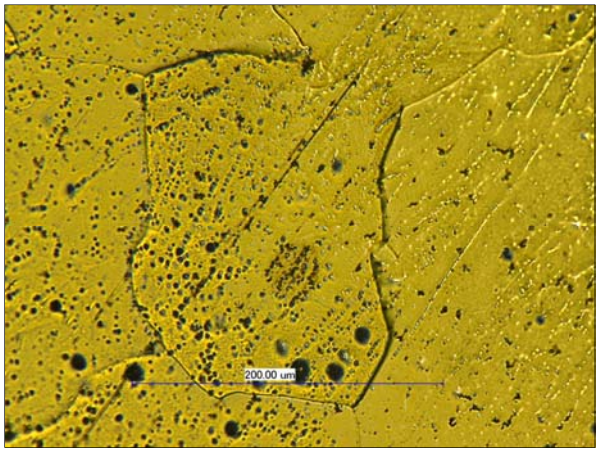

Fig. 4.2 Microstructure image for one grain of as-received IF steel taken by Keyence VHX-600K digital microscope using 700X magnification.

SEM micrographs using both secondary electrons and backscattered electrons of the transverse plane M of the three fabricated materials (billets) are shown in Fig. 4.3. Optical microscope or Keyence VHX-600K digital microscope could not observe any microstructure or any details in the fabricated billets since they have a very small grain size in the nanometer range. It can be seen from the three micrographs that there is variation on the grain sizes in the micrograph of each billet; some of the grains are big and some of them are small, but the majority are small. Moreover, the majority of the grains could be considered as equiaxed grains and the structure is homogenous. The black dots on the images represent vacancies between the grains or etching spots from the preparation process.

The grain size of each billet is measured using lineal intercept method of the transverse plane M using three micrographs of each billet. The mean grain size of billet 1 was found to be in the range 480nm-550nm, and this range matches to some extent with Niendorf et al results [5]. In addition, the mean grain size of billet 2 was found to be in the range of 530nm-650nm. Finally, the mean grain size of billet 3 was found in the range of 420nm-550nm.

Table 4.1 shows a summary of the grain size of the three billets. It can be seen from both the micrographs and the images that there is no significant variation exists between the grain size of both billet 1 and 3. However, billet 2 shows bigger grain size compared to billet 1 and 3.

In addition, Fig. 4.4 shows backscattered micrographs of the flow plane A, and the longitudinal plane/extrusion plane B of billet 1. The grain morphology is relatively heterogeneous and the features are a band-like structure. But as shown in the figures, the grains in plane A elongated more than the ones in plane B. It worth to mention that the grains are elongated in the same extrusion direction, but in the pictures they lookas they were inclined with an angle, and this is not an inherent feature of these planes, but it is because of the way the sample was placed inside the microscope. This will be found in both the flow plane A, and the longitudinal plane B micrographs of all the billets. Figs. B2 and B3 in appendix B show the flow plane and the longitudinal plane of both billet 2 and 3. Moreover, some over-etching defects are obvious on the grain boundaries in some micrographs of billet 2, see Fig. B.1.

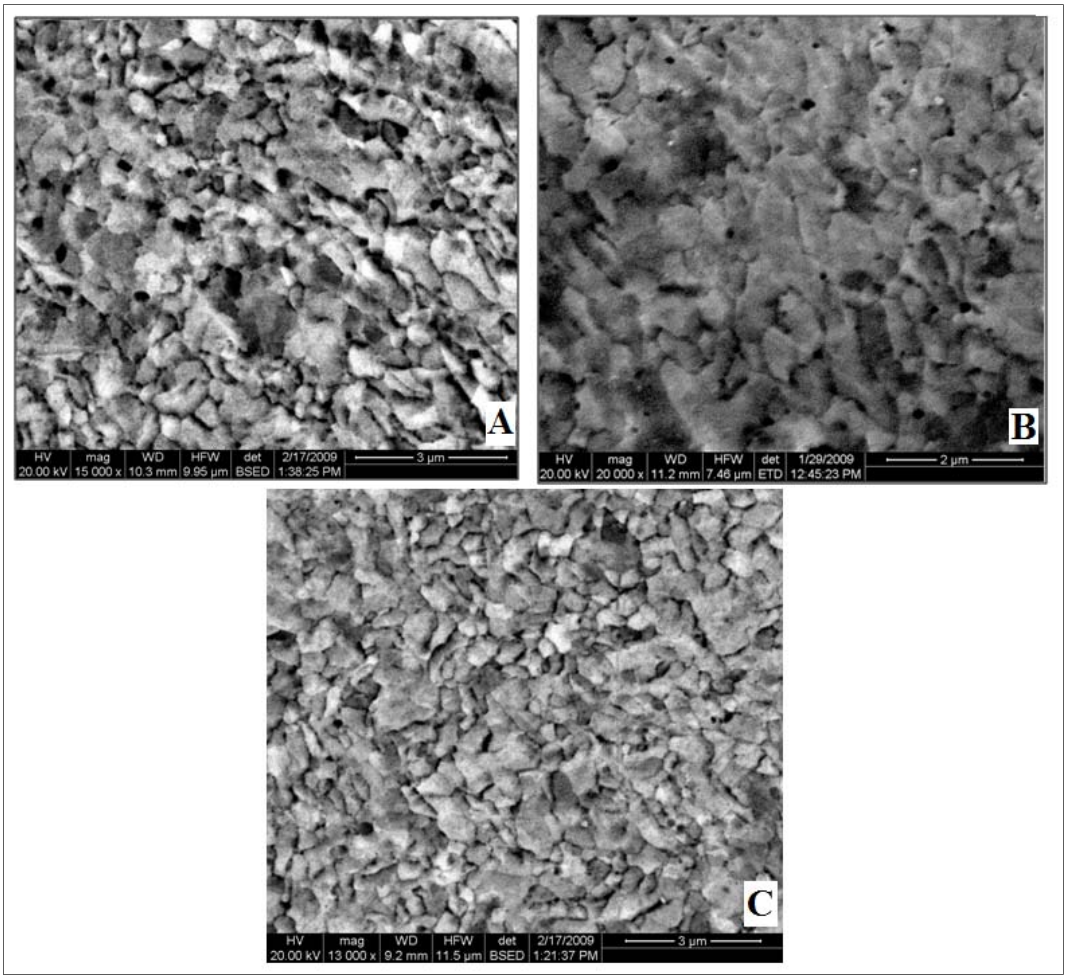

Fig. 4.3 FE_SEM micrographs of the transverse plane M (A) Backscattered SEM micrograph of billet 1-fabricated at room temperature and extrusion rate of 0.1in/sec, (B) Secondary electron SEM micrograph of billet 2 (fabricated at 200C^{o} and extrusion rate of 0.1in/sec) (C) Backscattered SEM micrograph of billet 3 (fabricated at room temperature and extrusion rate of 1in/sec for the first four passes, and 0.5in/sec for the second four passes).

Table 4.1

Summary of the mean grain size of each billet

Billet number	As-Received	Billet 1	Billet 2	Billet 3
Mean grain size (d)	250 micron	515±35 nm	590±60nm	485±65nm

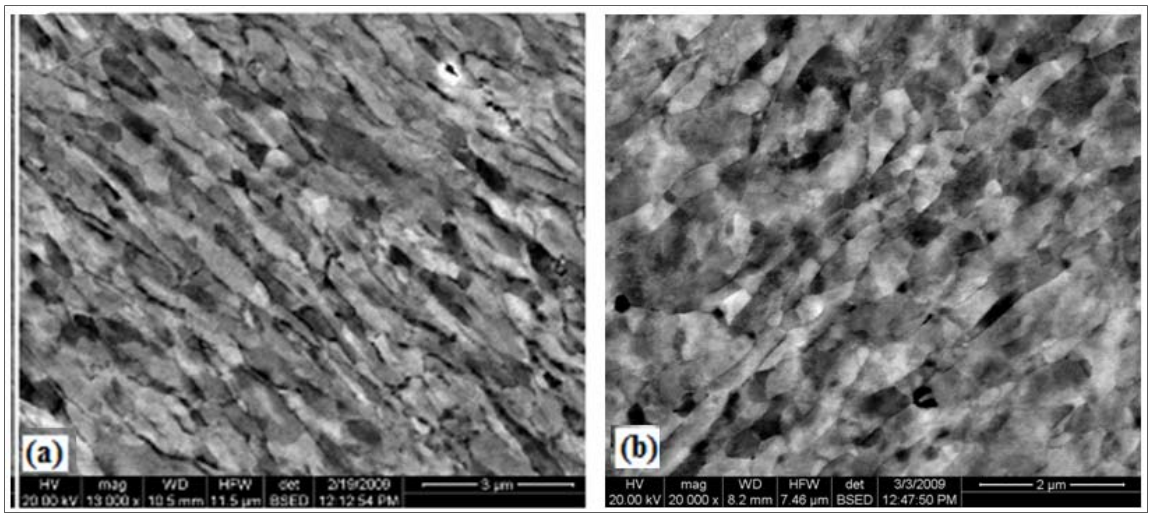

Fig. 4.4 (a) Backscattered SEM micrographs of billet 1 (a) flow plane A (b) Longitudinal plane B.

Based on what we have seen on the microstructure images we can conclude the following: First, route 8Bc can be used to refine the grain size from (200 -250 μm) of the as-received material to the range of (400nm-600nm) which means approximate reduction of the grain size in the order of 10^3. Second, we achieved a variation of the grain size between the three billets, but it is not significant as we expected especially between billet 1 and 3. For example, we expected that the grain size of billet 1 would be around 500nm and we achieved it. We expected the grain size for billet 2 to be around 1μm, but we found it to be around 600nm. And finally, the grain size of the billet 3 was expected to be around 200nm, but we found it to be around 450nm-500nm.So that based on these results we do not expect there will be any significant difference between the mechanical response of the three billets since the variation of their grain sizes is not significant. Third, the low quality of some images is partly caused by the limitation of the SEM focus ranges when using high magnification.

4.2 Tensile Testing and Deformation Behavior

Tensile test is the most fundamental type of mechanical tests that can be performed on the material. It is usually used to examine the mechanical behavior of the material. In this research tensile test is performed at room temperature and quasi-static loading conditions on two categories of specimens; smooth bar samples and notched bar samples machined from the three billets. The smooth bars are used to characterize the deformation behavior of the material, and the notched are used to characterize the fracture behavior (notch ductility). The ultimate tensile strength, the Young's modulus, the % elongation which is an indication of the ductility, and yield strength can be determined from the stress-strain behavior of the smooth bar samples. Special tensile tests have been developed to measure the effect of the specimen's conditions on the strengths and ductility on metals and alloys, these included the notched samples. So that the notched bar samples are used to determine the notch toughness, the fracture strain, and the initiation strain for both broken and interrupted samples. Test temperature and strain rate are generally controlled because of the effect of these variables on the metallurgical response of the specimen, so all of tests are performed at room temperature. Also, similar strain rate which is 0.01mm/sec is used of all of the smooth bars, and similar strain rate which is 0.001mm/sec is used for all of the notched bars. Each category of samples will be discussed separately.

Figures 4.5 and 4.6 show the engineering stress strain responses materials 1 and 2 respectively. Recall that material 1 was fabricated at room temperature and extrusion

rate of 0.1in/sec is shown whereas material 2 was fabricated at 200C^{o} and extrusion rate of 0.1in/sec.

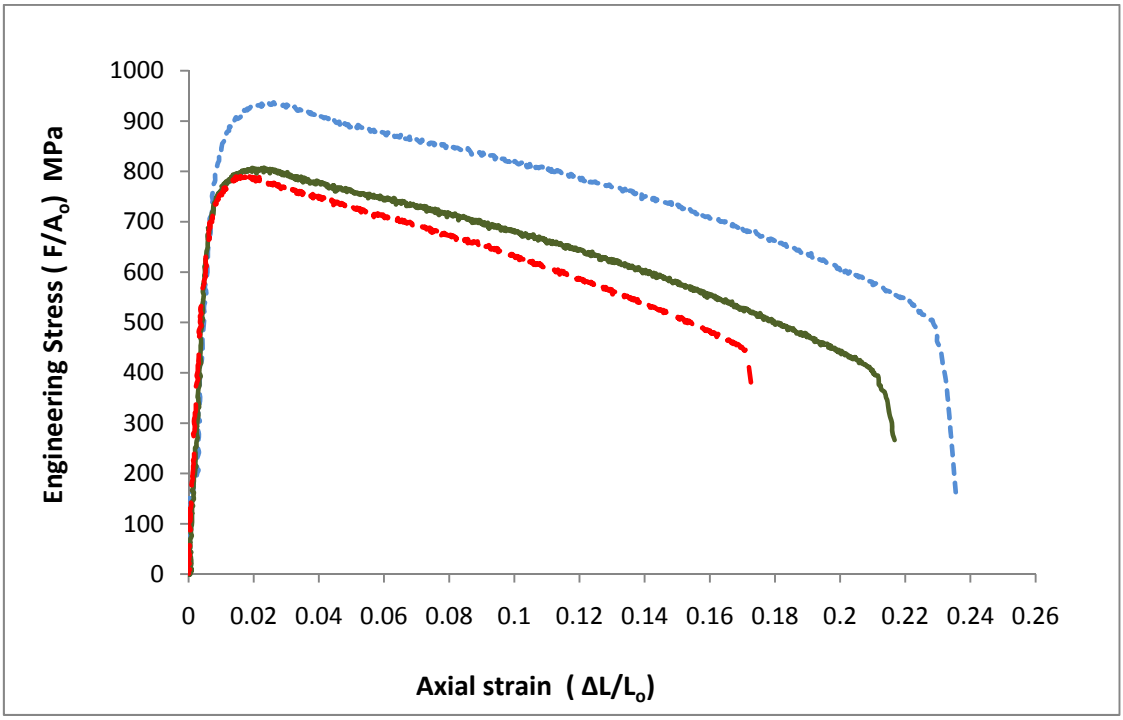

Fig. 4.5 Stress-strain diagram of 3 smooth bar samples made of UFG-IF steel fabricated at room temperature and extrusion rate of 0.1in/sec using route 8Bc (billet1). The initial diameter Φo of each sample is 4mm.

In general, the ultimate tensile strength (UTS) of both billets 1 and 3 was found to be around 800MPa, except for one of the billet 1 samples. The UTS of the samples made of billet 2, which is around 700MPa, is lower by over 100MPa compared to billets 1 and 3. It was found that there is a significant variation of around 500MPa between the as-received IF steel and the UFG version of it and this is consistent with the grain size measurements. It is worth mentioning here that the UTS is measured based on engineering stress.

To sum up, Fig. 4.7 shows representative responses of all three materials (billets) along with that of the as-received IF steel. The as-received IF steel data were taken from reference [5] for comparison purposes.

There is no significant difference in the axial strain to failure between smooth bars from both billets 1 and 3. A slight difference in the axial strain to failure was found between samples made from billets 1 and 3 and those from billet 2. For example, the axial strain to failure was found to be between 20%-24% in billets 1 and 3 whereas it is around 18% in the samples from billet 2.

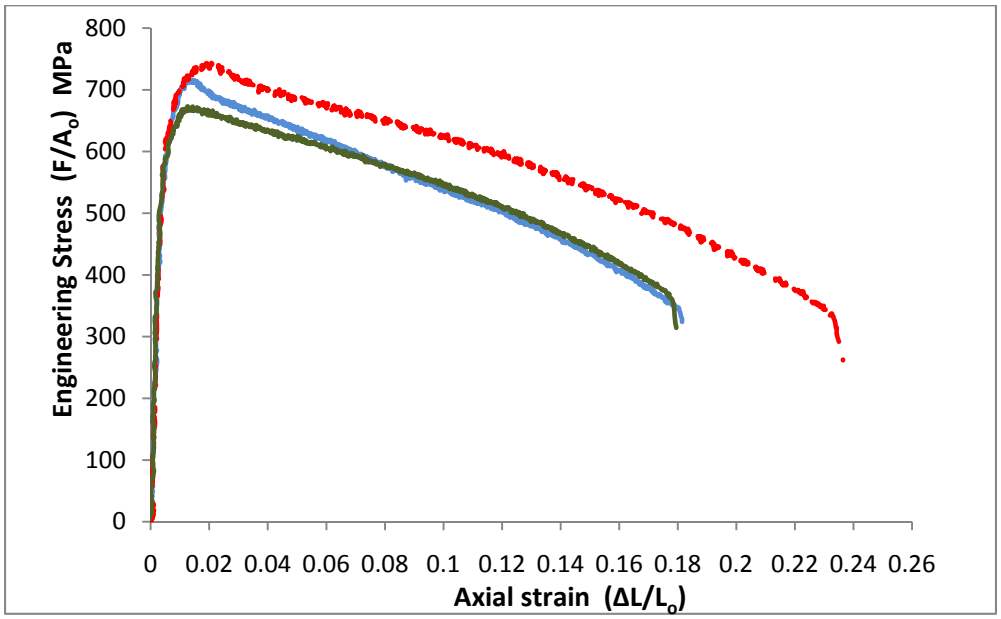

Fig. 4.6 Stress-strain diagram for 3 smooth bar samples made of UFG-IF steel fabricated at 200C^o and extrusion rate of 0.1in/sec using route 8Bc. The initial diameter Φo of each sample is 4mm.

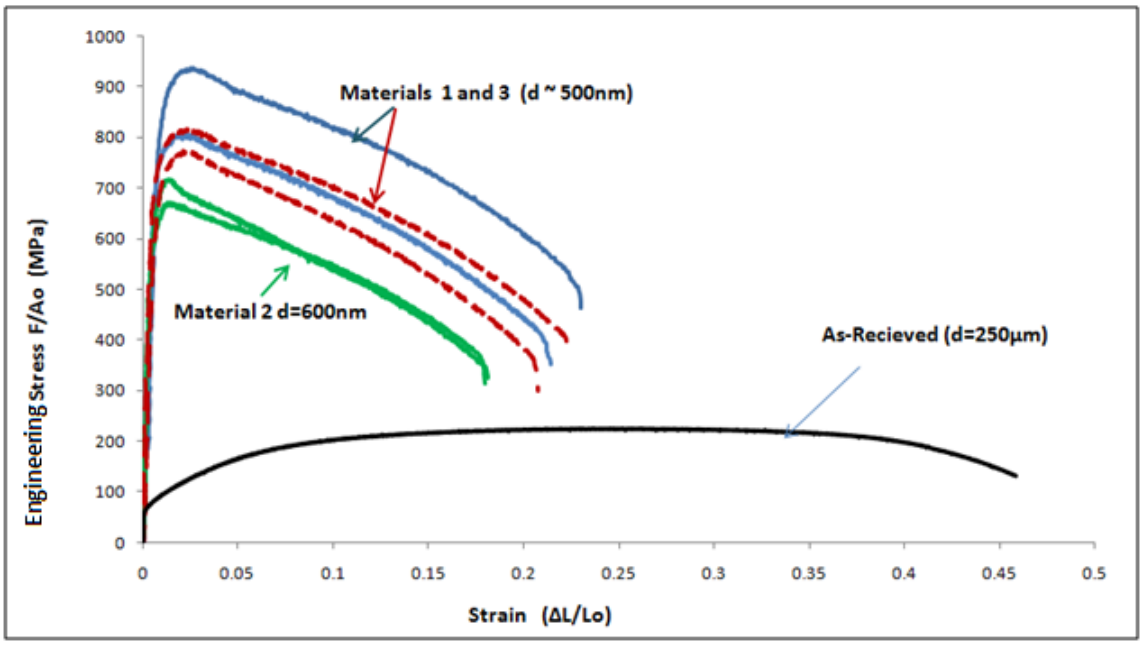

Fig. 4.7 Stress-strain diagram for smooth bar samples made of the three fabricated UFG-IF steel compared to the as received IF steel from Niendorf's paper.

Based on the stress-strain diagrams of the three billets shown in Figs. 4.5-4.7 and the summary plots in Figs. 4.8 and 4.9, the following can be concluded. First, the mechanical responses of billet 1 and 3 are close to each other. However, billet 2 shows a different response to some extent and these results are consistent with the grain size measurements. The microstructural details revealed a finer mean grain size in billets 1 and 3 as compared to billet 2. Second, it can be seen that the UTS of the three UFG materials has improved significantly compared to the as-received materials. Both the UTS and the axial strain values of the as-received material were found using Niendorf's work [5]. The true stress-true strain curve in Niendorf's paper was converted to engineering stress-engineering strain then the values from the latest curve were used here. Third, by comparing only the three UFG materials it can be seen that the strength

decreases significantly from the finest microstructures (billets 1 and 3) to the coarsest microstructure (billet 2); over 100MPa difference in the UTS. The conventional ductility, represented by the axial strain achieved before failure, was found to be similar between the three different billets tested. However, the conventional ductility was decreased in the UFG materials as compared to the as-received IF steel.

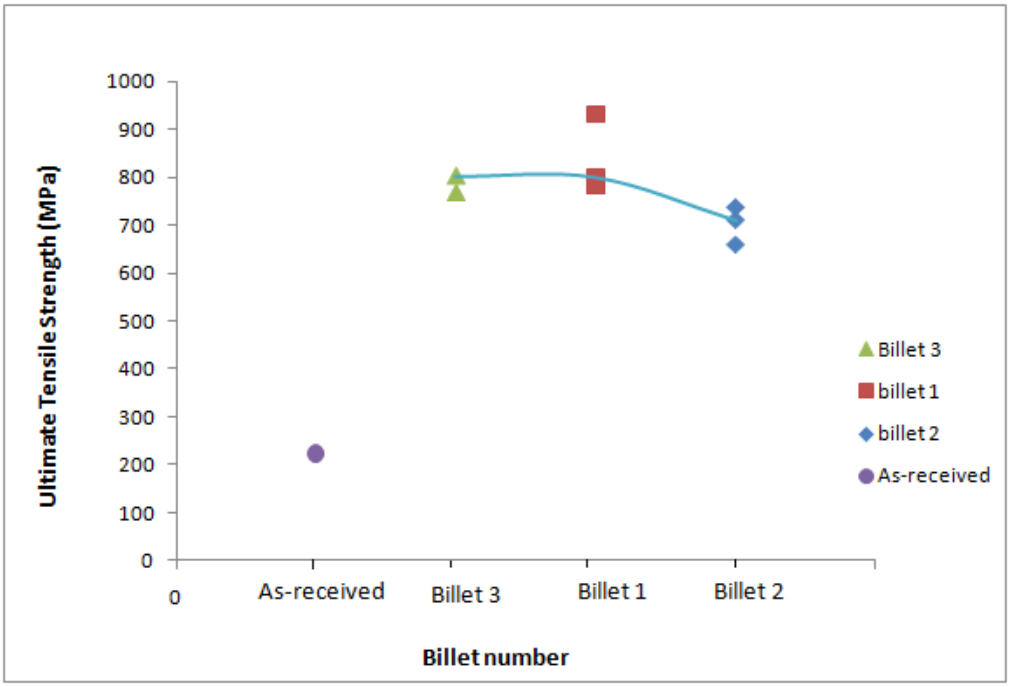

Fig. 4.8 Ultimate tensile strength vs the billet number of smooth bar samples made of the three types of material compared to the as-received material.

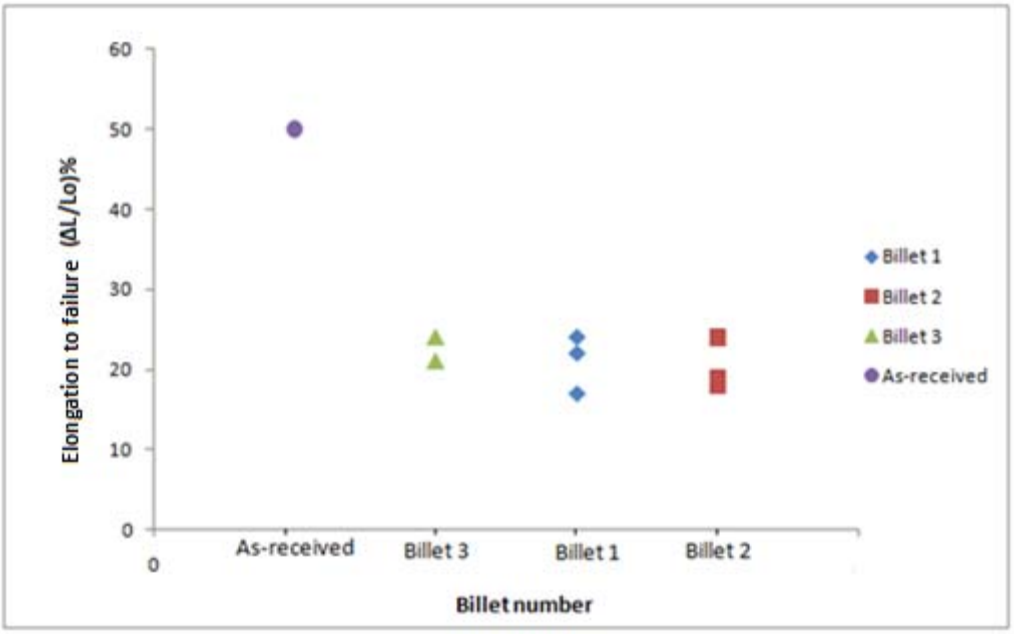

Fig. 4.9 Percentage elongation to failure vs the billet number of smooth bar samples made of the three types of material.

The variation of the behavior of the samples machined from the same billet (the scatter) maybe due to two reasons. It could be due to the position on the billet where the sample is cut from. This is because there are well deformed region on the billet and other non-uniformly deformed regions. Usually the center of the billet is the best position to cut samples from in order to study their behavior since it represents the well-deformed region during the extrusion process. This variation in case of billet 2 could be as a result of the non-uniform temperature distribution on the billet during the extrusion process.

Finally, the true stress-true strain curves for smooth bars were not shown in this research since the equations that changes from engineering to true values; $\varepsilon_{true} = ln(1 + \varepsilon_{eng})$, $\sigma_{true} = \sigma_{eng}(1 + \varepsilon_{eng})$, are valid only up to the necking point. Beyond the necking point Bridgman's analysis, based on the reduction in the diameter of the

sample, should be used. Such an analysis was not done in this study because the reduction in the diameter was not measured for smooth bars during the experiments.

4.3 Damage and Fracture Behavior

Analyzing ductile fracture is central to a number of engineering problems where toughness and ductility are required mechanical properties. Notched tensile testing has proven to be a suitable method to explore the stress state effect on ductile fracture and to characterize the fracture behavior. Fig.4.10 shows a typical force-diameter reduction diagram for a notched bar sample, the corresponding crack initiation point and the complete failure point. It is customary to define a mean strain to failure according to 4.1 where Φ_o is the initial minimum diameter of the sample, and Φ is the instantaneous diameter measured using the radial extensometer.

$$\bar{\varepsilon} = 2\ln\frac{\Phi o}{\Phi} \qquad 4.1$$

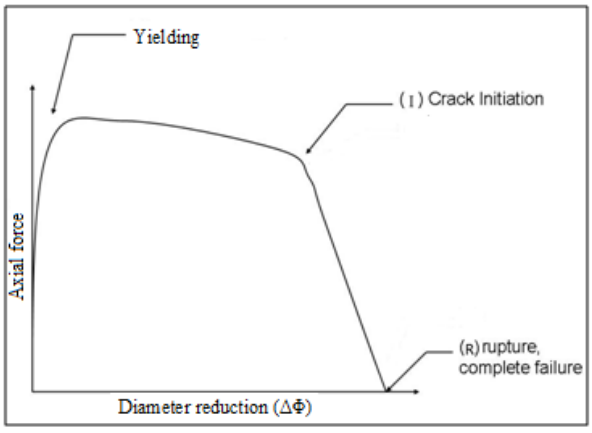

Fig. 4.10 schematic diagram for the axial force Vs diameter reduction showing the desired interruption stage (crack initiation stage) and the fracture stage.

In particular, the values of $\bar{\varepsilon}$ at crack initiation and complete failure are denoted by $\bar{\varepsilon}_i$ and $\bar{\varepsilon}_f$ respectively. The crack initiation strain can be found from the (stress-mean strain) diagram at the initiation point which can be determined by the sudden change in the slope of the loading response.

In this study some of the notched bar samples were tested up to fracture to study the full behavior of the notched samples up to fracture, to explore the fracture surfaces and relate them to the ductile fracture mechanisms, and to measure the fracture (final) strains ($\varepsilon_f = 2\ln (A_o/A_f) = 2\ln (\Phi_o/\Phi_f)$ and the initiation strains. Some specimens were unloaded at fracture initiation or during crack propagation and then sectioned along a meridian plane. In such bars with internal cracks, sectioning by EDM was used to avoid bar failure. Those interrupted samples were used to investigate the crack initiation and propagation mechanisms, and to find the crack initiation strain (ε_i).The fracture strain can be found from the (stress-mean strain) diagram at the fracture point. Another method to find the fracture strain that is used in this study is by measuring the initial diameter of the sample before the test Φ_o and measure the final diameter after the fracture Φ_f then using the relation ($\varepsilon_f = 2\ln (\Phi_o/\Phi_f)$) to find the fracture strain. The second method was used to find the fracture strain in the case of the smooth bar samples.

Two types of notched geometries were used, each geometry was identified by the parameter ζ with $\zeta=10R/\Phi o$ where R is the notch notched curvature radius, and Φo is the initial diameter of the notched region (minimal section diameter). Based on the definition ζ , decreasing the value of ζ corresponds to an enhancement of the stress triaxiality state. In our study we introduced two types of notched bar samples, shallow

with the value of ζ equal to 10, and sharp with the value of ζ equal to 2. The results of the shallow bars were discussed first. Moreover, it is worth mentioning that it was not possible to test some samples up to fracture point with the existence of the radial extensometer since the extensometer does not measure more than 22% radial strains. So that the extensometer was removed at some stage of the loading process then the sample was loaded without the extensometer up to fracture like the sample pointed by the arrow in Fig. 4.11.

4.3.1 Shallow Notched Bars

Figs. 4.11 show the mechanical response of the shallow notched bars made of the billet 1. The radial strain of the samples made of billet 1 is around 20% at the point when the test was interrupted. The radial strain was found to be between 18%-22% for billet 2, and 20% for billet 3. From these values it can be seen that there is no significant variation in the radial strain at the crack initiation between the three billets, except some samples that showed different behavior such as the one marked with the arrow in the case of billet 1. In the case of this sample the initial diameter of the sample is 3.4mm which is less than what it should be (3.9mm) because of machining problems. Therefore, it was not possible to keep the extensometer mounted to the sample up to fracture and the radial extensometer was removed when the radial strain was around 0.04. The fracture strain of this sample is 1.06 Table 4.2.

Fig. 4.12(a) shows the stress-strain response of billet 2 whereas (b) shows a typical stress versus mean strain diagram of shallow notched bar samples made of billet 2. The

same curve was plotted for both billets 1 and 3 to find the initiation and fracture strains of each sample from each billet. Table 4.2 and C.1 show summary of these values. Based on the values in Table 4.2 it can be seen that the initiation strain is always less than the fracture strain in the shallow bars made from the three materials. Moreover, the initiation strain and the fracture strain in both billets 1 and 3 look similar to some extent (fracture strain has the value of around 1 and the initiation strain has a value around 0.4). In addition, there is no significant difference in the initiation strain between billet 1, 2 and 3, but the fracture strain is less to some extent in the case of billet 2.

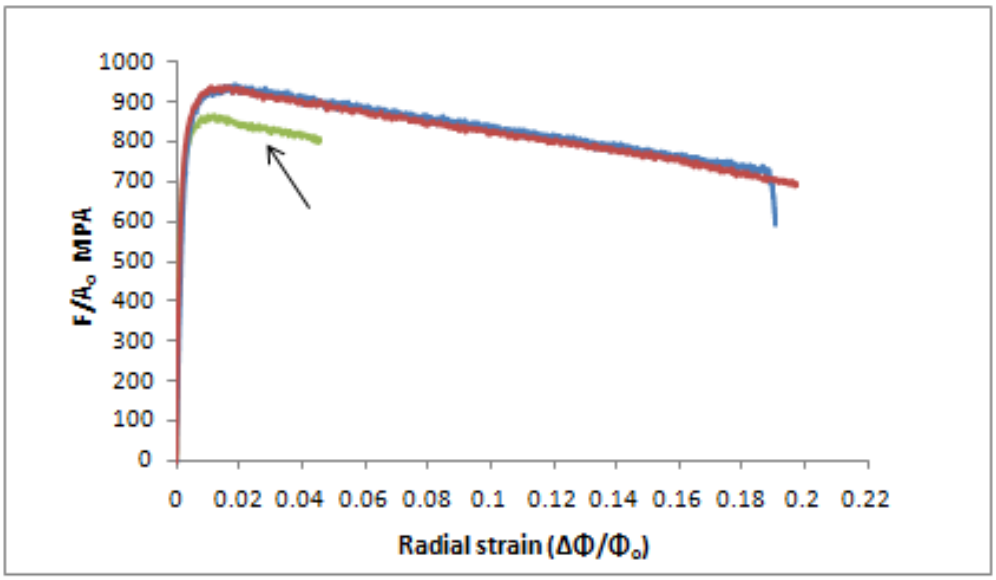

Fig. 4.11 Stress-strain diagram for 3 shallow notched bar samples made of UFG-IF steel fabricated at room temperature and extrusion rate of 0.1in/sec using route 8Bc (billet 1).

The variation in the response between samples made of the same billet could be as a result that the fracture is always scattered and it is not deterministic. Another reason of this variation could be as a result of the non-uniform temperature distribution during the

extrusion in the case f billet 2. Finally, it could be as a result of the existence of the defects inside the material.

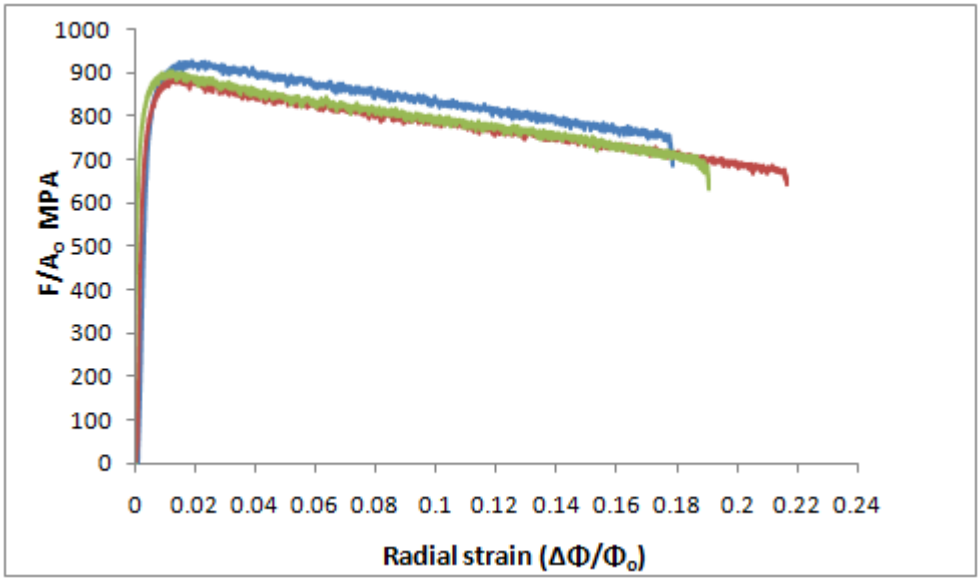

Fig. 4.12 (a) Stress-strain diagram for 3 shallow notched bar samples made of UFG-IF steel fabricated at 200C^o and extrusion rate of 0.1in/sec using route 8Bc (billet 2).

Based on the shallow notched bars' results including Fig.4.13, it can be concluded that the fracture strain is higher than the initiation strain of each individual billet. Moreover, the general response of billet 1 and billet 3 looks similar since they have similar grain size to large extent. For example, the UTS values of samples made from both billets1 and 3 are higher than 800MPa, where as it is 700MPa for billet2. Moreover, the initiation strain of samples from both billets1 and 3 is around 0.4, where as it is a little bit higher for billet2 (0.45-0.5). This is because billet 2 has higher grain size than billets1 and 3 to some degree; therefore, it is expected to show more ductility and less UTS than billets1 and 3.

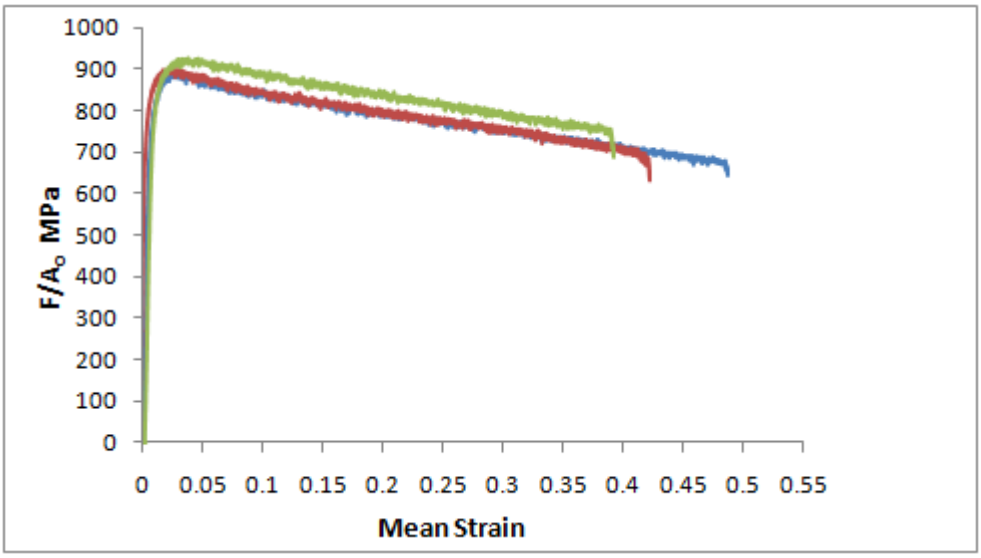

Fig. 4.12 (b) Stress-mean strain diagram for 3 shallow notched bar samples made of billet 2.

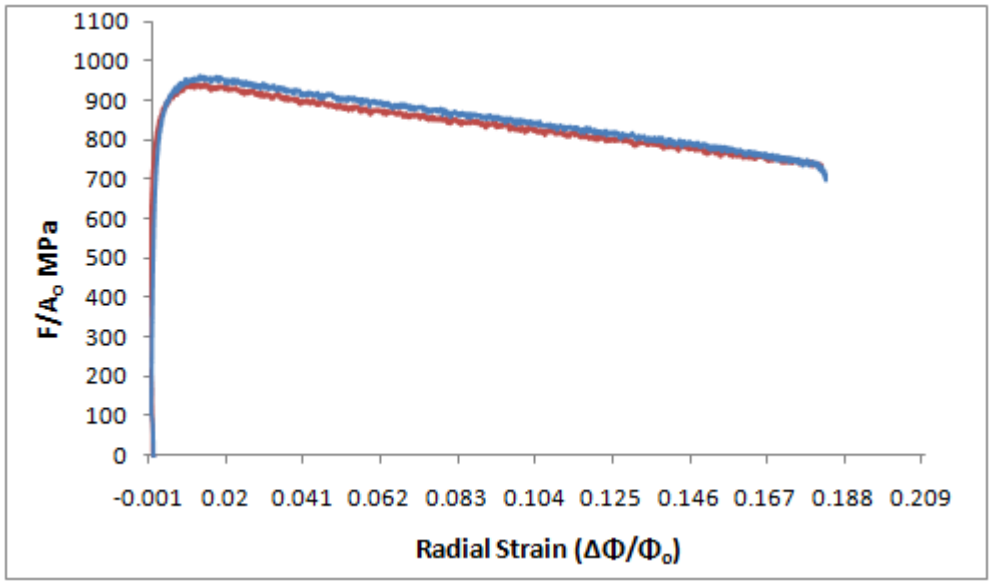

Fig. 4.13 Stress-strain diagram for 2 shallow notched bar samples made of UFG-IF steel fabricated at room temperature and extrusion rate of 1in/sec for the first four passes, and 0.5in/sec for the second four passes using route 8Bc (billet 3).

4.3.2 Sharp Notched Bars

Figs. 4.14- 4.17 show the mechanical response of the sharp notched bar samples made of the three billets. It is seen that the radial strain at fracture of the samples made of billet 1 is around 20%. The radial strain is between 24-25% for billet 2, and is 20% for billet 3. From these values it can be seen that there is no significant variation in the radial strain between the three billets, except a small difference of 4% in the case of billet2, which could be a result of the bigger grain size in this material.

Fig. 4.15 shows a typical stress-mean strain diagram of sharp notched bar samples made of billet 1. The same curve was plotted for both billets 2 and 3 to find the initiation and fracture strains of each sample from each billet. Table 4.2 and C.1 show a summary of these values. Based on the values in Table 4.2 it can be seen that the initiation strain is always less than the fracture strain in all the sharp notched bars made from the three billets. The average value of the initiation strain is almost the same in the case of billet 1 and 2 (around 0.2), but is found to be higher to some extent in billet 3 (0.27). The average value of the fracture strain, which is around 0.45-0.5, is almost the same for the three billets. Thus it can be concluded that there is no significant difference in both the initiation strain and the fracture strain between the sharp notched bars in the three billets.

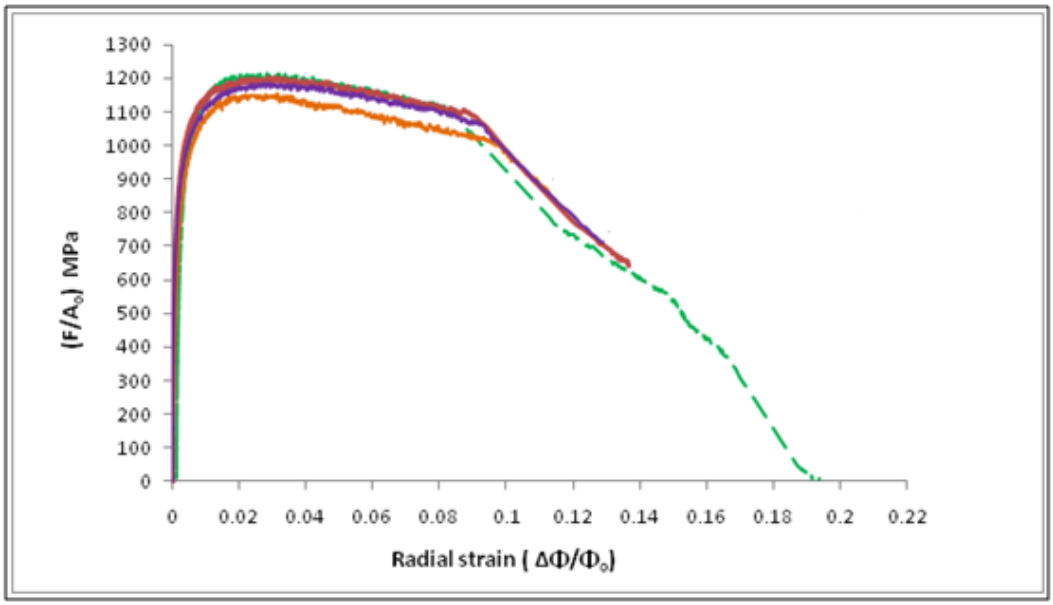

Fig. 4.14 Stress-strain diagram for 4 sharp notched bar samples made of billet 1.

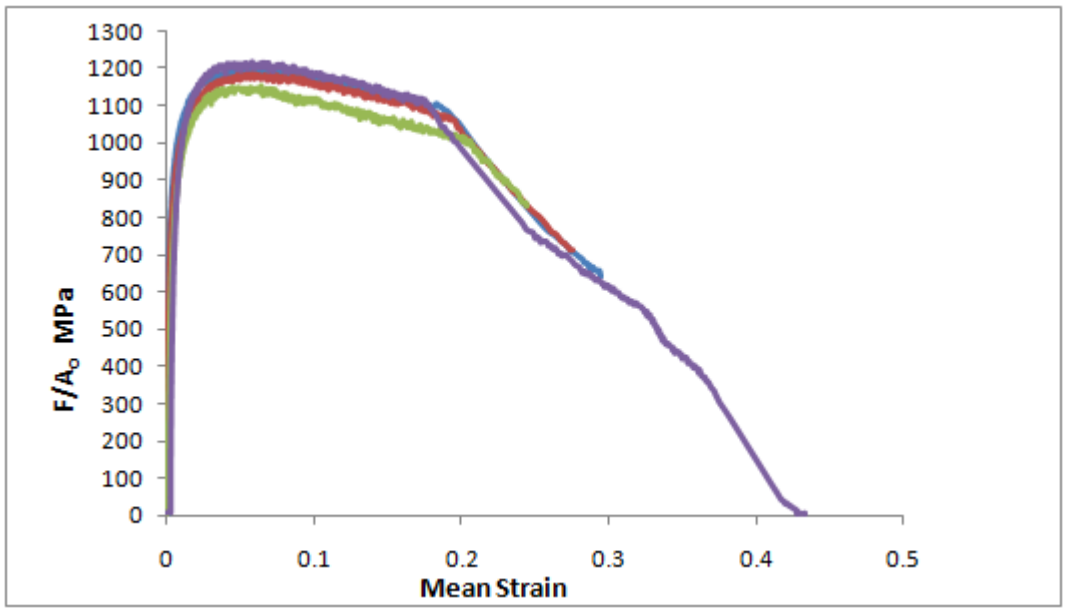

Fig. 4.15 Stress-mean strain diagram for 4 sharp notched bar samples made of billet 1.

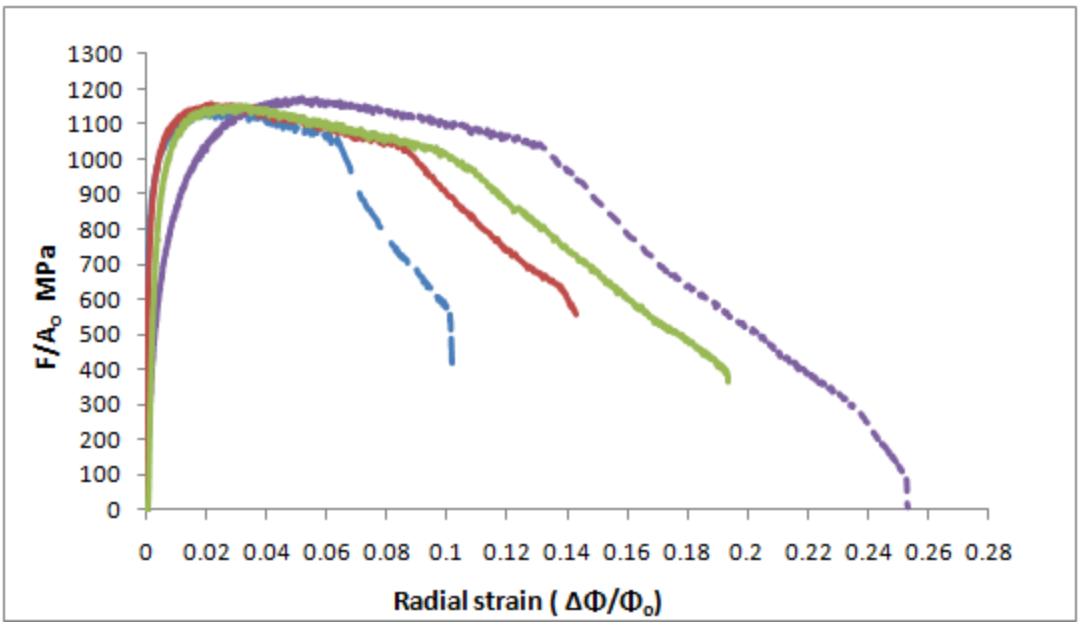

Fig. 4.16 Stress-strain diagram for 4 sharp notched bar samples made billet 2.

It can be noticed that there is a slight variation in the initial diameter of the sharp notched bar samples made of billet 2, and this can be seen in Table B.1. The variation in the response between samples made of the same billet could be as a result that the fracture is always scattered and it is not deterministic. Another reason as we mentioned earlier is the non-uniform temperature distribution in billet 2 during the extrusion.

Based on the sharp notched bar samples' results, it can be concluded that the fracture strain is higher than the initiation strain for each individual billet. Moreover, the general response in the matter of both the initiation strain and the fracture strain looks similar to the three billets.

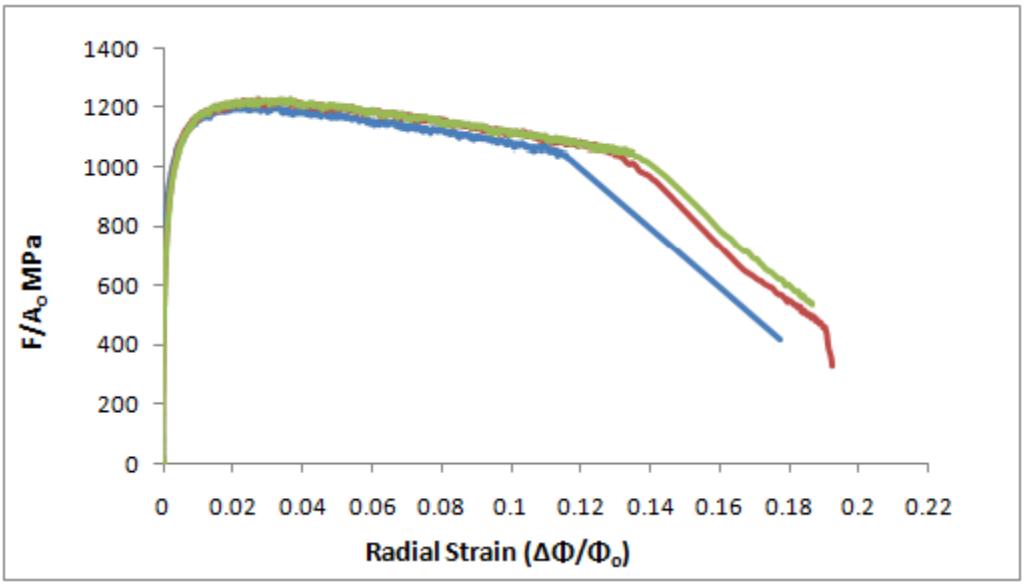

Fig. 4.17 Stress-strain diagram for 3 sharp notched bar samples made of billet 3.

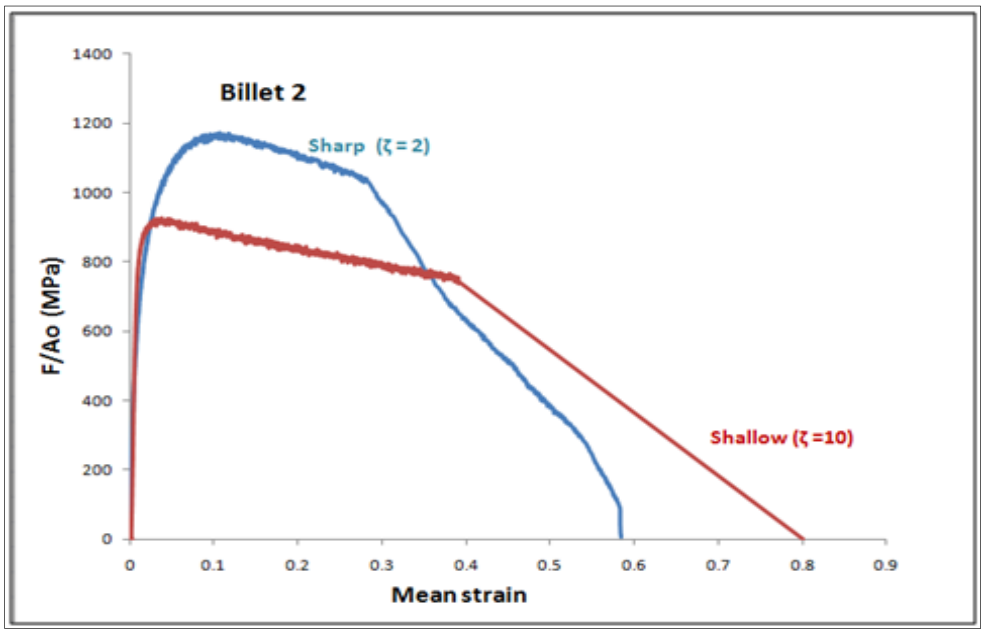

Fig. 4.18 Stress-mean strain diagram for samples made of billet 2 with different notch sensitivities.

Finally, based on the previous discussion and on Table 4.2 it can be concluded that:

(a) The fracture strain defined as the mean strain to failure is larger in smooth tensile bars than in notched bars. Sharp notched bars exhibit the lowest fracture strain.

(b) In all materials, the fracture strain is always significantly higher than the initiation strain for a given notch sensitivity ζ.

(c) There was no significant difference in the fracture strains among the UFG materials despite the variation in strength by more than 150MPa. This combination of strength and fracture property, represented by conventional ductility (elongation) and notch ductility is remarkable.

(d) Finally, from Fig. 4.18 we noticed that for a given material, the sharper the notch (ζ=2) the lower the fracture strain. Higher values of the measured axial stress are due to notch-induced stress concentrations. It is emphasized that the Von Mises equivalent stress (in the average sense) would be smaller for the sharp notch than for the shallow notch (CF. Modeling in chapter 5).

Table 4.2
Summary of the samples mean strain to failure

		Mean Strain to failure	
Material (Billet)	Specimen type	Initiation strain ($\overline{\varepsilon i}$)	Fracture (Final) strain ($\overline{\varepsilon f}$)
1	Smooth	-	1.44
		-	1.44
		-	1.39
	Shallow	-	1.06
		0.41	-
		0.43	-
	Sharp	0.19	0.446
		0.2	-
		0.2	-
		0.19	-
2	Smooth	-	1.49
		-	1.29
		-	1.44
	Shallow	0.4	-
		0.38	0.76
		0.47	-
	Sharp	0.22	-
		0.25	0.575
		0.12	0.435
		0.18	-
3	Smooth	-	1.29
		-	1.39
	Shallow	0.39	-
		0.39	0.94
	Sharp	0.27	0.46
		0.27	-
		0.25	0.395

4.4 Fractographs of Fracture Surfaces and Stable Crack Growth.

Fractography is the study of fracture surfaces of materials. Fractographic methods are used to determine the root cause of failure in engineering structures and to develop theoretical models of crack growth behavior. One of the aims of fractographic examination is to determine the cause of failure by studying the characteristics of a fracture surface, which can be used to help identify the failure mode. However, some times the overall pattern of cracking can be more important than a single crack.

An important aim of fractography is to examine how the crack initiates. Initial fractographic examinations are commonly performed on a macro scale using optical microscopes. Macro scale examinations allow us to determine the nature of failure and in some cases the causes of crack initiation and growth if the loading pattern is known. Common features that may cause crack initiation are inclusions, voids, points of stress concentration such as the triple junctions between grains, shear band intersections and other types of defects. This is because higher stress concentration enhances the void nucleation because it leads to decohesion between the source of the stress concentration and the material matrix. In many cases, fractography requires examination at a finer scale, which is usually carried out using SEM. Using SEM enables finer details to be easily recognized. Moreover, a method known as Energy-Dispersive Spectroscopy (EDS) can be performed using SEM, which enables small areas of the sample to be analyzed for their elemental distribution. The energy of the X-ray photons is used to characterize them. Each beam electron/atom interacting with the material's atoms produces a photon with an energy that is characteristic of that particular element.

In this study, fractographs of both the broken and the interrupted notched bar samples are taken using Quanta 600 SEM to investigate the fracture surfaces and to analyze the damage sources in the UFG-IF steel. Quanta 600 SEM is used since the magnification of the available optical microscope (150X) cannot resolve the fine details of the damage mechanisms. EDS is used to analyze the chemical composition of the second phase particles in the material so as to characterize the cause of damage in the material. In this section we present the results in the following order. We start with the fracture surfaces and the crack propagation surfaces of the shallow notched bar samples. Next, we discuss the fracture surfaces and crack propagation for the sharp notched bar samples. Multiple sets of images are presented for most of the samples since they are important in analyzing the fracture mechanisms. To make it easier to follow up between the discussion and introducing the images, the discussion of the both the shallow and the notched bar samples will be introduced first, then the images will be following the discussions, also, the most important images will be included after the discussion where other images that show similar ideas to what we present in the discussion are included in Appendix D. In addition, the EDS spectra of each group of fractographic images will be included in Appendix E. In the discussion, we will refer to each group of spectra by its figure number in Appendix E.

4.4.1 Shallow Notched Bars[1]

Figs. D.1 and D.2 show the fracture surfaces of a broken shallow notched bar sample of billet2. Fig. D.3 shows EDS spectra of the pointed particles in the

[1] For convenience all fractographs are shown in appendices D and E.

fractographs. The first observation is that the typical cup and cone shape of the fractured specimen can be seen in the center of Fig. D.1 . Also, the finer scale images around the central image show ductile fracture surfaces that have a rough and irregular appearance containing many microvoids and dimples. These observed microvoids and dimples in the fractograph are signatures of the original voids that coalesced to initiate the crack responsible for the failure of the sample. Another important observation is that there are voids of various sizes in the fractographs. The large void at the center of the broken sample is believed to be the cause of the failure. This feature is common in all the broken shallow samples representing the three billets. Most of the images show that the majority of the big voids have some particles inside them where as the majority of the small voids does not. It is believed that the big voids result from second phase particles even though the material contains very little alloying elements. As seen in Figs. D.1, D.2 and D.3, these particles have Aluminum, Titanium and Carbon in their composition. However, we know that Titanium exists in the IF steel to capture the carbon and form titanium carbides in order to make the steel interstitial free. Therefore, it is believed that this titanium and aluminum are titanium oxides, titanium carbides or aluminum oxides, and they cause the big voids to form, as can be seen from Fig. D.2. However, some of the spectra show only iron, which means that not all of the particles inside the big voids are second phase particles. Moreover, Fig. E.2 shows a crack formed inside the fracture surface. It is expected that this crack has formed from the coalescence of big voids since there are two big voids on its edges.

Figs. D.4 to D.11 show the crack initiation and propagation fractographs of the shallow notched bar samples made of the three billets. Some of the images are taken after polishing the samples and without etching, while the others are taken after polishing and etching the samples to explore the manner in which the crack propagates through the material, since this can give detailed insight into the mode of fracture. As seen in Figs. D.4-D.6 the crack has grown in size significantly since this sample is interrupted at late stage in the loading curve. The epoxy used to mount the samples fill the cracks in most of the samples. The epoxy can be distinguished easily since it is glowing in the images as indicated by the circle in Fig.D.4. The images taken at the crack edges show a large number of microcracks. Some of them have sizes similar to the grain size of the material and hence they appear to be intergranular cracks. It is believed that these cracks keep growing and propagating to cause the failure of the sample. Moreover, it can be seen in Fig. D.5 and D.6 that the cracks are intergranular and the grains bend around the crack. Unfortunately, this could not be seen clearly from the shown images although it could be seen while using the SEM microscope, or by observing the exact image in its original size. This is due to the difficulty in controlling the focus and the contrast while taking fractographs, since the surface is not smooth. Some alloying elements particles like titanium, aluminum, sulfur, copper and silicon can be distinguished inside the cracks by observing the associated spectra; see Figs. D.3 and D.8. These alloying elements could play role in the crack initiation and propagation inside the material. These elements are not found in the form of pure titanium or pure copper. This is expected since there is carbon in the chemical composition of the IF steel

so that the titanium/aluminium atoms could form carbides or oxides. However, although sulfur was found in small percentages, it could form manganese sulphides (MnS) to act as second phase particle that causes void nucleation [45]. Furthermore, both Figs. D.5 and D.6 show many ridges/steps appear on the surface of the sample. By observing these ridges at a finer scale it can be seen that they consist of many microcracks. These ridges/steps appear to be step-like shear bands [44]. Hence, these step-like shear bands could be considered as the source of void nucleation and crack propagation.

Fig. D.7 shows the fractographs of the shallow notched bar sample made from billet 2. This sample did not show significant crack initiation and propagation; instead it shows a clear coalescence of the voids. This could be due to the following reasons. First, it could be as a result of the test interruption at an early stage of loading so that no significant crack propagation can be observed, but coalescence of the voids is obvious in some of the images. Second, since billet 2 showed more elongation to failure compared to billet 1, so that the cracks will not propagate in billet 2 samples as significant as the samples from billet1. The first observation on the figure is that there are second phase particles such as Ti, Al, S, Si, N, and Cu as seen in Fig. D.8. These elements are expected to be in form of carbides and oxides, i.e in the form of titanium oxide, titanium carbide, titanium nitride, aluminum oxide, or manganese sulphides. It worth mentioning that there is silicon in the composition analysis as well, and the chemical composition of the IF steel contains silicon. Moreover, as we used the colloidal silicon to smear-out the voids; we expect that some of the silicon comes from the sample preparation as well. However, aluminum has not been used in the preparation of the sample and hence the

existing aluminum in the EDS investigation is expected to be from inherent second phase particle in the IF steel. Therefore, it is expected that these second phase particles will lead to void nucleation. Second, the necking mode of the void coalescence could be seen in the fractographs.

Figs. D.9 to D.11 show fractographs of the interrupted shallow notched bar sample 3T6-I. Fig. D.9 shows the sample after the first stage of polishing and without etching. In this image not many details can be seen except some initiation and coalescence of voids around the centre of the sample. Figs. D.10 and D.11 show more details after more polishing and etching the surface of the sample. A big void can be seen at the center of the sample and a crack is propagating from it. When analyzing the composition of this void, Fig. F.9, it has been found that it has Fe, Al, and Oxygen. Hence, two possibilities of the source of void nucleation may be expected. Either the aluminum oxide causes the voids to nucleate as a result of decohesion between the particle and the matrix, or there are internal defects in the material, such as the ones in Fig. D.12, that causes the void to nucleate. When investigating the crack at a finer scale, it can be seen that it consists of several microcracks joined together along the length of the crack. In addition, one can see that the nucleation is concentrated at the central region of the sample, where the stress triaxiality is found to be the highest which leads to faster void growth. Nevertheless, this does not rule out the possibility of nucleation on the edges.

Finally, it can be concluded that the voids in the shallow notched bar samples could be nucleated as a result of two sources. The first source is second phase particles that debond from the matrix, which could be titanium carbides, titanium oxides, aluminum

oxides, titanium nitrides, or even manganese sulphides. The second source is the step-like shear bands intersecting with each other, or their intersection with the grain boundaries, tripple junctions, void clustering, or internal defects as seen in Fig. D.12. It can be seen that the void nucleation usually occur at the center of the sample since the maximum stress triaxiality is expected at the center of the sample. But this does not prohibited the nucleation of the voids at any other places on the sample as we have seen in some of the samples. Moreover, the crack initiation and propagation features observed in the samples are affected by the stage where the test has been interrupted, since each stage of the interruption represents certain stage in the void nucleation and crack propagation processes. In addition, several polishing trials were done in order to reveal the fracture mechanisms in the material, since each trial reveals certain features in different planes of the material.

4.3.1 Sharp Notched Bars[2]

Figs. D.13 to D.16 show the fracture surfaces of the three broken sharp notched bar samples which represent the three billets. Figs. D.17 to D.21 show the crack propagation of the interrupted samples from the same three billets. The first observation from figures D.13 and D.15 is that the broken samples have the typical cup and cone shape expected in ductile fracture. In addition, finer scale images around the central image show ductile fracture surfaces, which have a rough and irregular appearance due to the presence of many microvoids and dimples. Another important observation is that there are small voids and big voids in the fractographs, but unlike in the shallow notched samples there

[2] For convenience all fractographs are shown appendices D and E.

is no big void at the center of the broken sample except in Fig. D.13. Even in this case the void is smaller than the one found in the shallow notched bar and is not located exactly at the center of the broken sample. Moreover, there are more big voids in the fractographs of the sharp notched bar samples compared to the shallow ones. Similar to the case of the shallow notched samples, most of the images show that a majority of the big voids have some particles inside them while the majority of the small voids do not. It is believed that the big voids result from second phase particles even though this material has very little alloying elements. But this time they have titanium particles only as seen in Fig. F.10. It is expected that they are titanium carbides or titanium oxides since the spectrum also shows the presence of carbon in small quantities. Some spectra only show Fe in the composition analysis, implying that not all of the particles inside the big voids are second phase particles. Therefore, there are other sources of the void nucleation other than the second phase particles. Moreover, some images show some shearing features such as Figs. D.13 and D.14 where small voids are arranged in traces. In this case it is expected that intersection of the shear bands with grain boundaries or other defects may cause the voids to nucleate.

Figs. D.17 to D.21 show crack propagation in the sharp notched bar samples. Some of the images are taken after polishing the samples and without etching while the others are taken after polishing and etching the samples to explore the manner in which the crack propagates through the material, since this gives great insight into the mode of fracture.

It is seen that the crack has grown in size significantly since this sample is interrupted at late stage in the loading curve. The epoxy can be seen trapped inside some of the cracks in the notched samples. The first observation is the zigzag shape crack. This feature is common in all of the interrupted sharp notched samples. The zigzag path is not an inherent feature of ductile crack growth. It only occurs in specific planes where the main mechanism that driving the crack to initiate and propagate relies on successive coalescence events in the internal necking mode. The internal necking mode can be clearly seen in Fig. D.7 for the shallow notched samples.

SEM fractographs are taken around the crack edges/tips to explore the sources of crack initiation and propagation. These fractographs show the presence of a large number of voids around the crack tips on either side. These voids show many important features of the fracture mechanism in this sample. First, it can be seen that most of these voids has particles inside them. When analyzing the composition of the particles it has been found that some of them are Fe while the others show Ti, Si, Cu, Zn and C; see Figs. D.18 and D.19. It is believed that the second phase particles TiC, Al2O3, TiO, TiO2 or silicon carbides cause the nucleation of some of the larger voids. However, Si can be seen many times in the composition analysis of the particles, which could be considered as a source of void nucleation, but since it was used for the sample preparation as well. However, aluminum oxide particles could be considered a source of void nucleation since it has not been used in the sample preparation.

Moreover, some voids do not show second phase particles, which means that there are other sources of void nucleation such as triple junctions between the grains,

vacancies, or the intersections of shear bands. Furthermore, Figs. D.18 and D.20 show important details about the way the crack propagates through the material. First, the crack seems to be intergranular since it propagates along the grain boundaries, and in some cases the grains bend around the crack, or the crack is propagating in a circular shape around the grains. Second, the voids coalesce in internal necking mode. Third, one can be seen that the microcrack in Fig. F.15 looks like a ridge, which indicates the existence of a step-like shear band in that position that intersects with some source of defects or with grain boundaries.

Moreover, it can be seen in Fig. D.20 and D.21 that there are microcracks connecting the two big voids to ease the propagation of the crack. This feature could be similar to what is so-called the void sheet mechanisms [50], since it is expected that there is a group of small voids that coalesce to form this microcrack which joins the two big voids together. It can be also seen that the voids are coalescing together through this microcrack through a shearing mechanism, which means that shear localization has a significant role in the fracture mechanisms in this type of samples. This is expected to be through the shear bands intersections with grain boundaries or with some defects in the material. In addition, the composition analysis of this sample indicates that the titanium carbide particles could play a role in void nucleation as well. Moreover, based on Figs. D.21 and D.22, the particle containing copper causes the first void to nucleate and coalesce with the other voids. It also shows the microcrack connecting the two big voids and the way the voids coalesce together in a necking mode.

Finally, it can been concluded that the voids in the sharp notched bar samples could be nucleated as a result of second phase particles such as titanium carbides, titanium oxides, aluminum oxides and manganese sulphides deboning from the matrix. However, shear bands could be considered as a source of void nucleation. Additionally, it can be seen that void nucleation usually happens at the center of the sample where the stress triaxiality is maximum. But this does not prohibited the nucleation of the voids at other locations. Moreover, it can be seen that the cracks in the sharp notched samples propagate further and have a larger size compared to the shallow ones since the stress triaxiality is more than in the shallow ones. And this justifies the reason behind the initiation of the crack at smaller strain values in the case of the sharp notched bars when compared to the shallow ones. It is worth mentioning that several polishing trials were done in order to better reveal the fracture mechanisms of the material, since each polishing trial reveals some new features in certain planes of the sample.

It can be concluded that the highest percentages of the alloying elements that causes the voids to nucleate are Ti, Al, and Si which could form carbides or oxides. However, S, Cu, Mg, C appear less in the EDS analysis. Shear bands and triple junctions are other sources of void nucleation.

CHAPTER V

MODELING THE ELASTO-PLASIC RESPONSE OF NOTCHED BARS

5.1 Introduction

The objective of this chapter is to model the deformation of notched axisymmetric bars with different notched radius subjected to uniaxial loading. The elastic and elasto-plastic regimes are investigated using ABAQUS software of UFG-IF Steel which was under room temperature and a strain rate of 0.1in/s (billet 1).

The experimental data collected from the tensile test of the smooth bar specimen are used to characterize the material's properties (Young's modulus, Poisson's ratio, initial yield stress, post yield behavior, yield offset (α), etc) corresponding to a chosen model. Tensile test simulation is then carried out for two notched bar featuring two different notched radii, the shallow and the sharp. The model that associate Von Mises (J2 flow theory) with Ramberg-Osgood hardening law was used to describe the nonlinear relationship between the stress and the strain with no existence of damage.

5.2 Constitutive Model

In order to observe how the stress fields evolve around the notch, a simple elastic model using Hook's law is initially used. The results show the typical stress concentration effect around the notch in the elastic regime. As a logical first step in the plastic regime, the Von Misses model (J2 flow theory) is associated with Ramberg – Osgood hardening law to study the non linear relationship between stress and strain in materials near their yield point. Ramberg-Osgood hardening law is useful for metals that

harden with plastic deformation, showing a smooth elastic-plastic transition. This model yields relatively good approximation to the experimental results.

Pure Elasticity Model :

This model uses the basic Hook's law for the stress and the strain,

$$\varepsilon^e = \frac{1+\nu}{E}\,\sigma - \frac{\nu}{E}\,\sigma I \qquad 5.1$$

or in the inverse form $\sigma = \lambda \varepsilon I + 2G\,\varepsilon$ 5.2

where λ is Lame elastic constant, G is the shear modulus, (I) is the identity matrix, $\boldsymbol{\varepsilon^e}$ is the elastic strain and $\boldsymbol{\sigma}$ is the stress tensor. Also, λ and G can be expressed in term of E (Young's elastic modulus) and ν (Poisson's ratio) by:

$$\lambda = \frac{E\,\nu}{(1+\nu)(1-2\nu)} \qquad and \qquad G = \frac{E}{2(1+\nu)} \qquad 5.3$$

Von Mises Model:

The so-called classical metal plasticity approach in ABAQUS uses the Von Misses yield surface and the associated flow rule. The Von Misses yield criterion suggests that the yielding of the materials begins when the second deviatoric stress invariant (J2) reaches a critical value K. For this reason it is sometimes called the J2 flow theory. Also, because the Von Misses yield criterion is independent of the first stress invariant (I1) it is applicable for the analysis of plastic deformation for ductile materials such as metals.

Since the hardening behavior of the material should be described, the Ramberg-Osgood hardening law is used associated with Von Misses model to fully describe the material's

stress- strain non linear relationship. In the last equation of the Ramberg-Osgood model the hardening behavior of the material depends on the material constants α and n.

$$The\ yield\ criterion\quad f(J2) = \sqrt{J2} - K \quad or \qquad f(J2) = \sqrt{3J2} - \sigma y \tag{5.4}$$

$$The\ flow\ rule \qquad d\varepsilon^p = d\lambda \frac{\partial f}{\partial \sigma} \tag{5.5}$$

$$The\ hardening\ law \qquad \varepsilon = \frac{\sigma}{E} + M\left(\frac{\sigma}{E}\right)^n \tag{5.6}$$

$$or \qquad \varepsilon = \frac{\sigma}{E} + \frac{\alpha\sigma}{E}\left(\frac{|\sigma|}{\sigma y}\right)^{n-1} \tag{5.7}$$

Or in Generalized to multiaxial stress state

$$E\varepsilon = (1+\nu)S - (1-2\nu)pI + \frac{3}{2}\alpha S\left(\frac{q}{\sigma_y}\right)^{n-1} \tag{5.8}$$

$$where \quad M\left(\frac{\sigma}{E}\right)^n = \alpha\frac{\sigma y}{E}\left(\frac{\sigma}{\sigma y}\right)^n \tag{5.9}$$

where J2 is the second invariant of the deviatoric stress tensor, σy is the yield stress, K is the yield stress of the material in pure shear, ε^p is the plastic strain, dλ is the loading parameter, ε is the strain tensor,σ is the stress tensor, E is the Young's modulus of the material is the constant depends on the material, n is the hardening exponent, α is the yield offset is the equivalent hydrostatic stress, q is the Misses equivalent stress, S is the stress deviator, and ν is the Poisson's ratio . The material here assumes to be incompressible.

5.3 Finite Element Implementation

The simulation is carried out for smooth bar sample as a first step and then for 2 different notched bar samples (shallow and sharp). Due to the axisymmetry of the problem, only a quarter of the specimen longitudinal cross-section needs to be investigated.. A coarse mesh and fine mesh is used in order to capture the stress concentration in the vicinity of the notch and in order to see the effect of the mesh refinement on the results. Linear elements are used in all of the cases. The material parameters used for the elastic model are derived from the experimental data for the smooth bar, and they are E = 140GPa and ν=0.3.

For the Von Misses model associated with Ramberg-Osgood hardening law, the elastic and plastic regimes are defined in ABAQUS using the so-called Deformation Plasticity, where the following parameters needs to be defined: E=140GPa, ν=0.3,α (yield offset) =0.002,yield stress = 700MPa and the hardening exponent **n**.The previous values are found from the experimental data for the smooth bar specimen.

The first estimation for the hardening exponent (n) is found to be 11.5 using the optimization method by comparing the experimental strain with the one from equation 5.8 , and then use this value to simulate the smooth bar sample response in tensile test using ABAQUS software, see Fig. 5.1.

However, since the true stress - true strain data up to fracture are not available for the used smooth bar specimen (only available up to 0.02 strain), an alternate estimation (n = 25 = 1/0.042) is found by using the equation obtained by the best fit power law to the

experimental results (up to 0.02 strain) and then modifying it to match the experimental results found by Niendorf [5] of the same type of the material, see Figs. 5.2 and 5.3.

The last estimation (n = 50=1/0.022) which was not used in von misses model is also found by using the equation obtained by the best fit power law to Niendorf's experimental data, see Fig. 5.4.

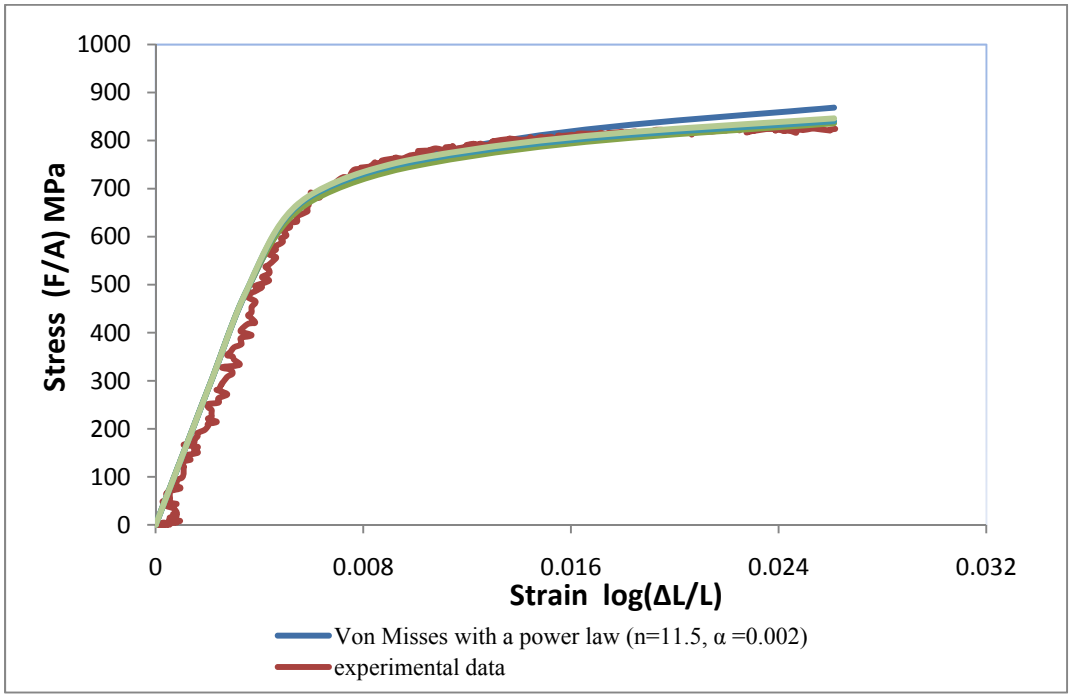

Fig. 5.1 Stress-strain diagram of smooth bar specimen made of billet 1. The young's modulus is 140GPa. The values of n were found using the least square method (several trials were done by changing the hardening exponent n and the yield offset α.

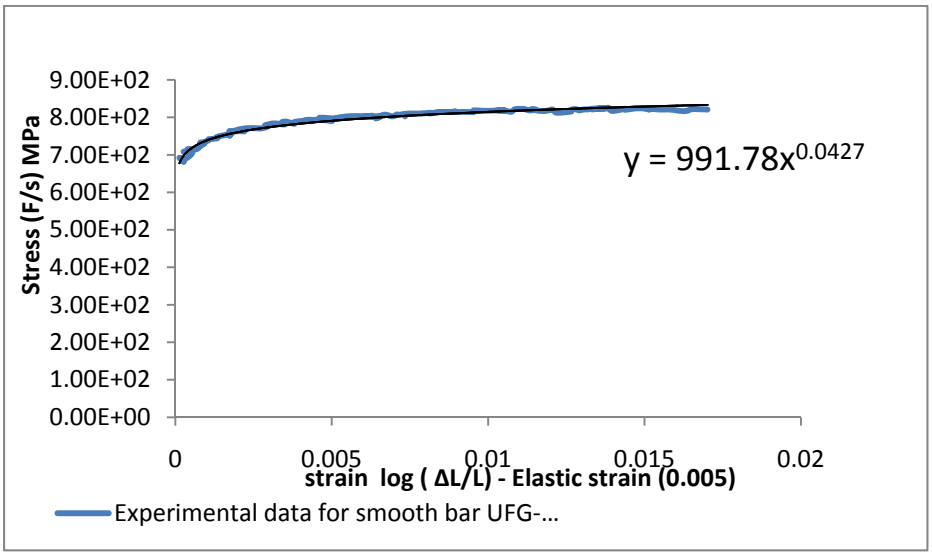

Fig. 5.2 Stress -strain diagram for smooth bar sample made of billet 1 with its best fit equation.

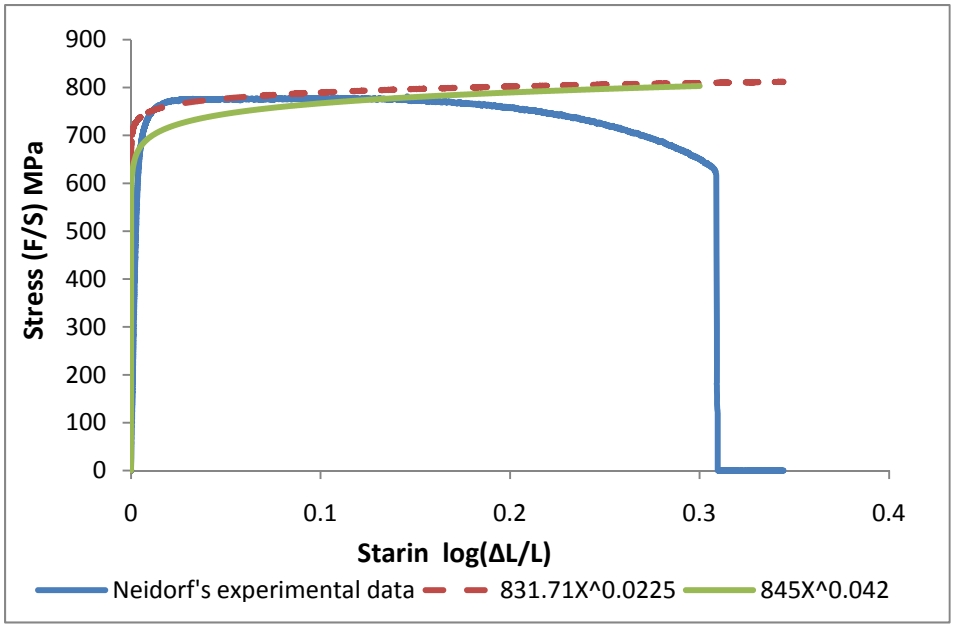

Fig. 5.3 Stress-strain diagram for Niendorf's experimental data of as compared to two fits. The experimental data taken for smooth bar specimen made of UFG-IF steel processed using route 8Bc at room temperature and strain rate of 0.1in/sec.

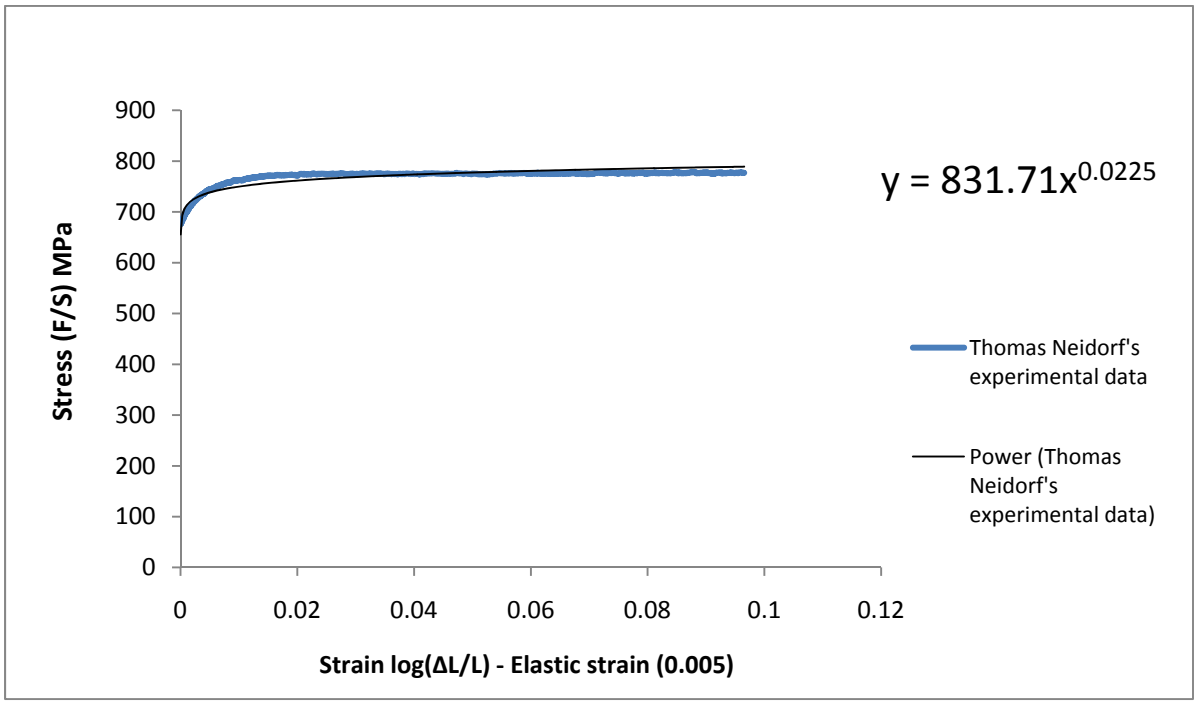

Fig. 5.4 Stress-strain diagram of Thomas Niendorf's experimental data with the best fit. The experimental data taken for smooth bar specimen made of UFG-IF steel processed using route 8Bc at room temperature and strain rate of 0.1in/sec.

5.4 Finite Element Results

As we said earlier two different mesh refinements were used in the modeling, but we will present only the fine mesh results except for some curves we will present both or one of them. This is because we have concluded after the simulation that Von Mises model is not sensitive to the mesh refinement.

As shown in Fig. 5.5 the simulation for the shallow notched bar using (n=11.5) with different mesh refinements does not fit exactly with the experimental data for the true stress (F/S) – True strain ($\Delta\Phi/\Phi$). Here F is the force, S is the current area, Φ is the current diameter, and $\Delta\Phi$ is the radial displacement. However, using (n=25) fits exactly with the experimental data for both the coarse and the fine mesh. Knowing that, the axial

stress is found as the average value of the axial stresses along the notch side, and the radial strain (ΔΦ/Φ) found at the outside element of the notched region.

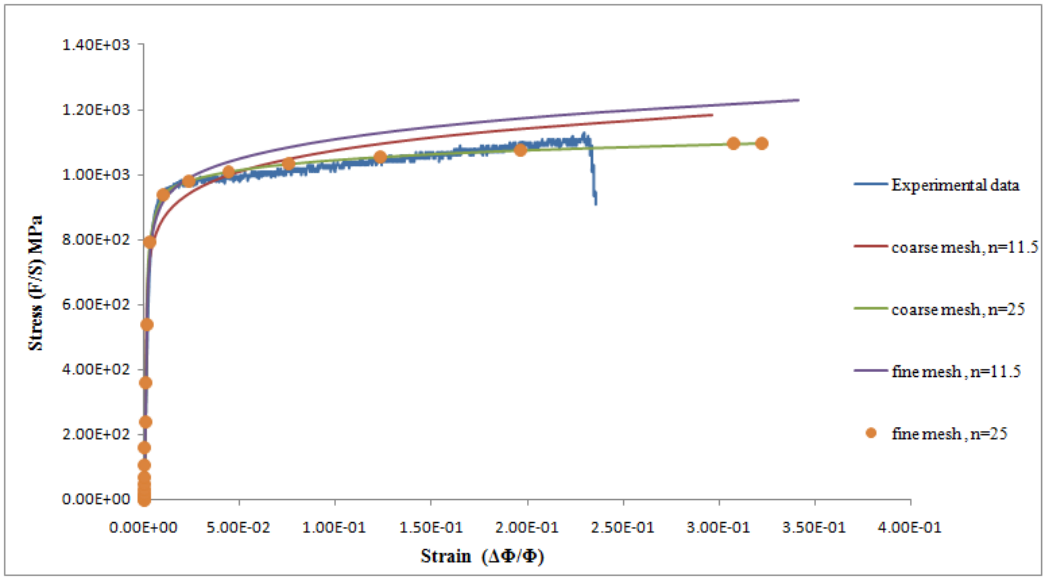

Fig. 5.5 Stress -strain diagram for the shallow notched bar sample using both experimental data and Von Misses model with Ramberg-Osgood Hardening law using different mesh refinements and power exponents.

As shown in Fig 5.6, the simulation using (n=25) with coarse mesh matches exactly with the experimental data for the engineering stress (F/S_o) –engineering strain ($\Delta\Phi/\Phi o$). Where S_o is the initial cross sectional area, and Φo is the initial diameter. In order to find the value of F (reaction forces) from the simulation, the average of the axial stresses along the notched edge is calculated and multiplied by the current area using 2D-planer modeling space instead of the axisymmetric (only in the case of finding the reaction forces). ΔΦ is found as the displacement at the outside node of the notched region.

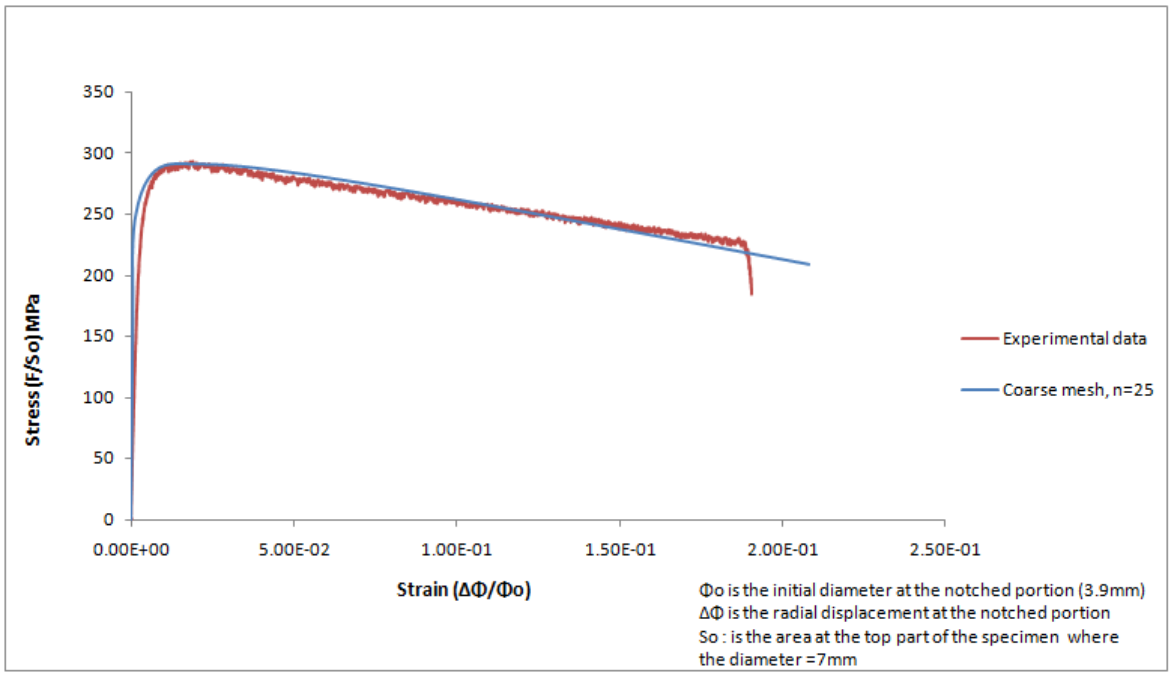

Fig. 5.6 Stress -strain diagram for the shallow notched bar sample using both experimental data and Von Misses model with Ramberg-Osgood Hardening law.

Figs. 5.7-5.10 are found by using n=11.5. Fig. 5.7 and 5.8 show the evolution of the axial stress for the shallow notched bar at the notched edge using both fine and coarse mesh. Each curve represents a stress profile along that edge at a particular time step, which is represented by the deformation ($\Delta\Phi/\Phi$) at that time step. It can be observed that the axial stress is approximately the same along the edge on the notched side in the elastic regime, but once the plastic deformation starts, there is an obvious higher level of the axial stress at the center of the specimen compared to the notched side.

As shown in Figs. 5.8 the variation of the radial stress between the center and the edge of the specimen is more even for small strain value and it is higher at the center of the specimen. So as a result of this the stress triaxiality ratio (Hydrostatic pressure/Misses

equivalent stress) is higher at the center of the specimen. This is because at the center of the specimen the hydrostatic pressure is maximum (σ11+σ22+σ33).

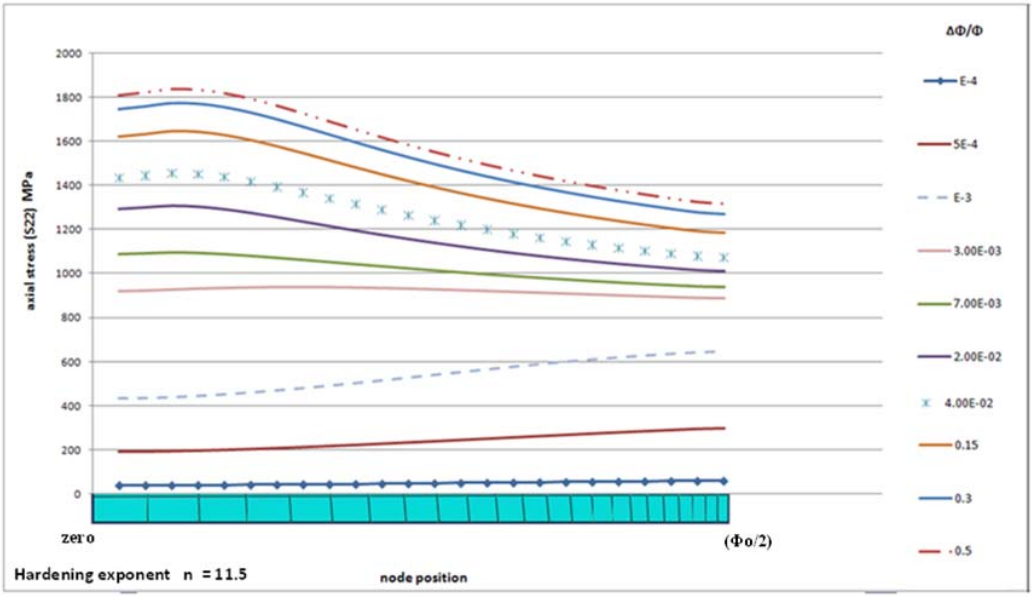

Fig. 5.7 Axial stress evolution along specimen notched side for Von Mises model-shallow notched bar-fine mesh.

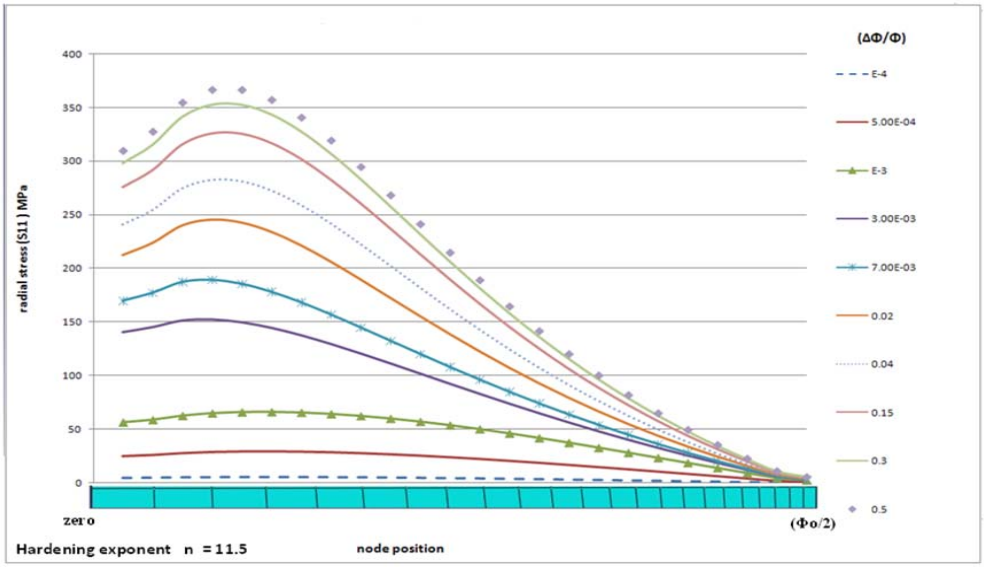

Fig. 5.8 Radial stress evolution along specimen's notched side for Von Misses model –shallow notched bar-fine mesh.

Figures. 5.9 and 5.10 show the evolution of the stress triaxiality along the shallow specimen notched side using Von Mises model. It can be seen that the maximum value of the triaxiality is located at the center of the sample, and it has a value of 0.8. As seen in both Figures there is no effect of the mesh refinement on the triaxiality value.

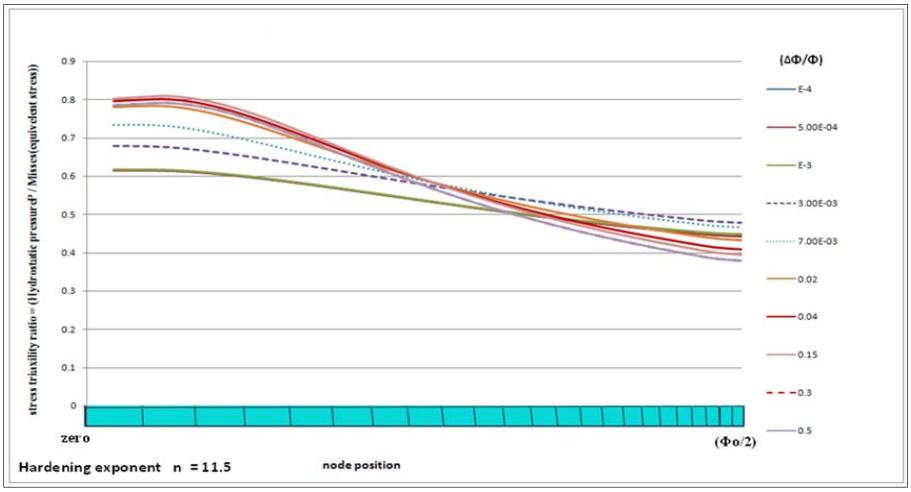

Fig. 5.9 .Stress triaxiality evolution along specimen's notched side for Von Misses model –shallow notched bar-fine mesh.

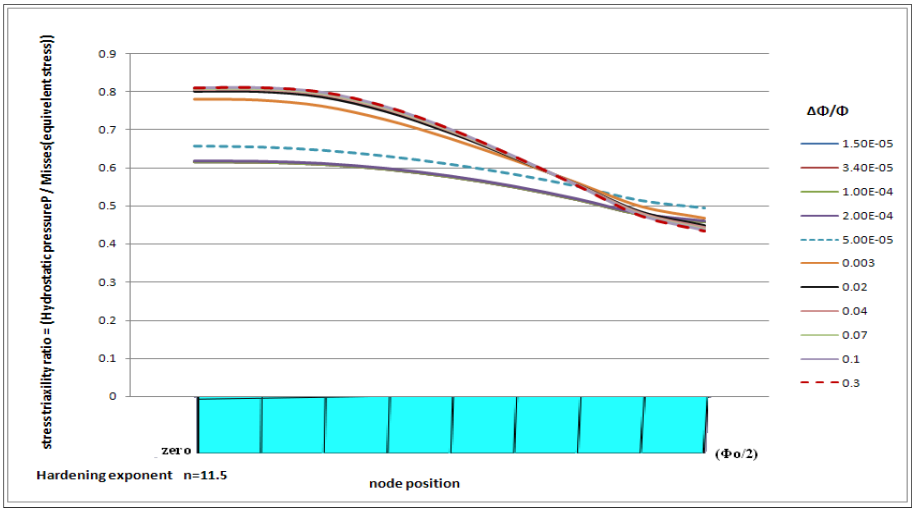

Fig. 5.10 .Stress triaxiality evolution along specimen's notched side for Von Misses model –shallow notched bar-coarse mesh.

Figs. 5.11 and 5.12 show the fine mesh of the shallow notched bars. One can see that the axial strain S22 increases with increasing the deformation, but it varies along the notched side. So it start to be maximum at the outside region of the notch away from the center at the beginning of the deformation process, and start to vary along the notched side toward the center to reach its maximum value there once the deformation increases. The same trend can be seen in the case of the equivalent plastic strain PEQQ.

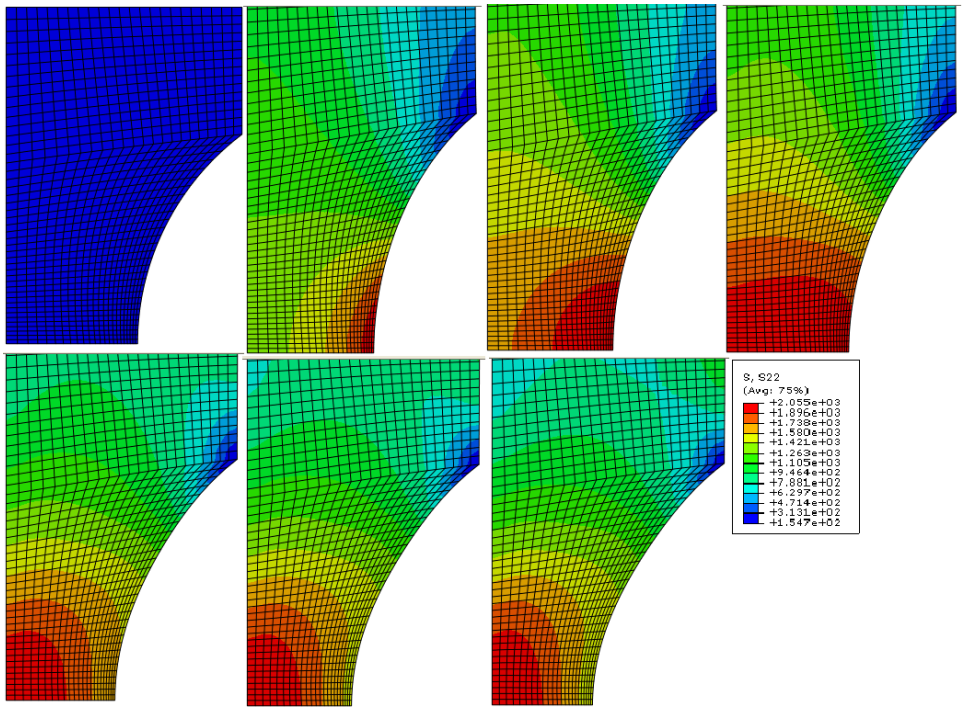

Fig. 5.11 Uniaxial stress evolution using Von Misses model for the shallow notched bar (fine mesh - hardening exponent n=11.5).

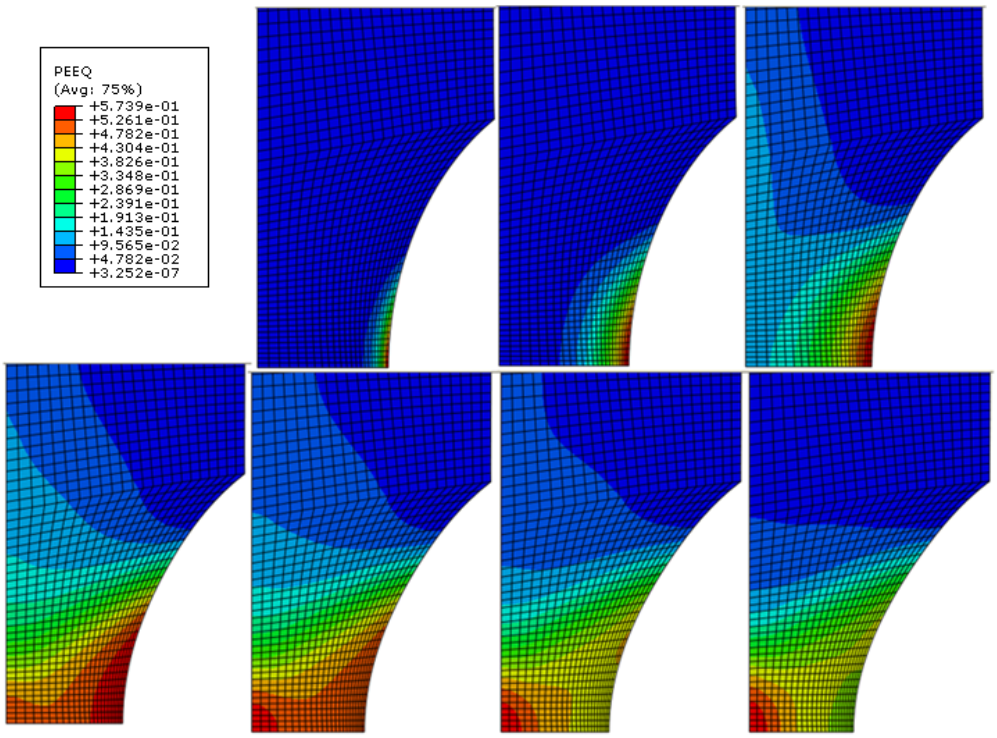

Fig.5.12 Equivalent plastic strain evolution using Von Misses model for the shallow notched bar (fine mesh - hardening exponent n=11.5).

Moreover, in the case of the sharp notched bars It is shown in Figs. 5.13and 5.14 that the results from the simulation for the sharp notched bar (n=25) using different mesh refinements fits exactly with the experimental data. But it does not fit exactly when n is 11.5.The same methodology for finding the stresses, strain, displacement and the reaction forces, used in the shallow notched bar, was used here.Based on Fig. 5.15 the simulation using (n=25) with coarse mesh matches the experimental data for the engineering stress (F/So) –engineering strain ($\Delta\Phi/\Phi o$).

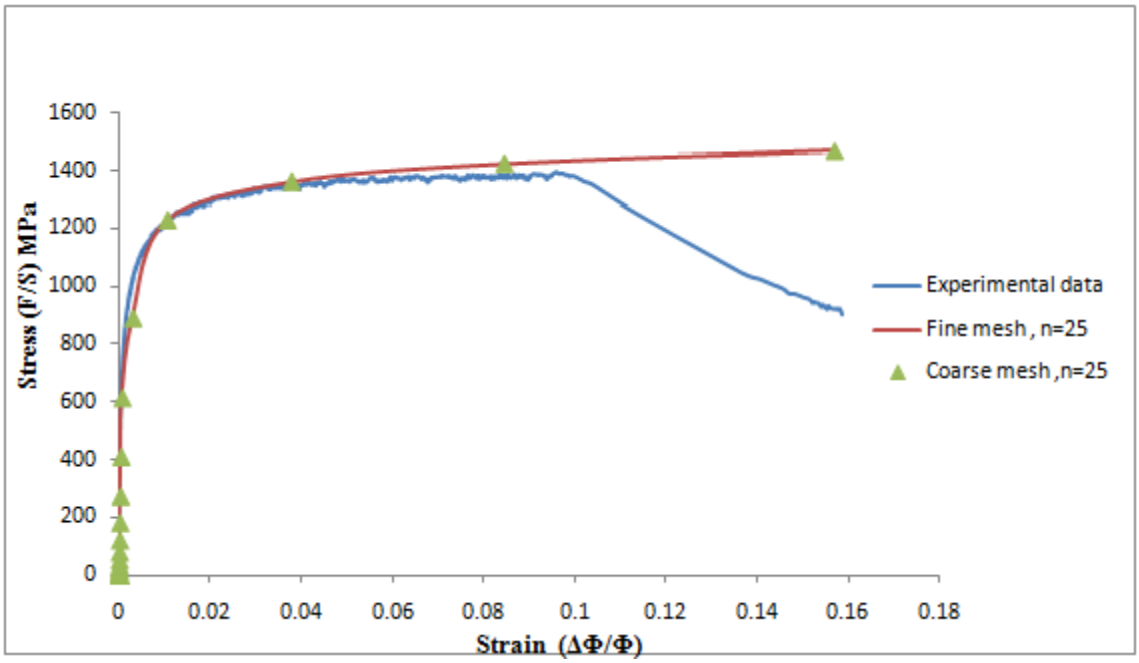

Fig.5.13 Stress-strain diagram of the sharp notched bar sample using both experimental data and Von Misses model with Ramberg-Osgood Hardening law using different mesh refinements.

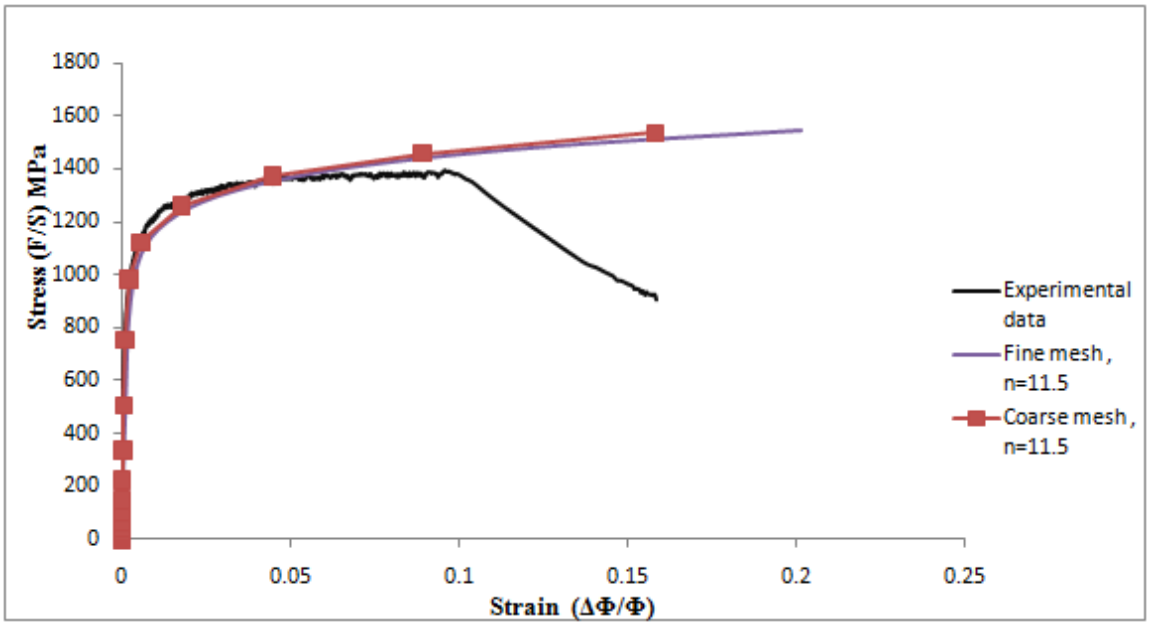

Fig. 5.14 Stress-strain diagram for the sharp notched bar sample using both experimental data and Von Misses model with Ramberg-Osgood Hardening law using different mesh refinements.

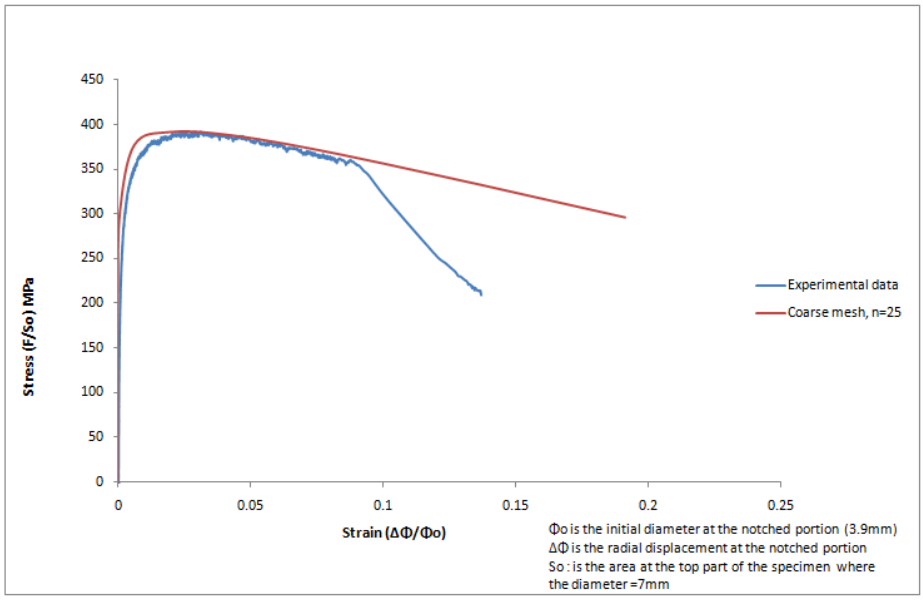

Fig.5.15 Stress -strain diagram for the sharp notched bar sample using both experimental data and Von Misses model with Ramberg-Osgood Hardening law.

Fig. 5.16 shows the evolution of the axial stress for the sharp notched bar at the notched edge using fine mesh. Each curve represents a stress profile along that edge at a particular time step, which is represented by the deformation ($\Delta\Phi/\Phi$) at that time step. It can be observed that the axial stress is approximately the same for small strain level, but it becomes higher at the vicinity of the notched side for higher strain levels. However, as shown in Fig. 5.17 the variation of the radial stress between the center and the edge of the specimen is more even for small strain value, and it is higher at the vicinity of the center of the specimen.

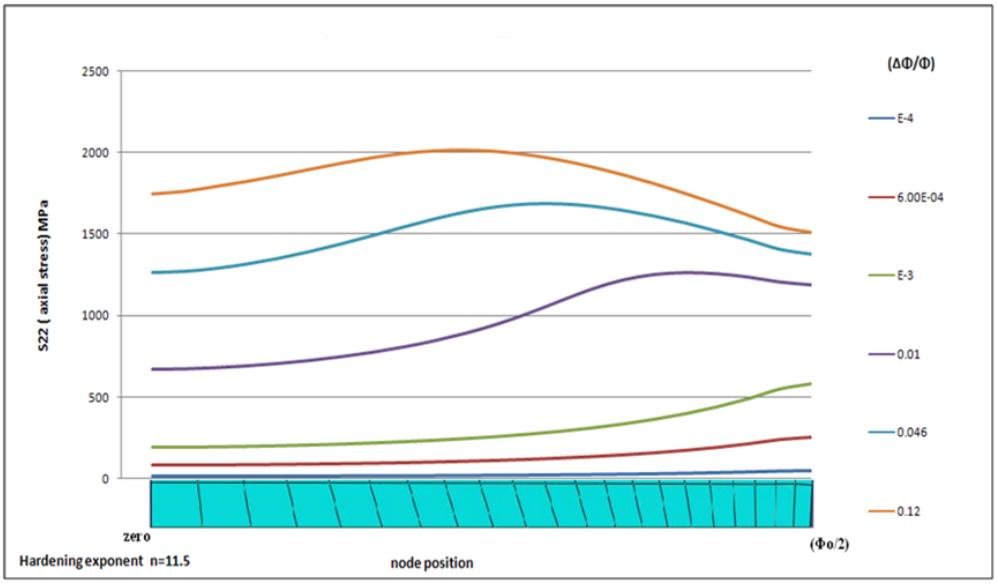

Fig. 5.16 Axial stress evolution along specimen notched side for Von Mises model-sharp notched bar-fine mesh.

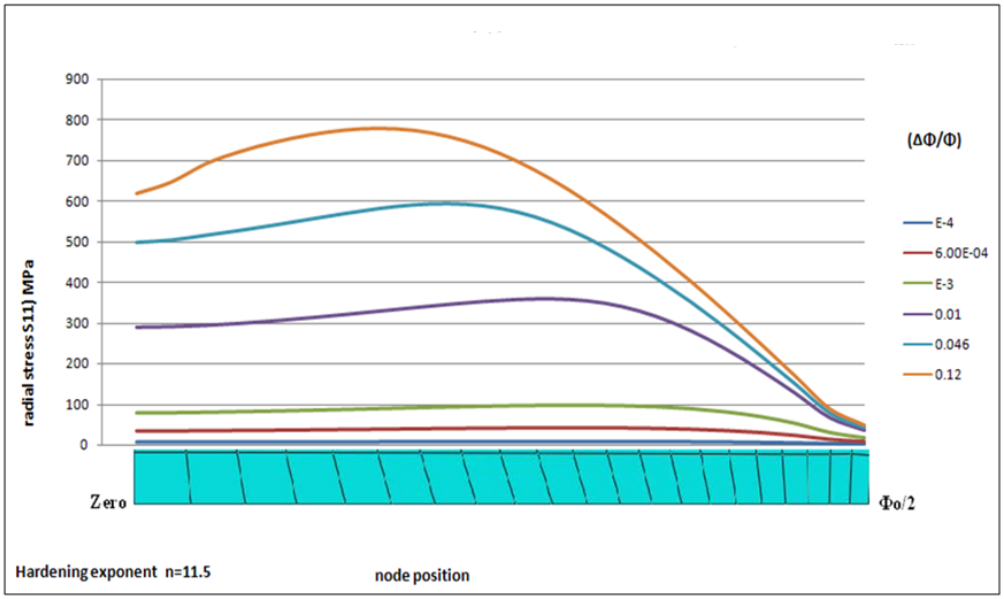

Fig. 5.17 Radial stress evolution along specimen notched side for Von Mises model-sharp notched bar-fine mesh.

Moreover, based on Figs. 5.18 and 5.19 one can see that stress triaxiality ratio in both of the fine and the coarse meshes has the maximum value around 1.2. However, in the

case of sharp notched bars the stress triaxiality is uniform starting half way from the center of the sample up to the center , but it has the lowest value at the vicinity of the notched side.

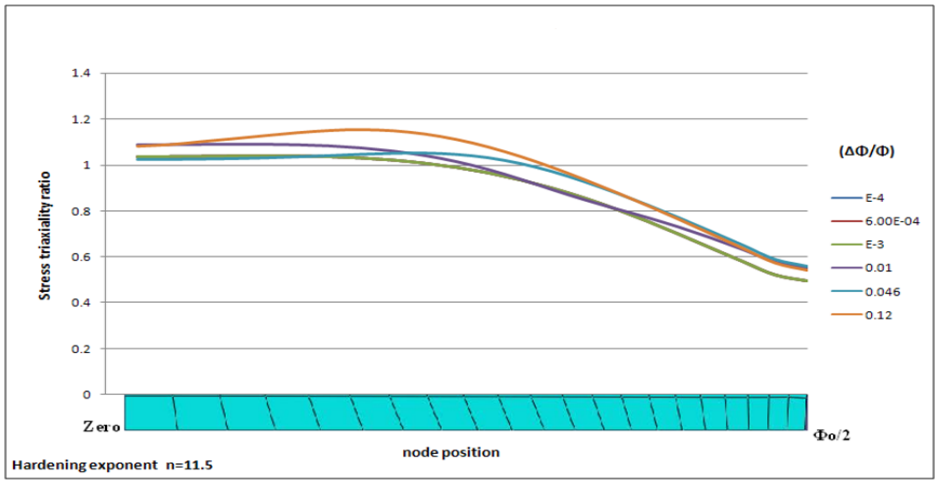

Fig. 5.18 Stress triaxiality ratio evolution along specimen notched side for Von Mises model-sharp notched bar-fine mesh.

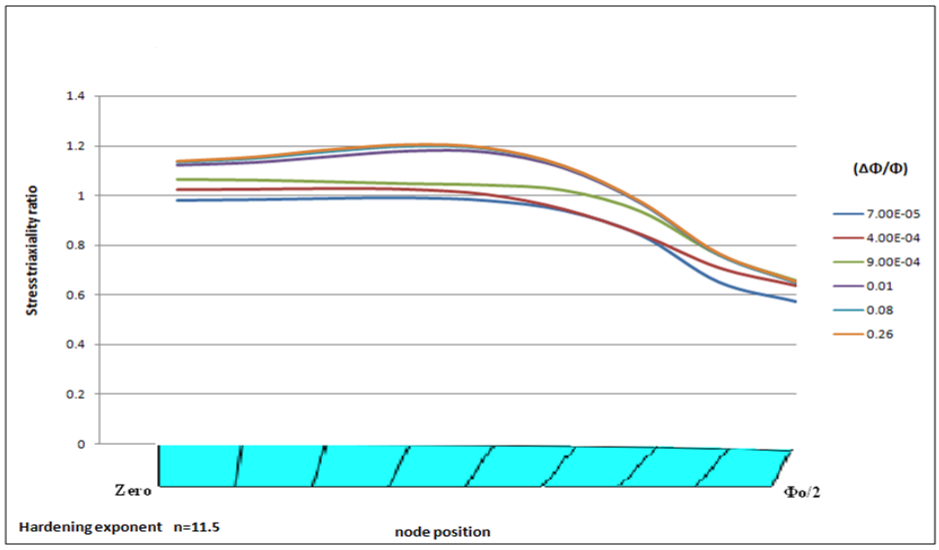

Fig. 5.19 Stress triaxiality ratio evolution along specimen notched side for Von Mises model-sharp notched bar-coarse mesh.

Figs. 5.20 shows the fine mesh that used to simulate the Von Mises model of the sharp notched bar, and it shows the axial stress evolution with deformation. The axial stress starts its maximum value at the vicinity of the notch edge and start to vary along the notch side toward the center with increasing the deformation. The same trend can be seen in the PEEQ in Fig. 5.21. But the stresses are higher in the sharp notched bar samples than in the shallow ones. However, the PEEQ is higher at the shallow ones.

Other calculations were done using the n=25 to find the stress triaxiality ratio. For the shallow notched bars it has the value of 0.8, but it has the value of 1.4 in the case of the sharp notched ones. So in the next sections these values will be used.

Based on the discussion for the Von Misses model using Ramberg-Osgood hardening law, for both the shallow and notched bar specimens the effect of the mesh refinement on the simulation results is not significant.

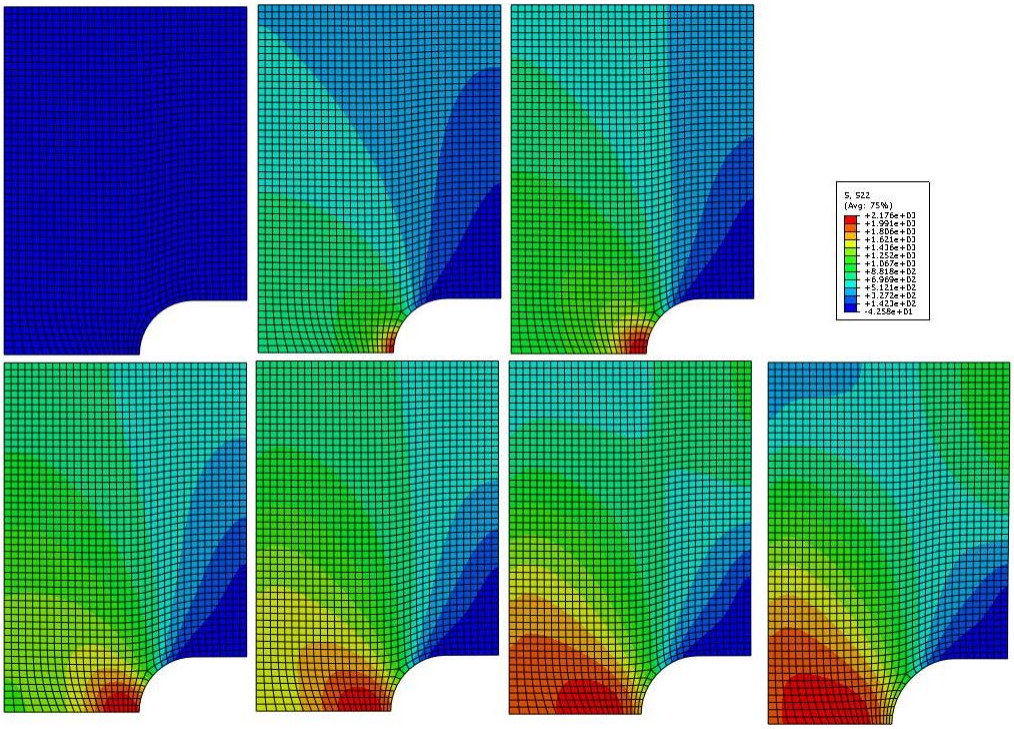

Fig. 5.20 Axial stress evolution using Von Misses model for the sharp notched bar (fine mesh -hardening exponent n=11.5).

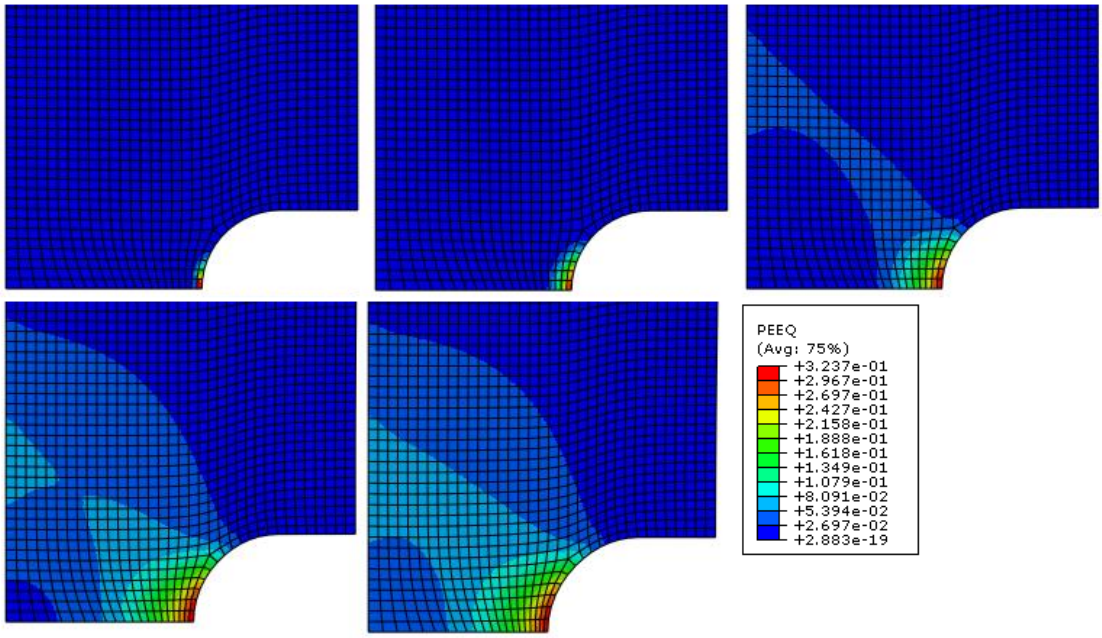

Fig. 5.21 Equivalent plastic strain evolution using Von Misses model for the sharp notched bar (fine mesh - hardening exponent n=11.5).

5.5 Mean Strain and Triaxiality of Notched Bar Samples.

In this section the stress triaxiality values that have been found from the simulation of the shallow and the sharp notched bars will be used with the mean strain to failure to characterize the notch ductility. Ductile fracture is sensitive to the stress triaxiality .ratio; moreover, to characterize the ductility quantitatively one cannot use only one value of stress triaxiality. Therefore, it is important to use notched bar samples with different radii since they allow probing a wide range of stress triaxiality and therefore characterize the notch ductility represented by the mean strain to failure. 0.8 triaxiality ratio was used for the shallow notched bars and 1.4 was used for the sharp notched bars. Equation 4.1 was used to find the mean strain to failure. The mean strain to failure can be described as the fracture strain (the final strain when the sample brakes) εf, or the initiation strain εi., when the crack starts to initiate and this can be seen when abrupt change in the stress-strain slope occur.

Figs. 5.22-5.23 show the mean strain to failure versus the triaxiality ratio of the three billets. These figures show one of the most important macroscopic observation about ductile fracture which is that the mean strain to failure decays exponentially with increasing the stress triaxiality. This is reasonable since the void growth is proportional to the triaxiality. Another observation is that the fracture strain is always higher than the initiation strain for each specific ζ value in each billet. And finally, the smooth bars has the highest values of the mean strain to failure, then the shallow ones, and finally the sharp.

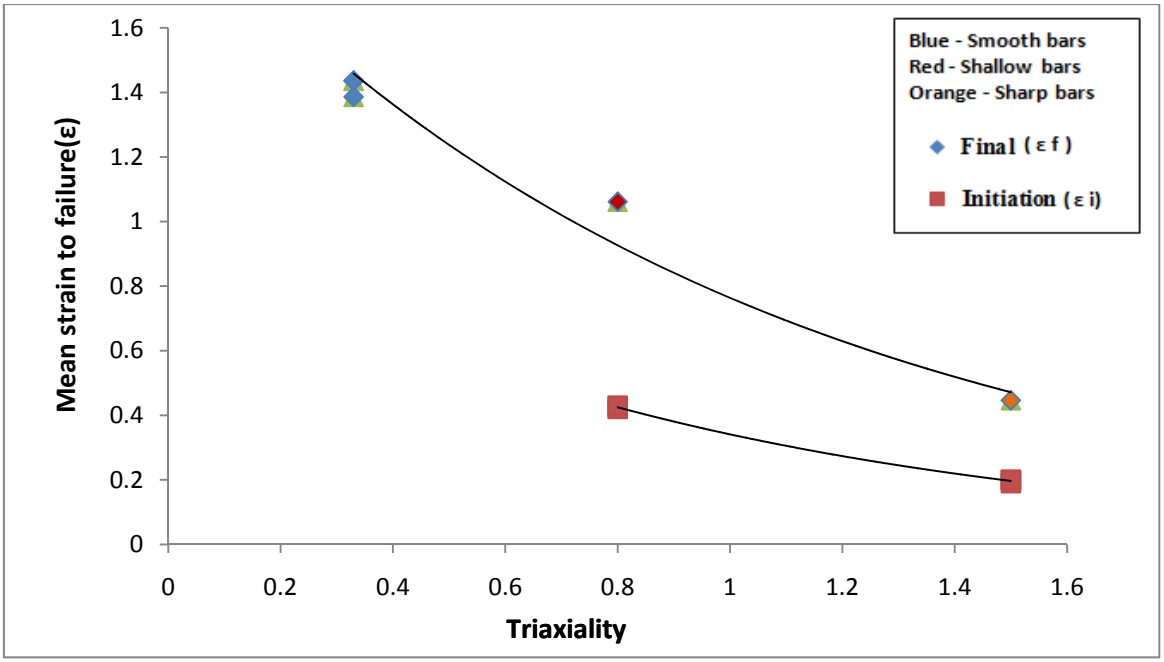

Fig. 5.22 Initiation strains and fracture strains versus the stress triaxiality of smooth bars, shallow notched bars, and sharp notched bar samples made from billet 1.

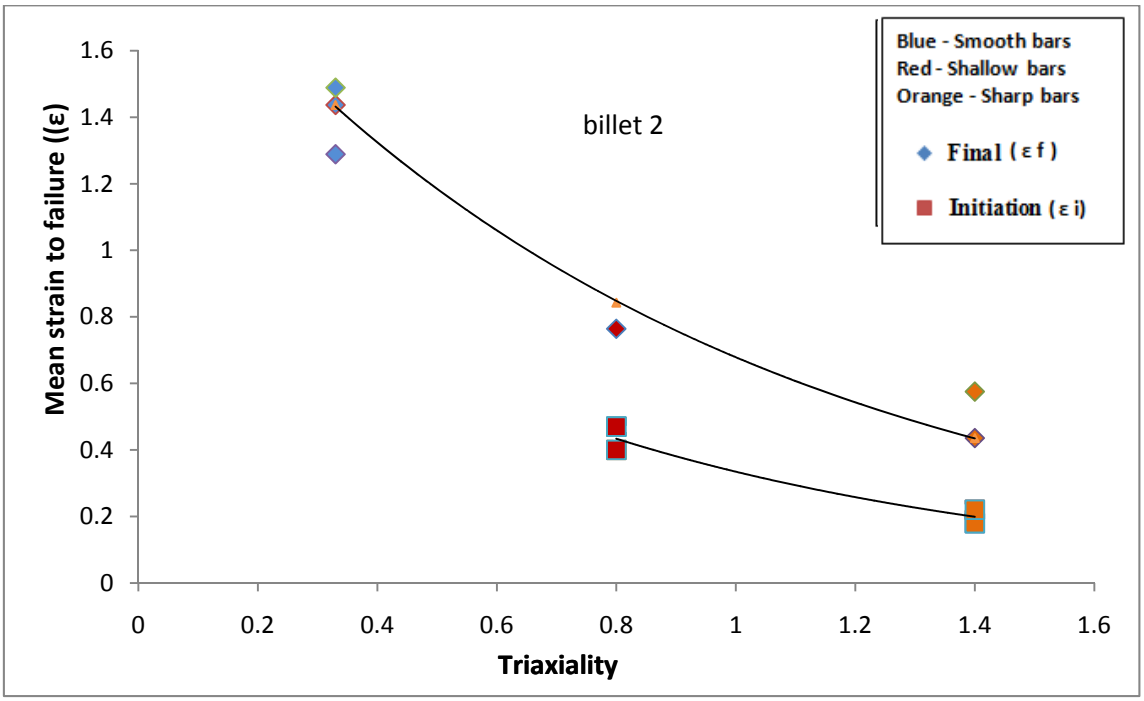

Fig. 5.23 Initiation strains and fracture strains versus the stress triaxiality of smooth bars, shallow notched bars, and sharp notched bar samples made from billet 2.

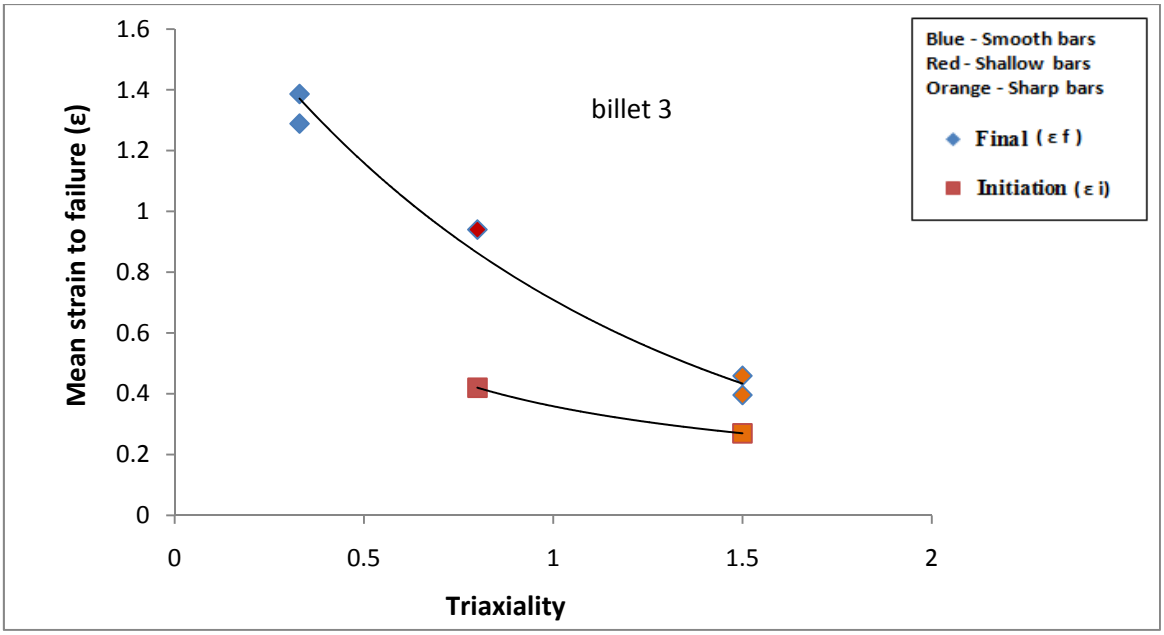

Fig. 5.24 Initiation strains and fracture strains versus the stress triaxiality of smooth bars, shallow notched bars, and sharp notched bar samples made from billet 3.

Figs. 5.25 and 5.26 show the fracture strain and the initiation strain versus the triaxiality of the three billets together. It can be seen that both the fracture strain and the initiation strain are proportional to the triaxiality. This is reasonable since the void growth which lead to the fracture is proportional to the triaxiality.Second, the smooth bar shows the higher value of the fracture strain, then the shallow ones, and finally the sharp. Third, within the same category of samples; i.e for the same ζ value, one cannot see a significant variation in the strain values among the three billets. This means that although there was a significant variation in the UTS between the finest grain size billets (1 and3) and the coarsest one (billet2) the fracture properties represented by the notch ductility remains intact.

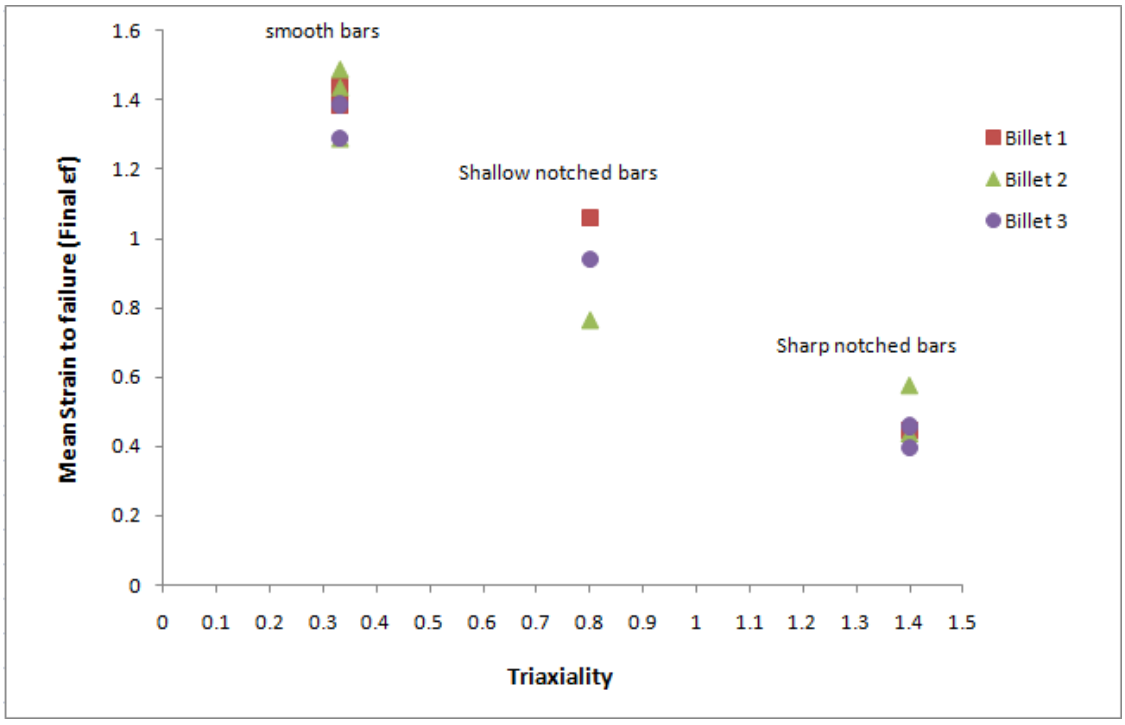

Fig. 5.25 Fracture strain versus the triaxiality ration of samples made of the three billets.

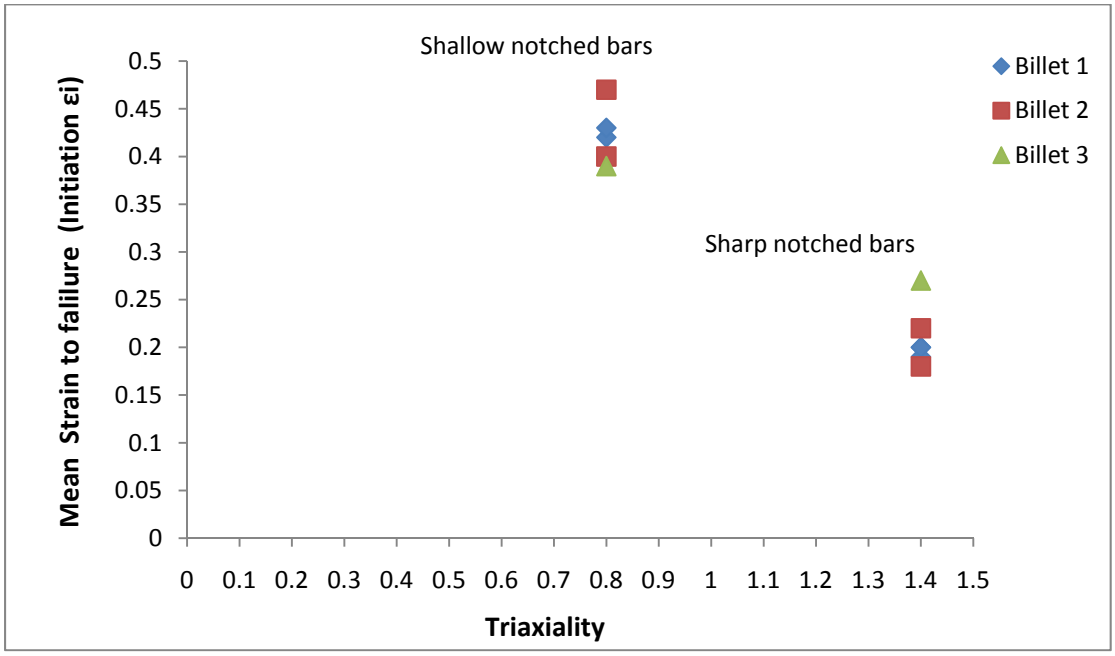

Fig. 5.26 Initiation strain versus the triaxiality ration of samples made of the three billets.

CHAPTER VI

CONCLUSIONS AND FUTURE WORK

6.1 Conclusions

Ultrafine grain and nano-crystalline materials with refined grain size in the range of 100nm-1μm show promise for many industrial applications including aerospace, automotive, and biomedical. Therefore, research regarding UFG materials is regarded as a matter of industrial importance. Severe plastic deformation through equal angular channel extrusion is used to refine the grain size of the interstitial free steel that has initial grain size in the range of 250 μm in the as-received conditions. Route 8Bc is utilized to fabricate three different materials using three different processing conditions in term of extrusion temperature and extrusion rate. The first material is fabricated using extrusion rate of 0.1in/sec and the extrusion at room temperature. The second material is fabricated using extrusion rate of 0.1in/sec and 200C^{o}. And the third material is fabricated at room temperature using two extrusion rates; 1in/sec for the first four passes and 0.5in/sec for the second four passes.

Significantly the grain size is refined of the interstitial free steel from 250μm range to 500nm range using route 8Bc. However, a slight variation in the grain size is found between the three fabricated materials. Material 1 has a grain size in the range 515±35nm, material 2 has grain size in the range 590±60nm, and material 3 has grain size in the range 485±65nm. Significant variation in the ultimate tensile strength and the

yield strength is found between material (1, 3) and material 2. However, material 2 higher values of the axial strain to some extent when compared to materials 1 and 3.

The ductility measured as strain to failure in smooth bars is highly sensitive to the specific geometry of the used sample (either it is round shape or flat shape samples), it seems that it tends to be larger in a flat specimen because of the diffuse necking. Moreover, smooth bar samples may not be a good measure of fracture properties because much of the diffuse necking is deformation induced and no significant damage take place. In addition, using only smooth bar samples will not give a clear idea about the fracture locus since we are using only one value of the stress triaxiality. Therefore, notched bar samples are used to allow probing a wider range of stress triaxiality.

Therefore, it can be concluded the following: First, one cannot vary the mean grain size at will in standard ECAE process (using route 8Bc and extrusion rate of 0.1in/sec) since increasing the number of passes beyond 4 passes simply changes the character of the High Angle Grain Boundaries (HAGB) that form but does not lead to further refinement in the dislocation cell structure. Second, one cannot vary effectively the grain size by changing the extrusion rate. This is because FCC materials show low sensitivity to the strain rate, and in the case of BCC material which are sensitive to the strain rate there was technical difficulties in applying high extrusion rates represented by the damage and localization. Third, the only viable way to control the grain size for a given material is to vary the processing temperature.

Significant enhancement is found in the Ultimate tensile strength between the as-received material and the UFG one. Nevertheless, by comparing only the UFG materials

one can say: although the strength decreases significantly from the finest microstructure (billet 1and3) to the coarsest microstructure (billet2) by the value of 100MPa, the fracture properties ,i.e conventional ductility represented by the percentage elongations and notch ductility represented by the mean strains to failure remain almost the same.

The tests of notched bars having the values of 10 and 2 of the parameter ζ respectively show that both fracture strain and the initiation strain decay exponentially with increasing the stress triaxiality ratio. Moreover, the fracture strain is higher than the initiation strain of the notched tensile test samples that has the same ζ value.

Detailed fractography of UFG-IF steel revealed that the fracture mode is ductile fracture since it has the dimples and irregular broken surfaces. Several fractographs show the three stages of the ductile damage which are: void nucleation, void growth, and void coalescence. Additionally, it is believed that the sources of the void nucleation in the UFG-IF steel can be divided into two types. The first void nucleation source is the existence of the second phase particles inside the material matrix. Decohesion between the particle and the matrix will lead to void nucleation. TiC, TiO, TiN, Al2O3, MnS are the second phase particles found in the three types of materials based on the EDS analysis that causing the voids to nucleate.

Second phase particles can trigger other damage mechanisms such as intergranular fracture (IGF) leading to abrupt falls in stress bearing capacity of notched bars. This suggests that the crack growth resistance must be studied as well. The IGF can be localized or diffuse, so that it does not depend on triaxiality.

The second source of the void nucleation can be considered as the following: shear band intersections with each other or with the grain boundaries, clustering of voids in the untested material, triple junctions between the grains, or any type of processing defects inside the material since it is well accepted that ECAE processes give rise to oriented distribution of defects such as dislocations and grain boundaries which can lead to void nucleation.

Finally, despite the low work-hardening capacity of the UFG materials, their room temperature ductility is remarkably good. However, a complete characterization of the fracture behavior of these materials would require: toughness measurements, investigation of the effect of temperature. From here the recommendations for future work become clear.

6.2 Recommendations for Future Work

Deformation and fracture behavior of the UFG materials deserve study since UFG materials show promise for many industrial applications. This research has added some contributions to what has been done so far in this field. First, this research is one of the first researches focusing on the ductile fracture mechanisms of a UFG material. Second, this is the first time that notched bar samples are used to characterize the fracture behavior of a UFG material, probing a wide range of stress triaxiality compared to what has been done using flat dog-bone shape samples, or round smooth bars.

The fracture behavior of UFG materials deserves further study. This research is considered as the basis for further studies in this field especially on the ductile to brittle transition when both the temperature and the grain size of the material are varied. In

order to be able to perform this future DBTT work some recommendation should be followed:

First, more billets should be fabricated using different routes or different processing conditions to vary the grain size especially in the range below 500nm.This may require changing the material of the study.

Second, in order to study the ductile to brittle transition, tensile testing will be performed at temperatures lower than the ambient temperature.

Third, a complete characterization of the fracture behavior of this kind of materials will require toughness measurements using for example compact tension (CT) specimens and investigation of the effect of temperature.

REFERENCES

[1] Valiev RZ, Kozlov VE, Ivanov Yu F, Lian J, Nazarov A, Baudele B. Acta Mater 1994;42:2467.

[2] Gleiter H. Progress in Materials Science 1989;33:223.

[3] Valiev RZ, Langdon TG. Prog Mater Sci 2006;51:881-981

[4] Lowe T, Valiev RZ. J Min Mets Mater 2004; 56.

[5] Niendorf T, Karaman I, Canadinc D, Maier H, Sutter S. Int J Mater Res 2006;97:1328.

[6] Ma A, Jiang J, Saito N, Shigematsu I, Yuan Y, Yang D, Nishida Y. Mater Sci Eng., A 2009;513:122.

[7] Liaw P. J Min Mets Mater 2001:30.

[8] Barbi G,Santos J,Serrini P,Gibson P,Horrillo M,Manes L. Sensors and Actuators B Chemical 1995;2:559.

[9] Elias C,Lima J,Valiev R. J Min Mets Mater 2008;6:46.

[10] Tsunoyama K. Phys Stat Sol 1998;167:427

[11] Hook R, Heckler A, Elias J. Metall Mater Trans A 1975;6:1683.

[12] Zhang X, Luo S, Du Z. Transactions of Nonferrous Metals Society of China 2008;18: 92.

[13] Berbon PB, Furukawa M, Horita Z, Nemoto M, Langdon TG. Metall Mater Trans 1999;30A:1989.

[14] Iwahashi Y, Wang J, Horita Z, Nemoto M, Langdon TG. Scripta Mater 1996;35:143.

[15] Furuno K, Akamatsu H, Oh-ishi K, Furukawa M, Horita Z, Langdon TG. Acta Mater 2004;52:2497.

[16] Nakashima K, Horita Z, Nemoto M, Langdon TG. Mater Sci Eng 2000;A281:82.

[17] Iwahashi Y, Horita Z, Nemoto M, Langdon TG. Acta Mater 1998;46:3317.

[18] Brandon DG. Acta Metar 1966;14:1479.

[19] Winning M, Rollett AD. Acta Mater 2005;53:2901.

[20] Wu Y, Baker I. Scripta Mater 1997;37:437.

[21] Shan A, Moon IG, Ko HS, Park JW. Scripta Mater 1999;41:353.

[22] Yamashita A, Yamaguchi D, Horita Z, Langdon TG. Mater Sci Eng 2000;A287:100.

[23] Chen YC, Huang YY, Chang CP, Kao PW. Acta Mater 2003;51:2005-2015.

[24] Nakashima K, Horita Z, Nemoto M, Langdon TG. Acta Mater 1998;46:1589.

[25] Terhune SD, Swisher DL, Oh-ishi K, Horita Z, Langdon TG, McNelley TR. Metall Mater Trans 2002;33A:2173.

[26] Mahallawya NE,Shehatab FA,Elhameedb MA,Abdelal MI. Materials Science and Engineering A 2009;517:46.

[27] Jianqiang B, Kangning S, Rui L, Runhua F, Sumei W. Journal of Wuhan University of Technology-Mater. Sci. Ed 2008;10:71.

[28] Valiev RZ, Islamgaliev RK, Alexandrov IV. Prog Mater Sci 2000;45:103.

[29] Zhu YT, Langdon TG. J Min Mets Mater 2004;56 (10):58.

[30] Valiev RZ, Alexandrov IV, Lowe TC, Zhu YT. J Mater Res 2002;17:5.

[31] Yamaguchi D, Horita Z, Nemoto M, Langdon TG. Scripta Mater 1999;41:791.

[32] Kim IY, Kim JY, Shin DH, Park JT. Metall Mater Trans 2003;34A:1555.

[33] Tipper CF. The Journal of the Iron and Steel Institute 1948;158:327.

[34] Pineau A, Pardoen T. Comprehensive Structural Integrity 2007:684.

[35] Garrison WM, Moody NR . J Phys Chem Solids 1987;48:103.

[36] Thomason PF. Ductile Fracture of Metals. Britain: B.P.C.C: Wheatons Ltd,Exeter,Devon,UK:Polestar Wheatons Ltd, 1990.

[37] Thompson AW, Williams JC. Advances in Research on the Strength and Fracture of Materials. vol. 2. New York: Pergamon Press, 1978.

[38] Stone RHV, Low JR., Jr, NASA Tech. Rep.I-Ti. Ptttsburgh.PA:Carnegie Mellon University. Pittsburgh,PA: 1973.

[39] Stone RHV, Low JR Jr, Shannon JL:,NASA Rep. CR-135120, Carnegie Mellon University Pittsburgh, PA:1977.

[40] Nieh TG, Nix WD. Scripta Mater. 1980;14: 365-368.

[41] Greenfield MA, Margolin H . Metall Trans 1972;3.

[42] Greenfield MA , Margolin H , Greenhut I. Titanium Science and Technology . vol . 3. New York: Plenum Press, 1973.

[43] Gysler A, Lutjering G, Gerold V. Acta Mater 1974;22:901

[44] Wu SD, Wang ZG, Jiang CB , Li GY, Alexandrov IV, Valiev RZ . Mater Sci Eng A 2004;387:560.

[45] Stone RHV, Cox TB, Low JR, Psioda JA. Int Metall Rev 1985;30:79.

[46] Stone RHV, Psioda JA. Metall Trans A 1975;6A.

[47] Palmer IG, Smith G C. Proc. AZME Co&Oxide Dispersion Strengthening, Bolton Landing,. New York: Gordon & Breach, 1967.

[48] Lassance D, Fabregue D, Pardoen T. Mater Sci Forum 2006;519-521:829.

[49] Argon AS, IM. J, Safoglu R.. Metall. Trans. A 1975;A6.

[50] Cox T B, Low J R. Metall Trans A 1974;5:1457.

[51] Psioda JA. Pittsburgh, PA: Carnegie Mellon University, 1977.

[52] Cane B, Middletown C. Mater Sci Eng A 1981;15:302.

[53] Smith C Jr, Low JR. Metall Trans 1974;5:279.

[54] Lassance D, Scheyvaerts F, Pardoen T. Eng Fract Mech 2006;73.

[55] Huber G, Brechet Y, Pardoen T. Acta Mater. 2005;53: 2749

[56] Pardoen T, Doghri I, Delannay F. Acta Mater. 1998;46:541.

[57] Benzerga A A, Besson J, Pineau A. Acta Mater. 2004;52:4623.

[58] Huber G, Brechet Y, Pardoen. T Acta Mater. 2005;53:2739.

[59] Weck A, Wilkinson D S. Acta Mater. 2008;56:1774.

[60] Benzerga A A. Rupture Ductile Des Toles Anisotropes. Ph.D. Dissertation. Paris, 2000.

[61] Panin AV, Panina AA, Ivanov YF. Mater Sci Eng A 2008;486:267.

[62] Dudarev EF, Markov AB, Bakach G, Tabachenko A, Polevin SD, Girsova NV, Kashin O, Zhorovkov MF, Rotshtein VP. Russian Physics Journal 2009;52.

[63] Sutter SG. The effect of strain and path change on the mechanical properties and microstructural evolution of ultrafine grained interstitial free steel during equal channel angular extrusion (ECAE). Mechanical Engineering, M.S.thesis, Masters, College Station: Texas A&M University. 2005.

APPENDIX A

SPECIMENS DRAWINGS

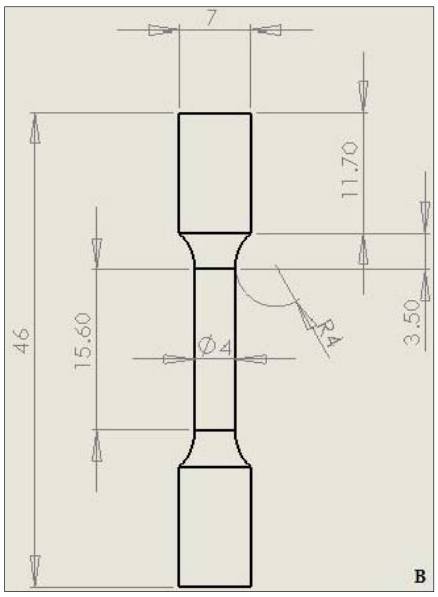

Fig. A.1 A schematic showing the dimensions of the smooth bar samples machined from 7 mm diameter cylinders.

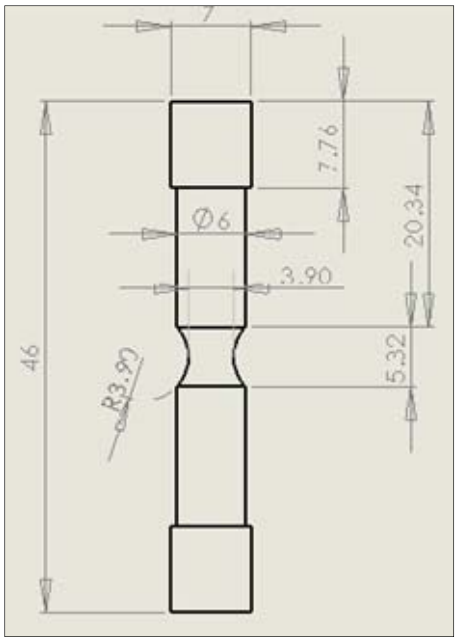

Fig. A.2 A schematic showing the dimensions of the shallow notched bar samples machined from 7mm diameter cylinders.

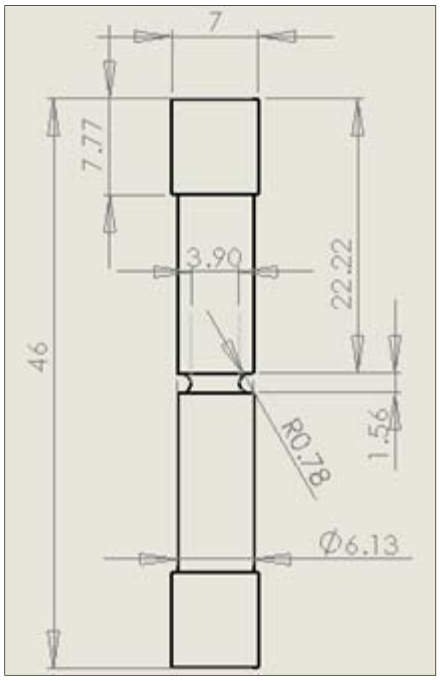

Fig. A.3 A schematic showing the dimensions of the sharp notched bar samples machined from 7 mm diameter cylinders.

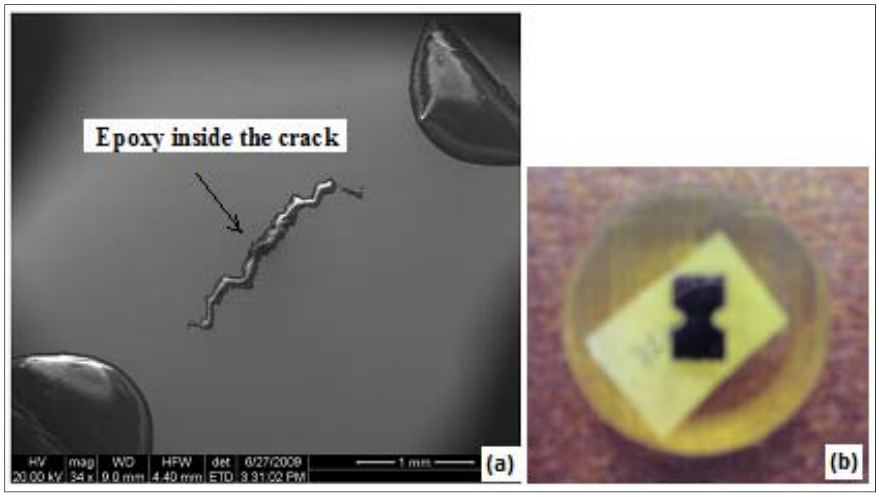

Fig. A.4 (a) The trapped epoxy inside the crack, (b) The crack propagation investigation sample mounted inside the epoxy.

APPENDIX B

MICROSTRUCTURES OF PROCESSED MATERIALS

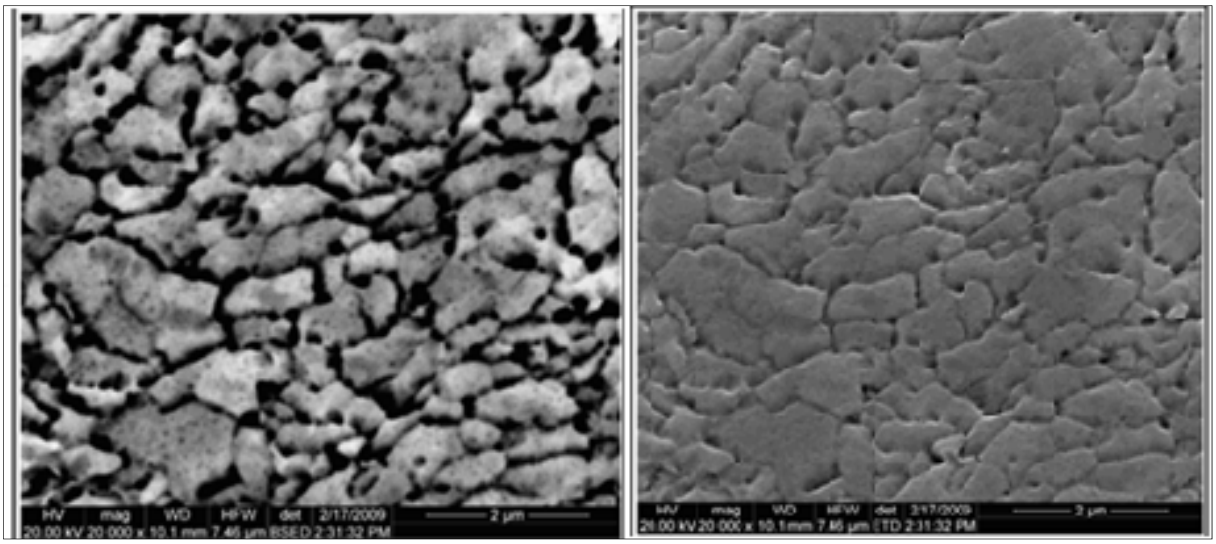

Fig. B.1 (a) Secondary electron–SEM micrograph of the transverse plane M from billet 2 (fabricated at 200C^{o} and extrusion rate of 0.1in/sec) (b) Back scattered –SEM micrograph of the same billet and plane. Both of the images show the over-etching attacks the grain boundaries.

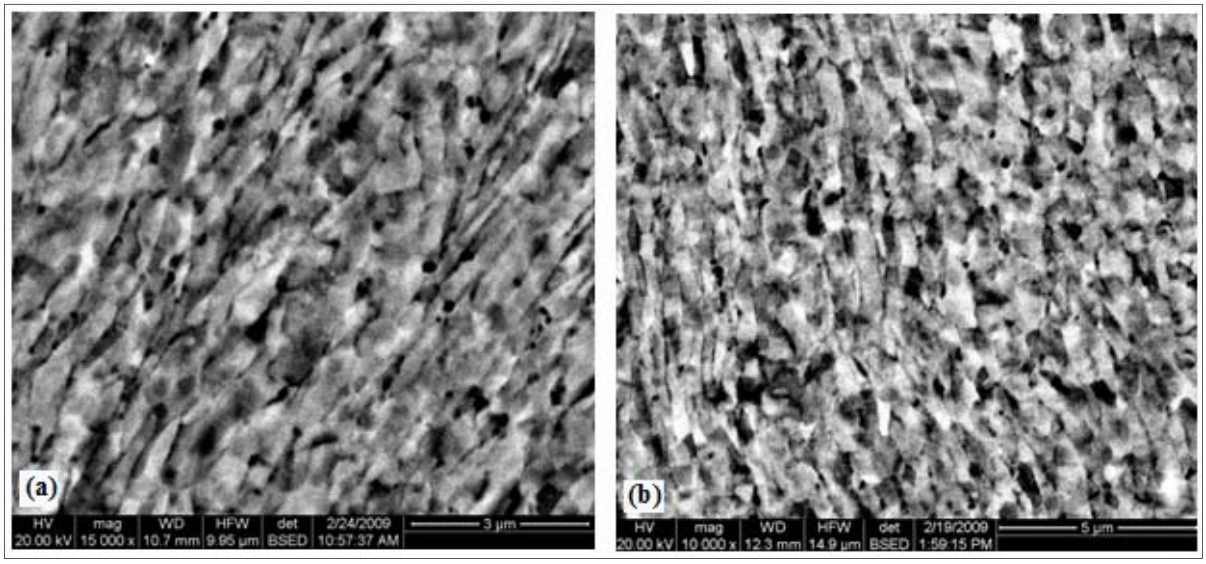

Fig. B.2 (a) Back-scattered –SEM micrograph of the flow plane A from billet 3 (fabricated at room temperature and extrusion rate of 1in/sec for the first four passes, and 0.5in/sec for the second four passes) (b) Back-scattered-SEM micrograph of the longitudinal plane B from billet 3.

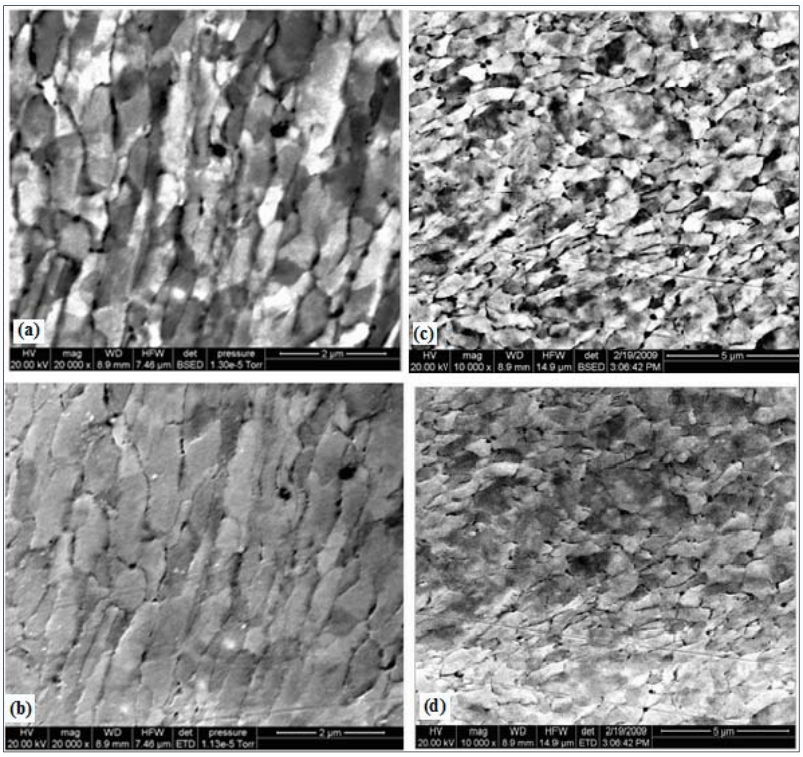

Fig. B.3 (a) Back-scattered –SEM micrograph of the flow plane A from billet2 (fabricated at 200C^{o} and extrusion rate of 0.1in/sec), (b) Secondary electron –SEM micrograph of the flow plane A, (c) Back-scattered –SEM micrograph of the longitudinal plane B from billet2 (b) Secondary electron –SEM micrograph image of the longitudinal plane B.

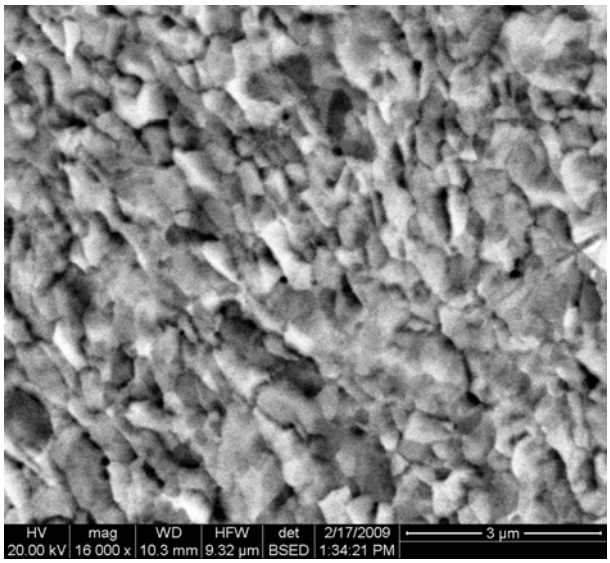

Fig. B.4 Back-scattered image of the transverse plane M from billet1 (fabricated at room temperature and extrusion rate of 0.1in/sec).

APPENDIX C

ADDITIONAL LOAD DEFORMATION CURVES

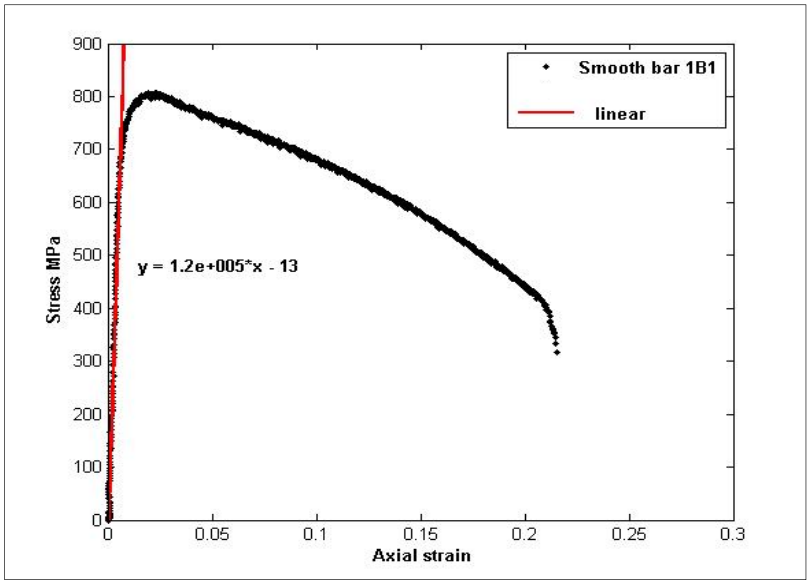

Fig. C.1 Stress-strain diagram of smooth bar sample of billet 1 showing its Young's modulus.

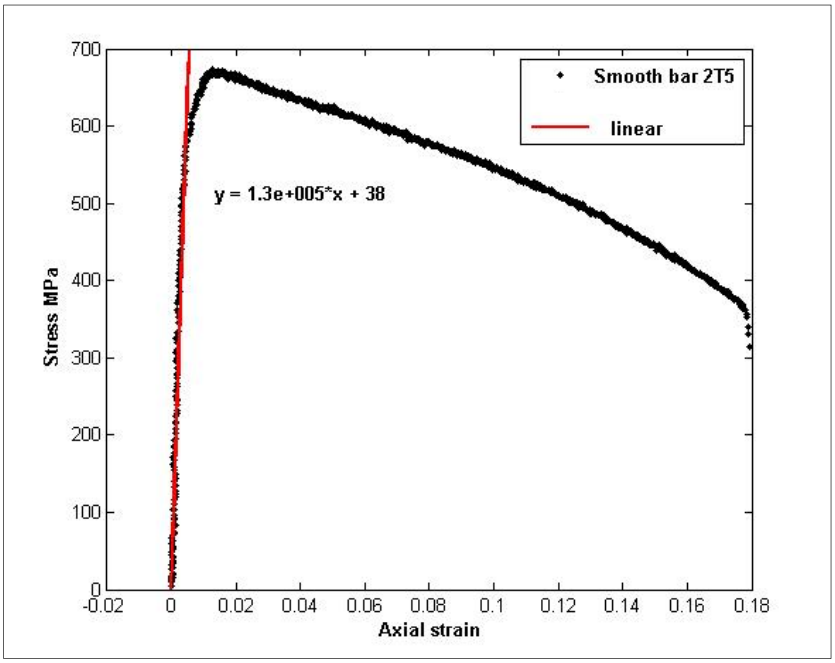

Fig. C.2 Stress-strain diagram of smooth bar sample of billet 2 showing its Young's modulus.

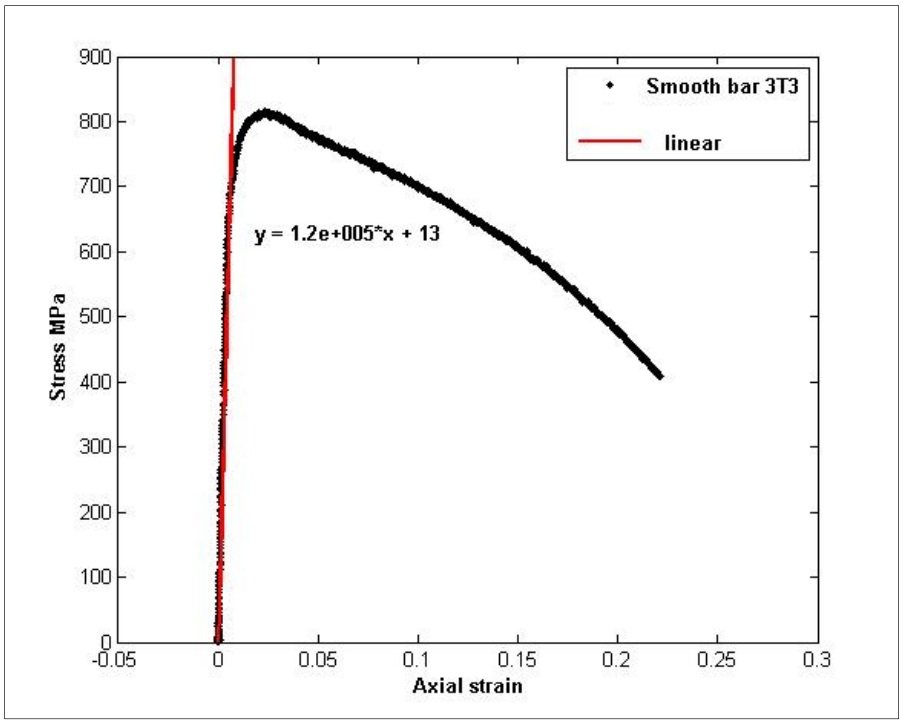

Fig. C.3 Stress-strain diagram of smooth bar sample of billet 3 showing its Young's modulus.

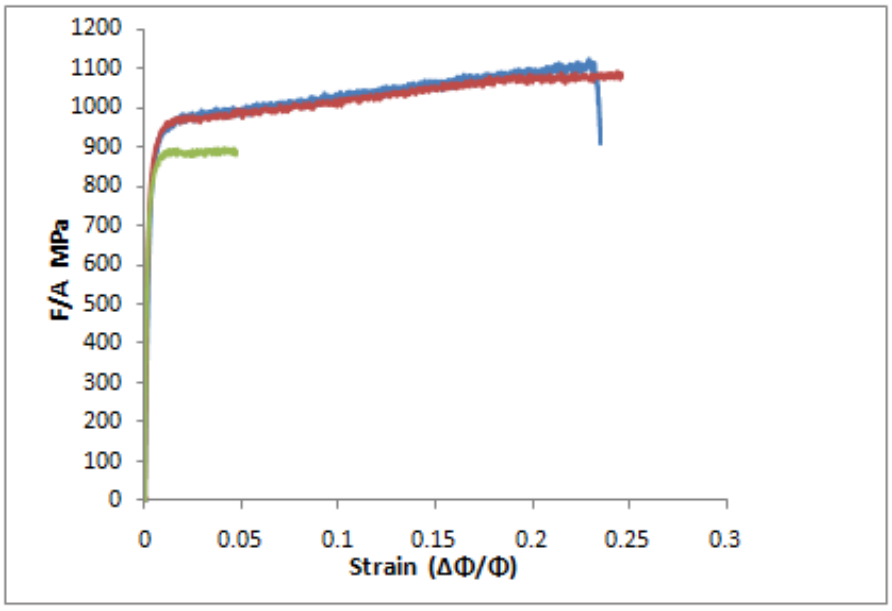

Fig. C.4 True stress-true strain of the shallow notched bar samples made of billet 1.

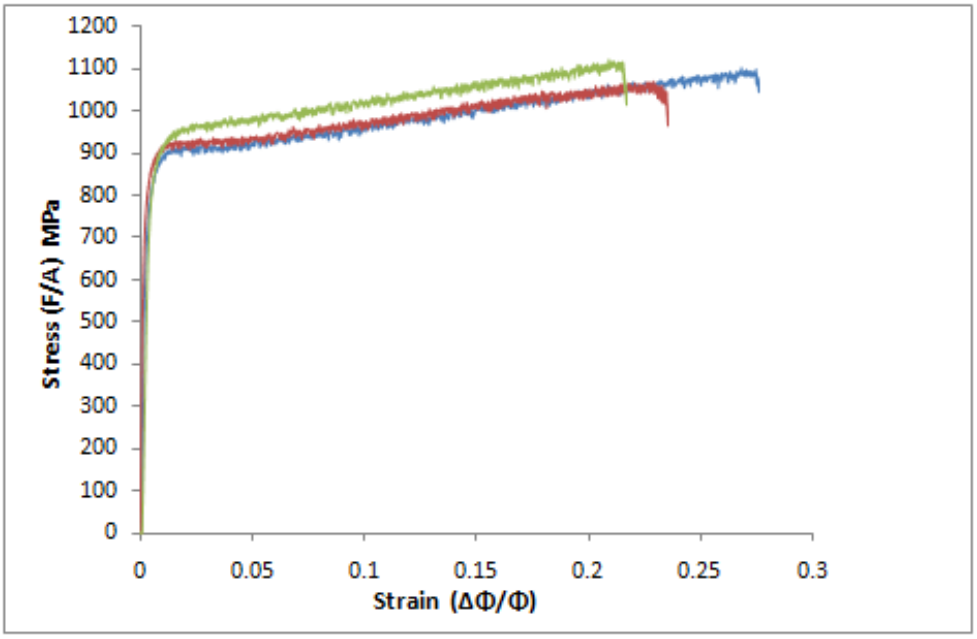

Fig. C.5 True stress-true strain of the shallow notched bar samples made of billet 2.

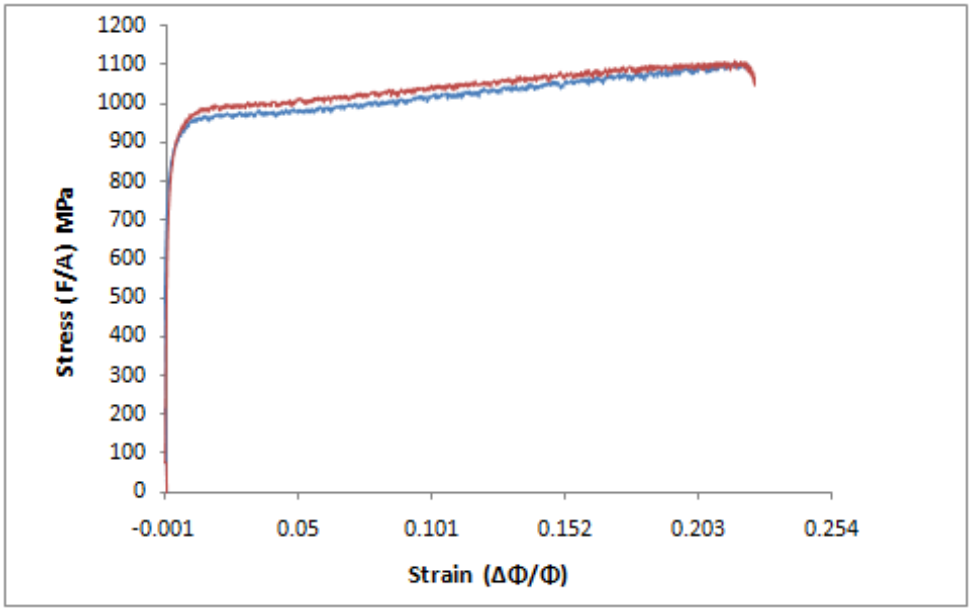

Fig. C.6 True stress-true strain of the shallow notched bar samples made of billet 3.

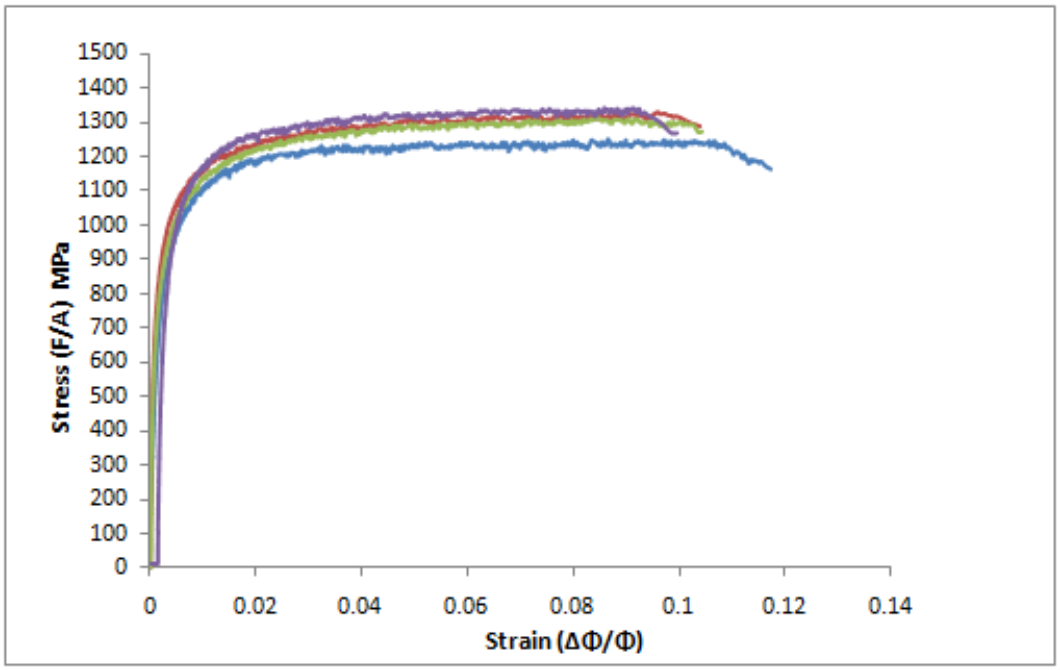

Fig. C.7 True stress-true strain of the sharp notched bar samples made of billet 1.

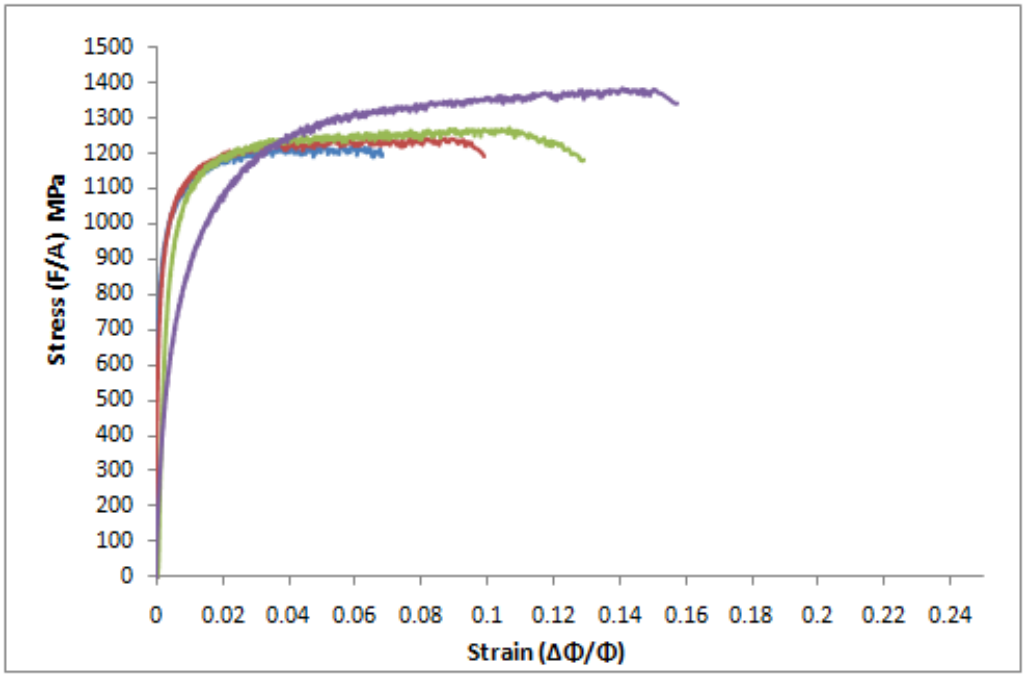

Fig. C.8 True stress-true strain of the shallow notched bar samples made of billet 2.

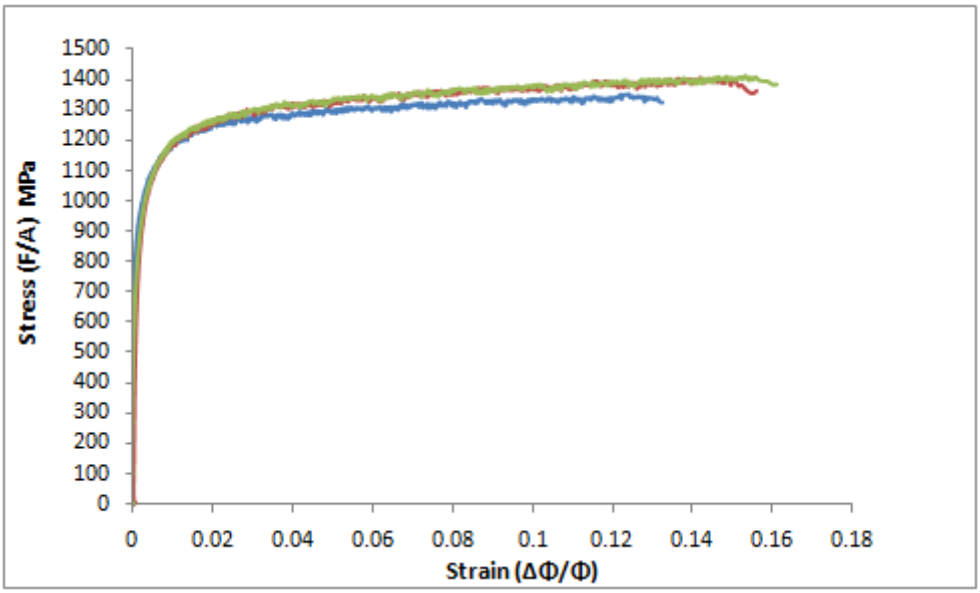

Fig. C.9 True stress-true strain of the sharp notched bar samples made of billet 3.

Table.C.1

Summary of the samples specifications

Sample name	Type	Initial dia (Φ_o) mm	Final dia (Φ_f) mm	Gage length(mm)	Interrupt/ Rupture	Young's modulus(GPa)	Triaxiality	εi	εf
Billet 1									
1T1	smooth	4	1.95	15	Rupture	130	0.33		1.44
1T5	Smooth	4.1	2	15	Rupture	120	0.33		1.44
1B1	Smooth	4	2	15	Rupture	120	0.33		1.39
1T2-R	Shallow	3.4	2		Rupture		0.8	0.1	1.06
1B2-I	Shallow	3.9			Interrupt		0.8	0.41	-
1B5-I	Shallow	3.9			Interrupt		0.8	0.43	-
1T3-R	Sharp	4	3.2		Rupture		1.4	0.19	0.446
1T4-I	Sharp	3.95			Interrupt		1.4	0.2	-
1B3-I	Sharp	3.9			Interrupt		1.4	0.2	-
1B4-I	Sharp	4			Interrupt		1.4	0.19	-
Billet 2									
2T1	Smooth	4	1.9	14.55	Rupture	120	0.33		1.49
2T5	Smooth	4	2.1	14.55	Rupture	130	0.33		1.29
2B1	Smooth	4	1.95	14.55	Rupture	130	0.33		1.44
2T2-I	Shallow	3.9			Interrupt		0.8	0.4	-
2B2-R	Shallow	3.81	2.6		Rupture		0.8	0.38	0.76
2B5-I	Shallow	3.95			Interrupt		0.8	0.47	-
2T3-I	Sharp	3.95			Interrupt		1.4	0.22	-
2T4-R	Sharp	4	4		Rupture		1.4	0.25	0.575
2B3-R	Sharp	3.73	3.73		Rupture		1.4	0.12	0.435

Table C.1 Continued

Sample name	Type	Initial diameter (Φ_o) mm	Final diameter (Φ_f) mm	Gage length(mm)	Interrupt/ Rupture	Young's modulus(GPa)	Triaxiality	εi	εf
2B4-I	Sharp	3.95			Interrupt		1.4	0.18	-
Billet 3									
3T3	Smooth	4	2.1	14.6	Rupture	130	0.33		1.29
3B3	Smooth	4	2	14.9	Rupture	140	0.33		1.39
3T6-I	Shallow	3.9			Interrupt		0.8	0.39	
3T8-R	Shallow	4	2.5		Rupture		0.8	0.39	0.94
3T4-R	Sharp	3.9	3.1		Rupture		1.4	0.27	0.46
3T5-I	Sharp	3.9			Interrupt		1.4	0.27	-
3B5-R	Sharp	3.9	3.2		Rupture		1.4	0.25	0.395

APPENDIX D
FRACTOGRAPHS

Shallow notched bar fractographs

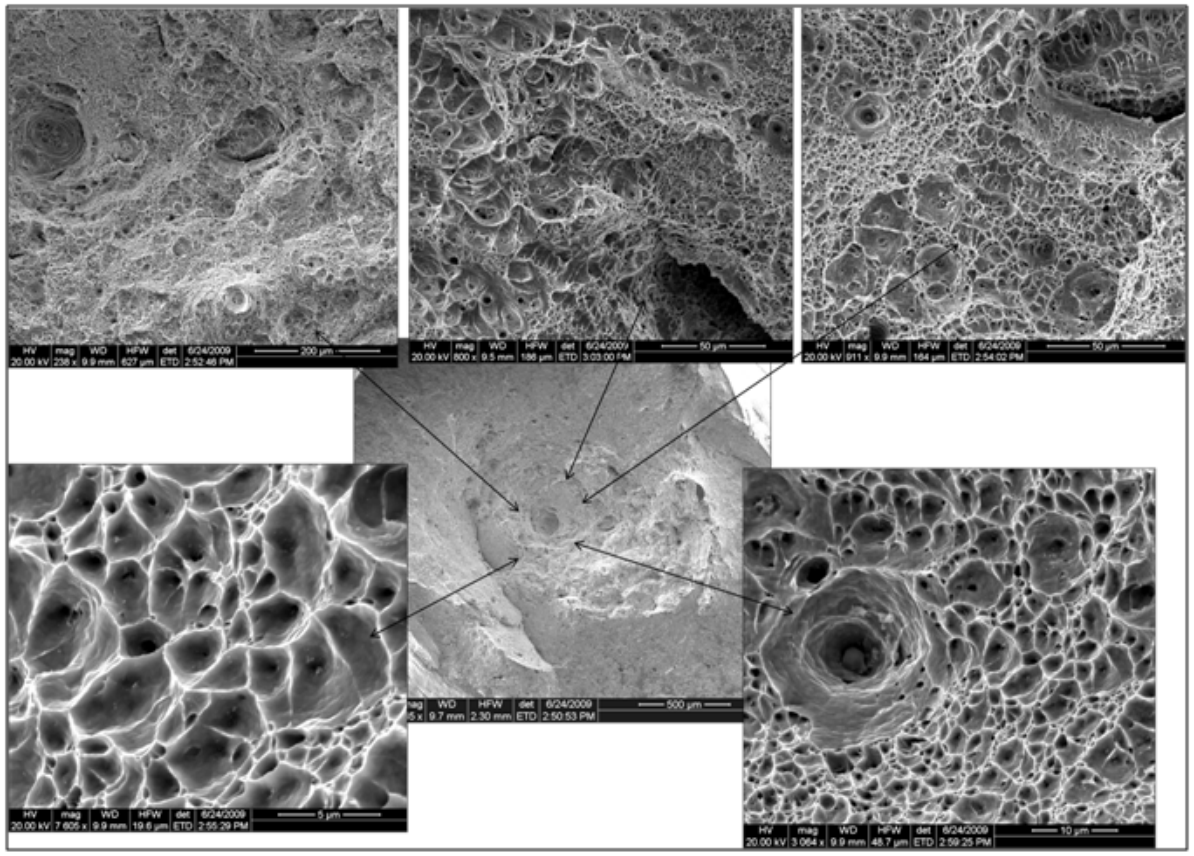

Fig. D.1 Fracture surfaces of the broken shallow notched bar sample 2B2-R.

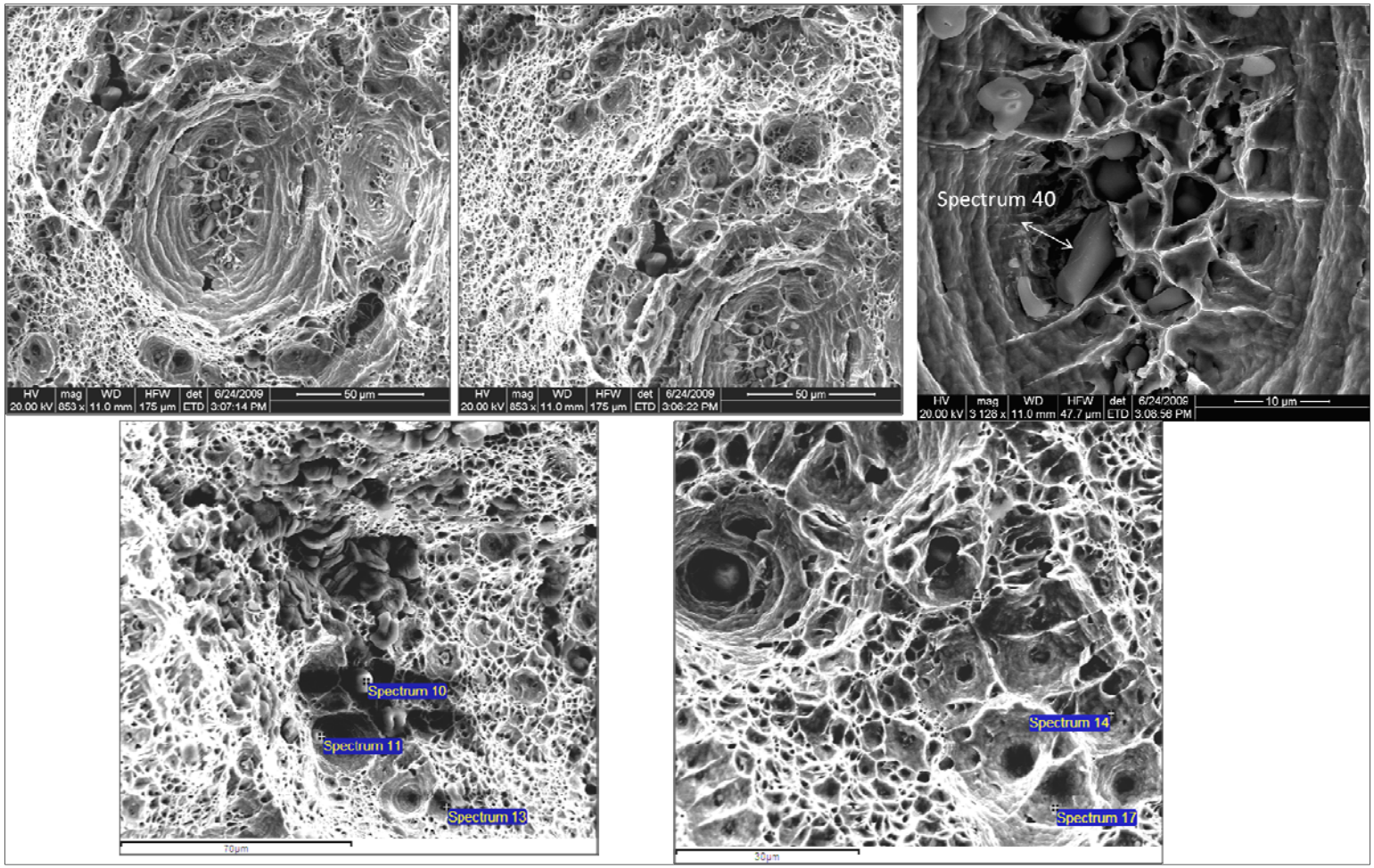

Fig. D.2 Fracture surfaces taken from the center of the broken shallow notched bar sample 2B2-R.

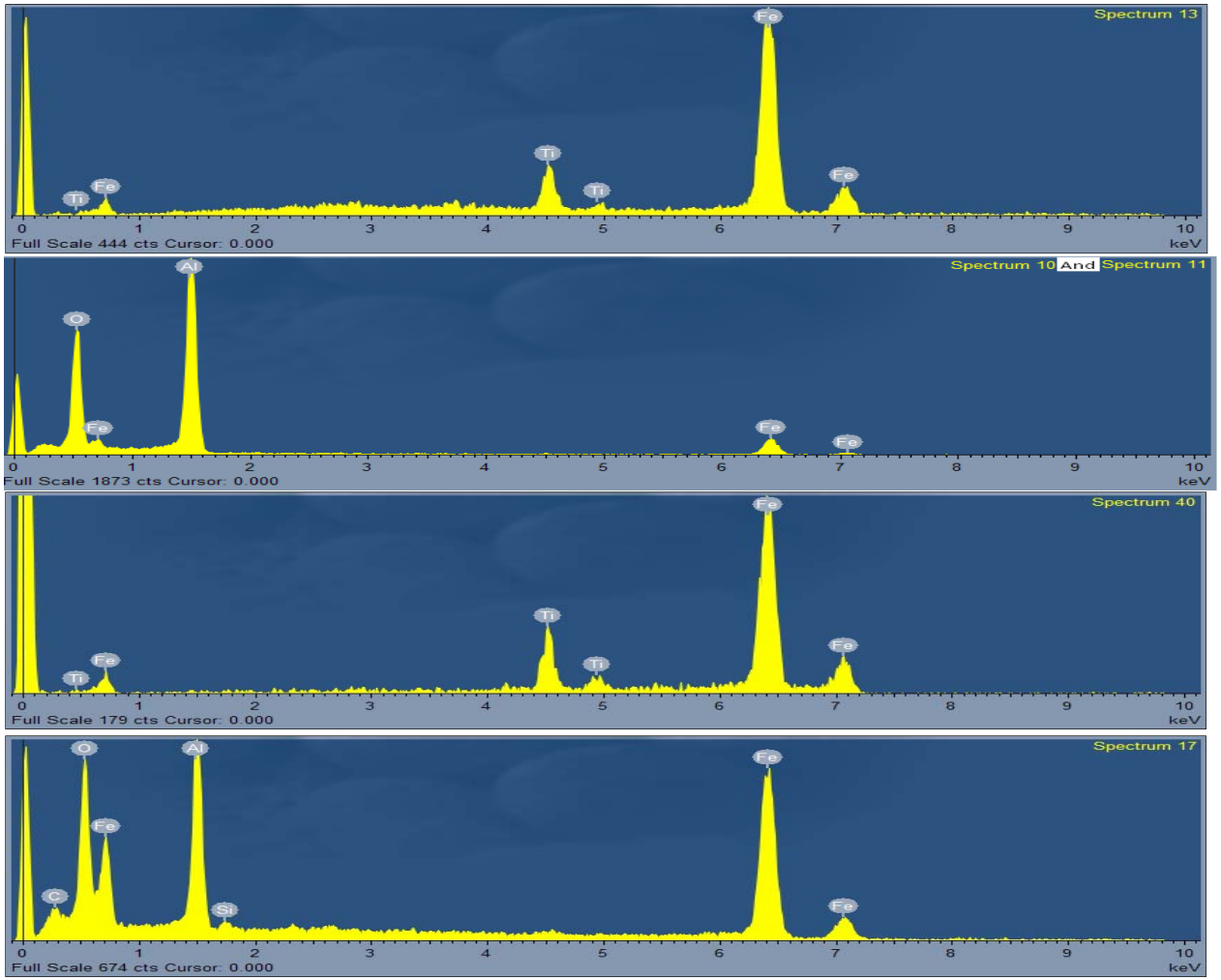

Fig. D.3 EDS energy spectrum diagram of the broken shallow notched bar sample 2B2-R.

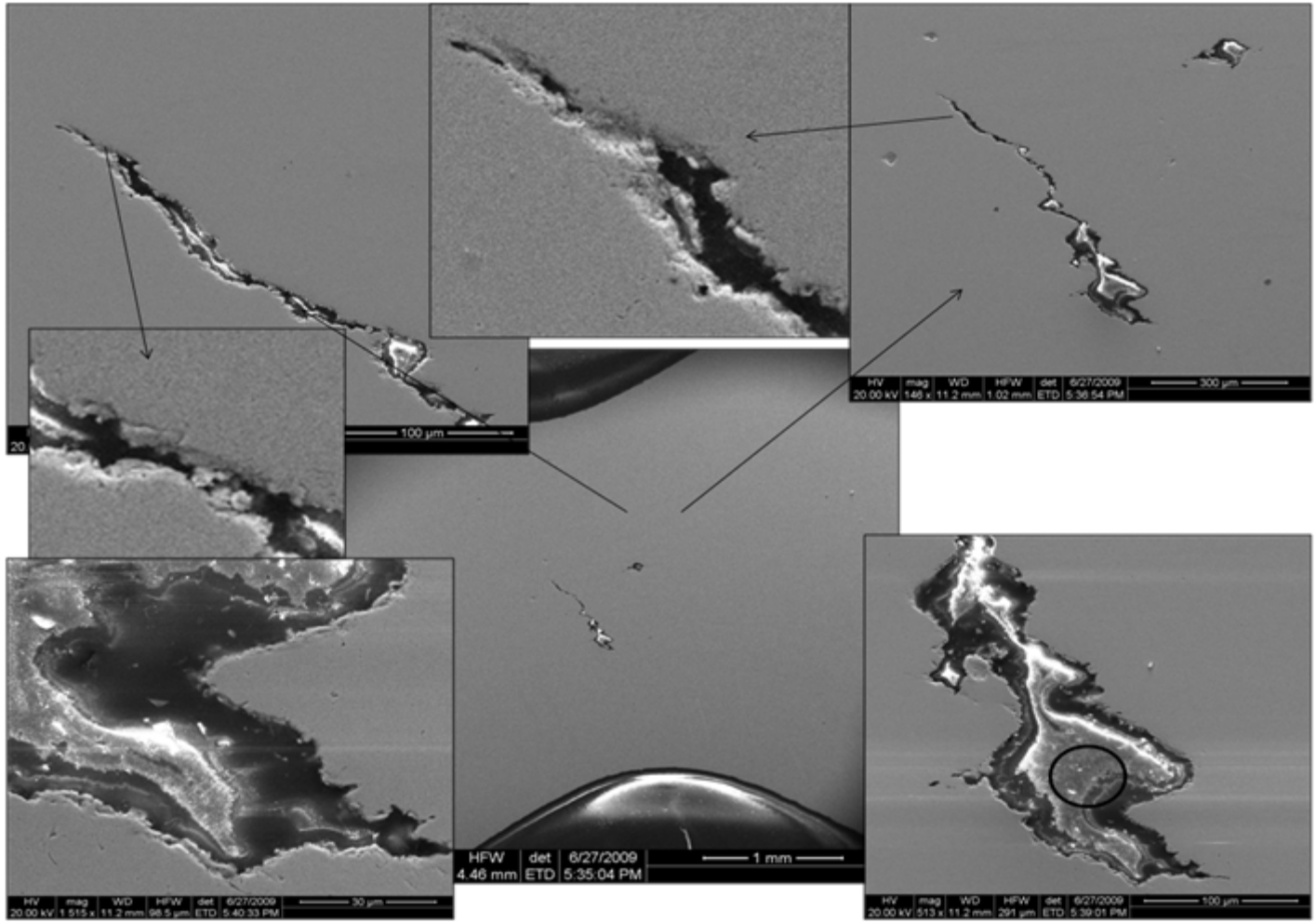

Fig. D.4 Crack initiation and propagation of the shallow notched bar sample 1B2-I.

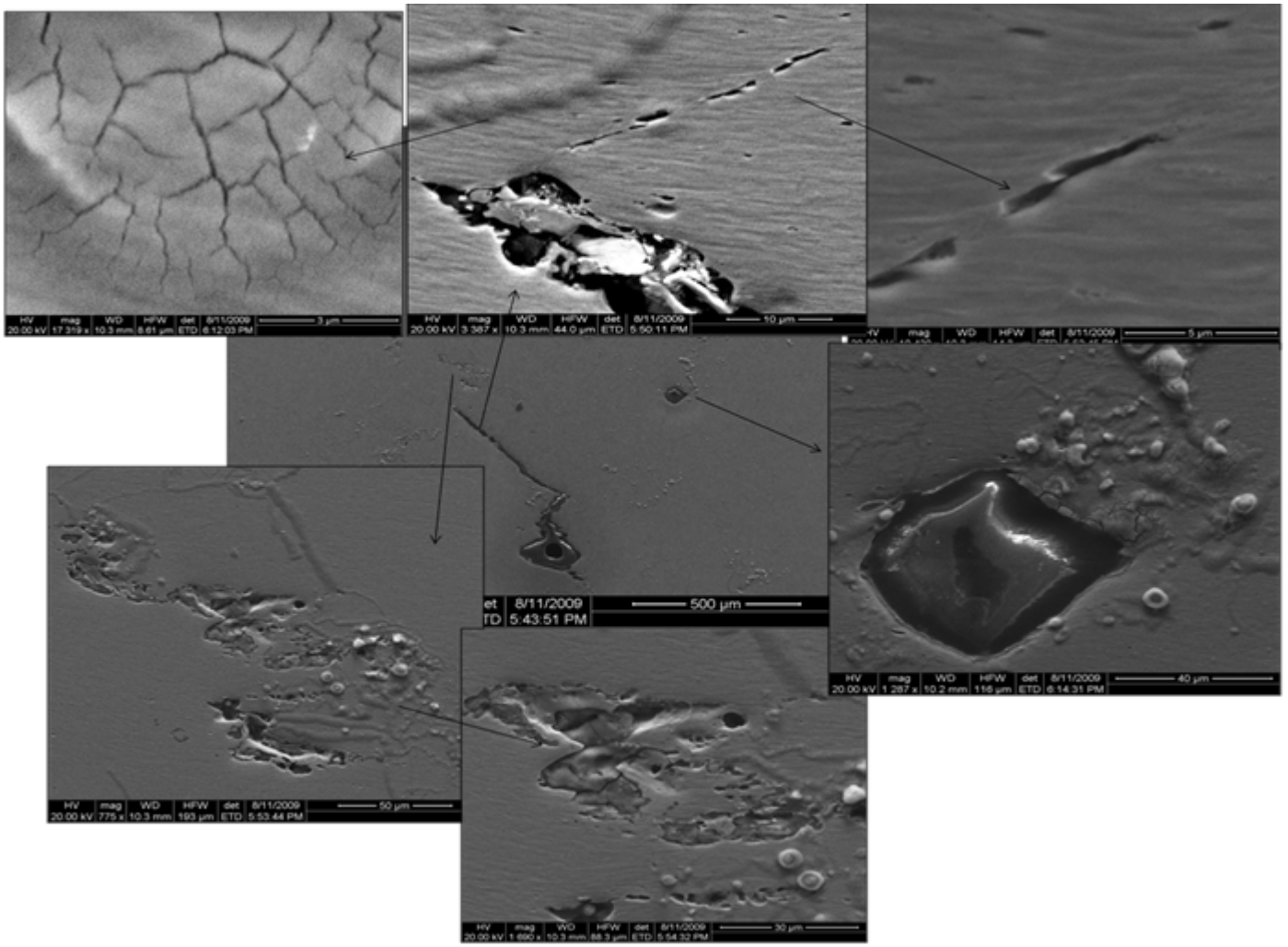

Fig. D.5 Crack initiation and propagation of the shallow notched bar sample 1B2-I.

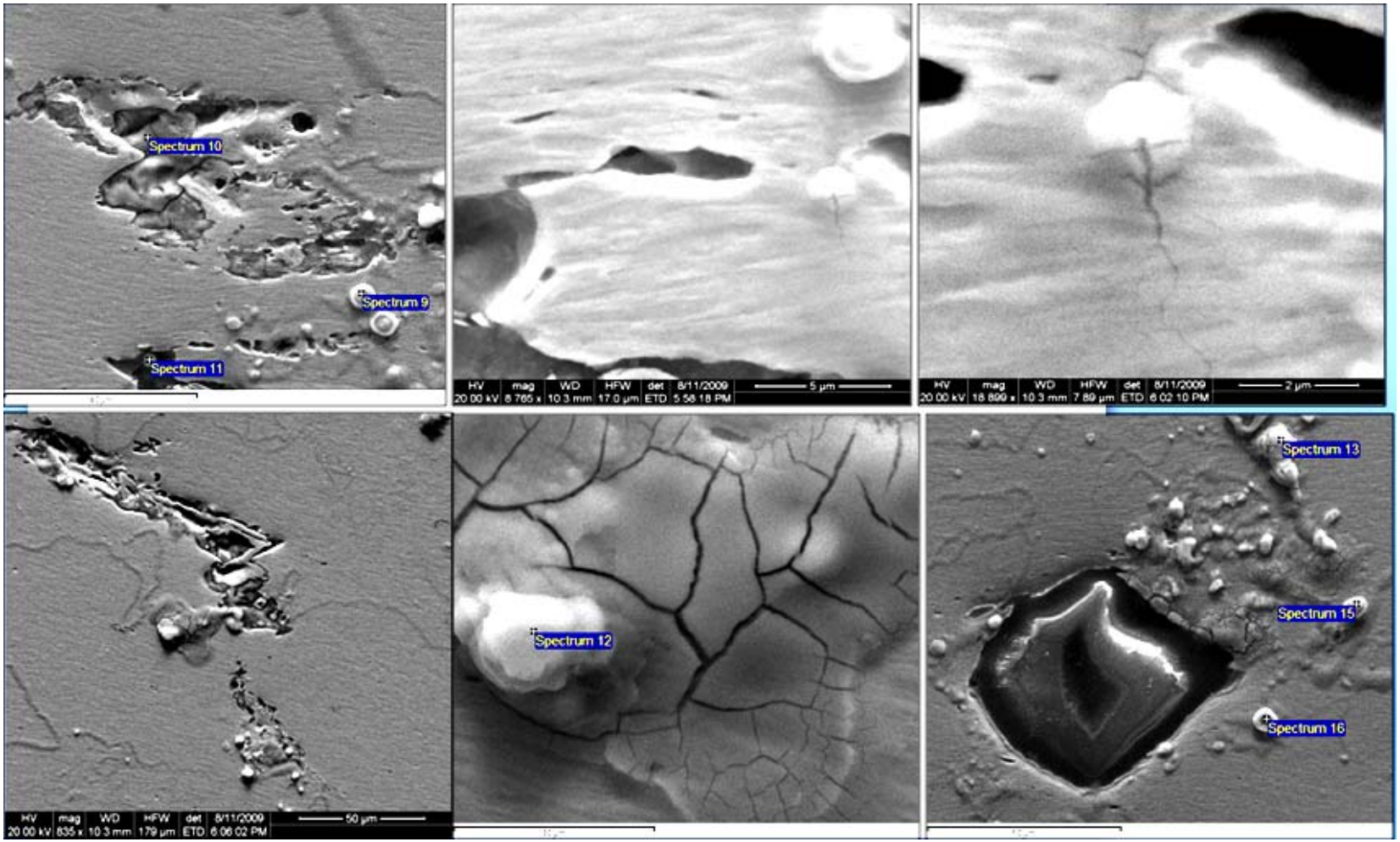

Fig. D.6 More crack initiation and propagation images of the crack edges of the shallow notched bar sample 1B2-I.

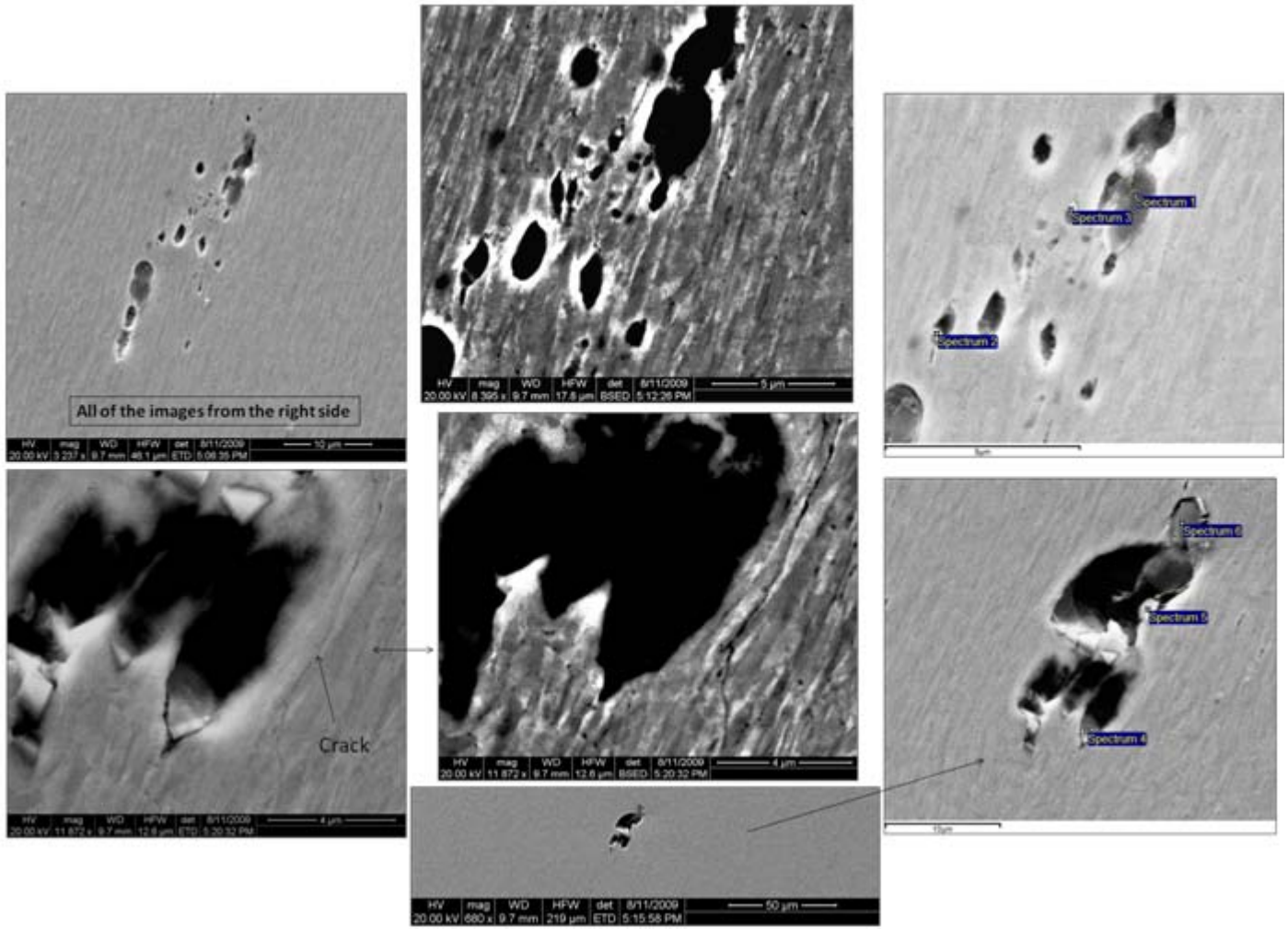

Fig. D.7 More crack initiation and propagation images of the crack edges of the shallow notched bar sample 2B5-I.

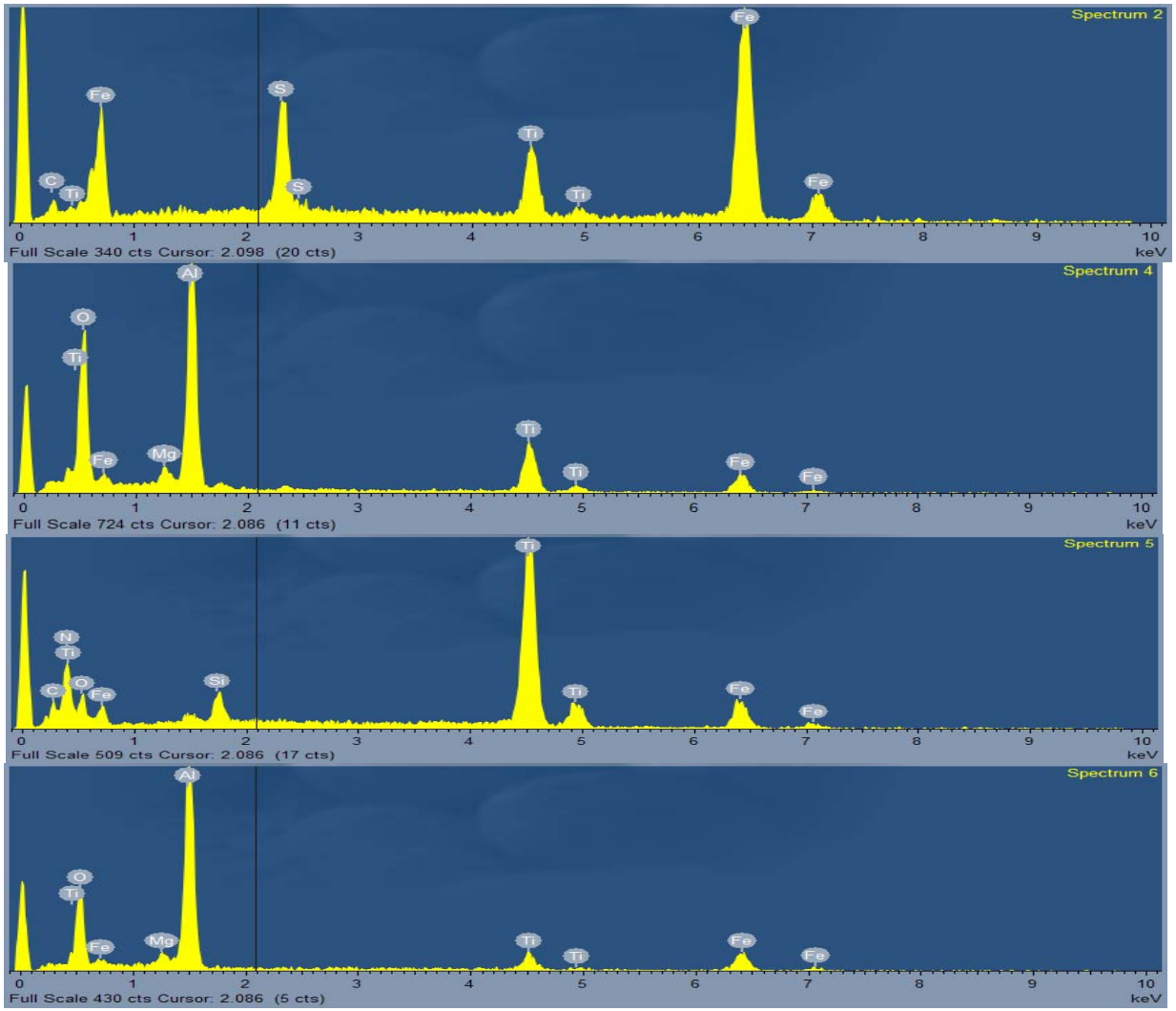

Fig. D.8 EDS energy spectrum diagram of the interrupted shallow notched bar sample 2B5-I.

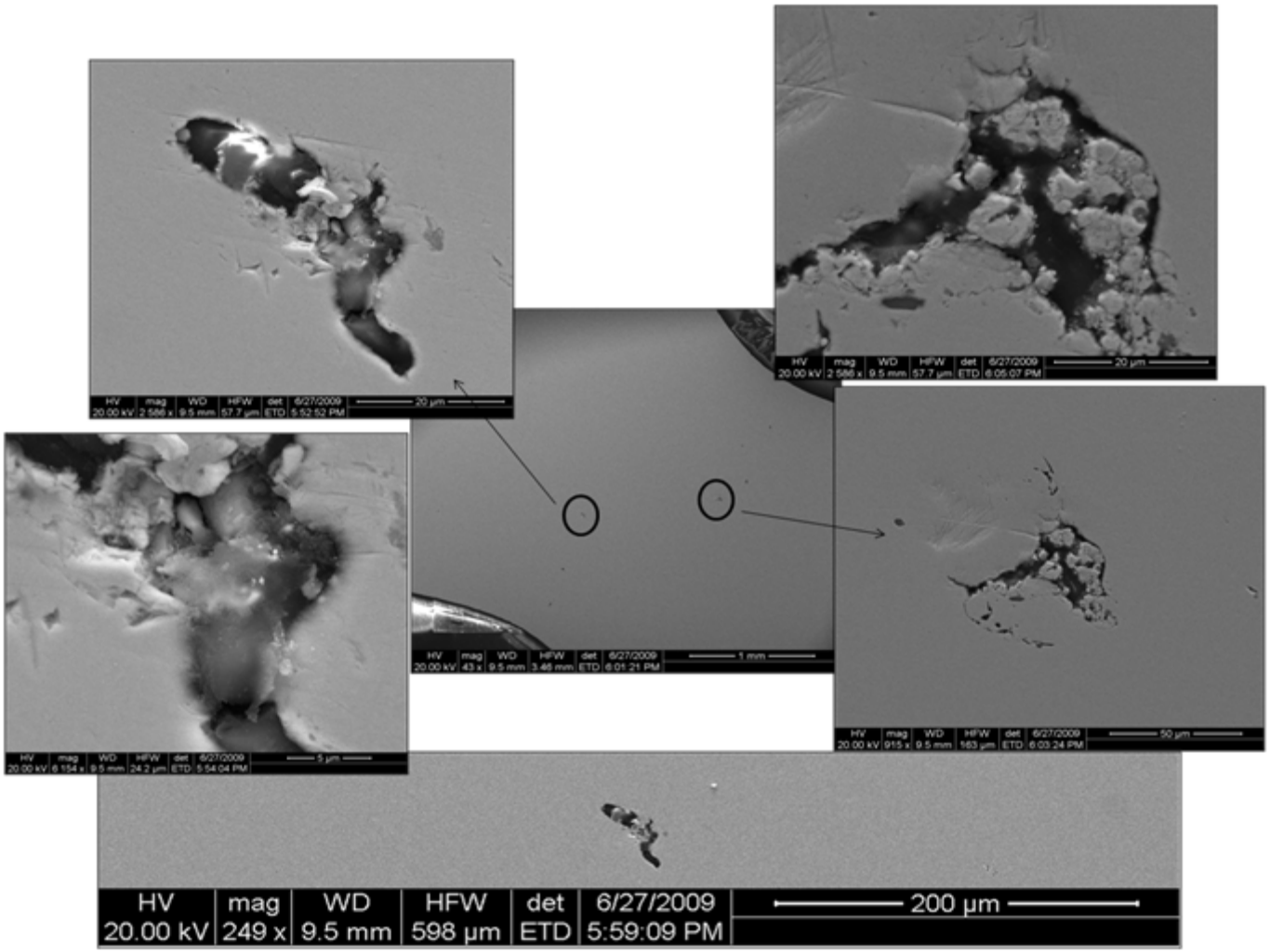

Fig. D.9 Crack initiation and propagation images of the crack edges of the shallow notched bar sample 3T6-I.

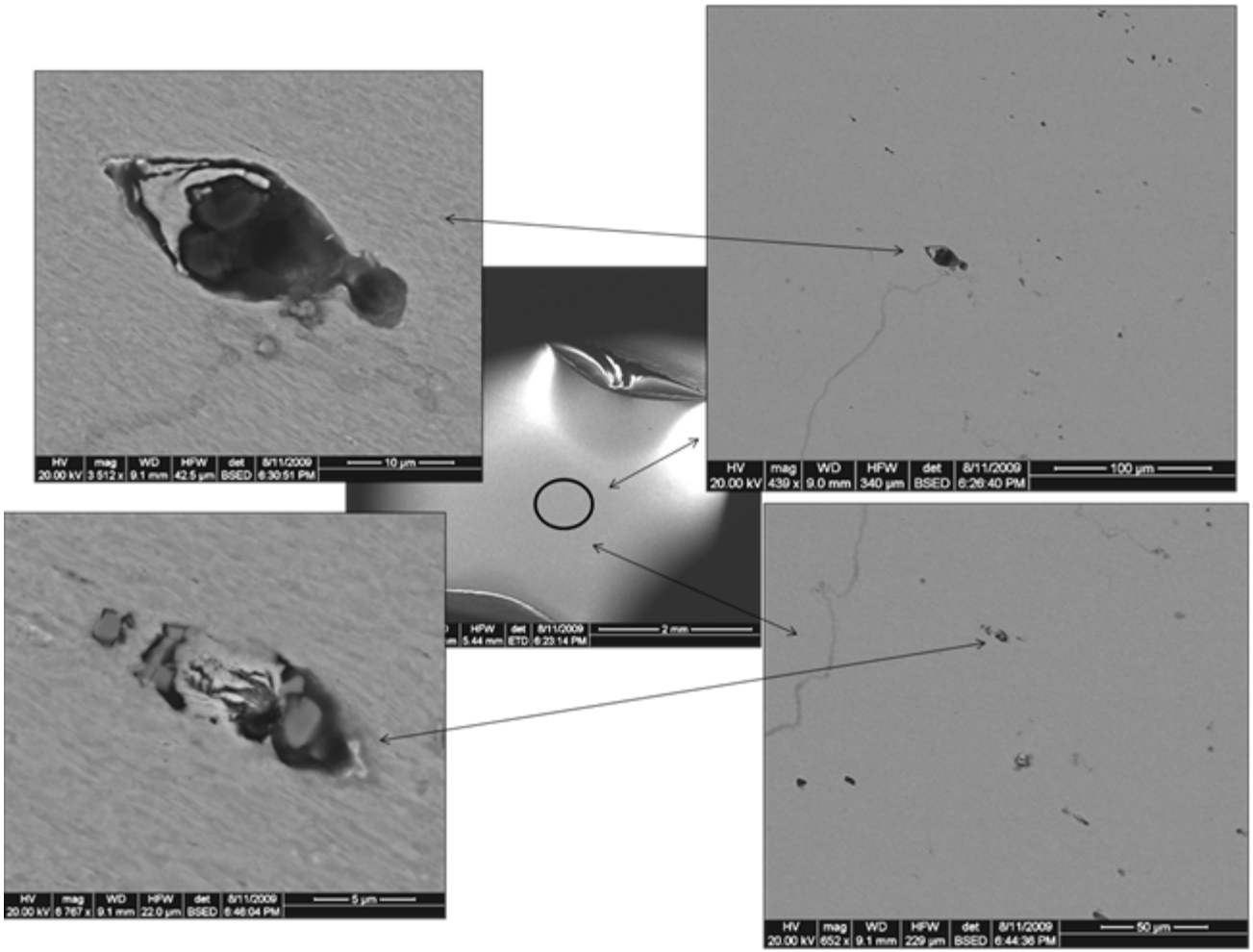

Fig. D.10 More crack initiation images of the crack edges of the shallow notched bar sample 3T6-I.

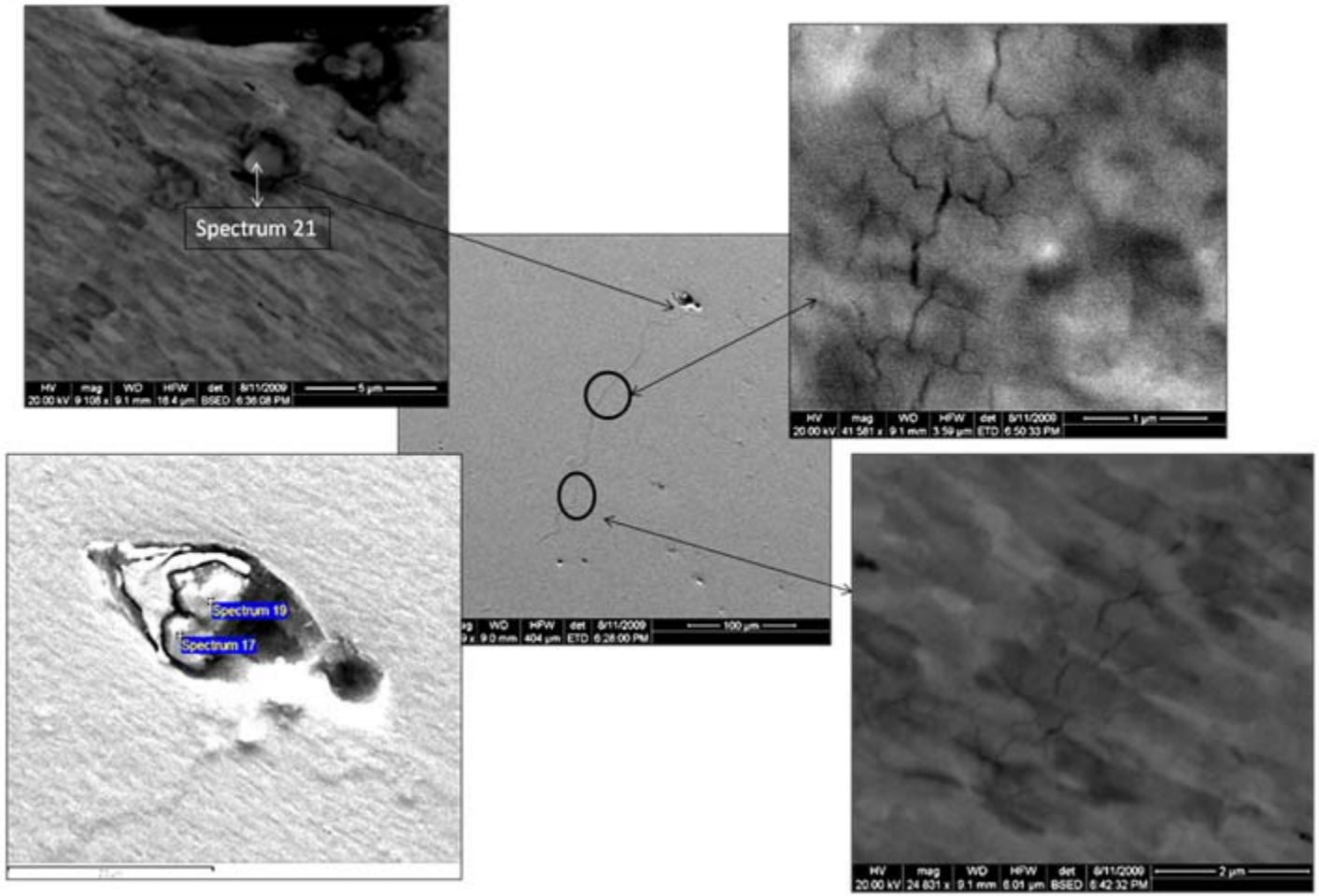

Fig. D.11 More crack initiation and propagation images of the crack edges of the shallow notched bar sample 3T6-I..

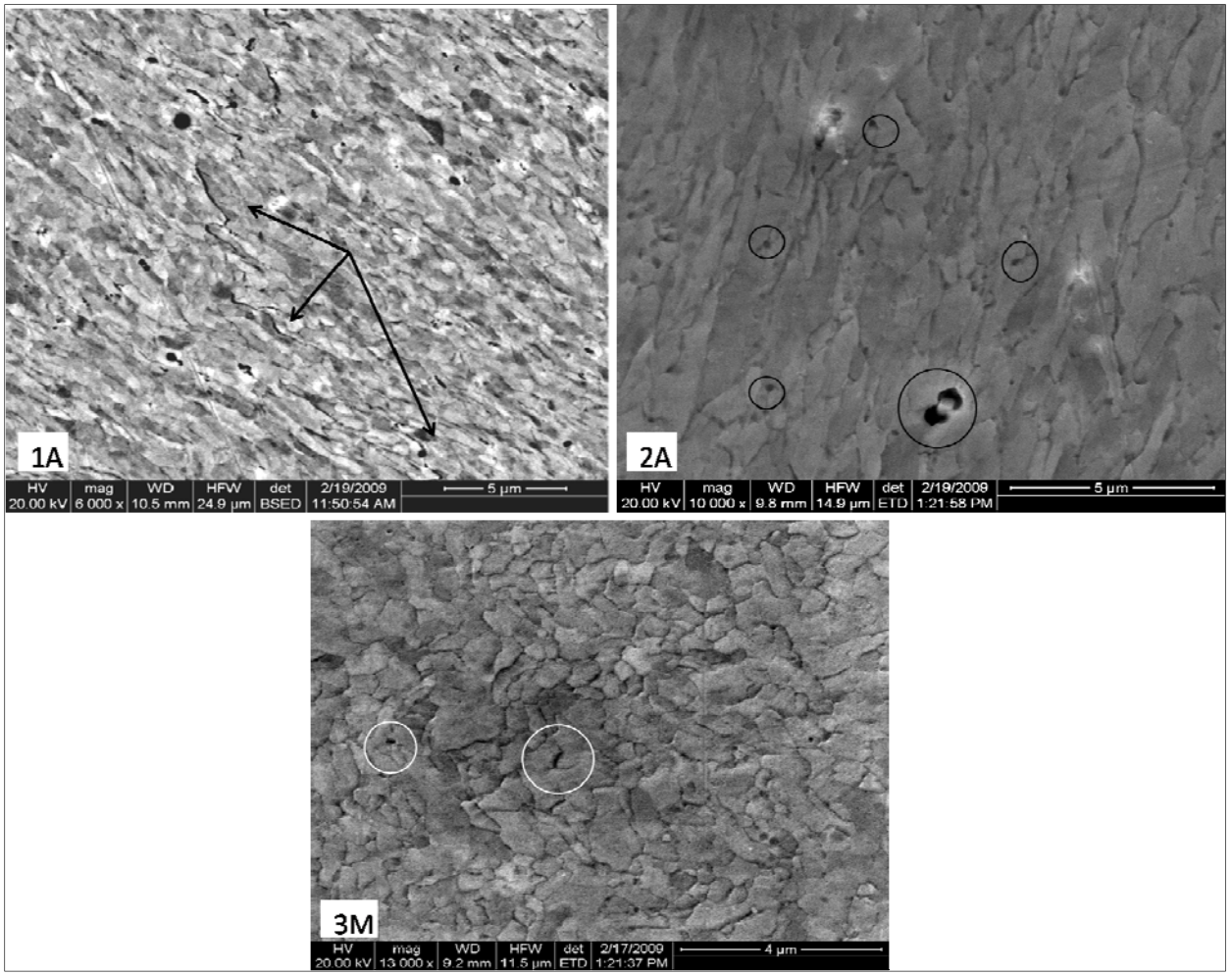

Fig. D.12 Microstructure images from the three billets showing the possible kind of defects in the materials, 1A which has been taken from billet 1 shows a microcrack, 2A which has been taken from billet 2 shows triple junction and vacancies, 3M which has been taken from billet 3 shows vacancies.

Sharp notched bar samples fractographs

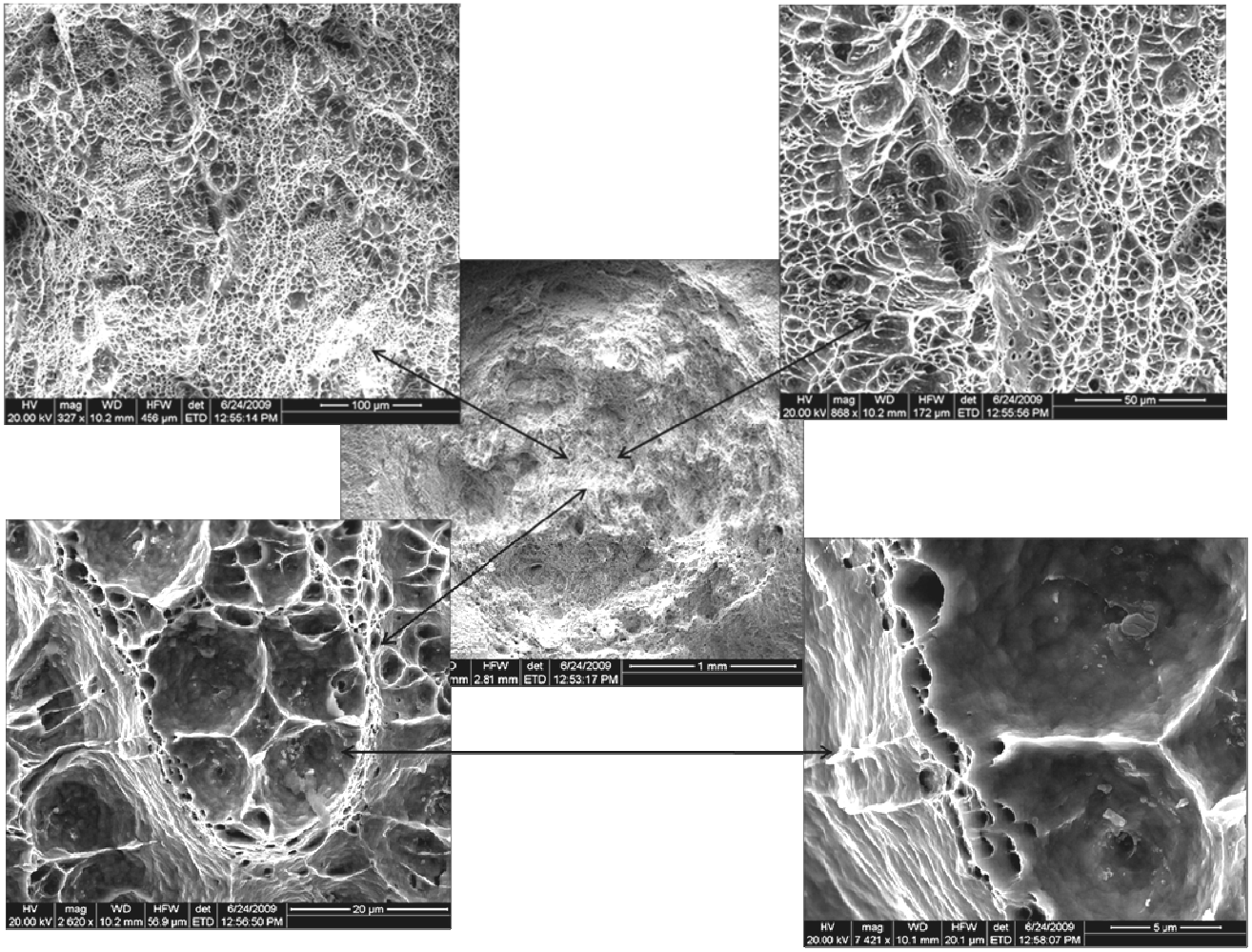

Fig. D.13 Fracture surfaces of the broken sharp notched bar sample 1T3-R.

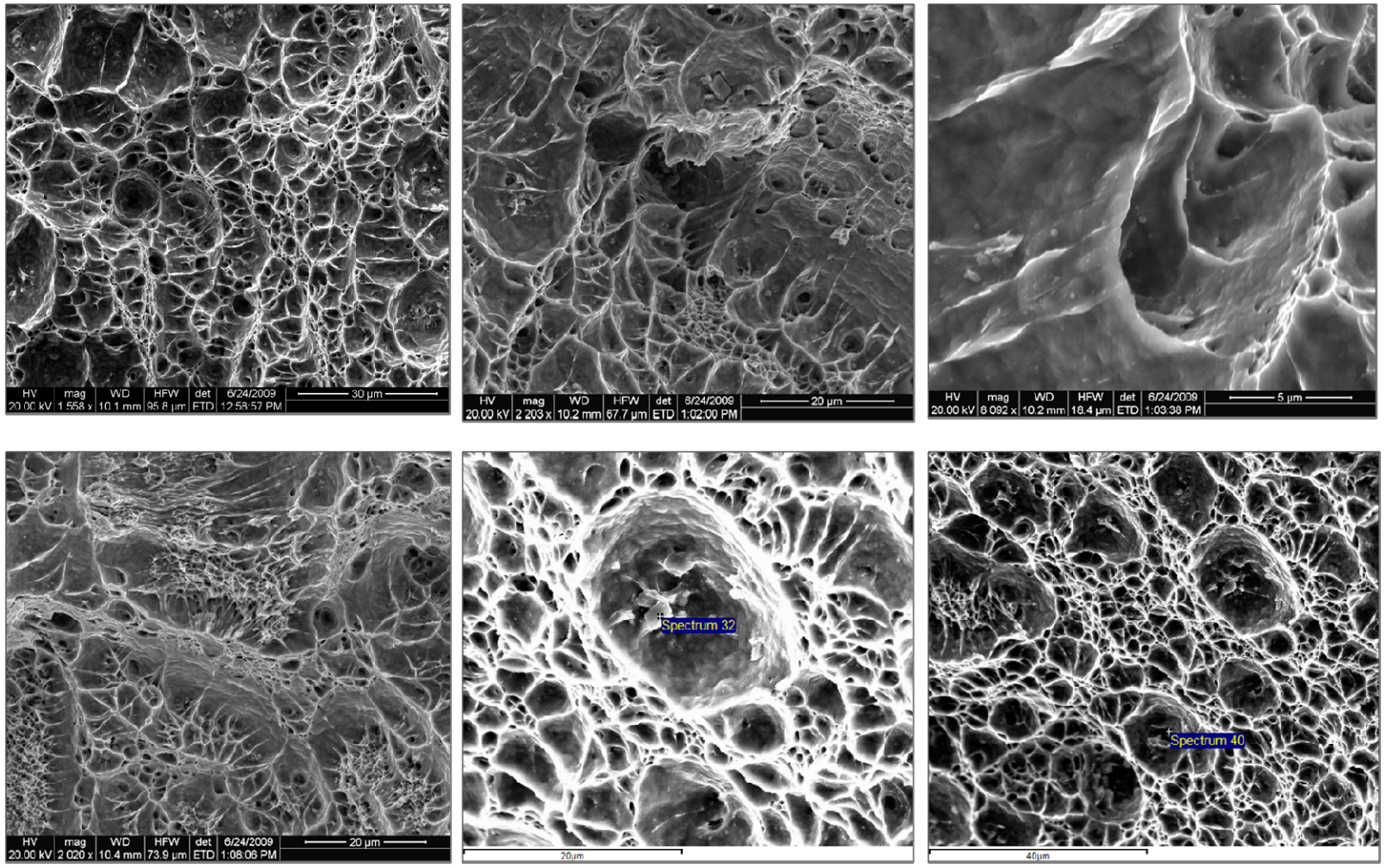

Fig. D.14 Fracture surfaces taken from the center of the broken sharp notched bar sample 1T3-R.

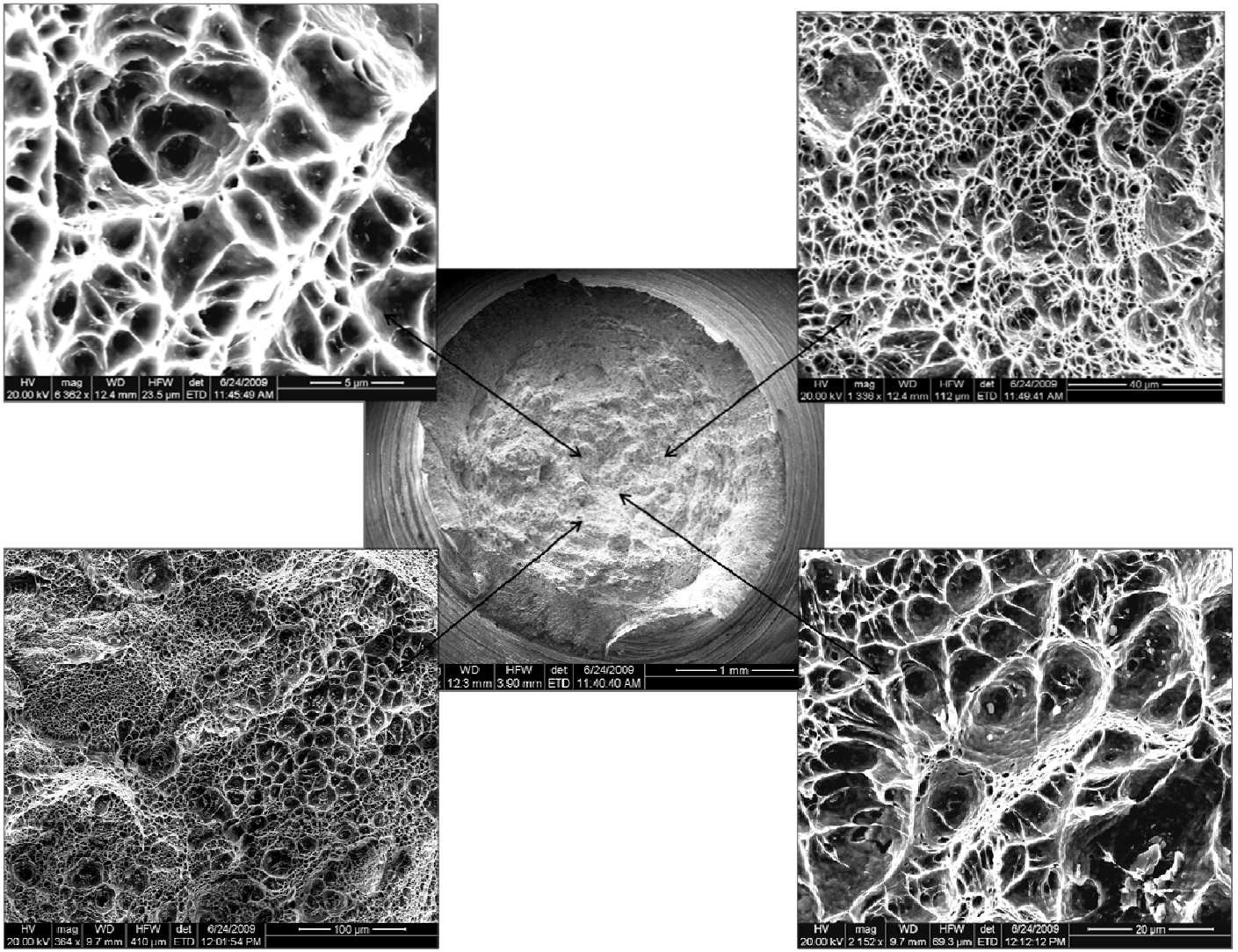

Fig. D.15 Fracture surfaces taken from the broken sharp notched bar sample 3T4-R.

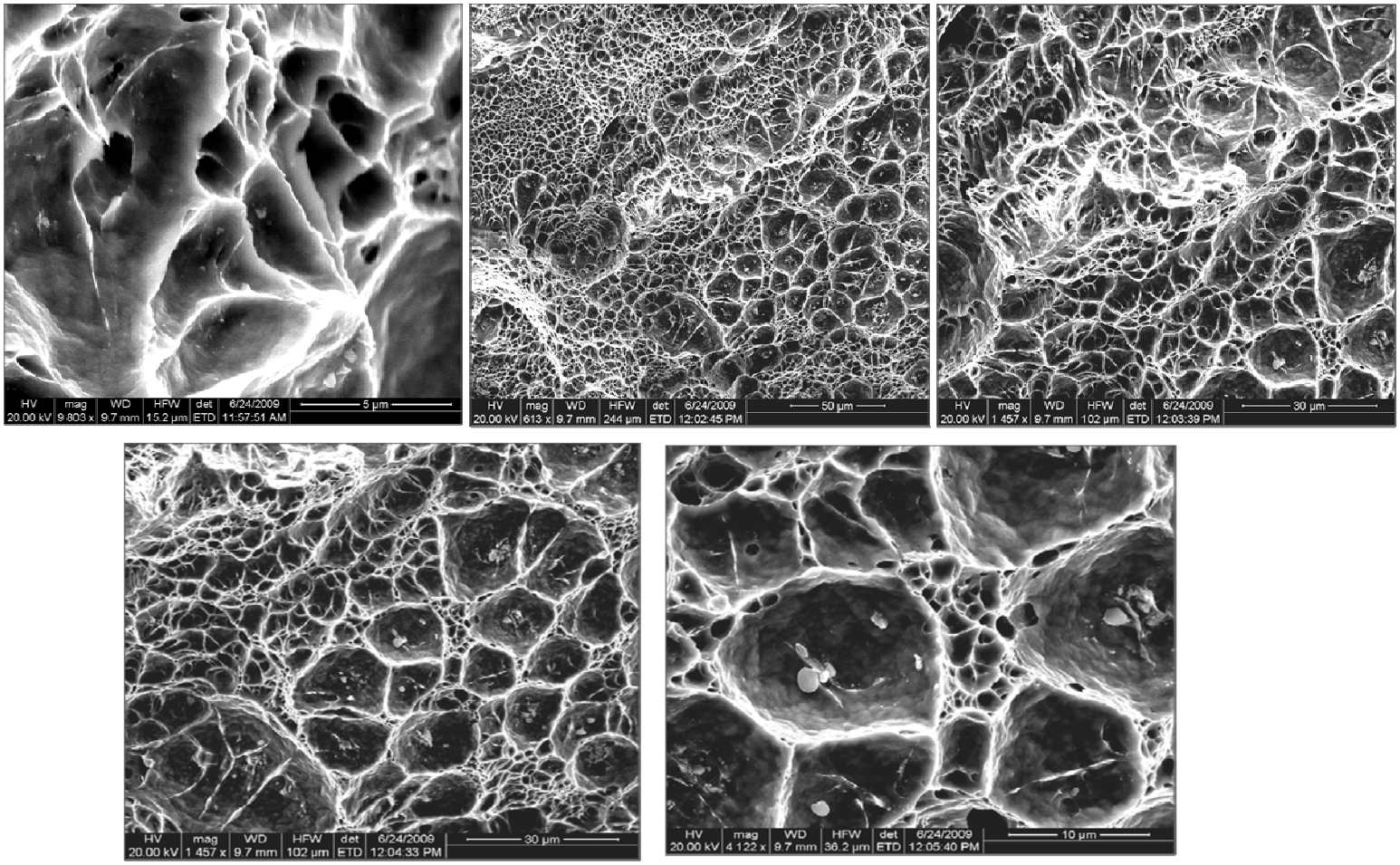

Fig. D.16 More fracture surfaces taken from the broken sharp notched bar sample 3T4-R.

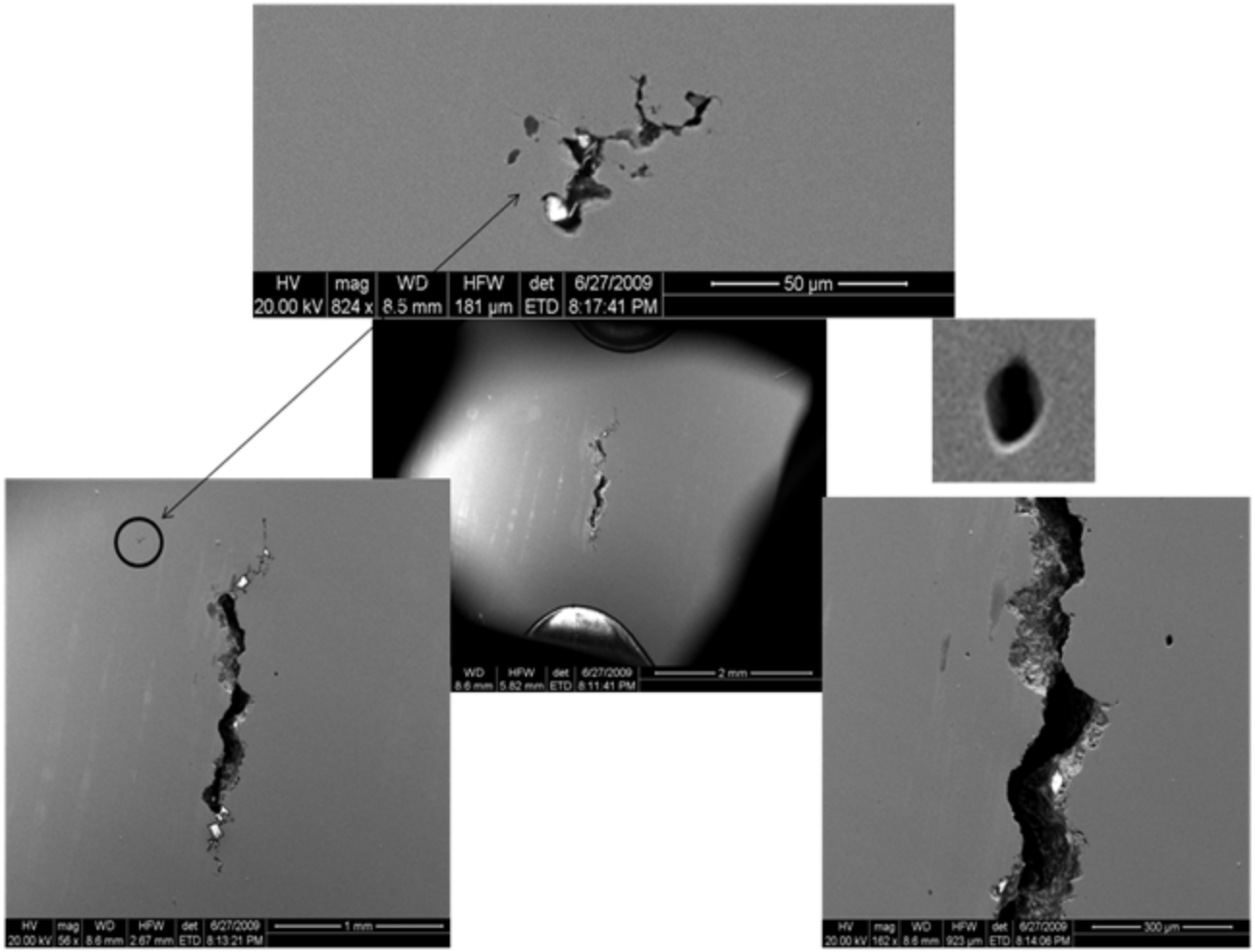

Fig. D.17 Crack initiation and propagation of the sharp notched bar sample 1B4-I.

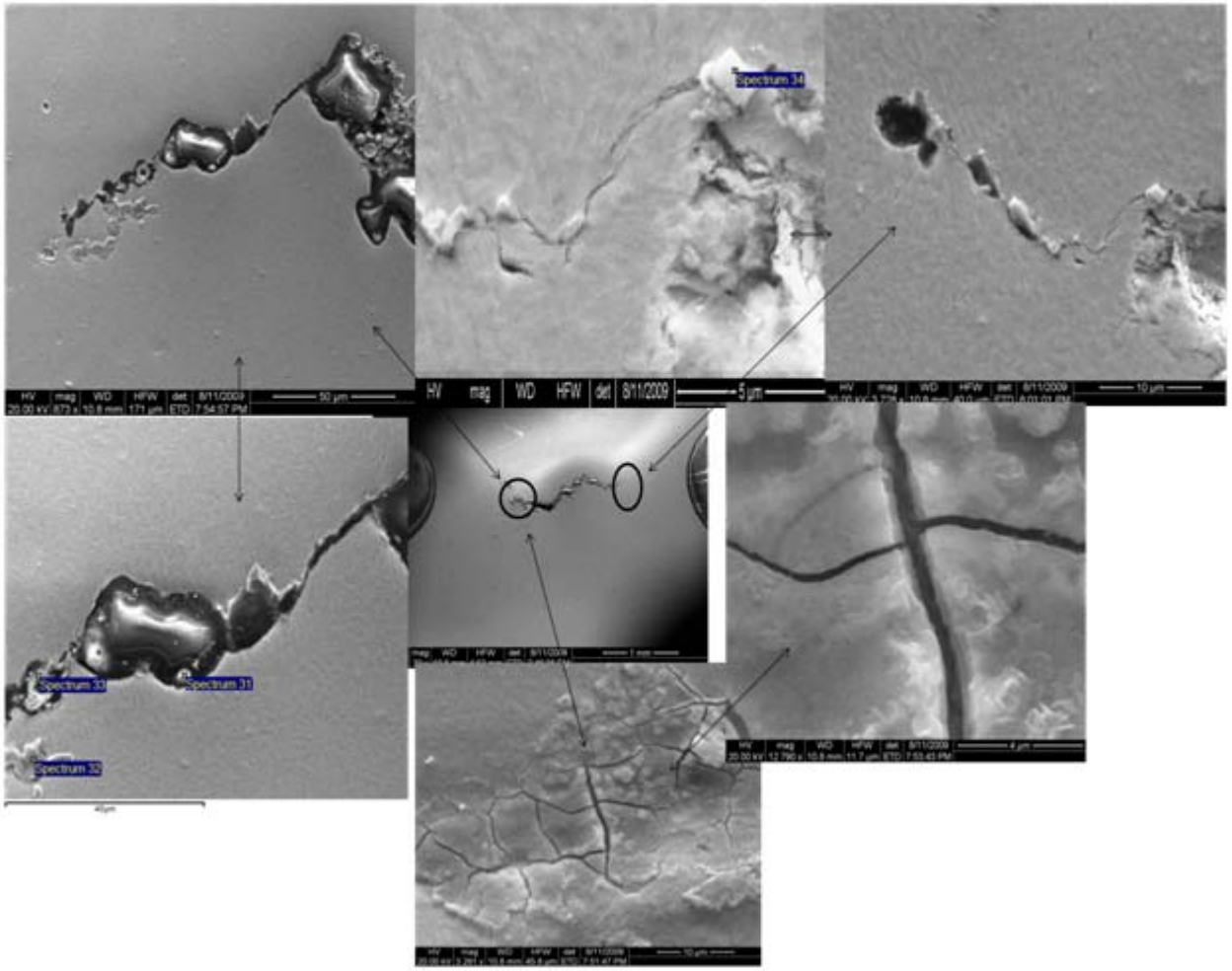

Fig. D.18 Crack initiation and propagation of the sharp notched bar sample 1T4-I.

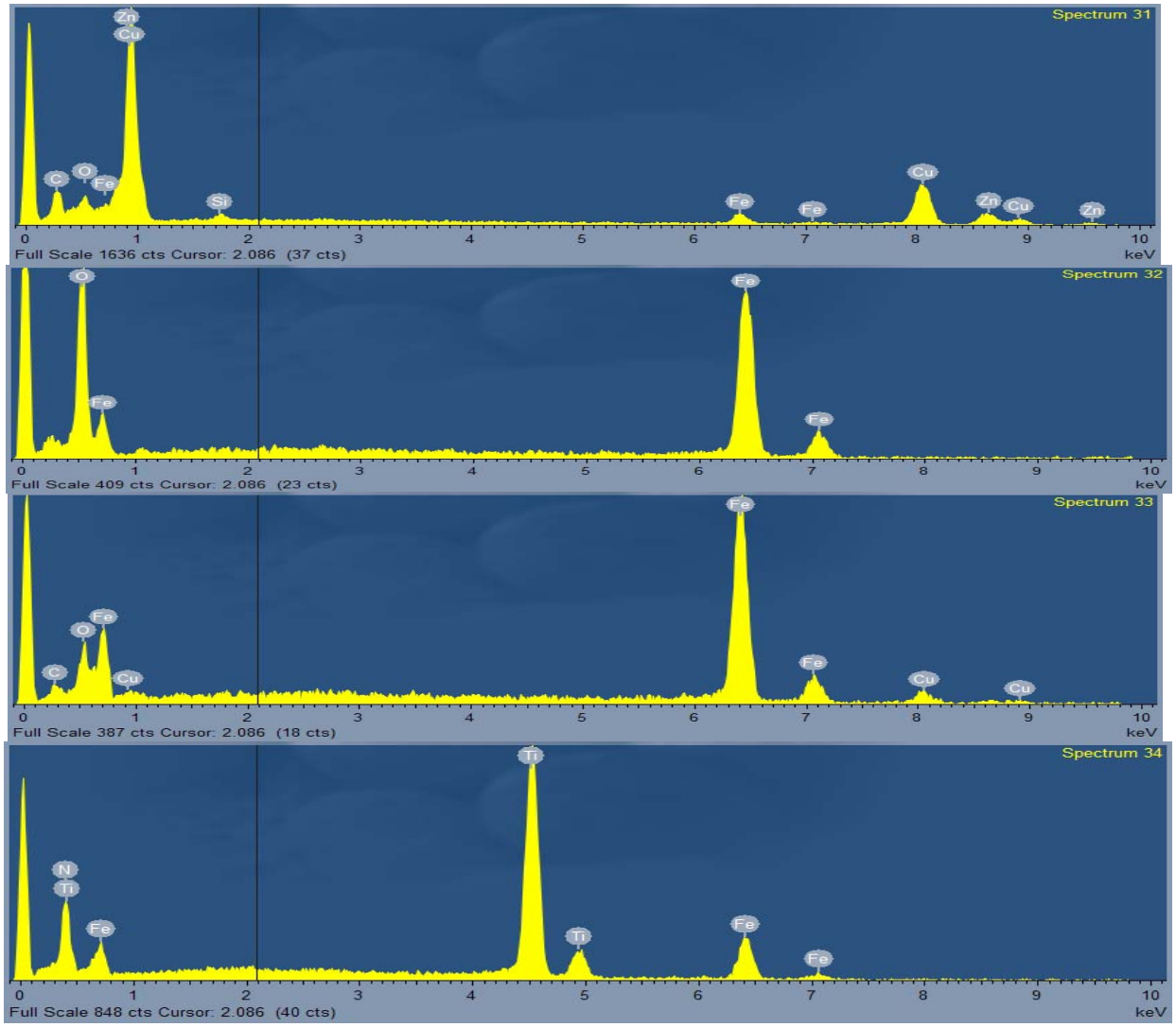

Fig..D.19 EDS energy spectrum diagram of the interrupted sharp notched bar sample 1T4-I.

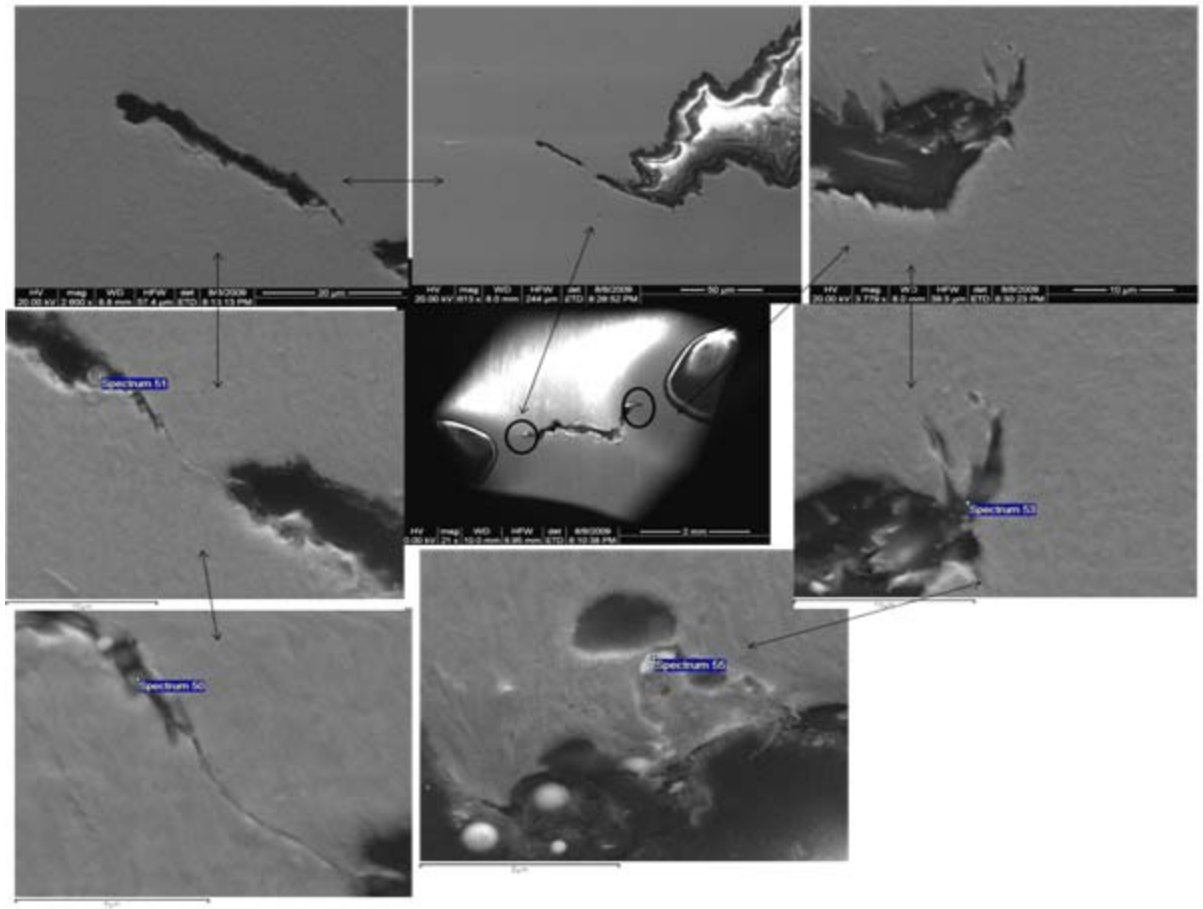

Fig. D.20 Crack initiation and propagation of the sharp notched bar sample 2T3-I.

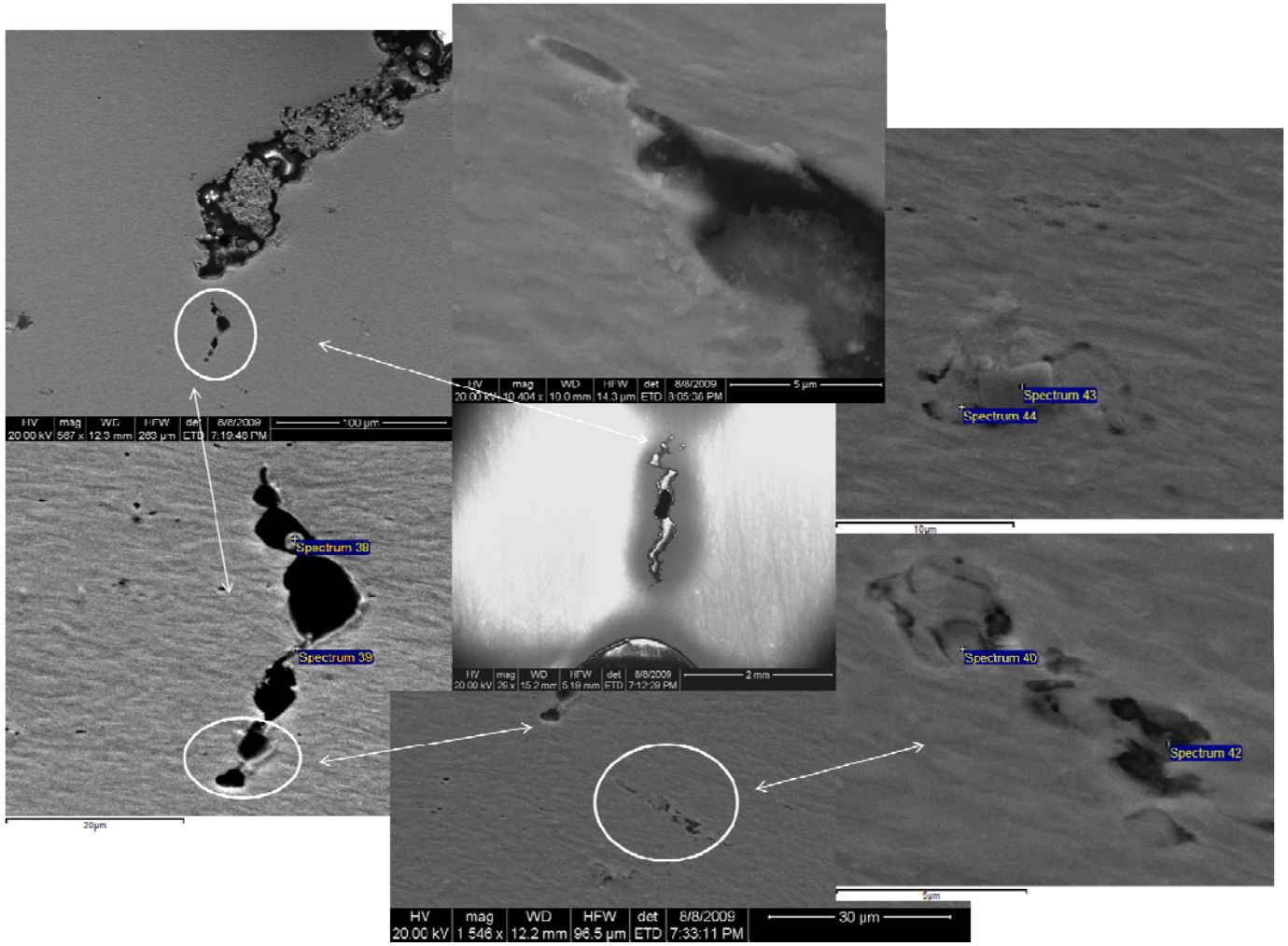

Fig. D.21 More crack initiation and propagation of the sharp notched bar sample 3T5-I.

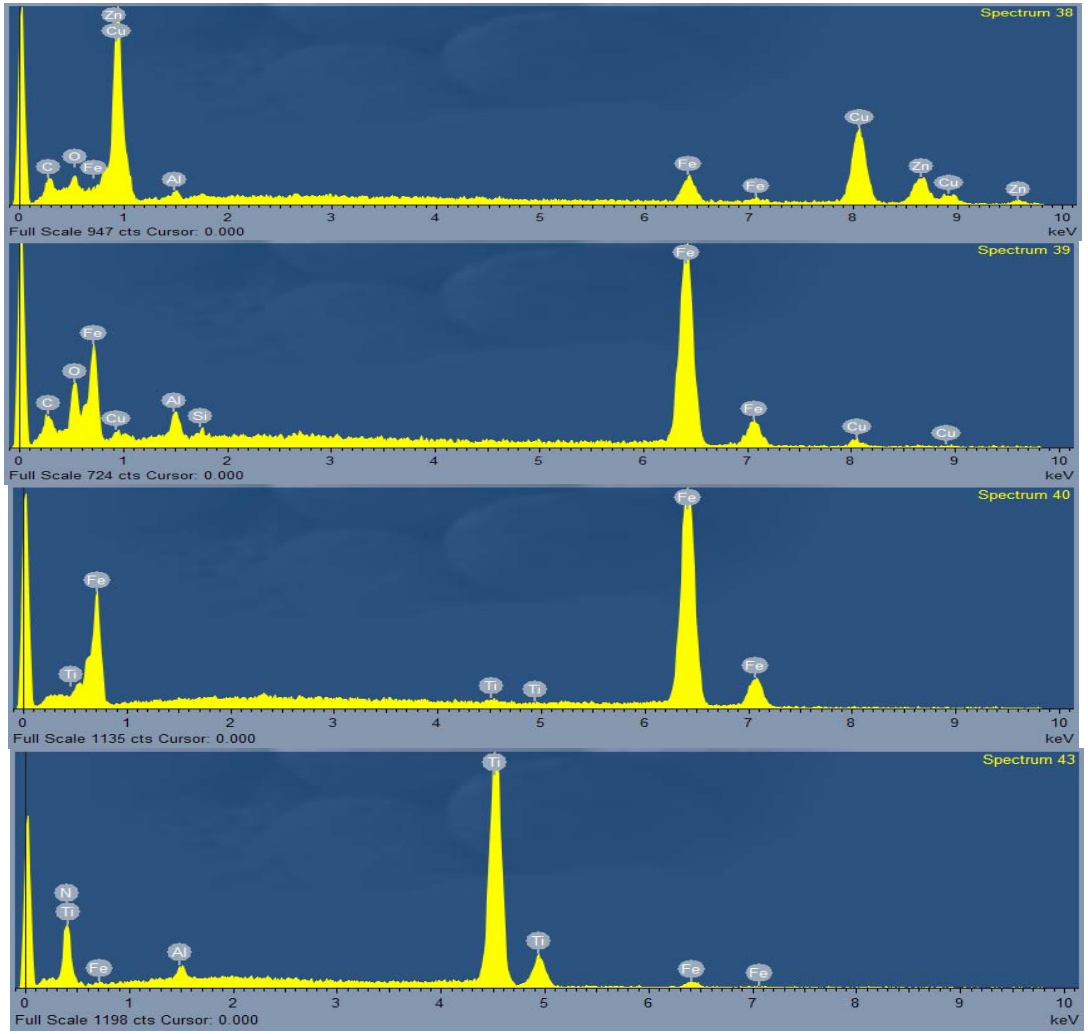

Fig. D.22 EDS energy spectrum diagram of the interrupted sharp notched bar sample 3T5-I.

APPENDIX E

ADDITIONAL FRACTOGRAPHS

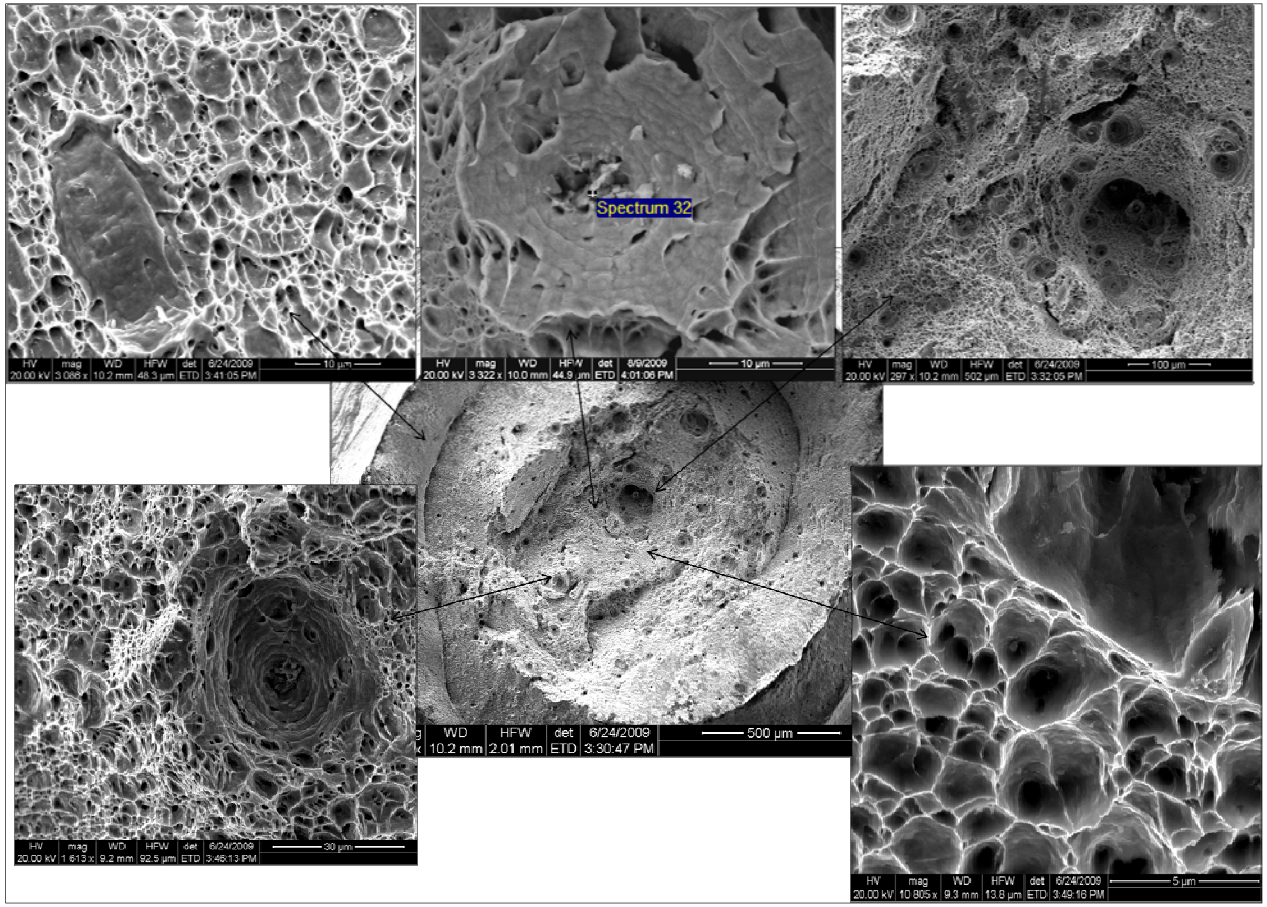

Fig. E.1 Fracture surfaces of the broken shallow notched bar sample 1T2-R.

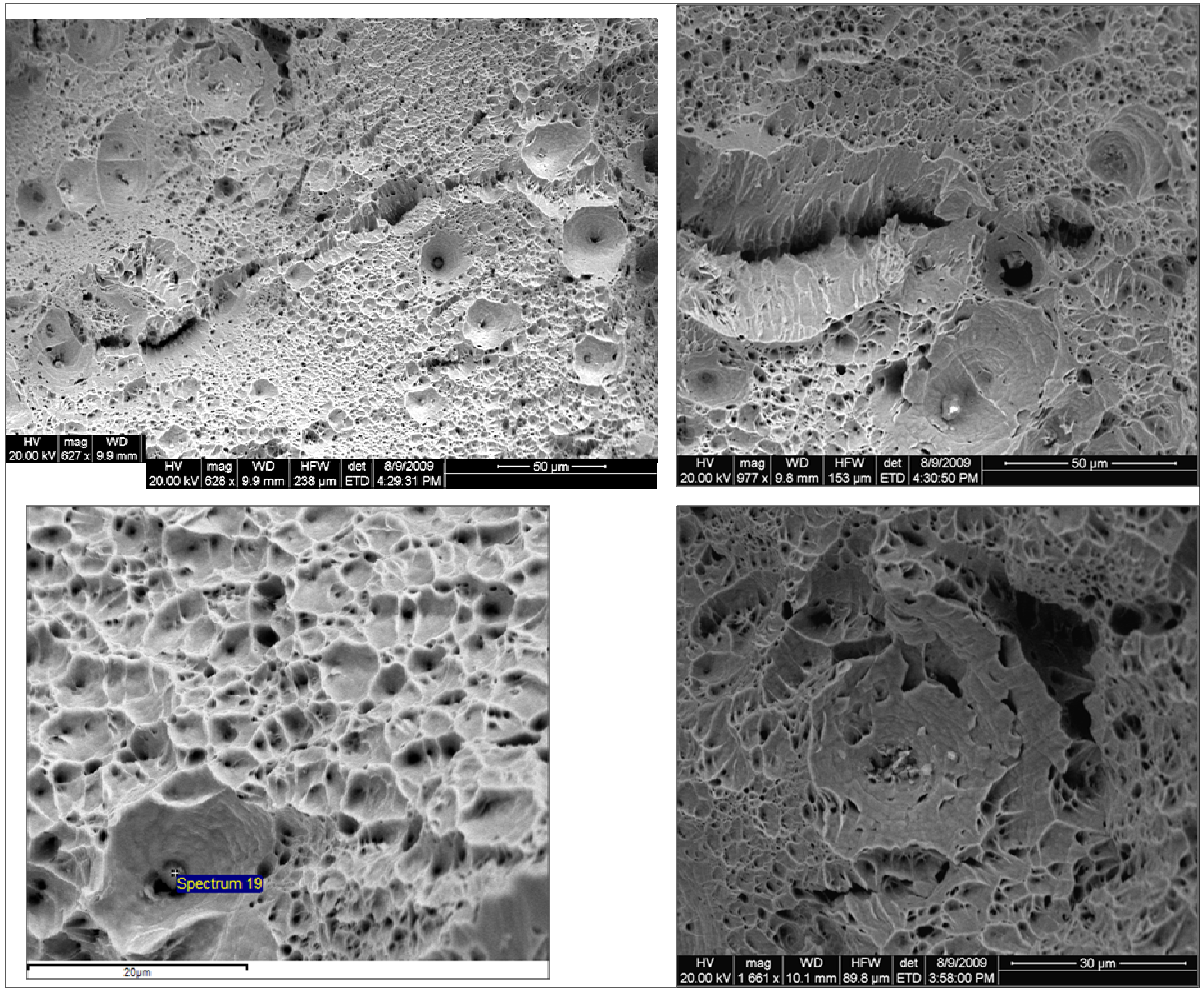

Fig. E.2 Fracture surfaces taken from the center of the broken shallow notched bar sample 1T2-R.

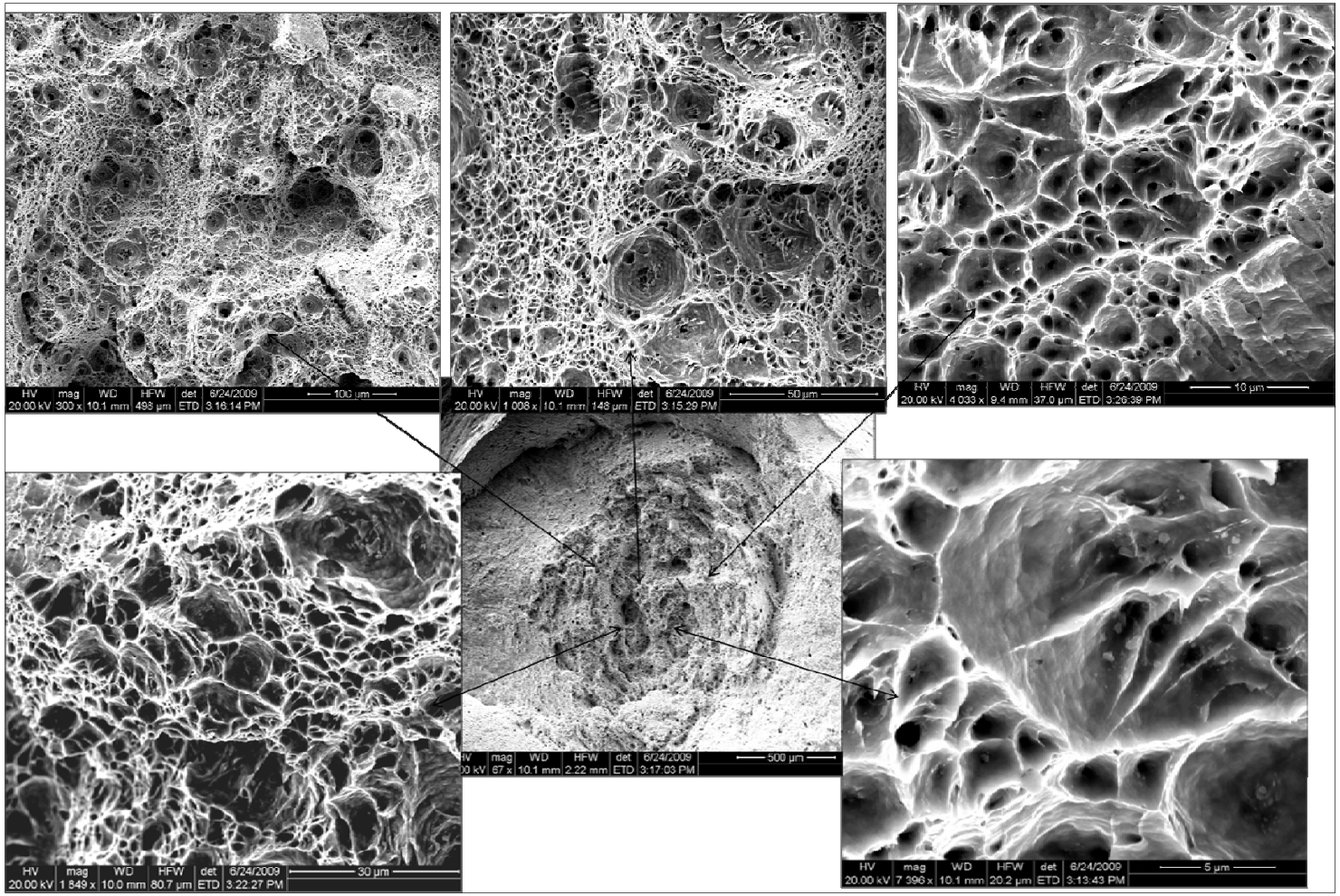

Fig. E.3 Fracture surfaces of the broken shallow notched bar sample 3T8-R.

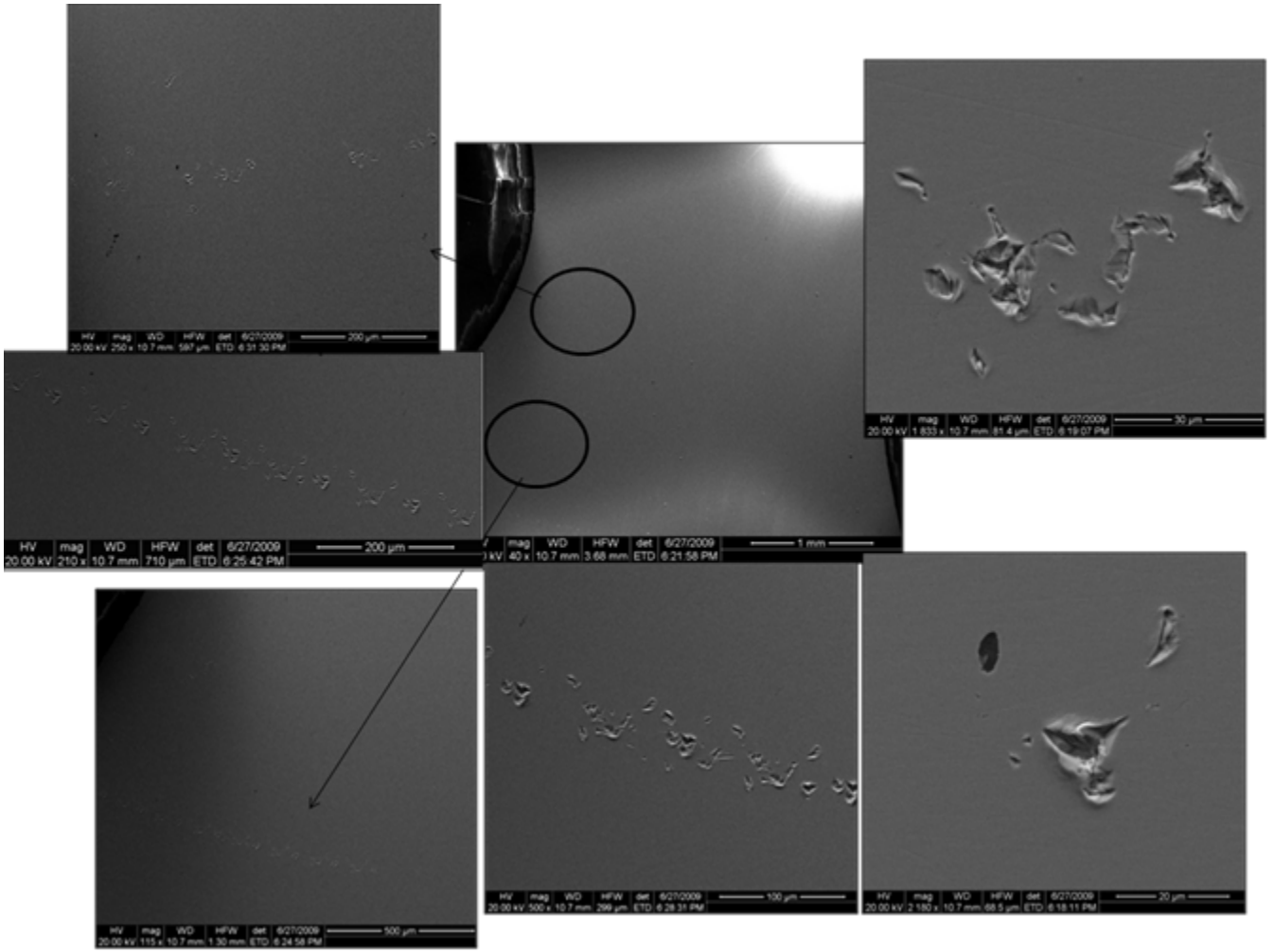

Fig. E.4 Crack initiation and propagation images of the crack edges of the shallow notched bar sample 1B5-I.

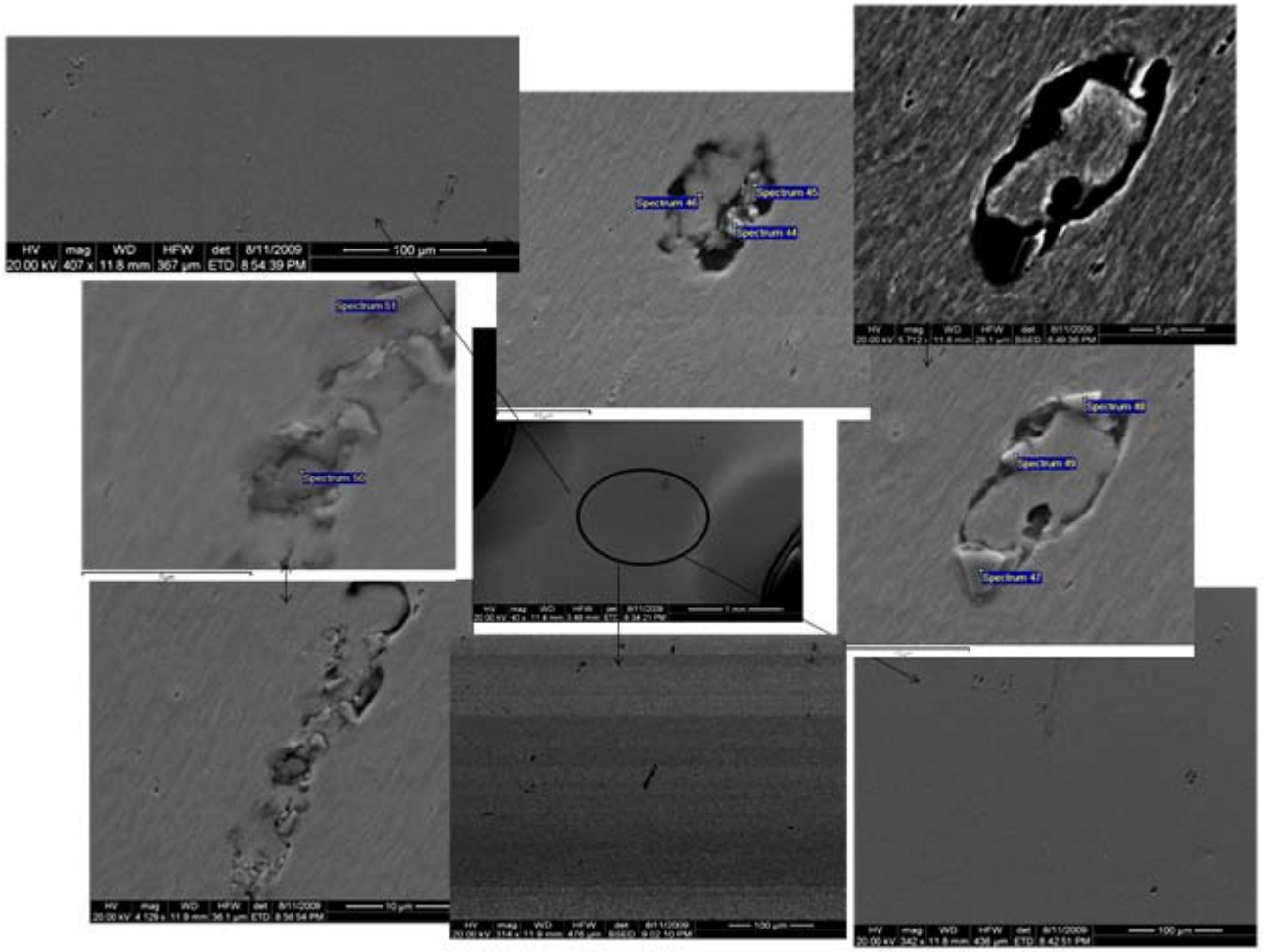

Fig. E.5 More crack initiation and propagation images of the crack edges of the shallow notched bar sample 1B5-I.

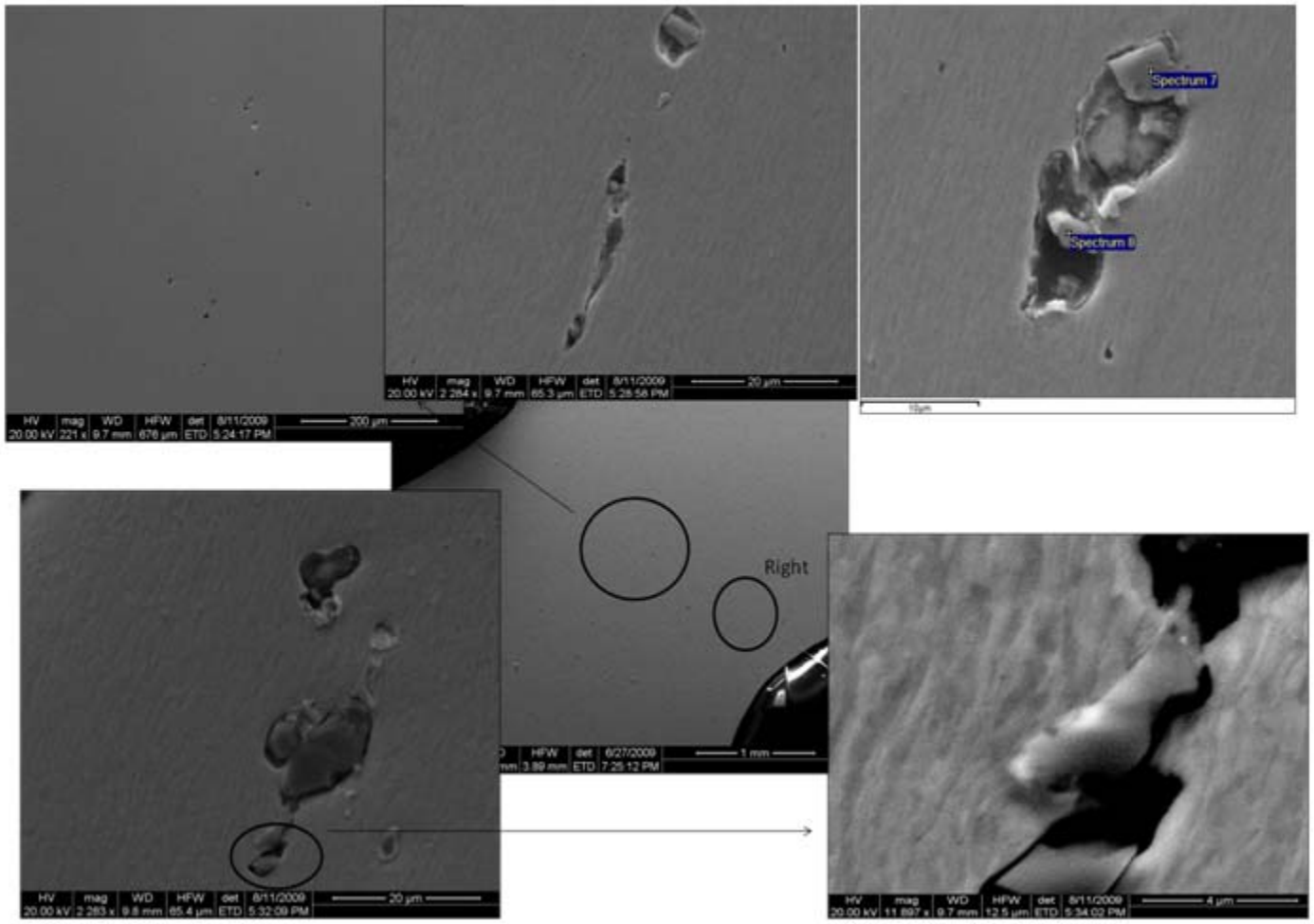

Fig. E.6 Crack initiation and propagation images of the crack edges of the shallow notched bar sample 2B5-I.

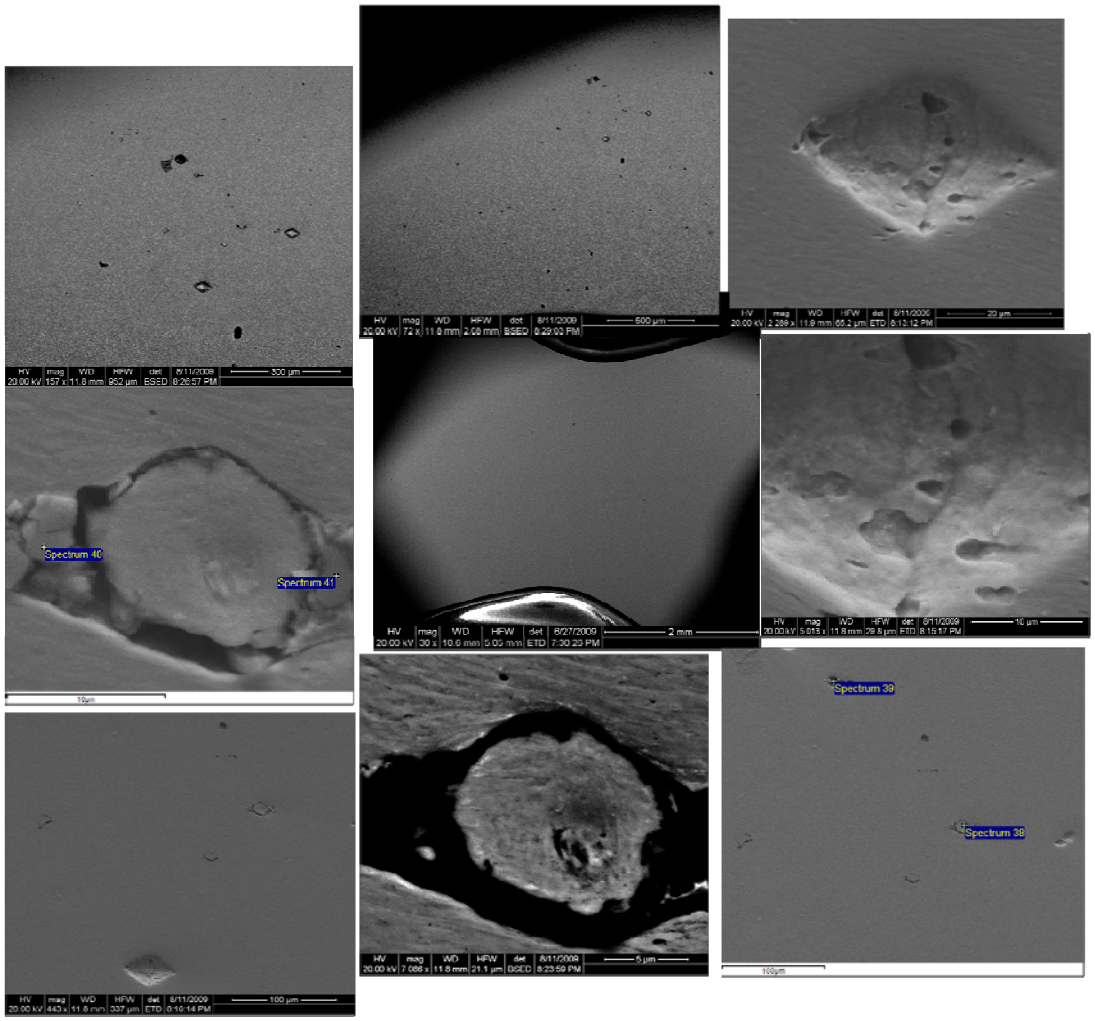

Fig. E.7 Crack initiation and propagation images of the crack edges of the shallow notched bar sample 2T2-I.

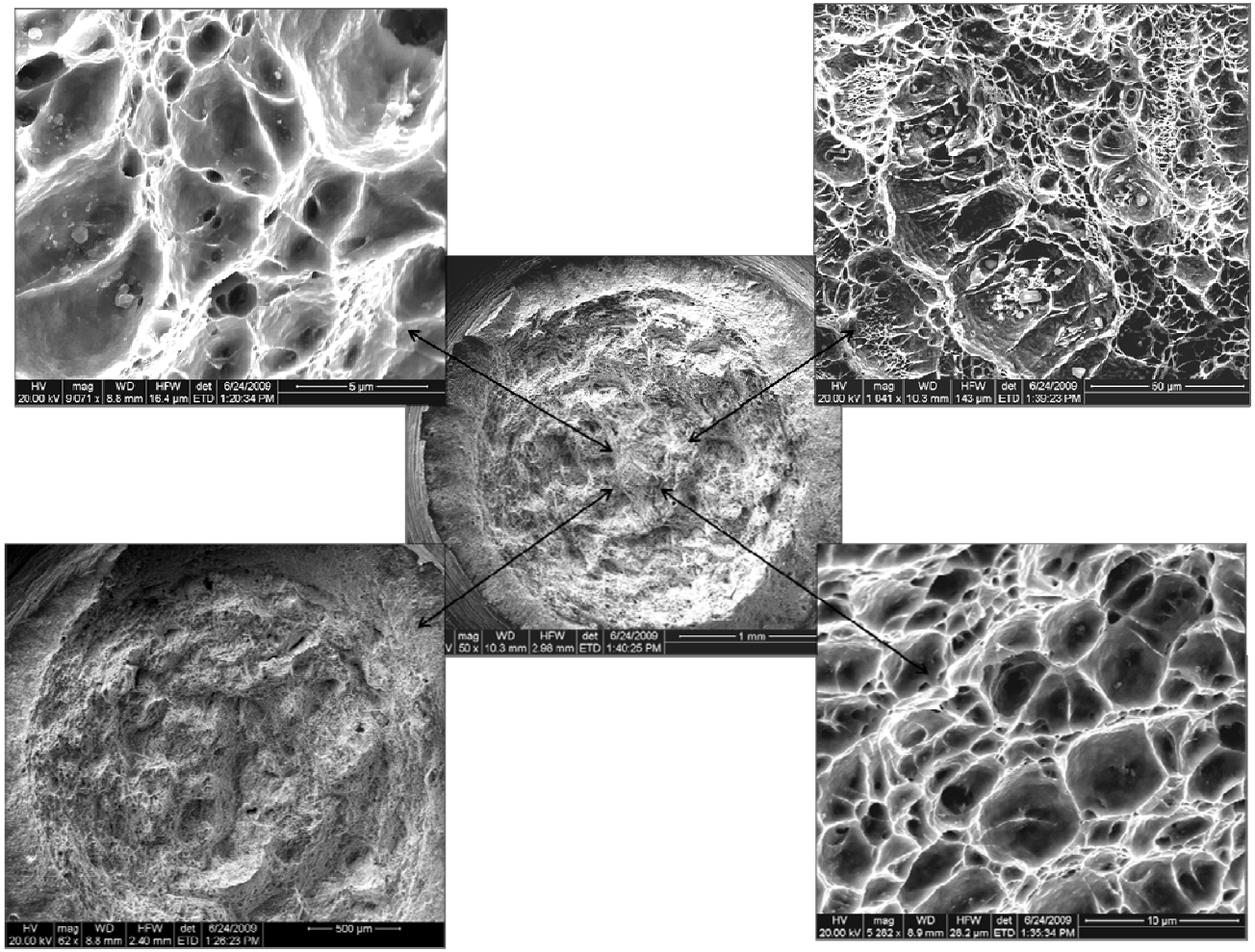

Fig. E.8 Fracture surfaces taken from the center of the broken sharp notched bar sample 2B3-R.

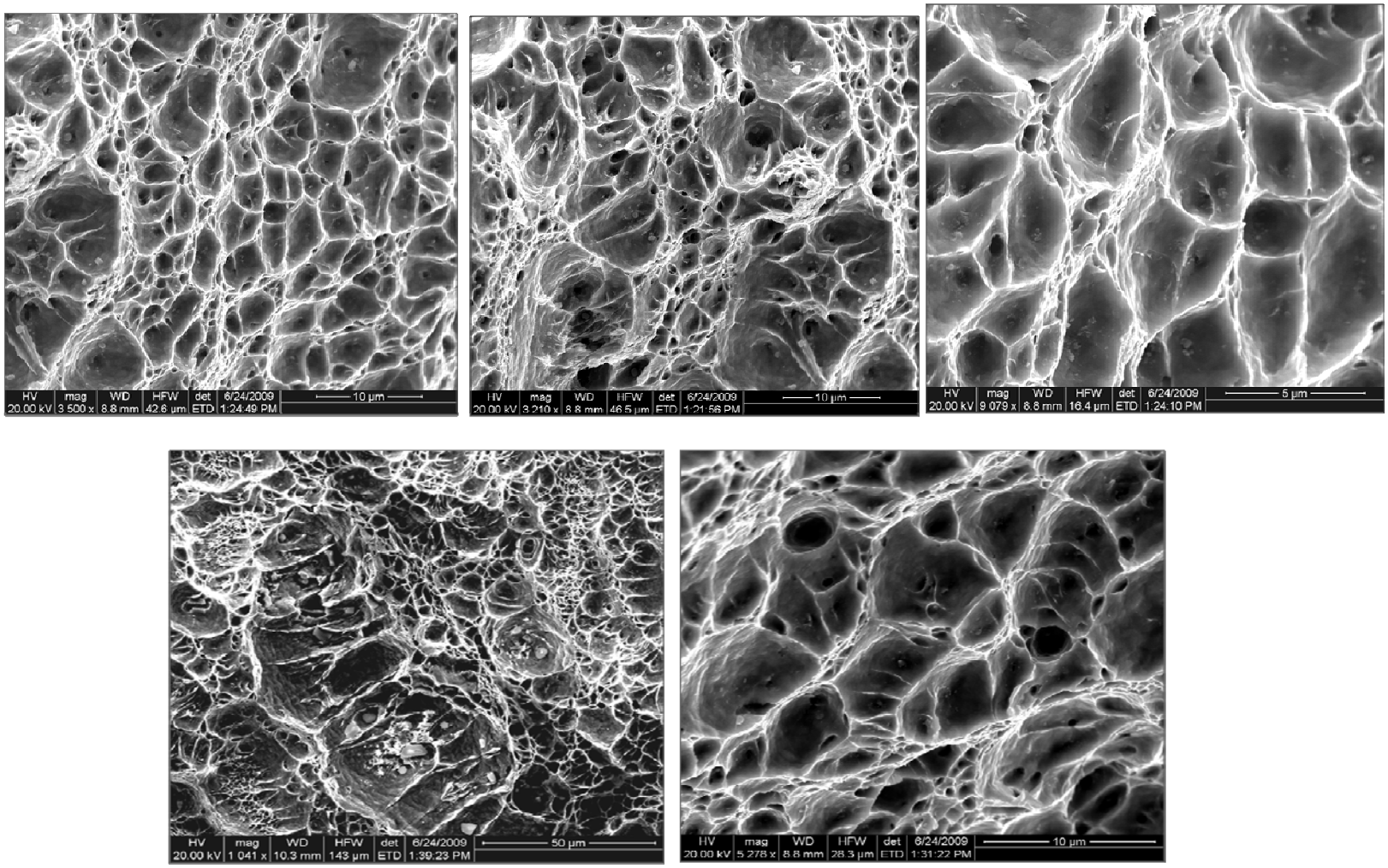

Fig. E.9 More fracture surfaces taken from the center of the broken sharp notched bar sample 2B3-R.

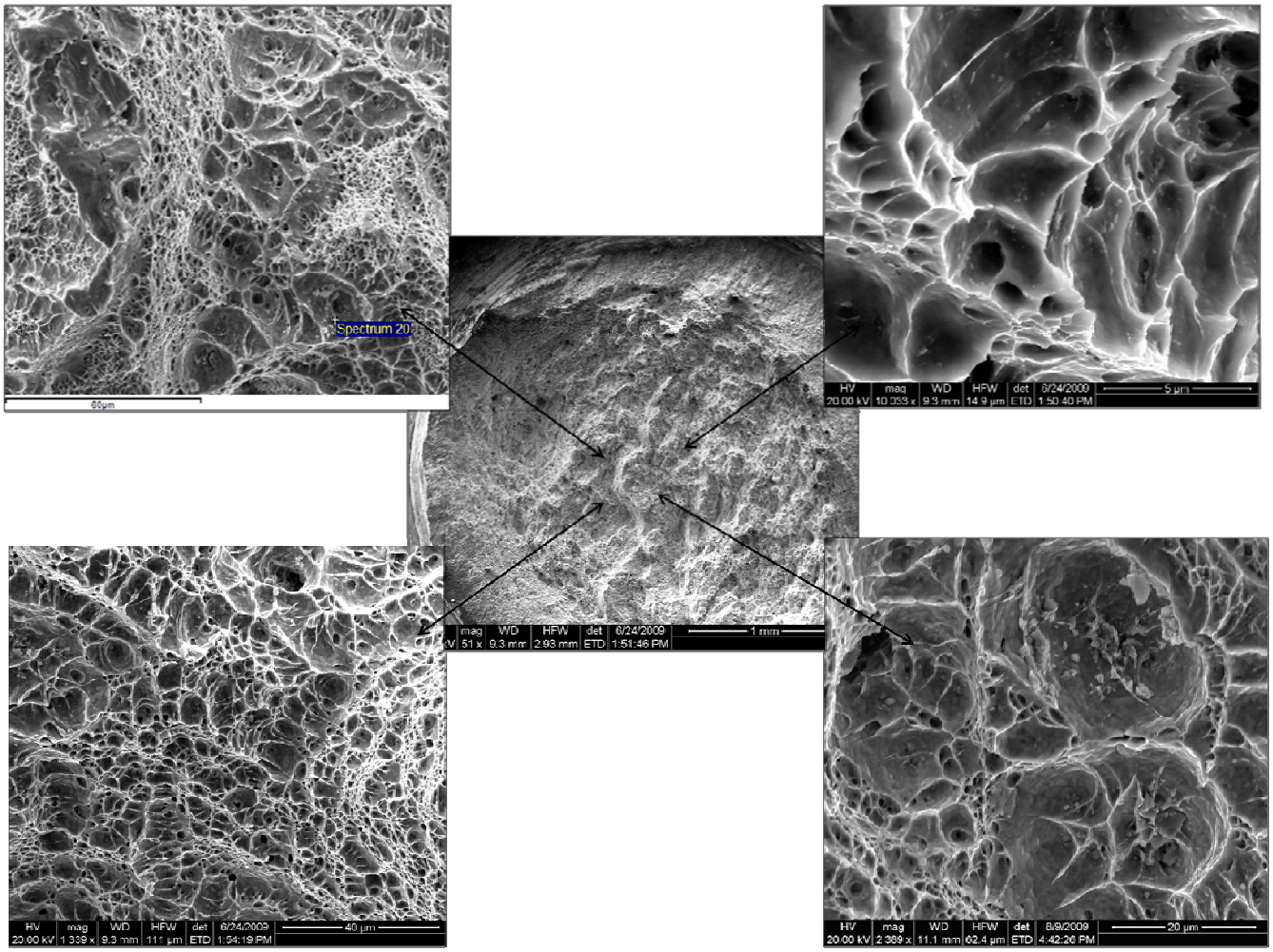

Fig. E.10 Fracture surfaces taken from the broken sharp notched bar sample 3B5-R.

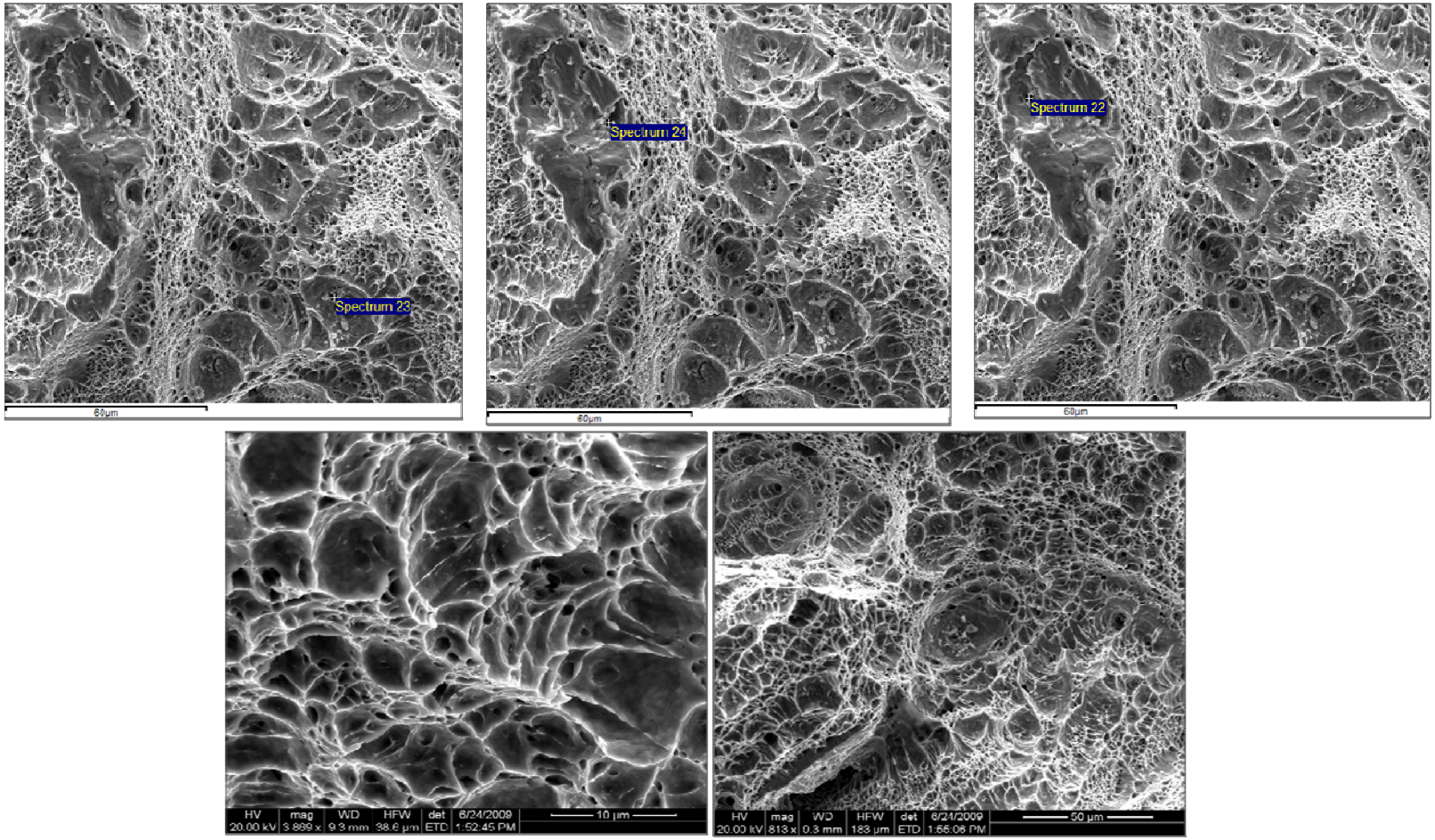

Fig. E.11 More fracture surfaces taken from the broken sharp notched bar sample 3B5-R.

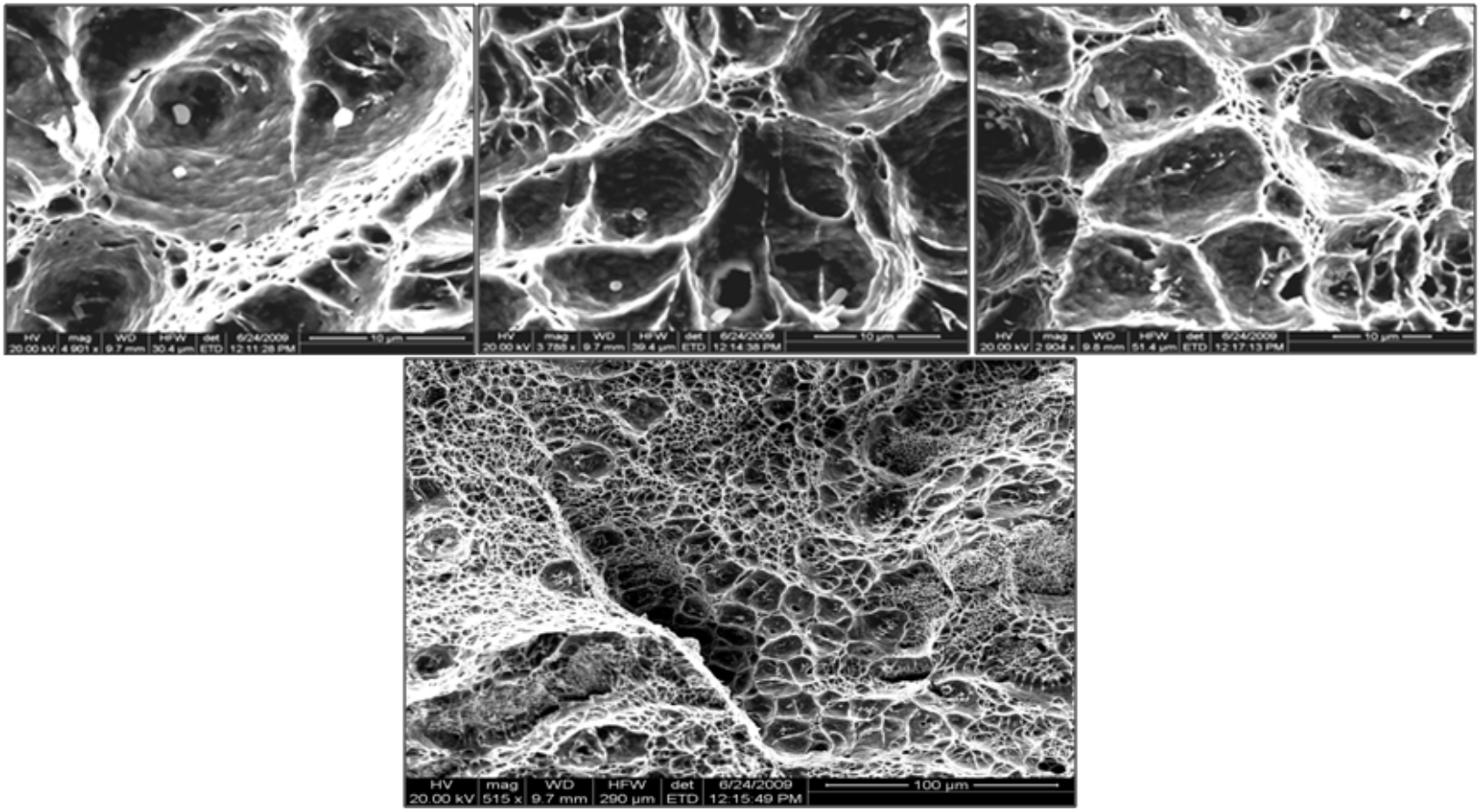

Fig. E.12 More fracture surfaces taken from the broken sharp notched bar sample 3T4-R.

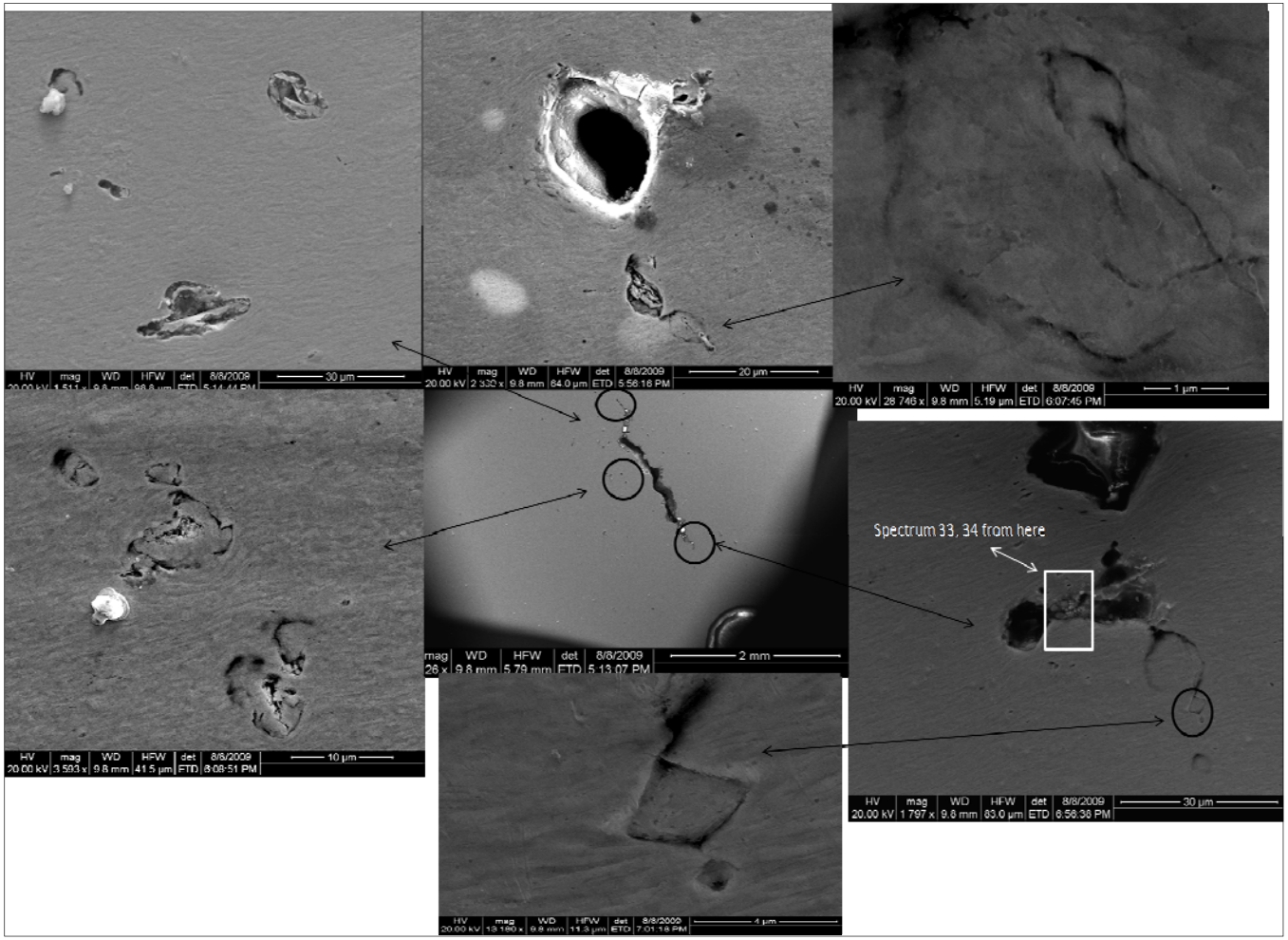

Fig. E.13 More crack initiation and propagation of the sharp notched bar sample 1B4-I.

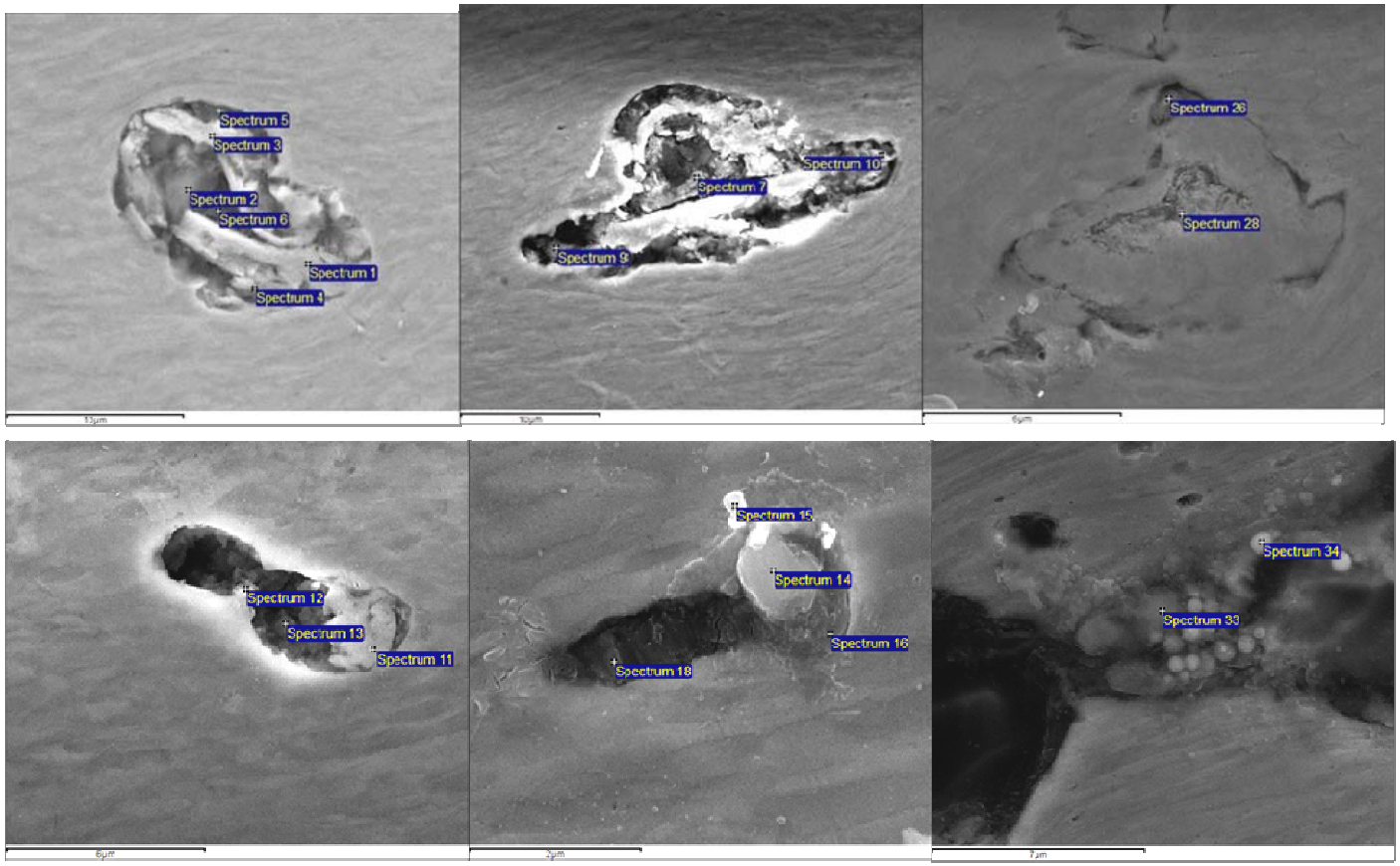

Fig. E.14 Crack initiation of the sharp notched bar sample 1B4-I.

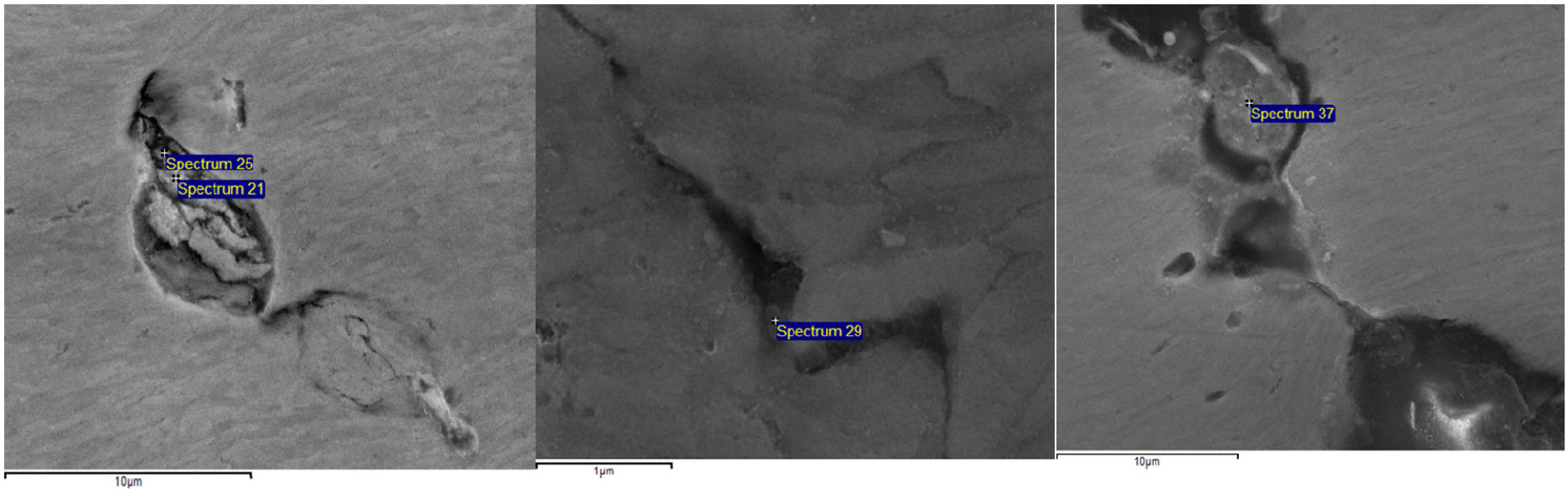

Fig. E.15 More crack initiation of the sharp notched bar sample 1B4-I.

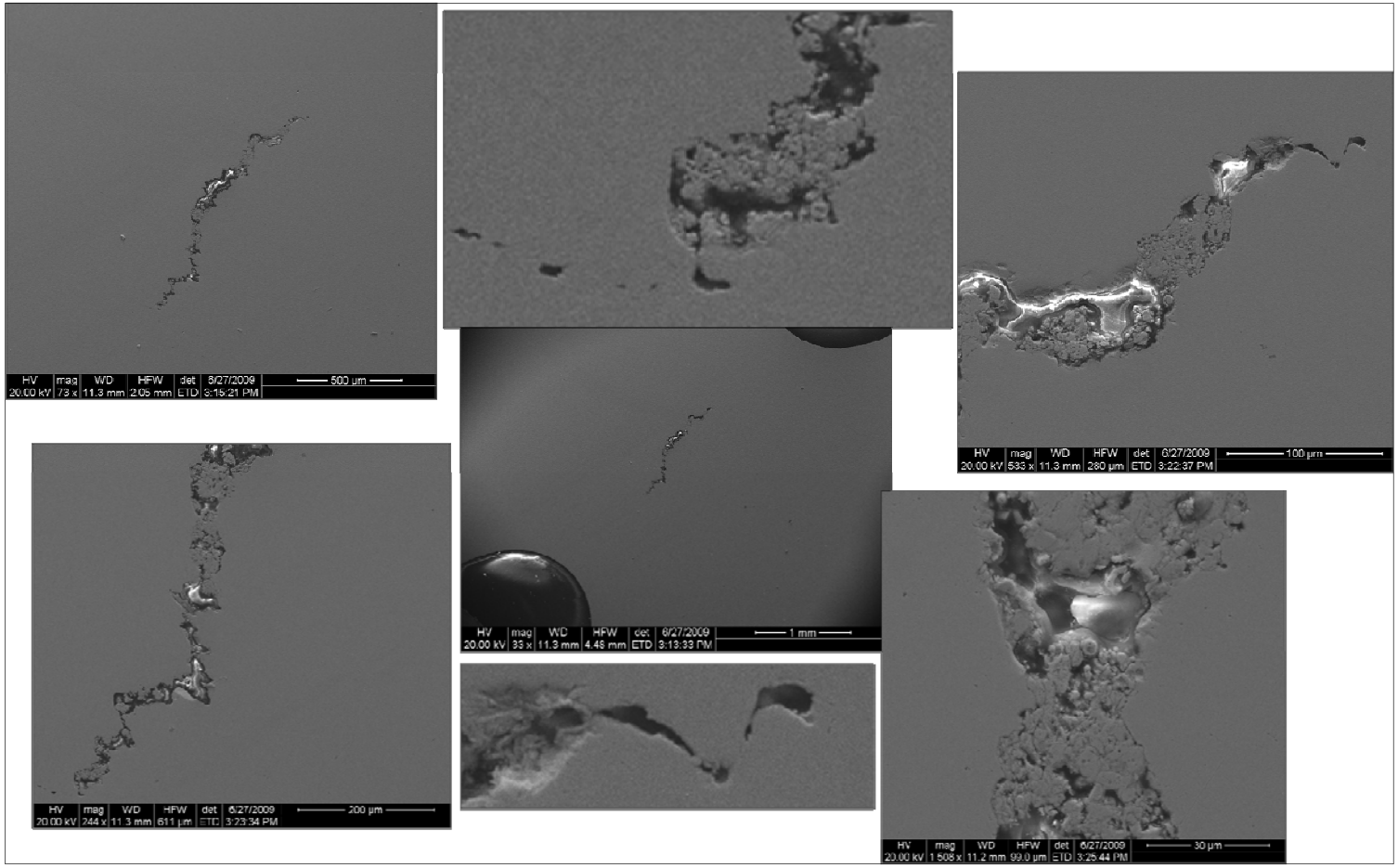

Fig. E.16 Crack initiation and propagation of the sharp notched bar sample 1B3-I, the images in the fine scale taken at the crack edges.

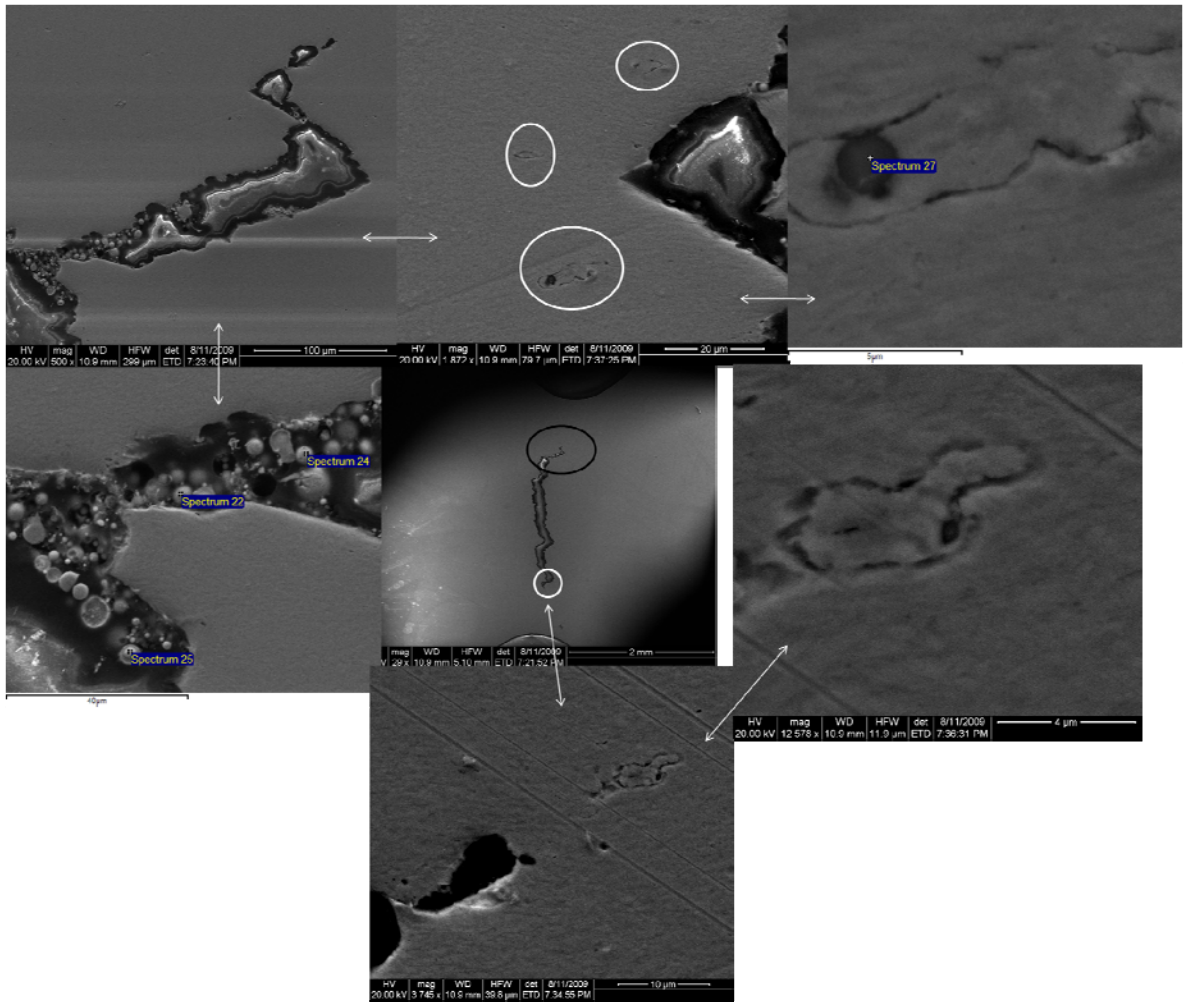

Fig. E.17 Crack initiation and propagation of the sharp notched bar sample 2B4-I.

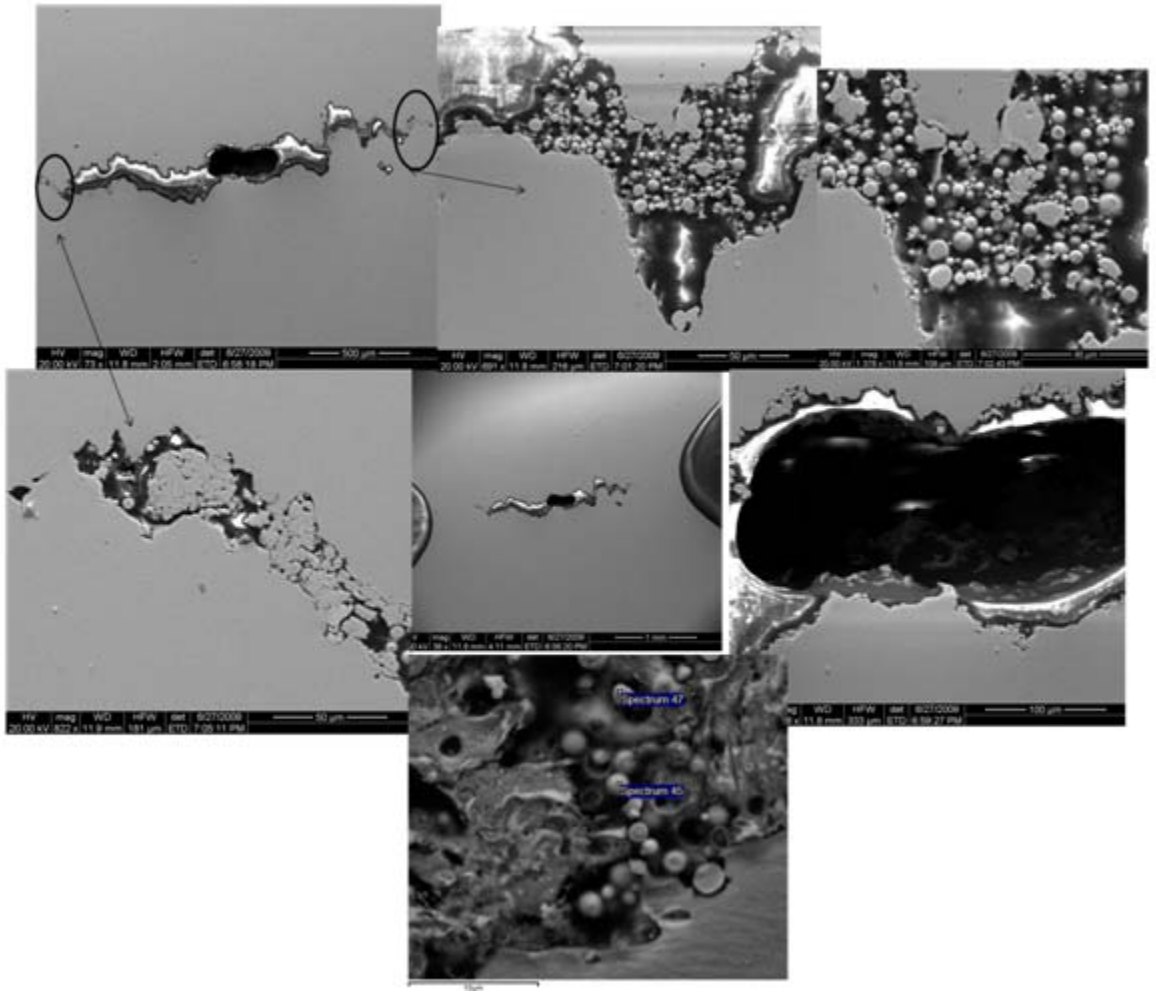

Fig. E.18 Crack initiation and propagation of the sharp notched bar sample 3T5-I.

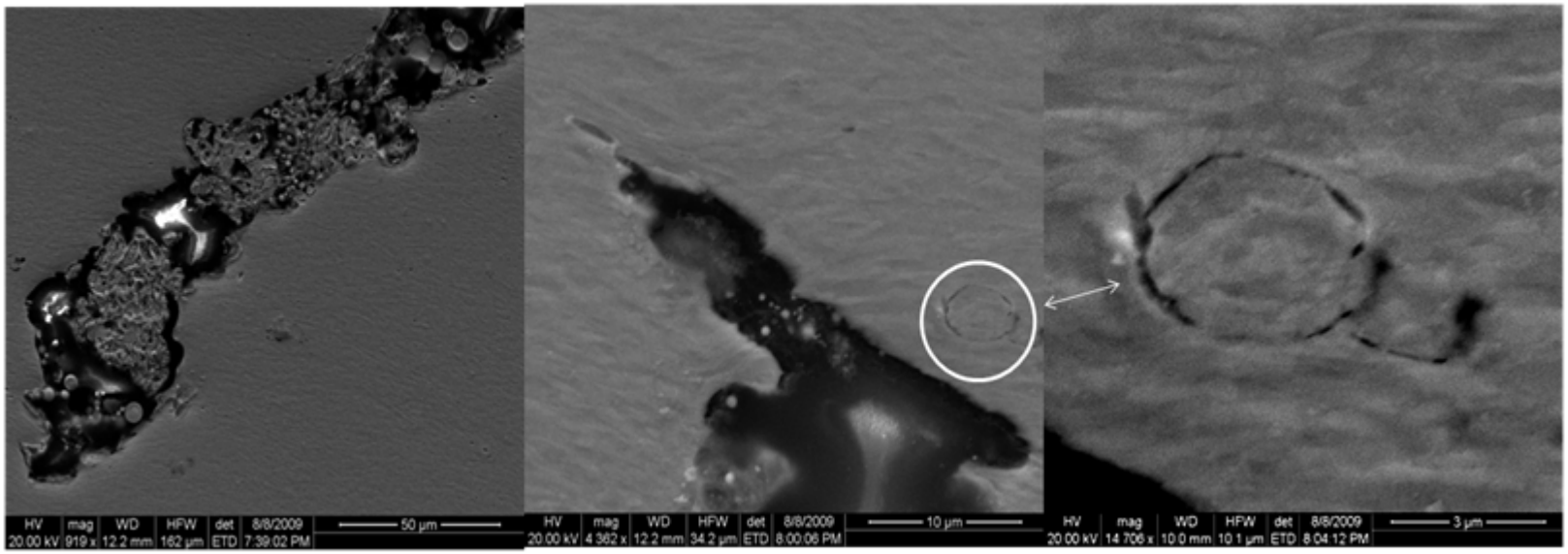

Fig. E.19 More crack initiation and propagation of the sharp notched bar sample 3T5-I.

APPENDIX F

SPECTRA FOR SECOND PHASE PARTICLES OF IF STEEL

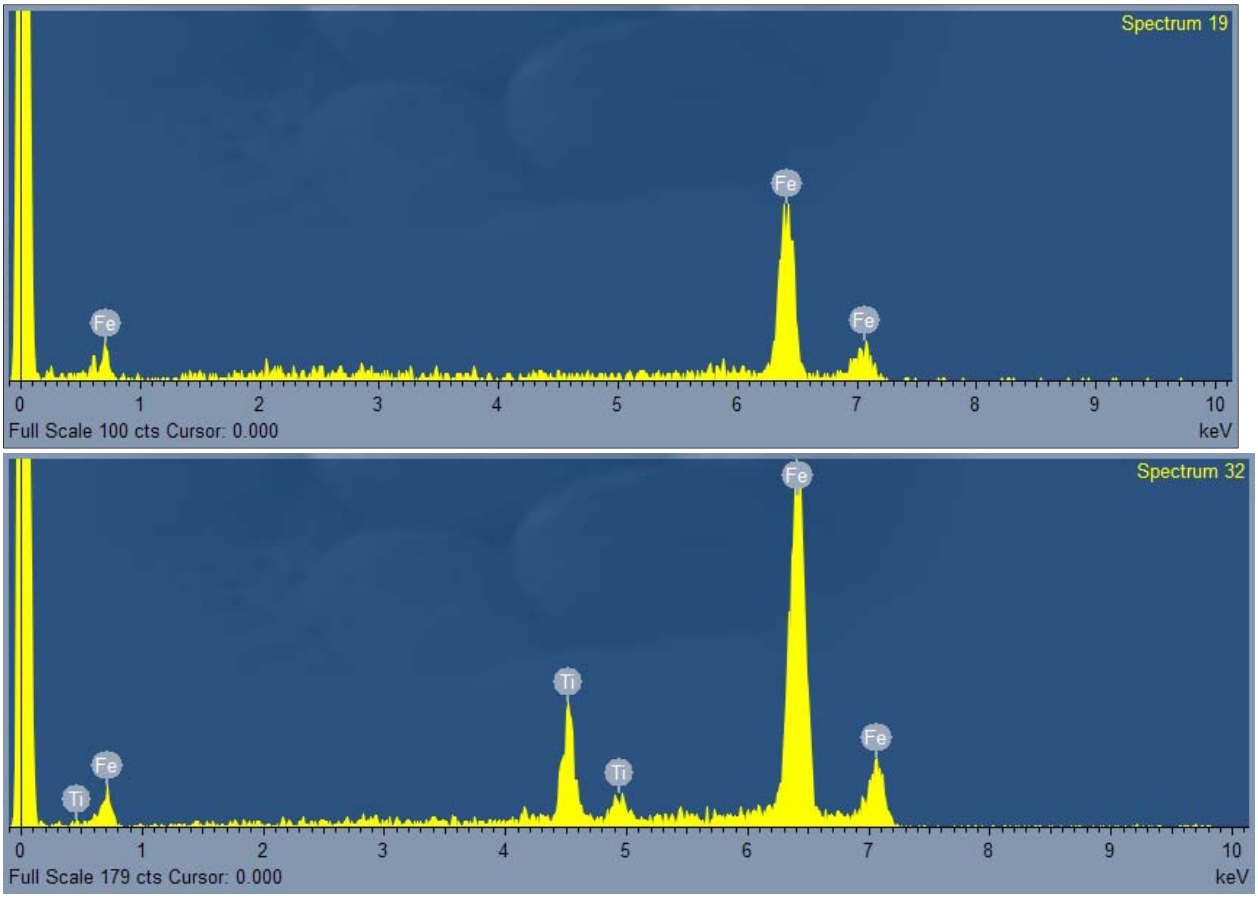

Fig. F.1 EDS energy spectrum diagram of the broken shallow notched bar sample 1T2-R.

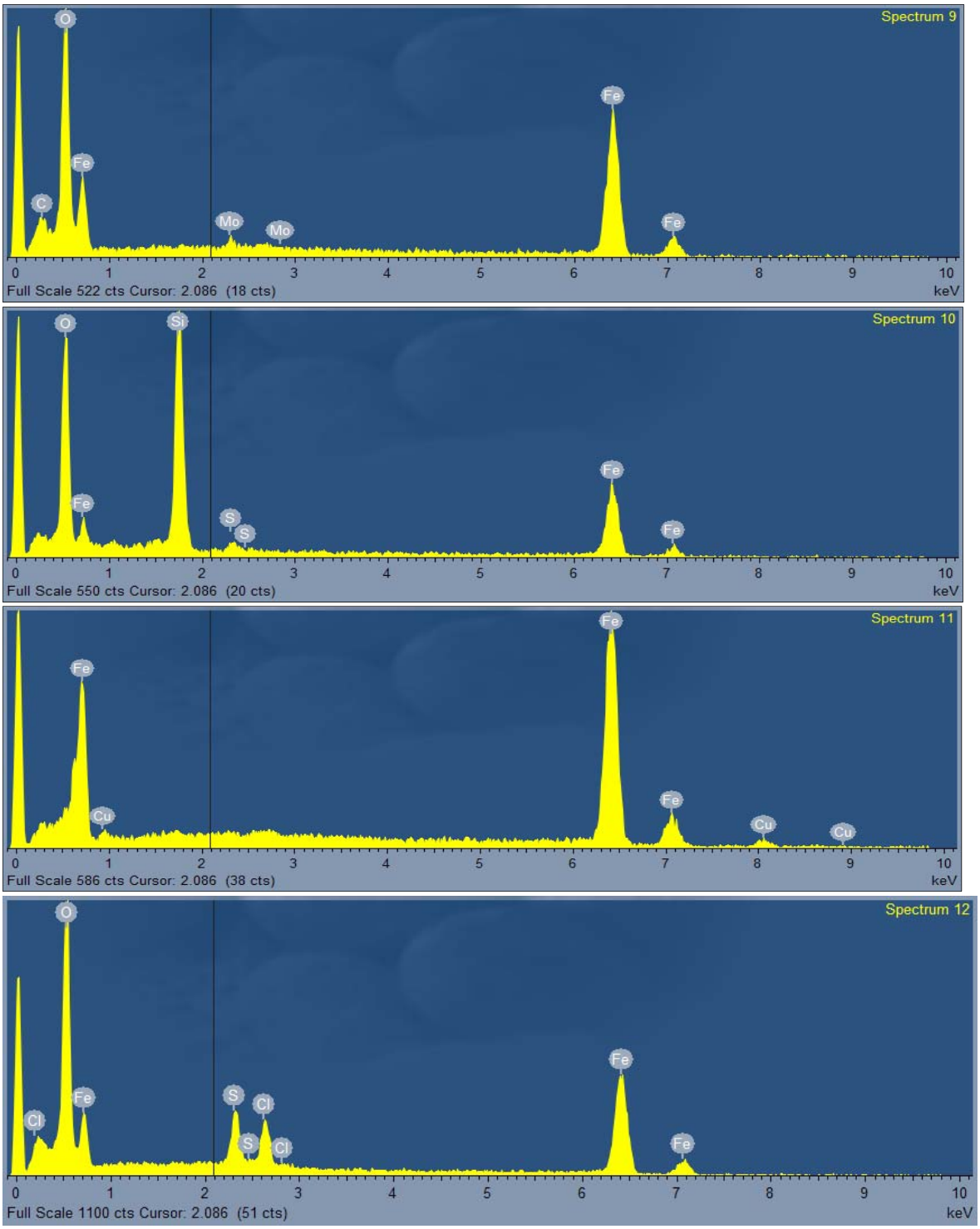

Fig. F.2 EDS energy spectrum diagram of the interrupted shallow notched bar sample 1B2-I.

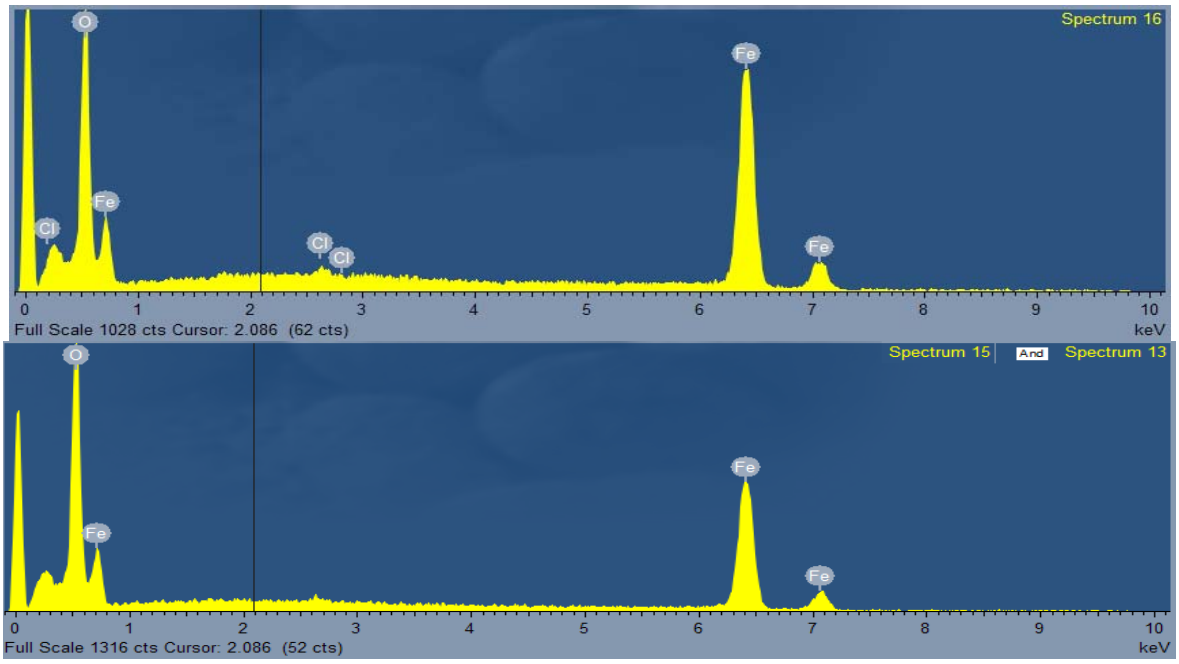

Fig. F.3 More EDS energy spectrum diagram of the interrupted shallow notched bar sample 1B2-I.

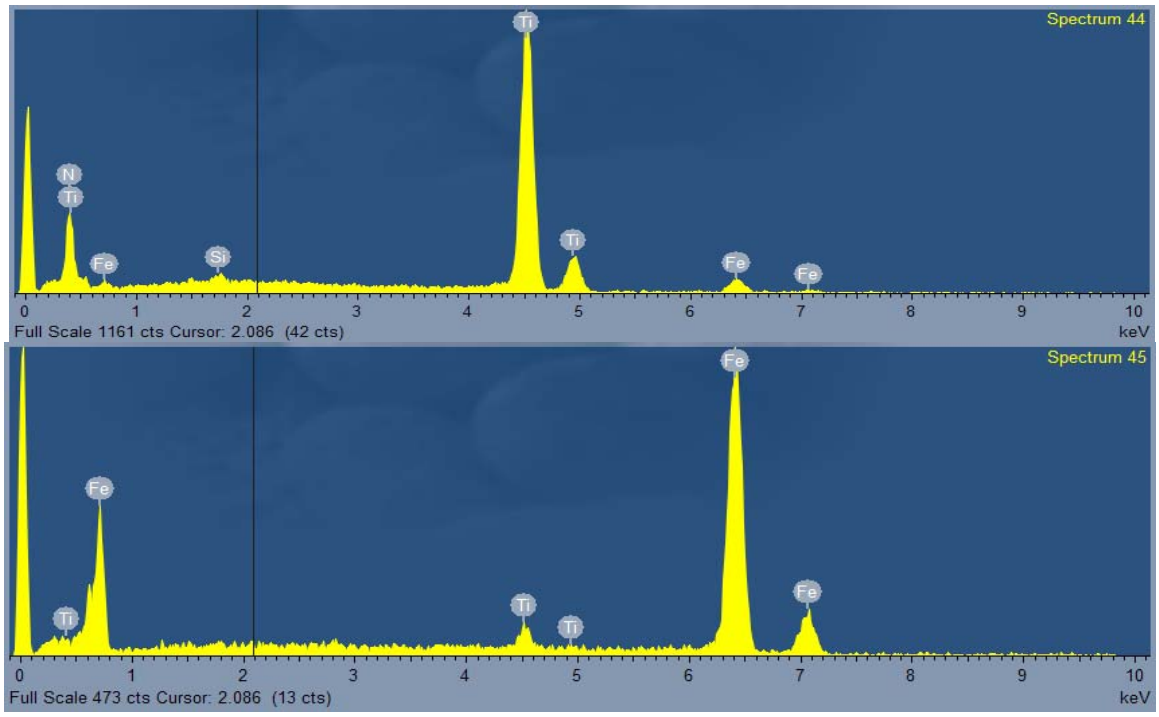

Fig. F.4 EDS energy spectrum diagram of the interrupted shallow notched bar sample 1B5-I.

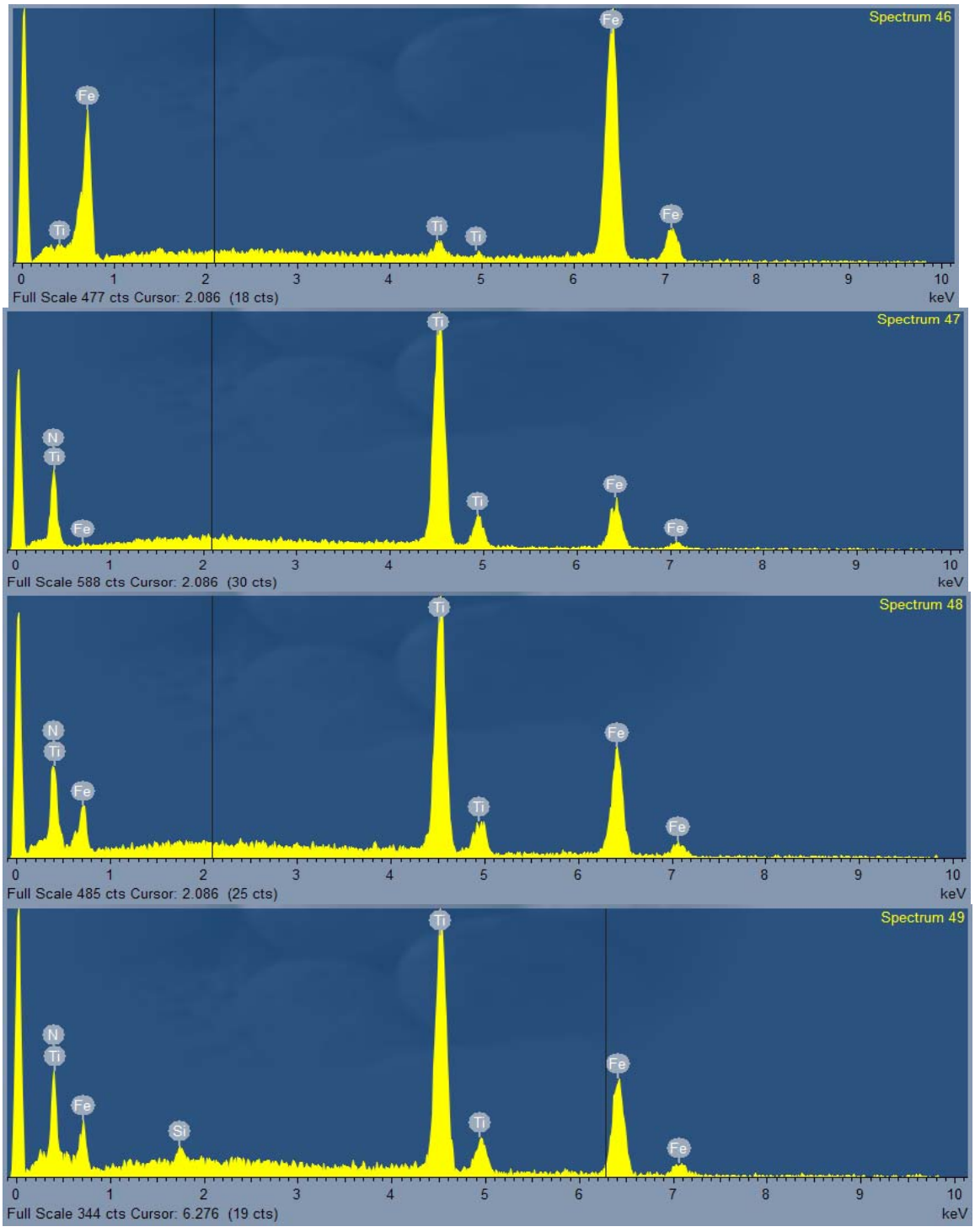

Fig. F.5 More EDS energy spectrum diagram of the interrupted shallow notched bar sample 1B5-I.

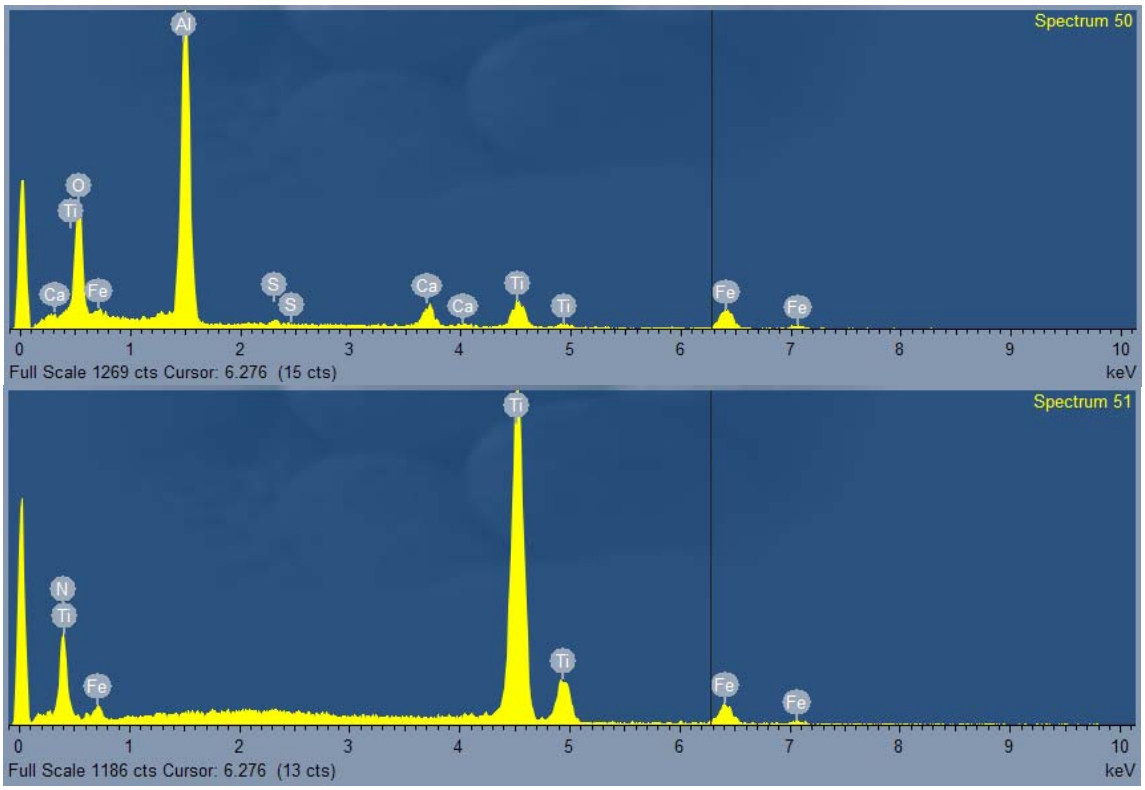

Fig. F.6 Additional EDS energy spectrum diagram of the interrupted shallow notched bar sample 1B5-I.

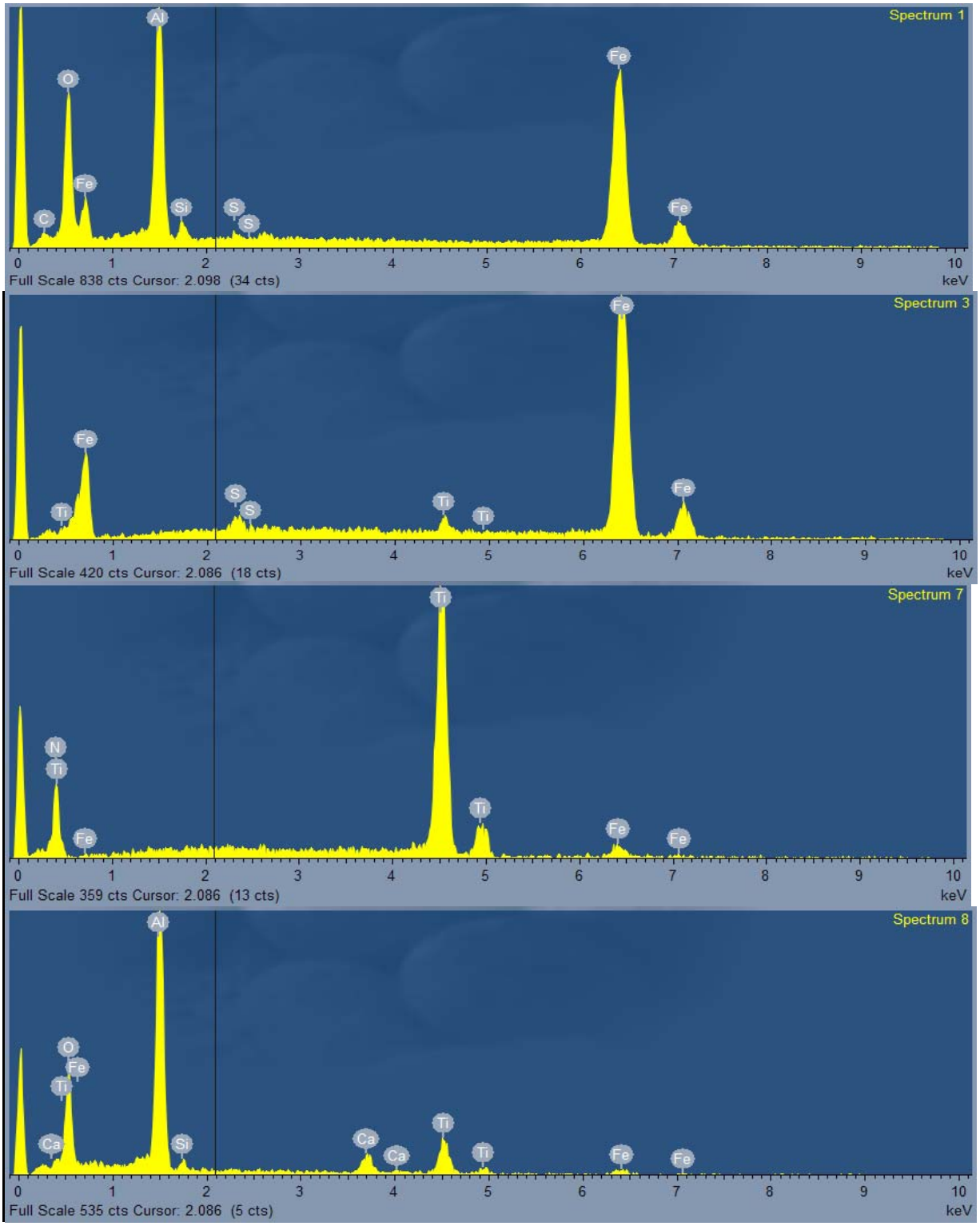

Fig. F.7 More EDS energy spectrum diagram of the interrupted shallow notched bar sample 2B5-I.

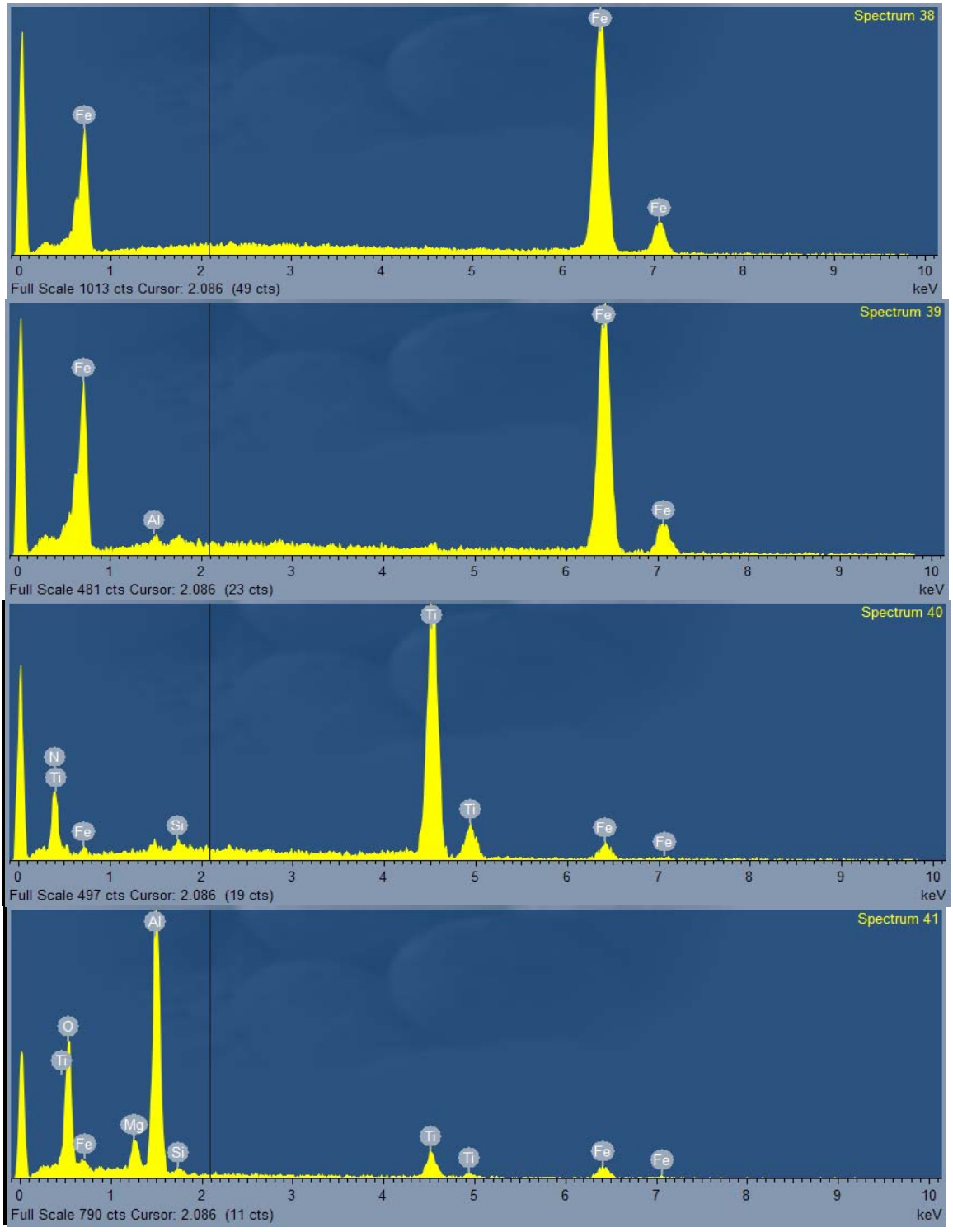

Fig. F.8 EDS energy spectrum diagram of the interrupted shallow notched bar sample 2T2-I.

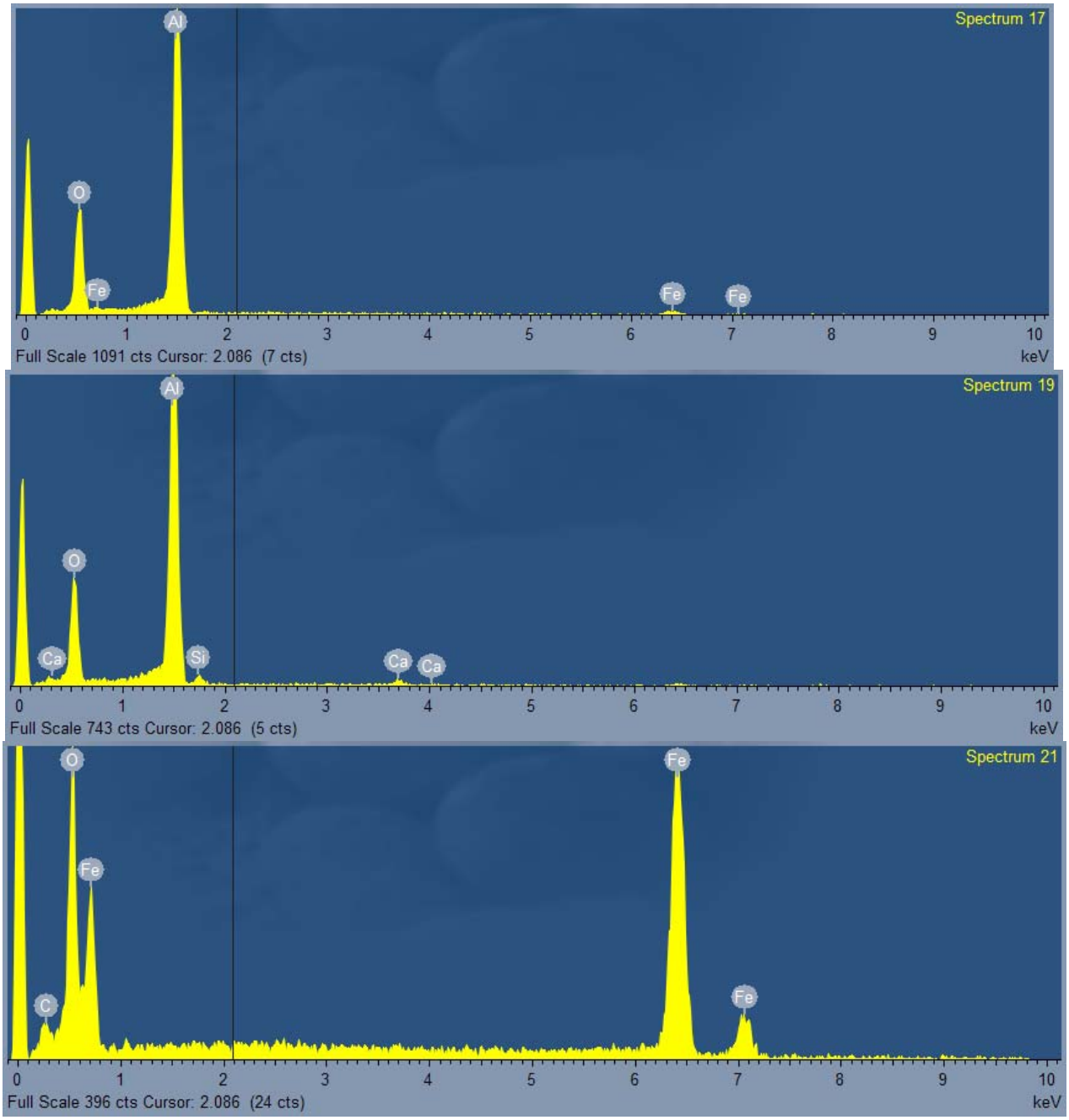

Fig. F.9 EDS energy spectrum diagram of the interrupted shallow notched bar sample 3T6-I.

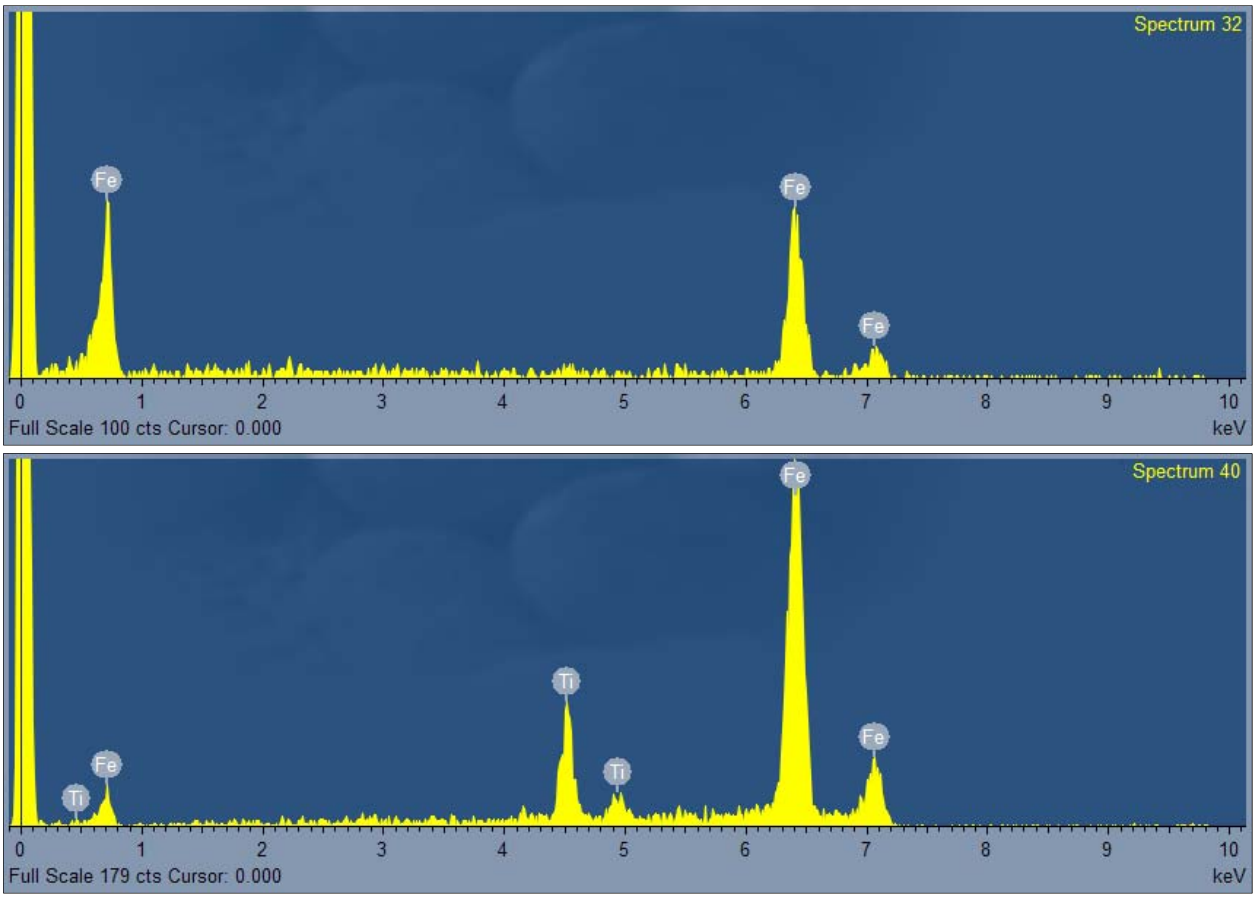

Fig. F.10 EDS energy spectrum diagram of the broken sharp notched bar sample 1T3-R.

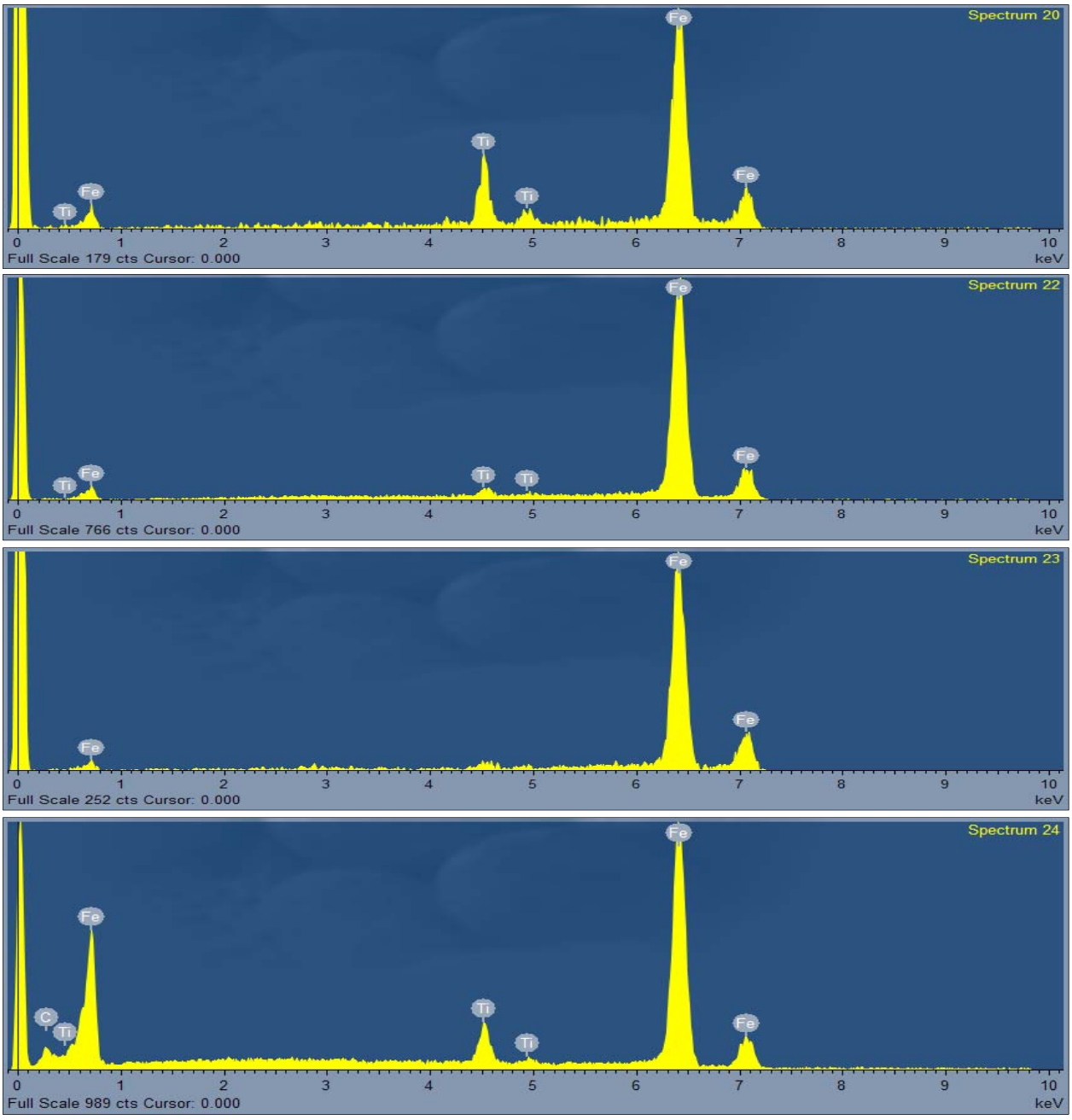

Fig. F.11 EDS energy spectrum diagram of the broken sharp notched bar sample 3B5-R.

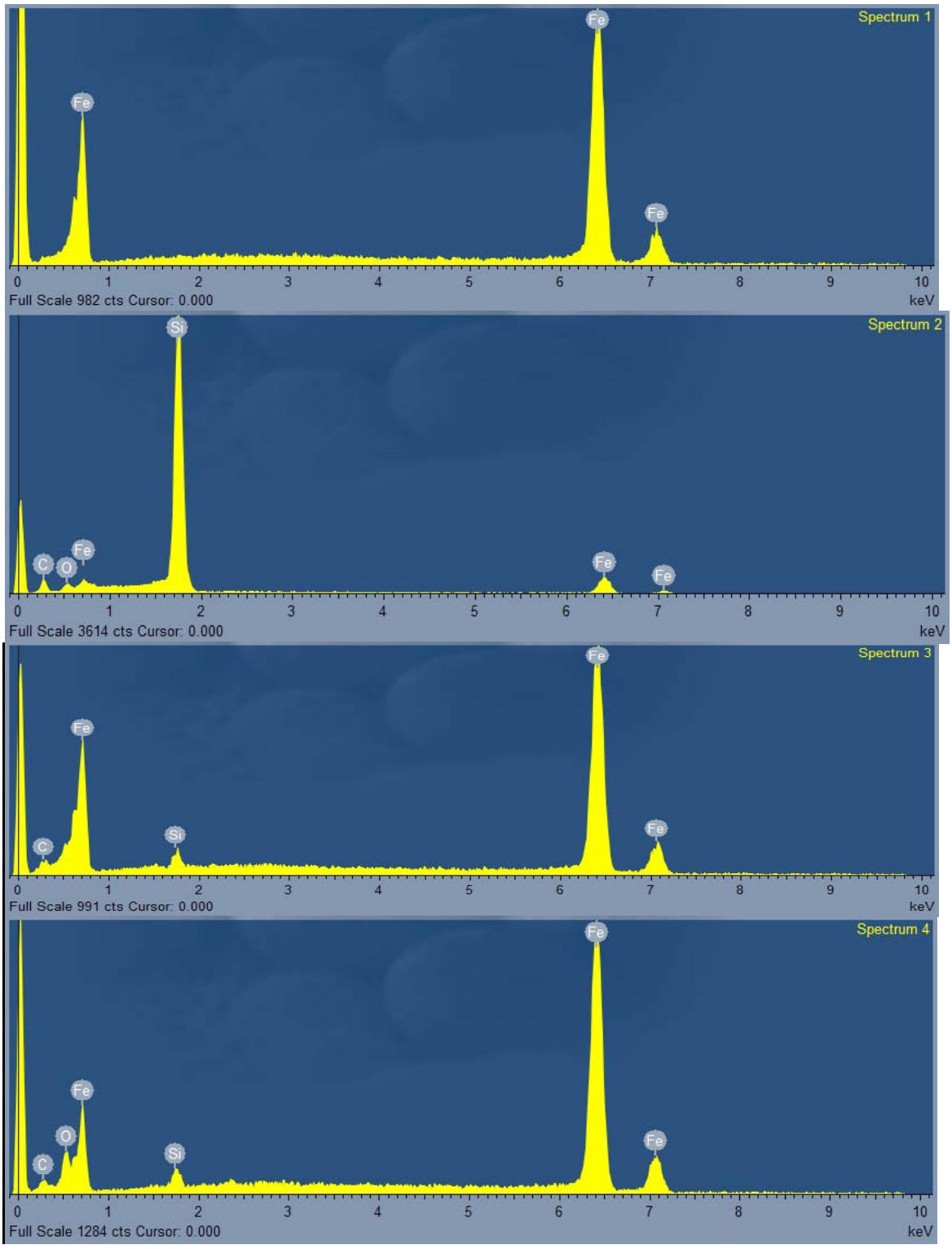

Fig..F.12 EDS energy spectrum diagram of the interrupted sharp notched bar sample 1B4-I.

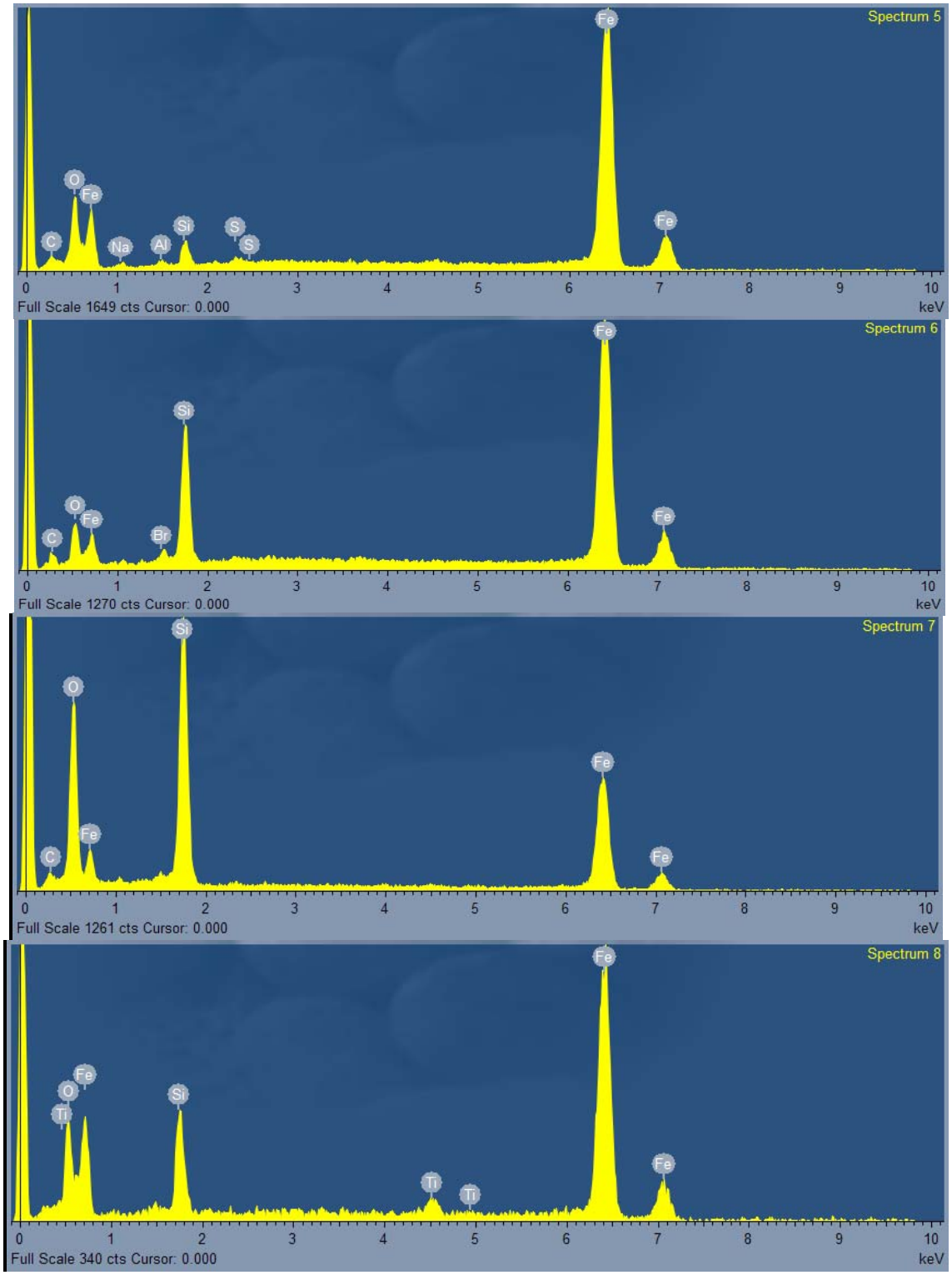

Fig. F.13 EDS energy spectrum diagram of the interrupted sharp notched bar sample 1B4-I.

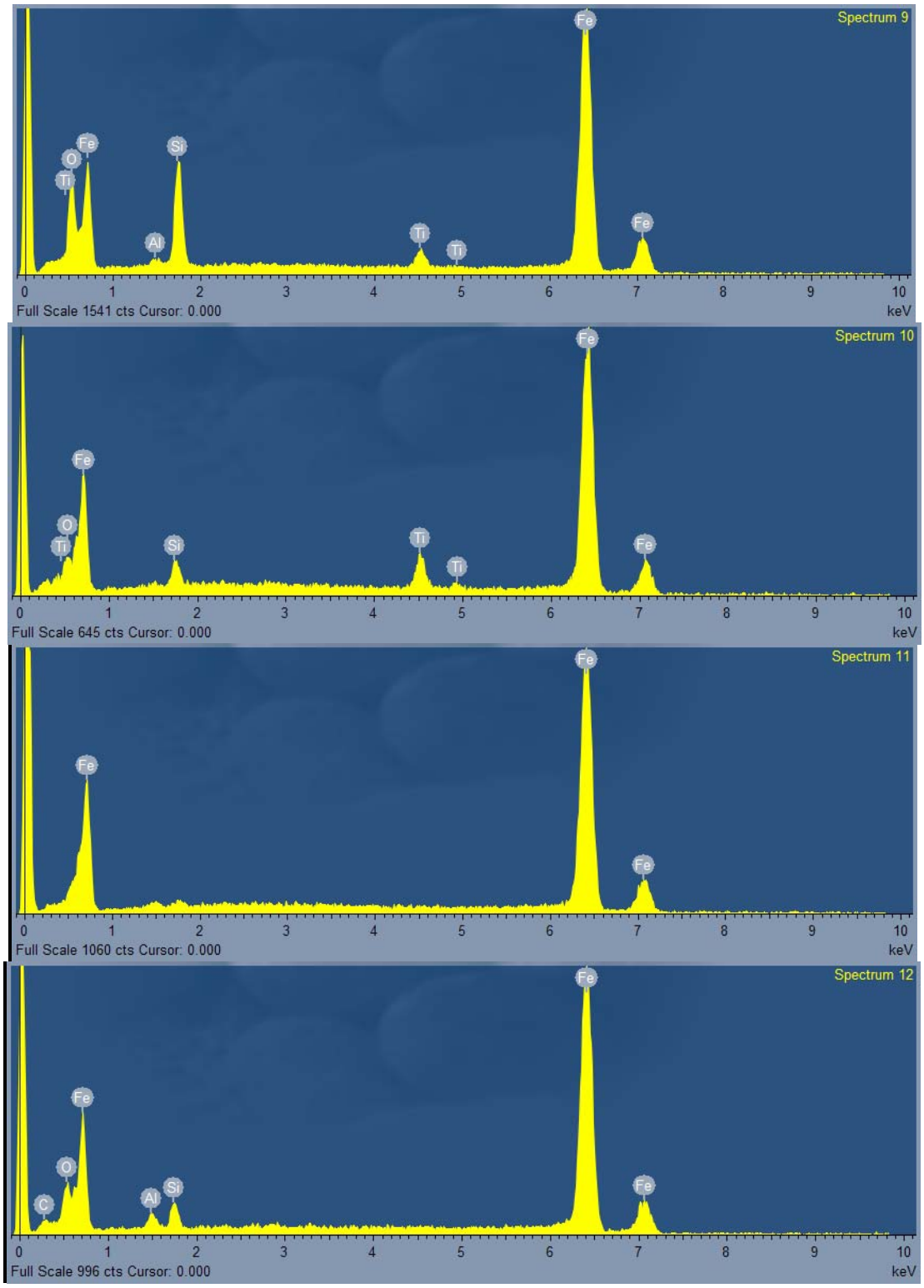

Fig. F.14 More EDS energy spectrum diagram of the interrupted sharp notched bar sample 1B4-I.

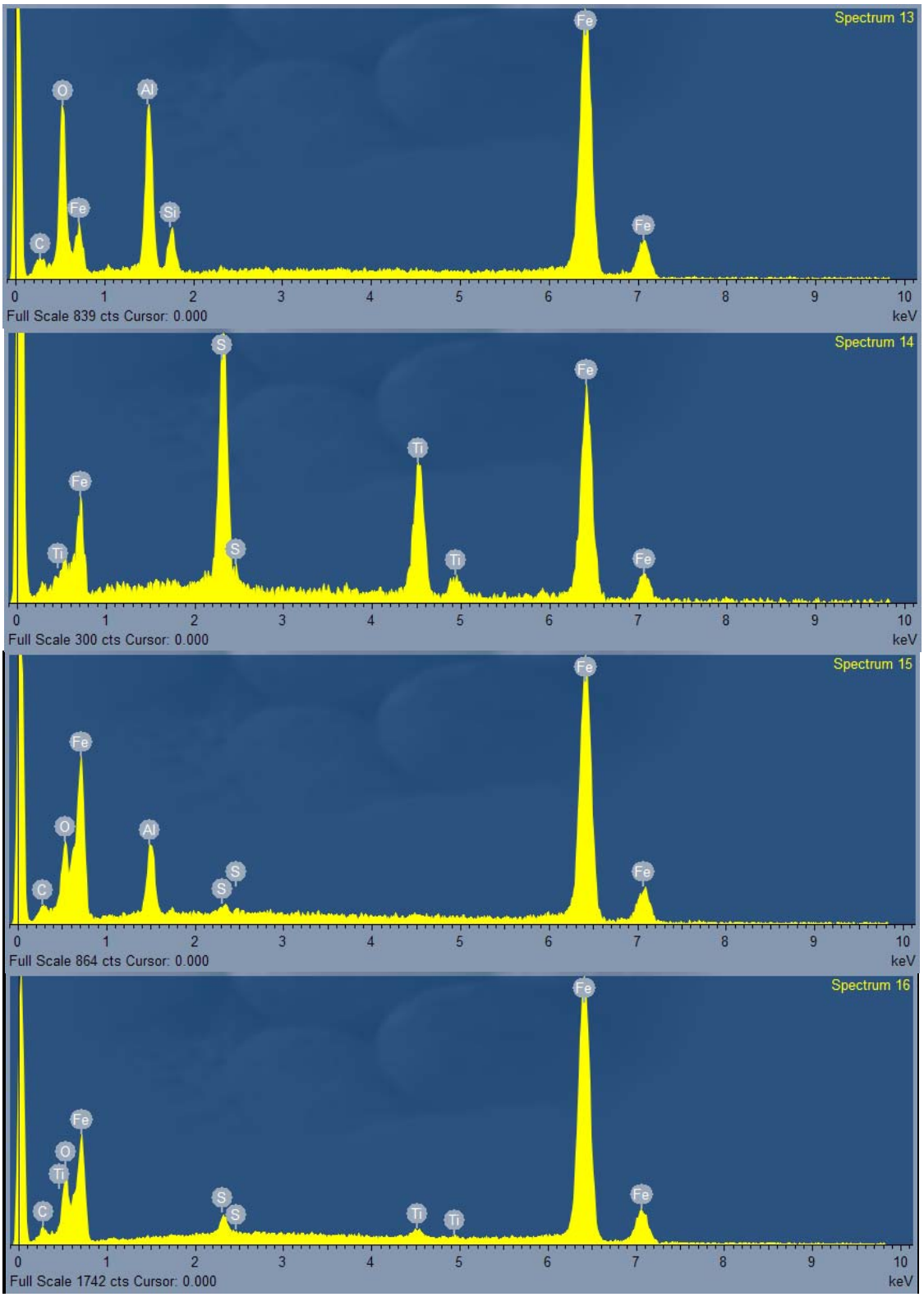

Fig. F.15 Additional EDS energy spectrum diagram of the interrupted sharp notched bar sample 1B4-I.

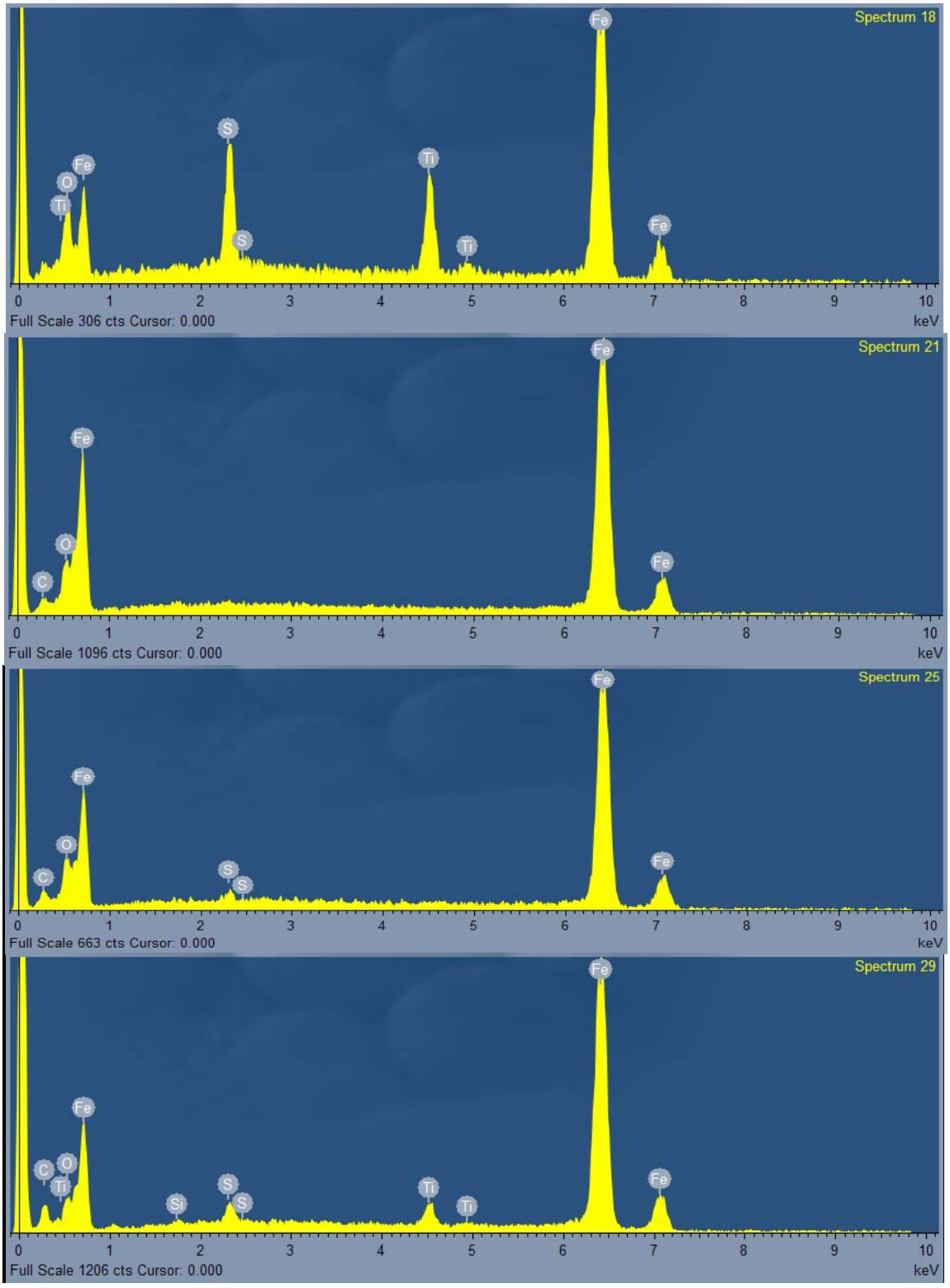

Fig. F.16 EDS diagram of the interrupted sharp notched bar 1B4-I.

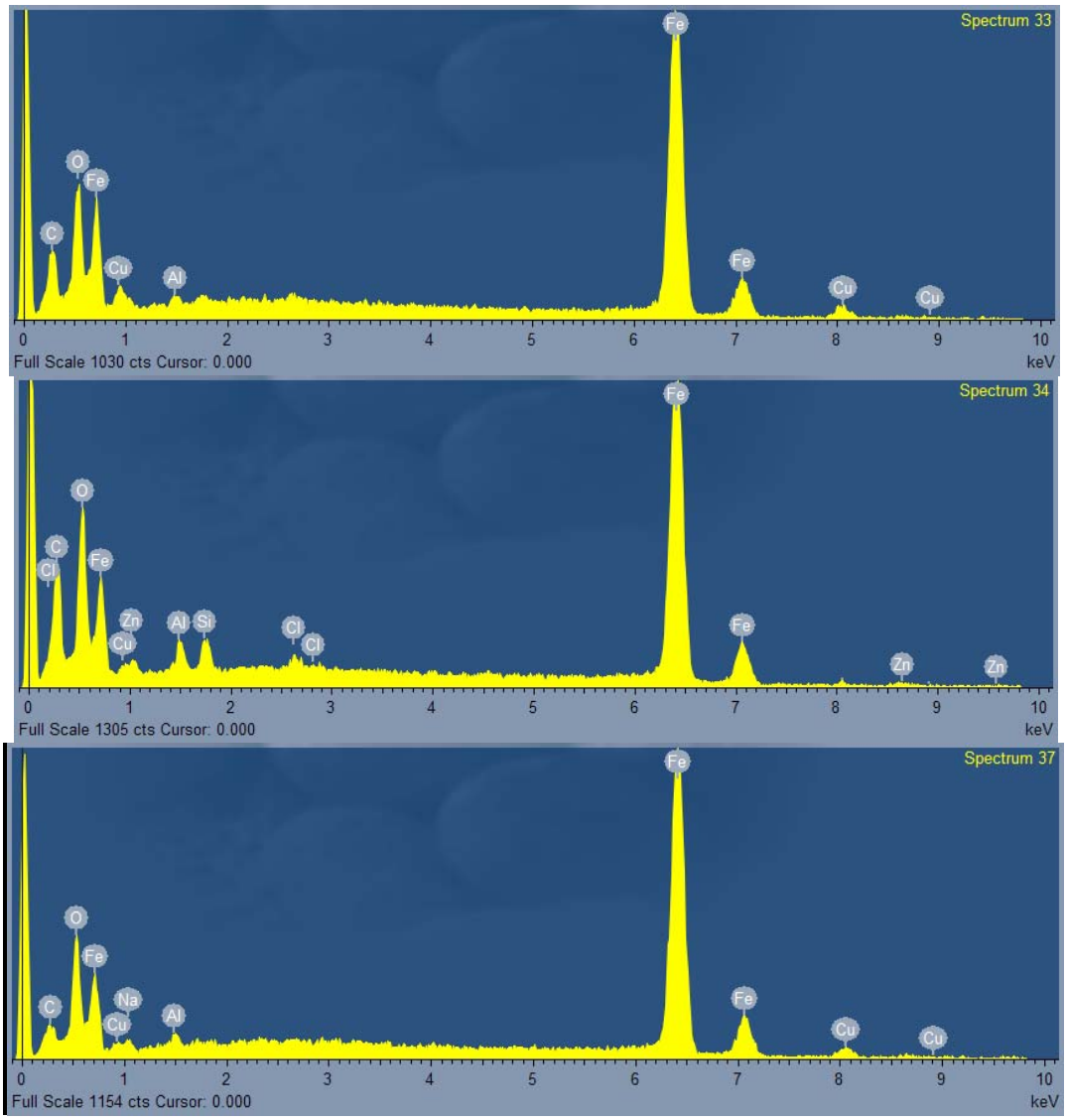

Fig. F.17 More EDS diagram of the interrupted sharp notched bar 1B4-I.

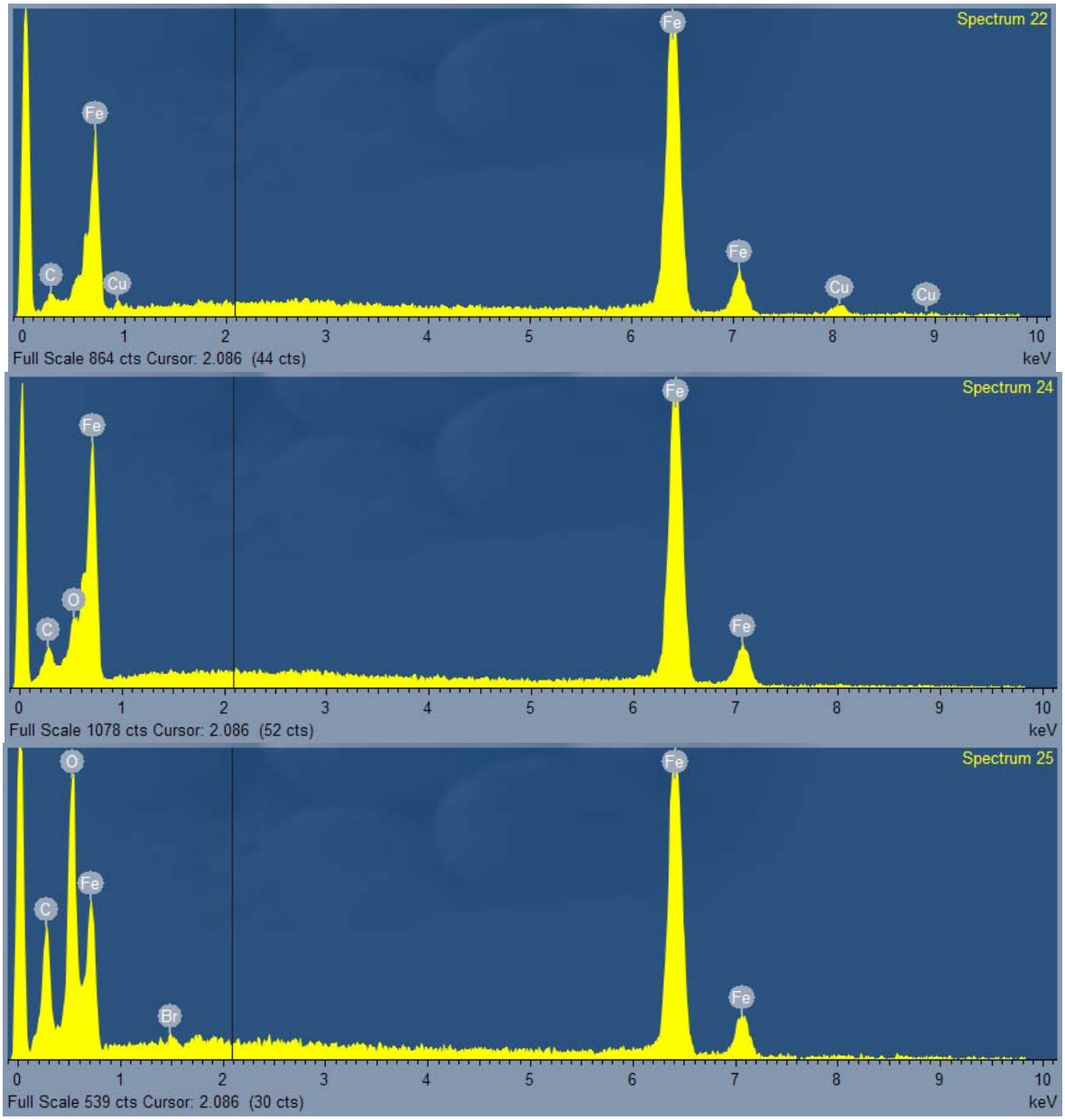

Fig. F.18 EDS energy spectrum diagram of the interrupted sharp notched bar sample 2B4-I.

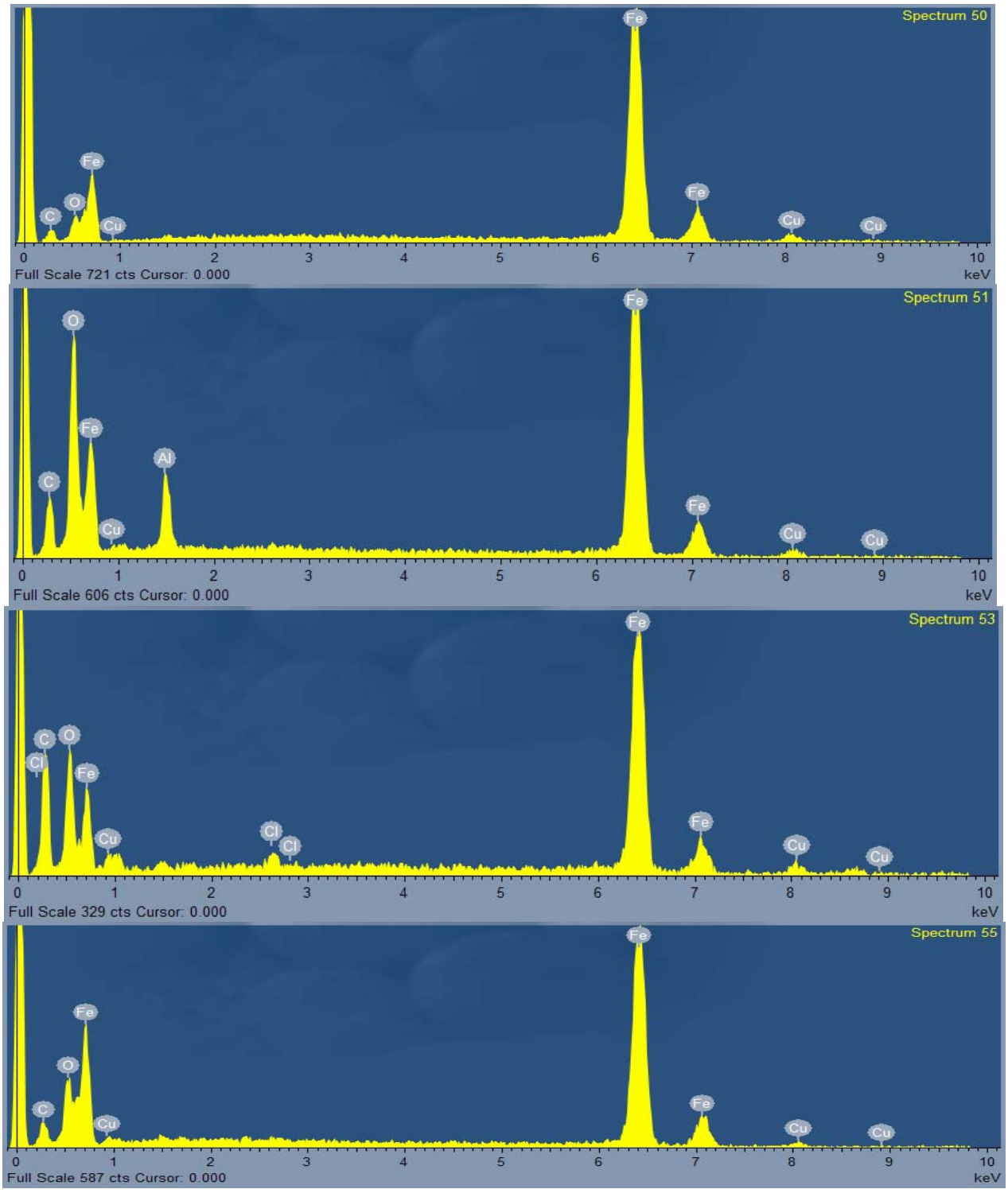

Fig. F.19 EDS energy spectrum diagram of the interrupted sharp notched bar sample 2T3-I.

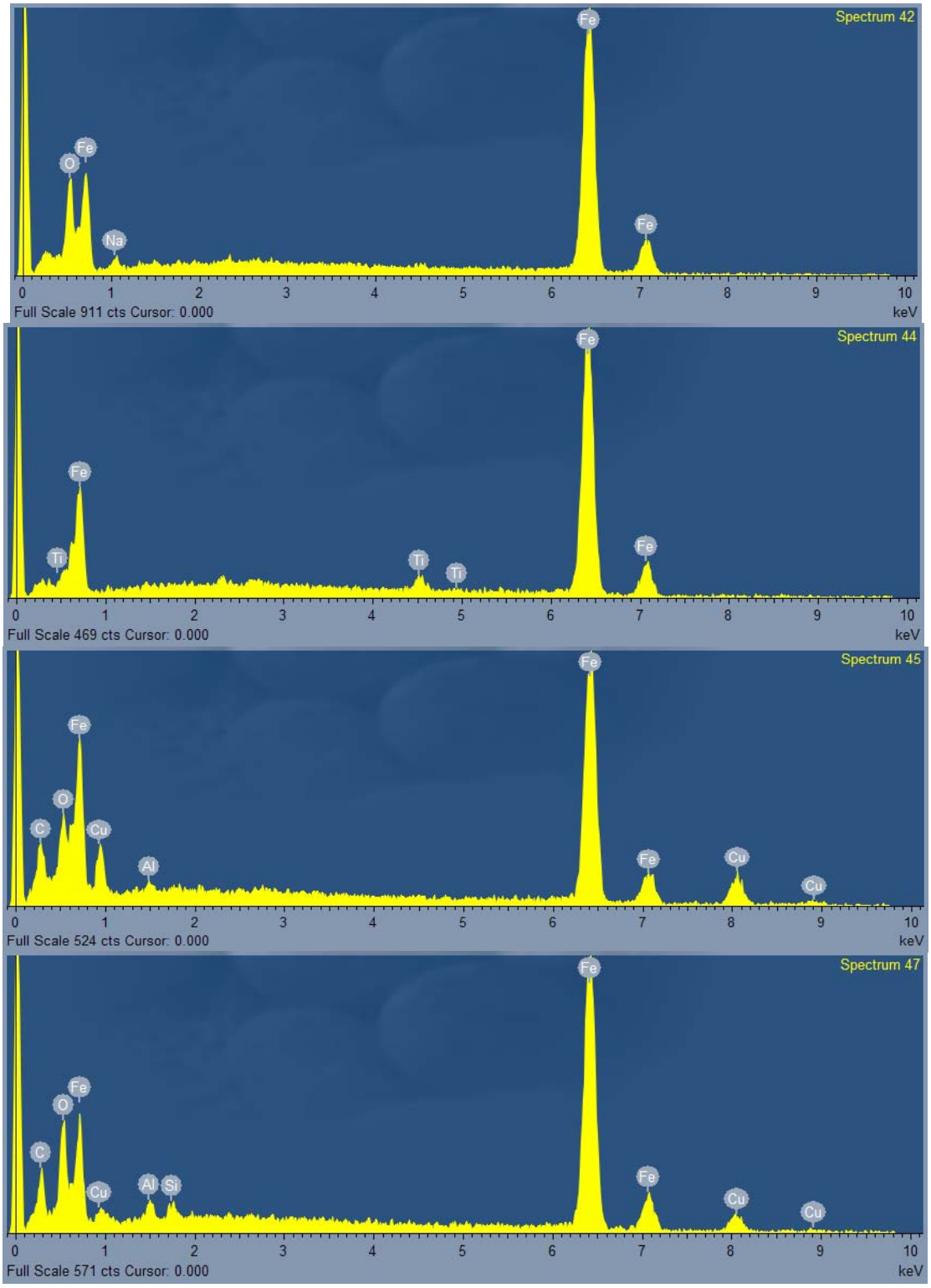

Fig. F.20 More EDS energy spectrum diagram of the interrupted sharp notched bar sample 3T5-I.

VITA

Nisrin Rizek Abdel Al was born in Irbid, Jordan. She attended her elementary and high school in Ramtha, Jordan, where she graduated with a 3.9 GPA. After that she was accepted into the Mechanical Engineering Department at Jordan University of Science and Technology. In 2005, she obtained her bachelor's degree in mechanical engineering with high honors.

She received a fellowship from Jordan University of Science and Technology to pursue her master's and Ph.D. degrees at Texas A&M University in the field of Aerospace Engineering, and she graduated in 2009.

She can be reached at the following address:

Texas A&M University

Department of Aerospace Engineering

H.R. Bright Building, Rm. 701, Ross Street - TAMU 3141

College Station TX 77843-3141

nasorahmech@yahoo.com